UNIVERSIDAD COMPLUTENSE DE MADRID

FACULTAD DE CIENCIAS FÍSICAS

TESIS DOCTORAL

Multifractalidad, dinámica exótica, comportamientos de escala y transiciones de fase cuánticas en sistemas complejos

Multifractality, exotic dynamics, scaling and quantum phase transitions in complex systems

MEMORIA PARA OPTAR AL GRADO DE DOCTOR

PRESENTADA POR

Isidoro González-Adalid Pemartín

DIRECTOR

Víctor Martín Mayor

UNIVERSIDAD COMPLUTENSE DE MADRID
FACULTAD DE CIENCIAS FÍSICAS

TESIS DOCTORAL

Multifractalidad, dinámica exótica, comportamientos de escala y transiciones de fase cuánticas en sistemas complejos.

Multifractality, exotic dynamics, scaling and quantum phase transitions in complex systems

MEMORIA PARA OPTAR AL GRADO DE DOCTOR

PRESENTADA POR

Isidoro González-Adalid Pemartín

DIRECTOR

Víctor Martín Mayor

UNIVERSIDAD COMPLUTENSE DE MADRID
FACULTAD DE CIENCIAS FÍSICAS

TESIS DOCTORAL

Multifractalidad, dinámica exótica, comportamientos de escala
y transiciones de fase cuánticas en sistemas complejos.

Multifractality, exotic dynamics, scaling
and quantum phase transitions in complex systems

MEMORIA PARA OPTAR AL GRADO DE DOCTOR

PRESENTADA POR

Isidoro González-Adalid Pemartín

DIRECTOR

Víctor Martín Mayor

A Nora.

A mi familia,
tanto a los que están
como a los que han estado
y a los que estarán.

Acknowledgements

I am grateful to the Ministerio de Ciencia, Innovación y Universidades (MCIU, Spain) which has supported my PhD. through FPU grant No. FPU18/02665.

This thesis was partially supported by Ministerio de Economía, Industria y Competitividad (MINECO, Spain), Ministerio de Ciencia, Innovación y Universidades (MCIU, Spain), Agencia Estatal de Investigación (AEI, Spain, 10.13039/501100011033), and European Regional Development Fund (ERDF, A way of making Europe) through Grant PID2022-136374NB-C21 and PGC2018-094684-B-C21.

This thesis has benefited from two EuroHPC computing grants: specifically, we had access to the Meluxina-GPU cluster through grant EHPC-REG-2022R03-182 (158306.5 GPU computing hours) and to the Leonardo facility (CINECA) through a LEAP grant (2×10^6 GPU computing hours). Besides, we received a small grant (10000 GPU hours) from the *Red Española de Supercomputación*, through contract no. FI-2022-2-0007.

Agradecimientos

Me gustaría que estos agradecimientos no solo se centraran en estos últimos años en los que he hecho el doctorado, ya que esto no es más que el culmen de un largo viaje que, sin saberlo, empezó hace mucho tiempo y por el que han pasado muchas personas. Sin embargo, resulta imposible (al menos para mi) expresar y abarcar esos sentimientos, así como recordar a todas las personas que deberían aparecer en estos agradecimientos. Por eso, antes de empezar quiero daros las gracias a todos aquellos que por algún motivo, por mínimo que sea, me han conducido hasta aquí.

Supongo que la primera persona que tiene que ser mencionada es Víctor, quien ha dirigido esta tesis y una de las personas que la ha hecho posible. Gracias por estar siempre dispuesto a dedicar mañanas enteras a explicarme o re-explicarme las cosas. También has demostrado una paciencia enorme, por aguantar todas esas veces que entraba a tu despacho pensando que era el fin del mundo. Gracias por haber tenido la paciencia de pasarte horas explicándome código, programando juntos para ayudarme a entender las cosas, o *debuggear*, porque “lo que no puede ser no puede ser, y ademas es imposible”. También gracias por todo lo que te has preocupado por mí, por haber valorado mi trabajo y haberme enseñado a hacerlo yo, por la dedicación, pero por encima de todo, por haberme hecho sentir un investigador más, a pesar de todo lo que tenía (y tengo) que aprender.

Respecto a esto último, quiero incluir a todos nuestros colaboradores, tanto de la colaboración Janus como no. Todos ellos han mostrado un interés genuino por mi trabajo y me hacían sentir como un igual, se han preocupado por mi y me han dado la oportunidades de aprender y crecer como investigador.

También quiero agradecer a Luis Antonio y David el hecho de haber estado dispuestos a ayudarme siempre con cualquier tipo de duda o problema, y sobre todo, haber mantenido a flote los ordenadores y el NAS del grupo (o directamente haberos peleado con ellos o con Janus). Porque sí, tener detrás a gente como vosotros dos hace que uno pueda estar más tranquilo. Quiero aprovechar y hacer especial énfasis en mi agradecimiento a David, que ha montado y mantenido todos y cada uno de los “juguetes” nuevos que compraba Víctor, y sin los cuales muchos, o ninguno, de los resultados contenidos en esta tesis habrían sido posibles de obtener.

Ilaria y Javier, gracias por haberme ayudado cuando lo he necesitado, así como haber caminado delante de mí y haberme allanado el camino. Vuestro trabajo me ha servido de inspiración y guía para materializar esta tesis.

Massimo ti ringrazio molto per avermi dato l’opportunità di recarmi a Roma per il soggiorno e lavorare con te. Ho potuto imparare molto, cose che non avrei mai immaginato di poter fare, godendomi il processo. Voglio anche ringraziarti per tutte le ore che hai dedicato ad aiutarmi a migliorare i programmi che abbiamo fatto e, soprattutto, a lottare con Leonardo e gli altri centri di calcolo. Non so davvero cosa avremmo fatto senza di te.

Agradecer al departamento de Física Teórica de la Universidad Complutense por haberme acogido y haber avalado esta tesis doctoral. Pero también por haberme brindado la oportunidad de conocer a gente estupenda.

También quiero agradecer al BIFI de la Universidad de Zaragoza y a todos sus miembros, en particular a Alfonso y David, no sólo por la cantidad de horas de cálculo, si no también por la ayuda que nos han brindado siempre.

¿Merienda? Muchas gracias a todos mis compañeros de doctorado. Sois un montón y por eso espero que me perdonéis por no poner vuestros nombres. Estábamos todos en el mismo barco y habéis hecho que la travesía sea mucho más fácil. Gracias por las pachangas, las cenas de Navidad, las quedadas, las meriendas, las sobremesas, los seminarios aperitivos, las tardes de juegos, las de karaoke, las salidas de fiesta, las sesiones *frikis* por la calle de la Luna, las risas, los ánimos, ... ¡LOS PATOS!. Gracias por todo eso y más chicos.

Alex, Quique, Colche y Edu, aunque desde que termino el grado nos vemos poco debido a que estamos algo desperdigados, gracias por hacer del grado casi una fiesta, por las quedadas en Murcia para ponernos al día, por los días de playa, por, por ejemplo, pasear por la cima del Teide a la una de la mañana. Gracias por vuestro apoyo.

Tere y David, aunque me habéis convertido en un “padre de dos adolescentes” de la noche a la mañana, gracias por estar ahí estos últimos años. Habéis hecho que la recta final, la más dura, fuera mucho más divertida y fácil de sobrellevar.

También quiero agradecer a mi familia (Tere, si quieres te puedes incluir aquí también, jeje) ya que, cada uno a su manera, me han estado apoyando de principio a fin. Especial mención se merece mi Abuela, por haberme aguantado en su casa los primeros años del doctorado. Gracias por todo *Lalá*, por los fines de semana en tu casa desde pequeño, por cada Navidades, por los veranos en La Manga, por haber estado tan orgullosa como sólo una abuela puede estarlo.

Mamá y Papá, millones de gracias. Siempre habéis estado ahí, cuidándome y apoyándome. Por eso aprovecho estas palabras para agradeceros por una vida, por haber estado dispuestos a darlo todo por mi y dejarme ser quien soy, por un montón de cosas que no cabrían en las páginas de ninguna tesis. Gracias Julica por haber sido la mejor hermana del mundo y por haberme cuidado desde siempre. Sin vosotros tres no sería quien soy, ni habría llegado hasta donde estoy, así que esta tesis también es vuestra. Julica, tengo que darte las gracias por algo más, ya que estos últimos años no habrían sido lo mismo sin Jorge, Oli y Ali. Gracias por invitarme a vuestra casa y preocuparos por darme ricos cocidos y migas, por las invitaciones a todas las celebraciones, y por ayudarme a desconectar y disfrutar. Oli y Ali, gracias por mirarme con una admiración infinitas cada vez, por compartir recordarme lo que es jugar, por venir todos los días a decirme que hay que ir a la playa o a la piscina o al parque, y por toda la alegría que lleváis a cualquier parte.

Antes de terminar me gustaría darle las gracias a un par de personas que, aunque hace mucho que no se nada de ellas, siempre recordaré. Por haber ayudado a sembrar y cultivar mi amor por las ciencias y las matemáticas desde cuando aún no sabia ni lo que eran, millones de gracias Begoña y Benito. Ojalá todos los profesores del mundo pudieran ser lo que vosotros fuisteis para mí.

Estos agradecimientos no podrían estar completos sin la persona que realmente hizo que empezara y acabara el doctorado. Nora, muchas gracias por haber estado a mi lado todos estos años y por haber sido el mayor apoyo que he tenido. Gracias por haber estado ahí para ayudarme y escucharme en todo momento, pasara lo que pasara. Ha sido un viaje largo y difícil, pero contigo he sentido que no había nada que no pudiera aguantar o hacer. Gracias por todo tu esfuerzo y por ser un ejemplo a seguir. Sin ellos, no habría sido capaz de dar lo mejor de mi para terminar. Pero también te doy las gracias por haber aguantado el tostón de explicaciones que te daba sobre mis programas y problemas, por las mañanas y tardes trabajando juntos, por las excursiones y viajes para desconectar, por los días de playa, por los cines de verano, etc. Sencillamente gracias por estar ahí en cada momento. Contigo también tengo que añadir un gracias a Paco, Amina e Ismael, a los que obligaste a tenerme en sus vidas, pero que me acogieron en su familia como uno más. Gracias a los 3 (bueno, ahora 5) por haber ayudado a hacer el viaje más fácil.

Contents

List of Figures

List of Tables

Abstract

This thesis, entitled “Multifractality, exotic dynamics, scaling and quantum phase transitions in complex systems”, focuses on studying the Ising-Lenz and Edward-Anderson models from the numerical point of view. In this study, we have verified how, despite their simplicity, these models can exhibit complex behaviors that still surprise us today. In this sense, numerical simulations have played a crucial role in the detailed exploration of these phenomena, some of which have only been possible through specially dedicated computers such as Janus I and Janus II or through highly optimized programs to be run on GPUs.

Part I of this thesis contains an introduction to spin glasses. For this purpose, we give a brief historical introduction followed by the basic concepts of spin glasses, which we complete with a short description of the theoretical concepts of significant relevance for this thesis. Finally, to establish a common methodology, we introduce the different techniques used throughout this dissertation and the fundamental magnitudes that are considered in the different performed analyses.

In Part II, we have studied exotic phenomena associated with out-of-equilibrium dynamics and ways to exploit these behaviors to accelerate the dynamics. For this, we have considered Ising models in one and two dimensions. In Chapter 2, we have established a simple methodology that allows us to understand and control these phenomena from measurable observables in situations where there is a separation of time scales in the system. In Chapter 3, we have focused our attention on systems without time-scale separation. However, by studying the growth of magnetic domains, we have been able to control the system dynamics as well.

The discussion presented in Part III focuses on studying the susceptibility in spin glasses in the presence of a finite-dimensional magnetic field in the region of large fluctuations. In this scenario, due to the complexity of the theory, many hypotheses try to explain the observed phenomena. Our numerical results for spin glasses in 4 dimensions agree with the theoretical predictions of Field-Theory near the upper critical dimension, $D_{\mathrm{u}} = 6$.

Part IV addresses a fean that has so far gone unnoticed in spin glasses: multifractality. For this purpose, we have analyzed out-of-equilibrium configurations of three-dimensional systems generated with the dedicated supercomputer Janus II. Indeed, the results have allowed us to find that the local correlations at mesoscopic distances are characterized by a distribution with a heavy tail, which we have characterized through the formalism of multifractality.

In Part V, we have characterized the phase transition for a two-dimensional quantum spin glass. Our results resolve a long-lasting debate on the value of the dynamical critical

exponent z. To do so, we have needed to resort to extensive numerical simulations on GPUs using specifically designed codes and to a careful consideration of a fundamental property of the system: the spin-flip symmetry. We have thus verified that the system has two dynamical exponents: one associated with the interplay of states of different parity, z, which appears to be divergent, and another exponent related to states of the same parity, z_{e}, which remains finite. The latter result, i.e., z_{e} finite, has significant practical implications since it implies that there are no restrictions to carry out the process of quantum annealing for solving optimization problems, at least as far as going through the phase transition is concerned.

The dissertation ends in Part VI, where the most important conclusions and results of each of the chapters are presented. In addition, several appendices have been included that address the various technical aspects of this dissertation. In Appendix A, we discuss the Trotter-Suzuki approximation for a two-dimensional quantum spin glass. Appendix B discusses the transfer matrix formalism. The technical aspects of the diagonalization of the transfer matrix for the cases studied are contained in Appendix C. Appendices D, E and F describe the various techniques employed to carry out our Monte Carlo simulations. In Appendices G and H, we describe the techniques used to study the correlation functions. Finally, Appendix I contains technical aspects of the calculation explained in Part III.

Resumen

Esta tesis, titulada "Multifractalidad, dinámicas exóticas, comportamientos de escala y transiciones de fase cuánticas en sistemas complejos", se ha centrado en el estudio de los modelos de Ising-Lenz y Edward-Anderson desde el punto de vista numérico. En este estudio hemos podido comprobar como, a pesar de su sencillez, estos modelos albergan la capacidad de exhibir comportamientos complejos que a día de hoy aún nos sorprenden. En este sentido, el uso de simulaciones numéricas ha desempeñado un papel crucial en la exploración detallada de estos fenómenos, algunas de las cuales sólo han sido posibles mediante el uso de ordenadores especialmente dedicados como Janus I y Janus II, o mediante programas altamente optimizados para ejecutarse en GPUs.

La Parte I de esta tesis contiene una introducción a los vidrios de espines. Para ello, damos una breve introducción histórica seguida de los conceptos básicos de los vidrios de espines, que completamos con una breve descripción de los conceptos teóricos de mayor relevancia para esta tesis. Finalmente, a fin de establecer una metodología común, introducimos las distintas técnicas que se emplean a lo largo de esta disertación, así como las magnitudes fundamentales de los distintos análisis realizados.

En la Parte II hemos estudiado distintos fenómenos exóticos asociados a la dinámica fuera del equilibrio, y maneras de aprovechar estos comportamientos para acelerar la dinámica. Para ello hemos considerado modelos de Ising, en una y dos dimensiones. En el Capítulo 2 hemos establecido una metodología sencilla que permite entender y controlar estos fenómenos a partir de observables medibles en situaciones donde existe una separación de escalas de tiempo en el sistema. Por otro lado, en el Capítulo 3 hemos centrado nuestra atención en sistemas que no presentan separación de escalas de tiempo. Sin embargo, estudiando el crecimiento de los dominios magnéticos hemos sido capaces de controlar la dinámica del sistema.

La discusión presentada en la parte Parte III se centra en el estudio de la susceptibilidad en vidrios de espines en presencia de un campo magnético en dimension finita en la región de grandes fluctuaciones. En este escenario, debido a la complejidad de la teoría, son muchas las hipótesis que tratan de explicar los fenómenos observados. Nuestros resultados numéricos para los vidrios de espines en 4 dimensiones coinciden con las predicciones de la teoría de campos cerca de la dimensión crítica superior, $D_{\mathrm{u}} = 6$.

La Parte IV trata un aspecto que hasta ahora ha pasado inadvertido en los vidrios de espines, la multifractalidad. Para ello hemos analizado configuraciones fuera del equilibrio equilibrio de sistemas tridimensionales generadas con el superodenador Janus II. Efectivamente, los resultados obtenidos nos han permitido constatar que las correlaciones locales a distancias mesoscópicas se caracterizan por tener una distribución con una cola pesada, la cuál hemos

tenido que caracterizar mediante el formalismo multifractal.

En la Parte V hemos caracterizado la transición de fase para un vidrio de espines cuántico bidimensional. Nuestros resultados resuelven una larga discusión sobre el valor del exponente crítico dinámico z. Para ello hemos necesitado, recurrir tanto al uso de extensas simulaciones numéricas en GPUs mediante códigos específicamente diseñados, como a una cuidadosa consideración de una propiedad fundamentales del sistema: la simetría de *spin-flip*. Hemos comprobado así que el sistema tiene dos exponentes dinámicos: uno asociado a la interrelación de estados de distinta paridad, z, que parece ser divergente, y otro a la interrelación entre estados de de la misma paridad, z_e, que permanece finito. Este último resultado, es decir z_e finito, tiene grandes implicaciones prácticas, ya que implica que no hay restricciones para llevar acabo el proceso de *quantum annealing* para la resolución de problemas de optimización, al menos en lo que respecta a atravesar de manera adiabática la transición de fase.

La tesis acaba en su Parte VI, donde recogemos las conclusiones y resultados más importantes de cada uno de los capítulos. Además, se han incluido varios apéndices que abordan los distintos aspectos más técnicos de esta disertación. En el Apéndice A tratamos la aproximación de Trotter-Suzuki para un vidrio de espines cuánticos bidimensional. En el Apéndice B discutimos el formalismo de la matriz de transferencia. Los aspectos técnicos de la diagonalización de la matriz de transferencia para los casos estudiados está contenida en el Apéndice C. Los Apéndices D, E y F describen las distintas técnicas empleadas para llevar acabo nuestras simulaciones de Monte Carlo. En los Apéndices G y H describimos las técnicas empleadas para el estudio de las funciones de correlación. Por último, el Apéndice I contiene aspectos técnicos del cálculo empleado en la Parte III.

Part I

Introduction

1

Some relevant facts about spin glasses

> **"...a real scientific mystery is worth pursuing to the end of the Earth for its own sake, independently of any obvious practical importance or intellectual glamour"**
>
> *P. W. Anderson*
>
> *Spin Glass I: A Scaling Law Rescued*
> Physics Today **41**, 1 (9-11)
>
> `https://doi.org/10.1063/1.2811268`

Spin glasses will be important in this thesis. Thus, we start by providing a brief introduction to this vast field. Due to space limitation, we provide only a brief historical overview and describe the most relevant concepts and basic tools. We shall not attempt to be general in our exposition, which we know leaves aside, among others, models of great relevance in the study of the glassy phase, such as the p-spin [Gar85, CS92], the Heisenberg [Kaw98, HK05, CCAMM$^+$06, FMMPG$^+$09] or the Potts model [HKL90, BK11]. Then, we shall emphasize the tools and ideas used in this dissertation –with the corresponding reference to the original work. For a more detailed and comprehensive discussion of some of the topics mentioned in the following sections, the reader may find useful [BY86, MPV87, Myd93, FH91, You98, Dot01, dDG06, CMM$^+$23, Par23].

The end of the '50s and the '60s were marked by some experiments on diluted magnetic ions in insulators (i.e., alloys between noble and transition metals), such as Gold-Iron alloy (AuFe) or Copper-Manganese alloy (CuMn). These experiments showed some unusual behaviors of these alloys at low temperatures. Among others, we are referring to: (i) the measure of the specific heat at low temperatures [dNC59, Zim60] for different diluted concentrations, (ii) studies of the time-dependent residual magnetism [Kou60, Kou61], and (iii) observations of the electron spin resonance spectroscopy (ESR spectra) [OBKK56, VB66, VB67, Bec71] which tried to test the proposed Ruderman-Kittel-Kasuya-Yosida (RKKY) interaction between spins [RK54, Kas56, Yos57].

The most relevant results from the above experiments were the thermodynamic measurements of the specific heat C and the magnetic susceptibility χ for these alloys. In particular, the specific heat as a function of temperature, T, presents a peak at a dependent concentration temperature T_0 and is linear with T at low temperature [Zim60]. In the case of the magnetic susceptibility χ, it gets up from a constant value, at high temperature, to a broad peak near T_0, then falls off approximately following the Curie law $\chi \propto T^{-1}$. A possible explanation of these results was formulated through the RKKY interactions, taking into account the random nature of the impurities, which implies that each spin feel a random effective magnetic field [Mar60], and the strong correlation between spin that form clusters [KB63].

With the new superconducting quantum interference device (SQUID) magnetometers [Cla04], a new set of very precise measures of the susceptibilities were taken in different experiments [TT74]. With the more accurate results, the hypothesis of a possible low-temperature magnetic ordered phase took form (later known as spin glass (SG) [And70]), which exhibits different characteristics from other known condense-matter phases. However, this idea of a phase transition from a high-temperature phase to a low-temperature phase, which possibly described the experiments, was widely questioned during the '60s and the early 70's [VB66, VB67, Bec71, TT74]. Although different experiments showed the sharp cusp in the susceptibility of spin glasses [CMB71, CM72], and they unveiled the curved nature of the susceptibility [MvDM81, MvDM82], only after [BMdPSFdsdE86, GSN$^+$91] the existence of the phase transition in experimental spin glasses was widely accepted. Refs. [BMdPSFdsdE86, GSN$^+$91] were the first ones that attempted to measure the critical temperature and critical exponents for different alloys. In both cases, they had to overcome the problem of ensuring the equilibration of the system above the transition point to establish the existence of the phase transition in experimental spin glasses rigorously.

One of the most controversial aspects of the phase-transition hypothesis came from the neutron scattering experiments [Arr65], where the results showed the absence of any order of the elements responsible for the magnetization, the spins, in the low-temperature phase. In fact, the combination of this absence and the sharp cusp in the susceptibility led [EA75] to propose a new mean-field theory that considers a random interaction following a probability distribution instead of the RKKY. With this change, a new paradigm was opened, where the spatial order of spins is neglected in favor of the long-range order *in time* [EA75] (later known as *non*-ergodicity). The new theory boosted the interest in spin glasses, thanks to its simplicity and because it allowed the study of different systems using the same tools. In particular, the replica method was used to compute the partition function [EA75]. However, the results obtained in Ref. [SK75] caused doubts about the replica methods because it predicts a negative entropy for the Sherrington-Kirpatrick model (SK) (where the mean-field theory is exact). In order to solve the problem without the replica method, [TAP77] proposed the Thouless-Anderson-Palmer (TAP) theory. Both theoretical approaches agreed on their predictions, except the negative entropy of the SK model. The TAP approach remarkably identified the problem in the replica method [known as replica symmetry breaking (RSB)] [dAT78]: below a specific line in the magnetic field-temperature phase diagram, a new structure appears in the solutions of the TAP equations. It was not until [MPS$^+$84a], with the consideration of an ultrametric tree of different solutions to the TAP equations, that the RSB problem was understood.

RSB [Par79a] is one of the crown jewels of theoretical physics. However, it was not enough to approach the theoretical and experimental research on spin glasses. Some tentatives in this respect were the scaling theories of magnetic domains growth [FH88b, KH88, OHV90, BDHV01], but they were not enough to unify the theory and experiments. Part of the difficulties comes from the glassy nature of SGs: the slow dynamics at low temperatures imply that the experiments are always carried off equilibrium. At the same time, theory is concerned with equilibrated configurations in the thermodynamic limit.

In this scenario, numerical simulations have always played an important role by providing a bridge between theory and experimental results. However, up to 15 years ago, only small systems at thermal equilibrium (very far from the thermodynamic limit and the experiments) or out-of-equilibrium simulations in a much shorter time scale than the experimental ones could be achieved. In addition, the RSB theory teaches us that the solutions of the TAP equations live in a *rugged* free-energy landscape with many minima of the free-energy separated by hich barriers, which implies that going from one solution to another requires an unachievable amount of time. Fortunately, the continuous development of different algorithms, such as simulated annealing [KGV83] or multispin coding [FG88], and the growing computational power have allowed to reduce the gap drastically.

In this sense, projects such as Janus [BMP+06], in which specific computers were designed, built, and programmed to study spin glasses, deserve special mention. In particular, the most recent Janus II [BJBnC+14c] has allowed us to close the gap between theory and experiments [Pag21]. This brings the understanding of very different and complex properties presented in the SGs like aging and memory [BJCC+23], metastability and temperature chaos [MG21]. In this context, it is essential to note that these results were made possible by having access to microscopic information about the system in situations comparable to those in an experimental laboratory (i.e., in the thermodynamic limit) [ZPBJ+20, PZBJ+21, ZOS22, PZBJ+23].

The rest of this chapter is organized as follows. In Sect. 1.1, we will discuss some basic models of spin glasses and some of the experimental results that have led to their formulation. In addition, we will look at some examples of the interdisciplinary application of spin glasses. Then, in Sect. 1.2 we will briefly review the main theoretical concepts. In Sect. 1.3, we will discuss some of the main techniques used to study these systems. Finally, to establish a common framework for the whole thesis, in Sect. 1.4 we will discuss the fundamental observables on which the analyses shown in this dissertation are based.

1.1 Some basic concepts in spin-glasses modeling

The spin glass phase is a condensed matter state of some amorphous magnetic materials (they present both disorder and randomness) and has slow dynamics at low temperatures. As it was described above, the SG model was first introduced in Ref [EA75] to explain the behavior of magnetic dilutions at low temperature [dNC59, Zim60]. The model considers that each particle at position $\vec{r}$ has a spin (i.e., a magnetic moment) that we denoted by $\vec{s}_{\vec{r}}$. Given a pair of spins, $\vec{s}_{\vec{x}}$ and $\vec{s}_{\vec{y}}$, they interact through a interaction *coupling* $J_{\vec{x},\vec{y}}$. Then, the most general Edwards-Anderson Hamiltonian for the model is:

$$\mathcal{H} = -\sum_{\vec{x}\neq\vec{y}} J_{\vec{x},\vec{y}}\vec{s}_{\vec{x}}\vec{s}_{\vec{y}} - \sum_{\vec{x}} \vec{h}_{\vec{x}}\vec{s}_{\vec{x}}\,, \tag{1.1}$$

where the last term is included to consider the interaction with a magnetic field, $\vec{h}_{\vec{x}}$. With these simple ingredients, fundamentally by treating the couplings $J_{\vec{x},\vec{y}}$ as random variables, Edwards and Anderson were able to qualitatively reproduce the experimental results [EA75]. In addition, thanks to its simplicity and versatility —using different couplings, which define groups of interacting spins, external field, or the nature of the spins themselves — one can consider a large number of situations (in physics and beyond), including quantum spin glass —see Chapter 6.

We have organized the rest of this section as follows: Sect. 1.1.1 shortly explain the basic ingredients in Eq. (1.1) that produce glassy behavior. Sect. 1.1.2 recalls some experimental results on the glassy dynamics. Finally, in Sect. 1.1.3 we collect some examples of applications of SGs in fields other than physics.

1.1.1 Frustration, randomness and non-ergodicity

Let us consider the main properties of the Hamiltonian (1.1) that make it so interesting to study the glassy behavior. These are *frustration* and the *randomness*, which we discuss below.

Frustration is associated with the impossibility of finding an optimal solution when there are many sub-optimal choices (or configurations of the system), all degenerated from the point of view of, e.g., the energy. It is important to note that frustration is not produced only by having anti-ferromagnetic interaction (i.e., all couplings are negative). For example, in an anti-ferromagnetic system in a square lattice, two spin sublattices ordered in opposite directions are not frustrated even though all interactions are negative.

Frustration, in itself, is an insufficient condition to produce glassy dynamics. As a counterexample, consider the anti-ferromagnetic triangular lattice, which is analitically solvable and it does not present a glassy behavior [Wan50].

As it was anticipated, the other main feature of Hamiltonian (1.1) is the randomness. Indeed, the couplings and/or the magnetic fields in the Hamiltonian are drawn from some probability law. Similarly to frustration, the mere presence of randomness does not guarantee a glassy low-temperature phase, as the following example will show. For example, the Random-Field Ising model (RFIM) considers deterministic nearest-neighbors interactions but a site-dependent random magnetic field $h_{\vec{x}}$ (it is quite common to take the $h_{\vec{x}}$ as normally distributed random variables). And, as anticipated above, it is well known that the low-temperature phase of the RFIM is ferromagnetic [Nat98].

Interestingly enough, in the case of the spin glasses, randomness introduces disorder, which is a way to realise frustration. To understand this relation consider the situation represented in Fig. 1.1, where there is a group of spins that are only oriented along the z-axis, i.e., they have only two possible estates: $s_i = +1$ (↑), or $s_i = -1$ (↓). They are at the nodes of a square lattice without any field (i.e., $\vec{h}_{\vec{x}} = 0$ for all $\vec{x}$), and each of them only interacts with its nearest neighbors, with a randomly choosing coupling $J_{\vec{x},\vec{y}}$ which can be $+1$ or -1 —represented in red (+1) or blue (-1) in Fig. 1.1. Notice that the spins try to minimize the energy given by the Hamiltonian in Eq. (1.1), so if the coupling is positive, they prefer to be oriented in the same direction. In contrast, if the coupling is negative, the spins prefer to point in different directions. Now, consider the bottom left corner spin and, for example, think it is in the ↑ state. Moving in the clockwise direction and choosing the less energetic state for the next spins, i.e., ↑, ↑, we see that the last spin is *frustrated* because its neighbors give opposite information to the spin.

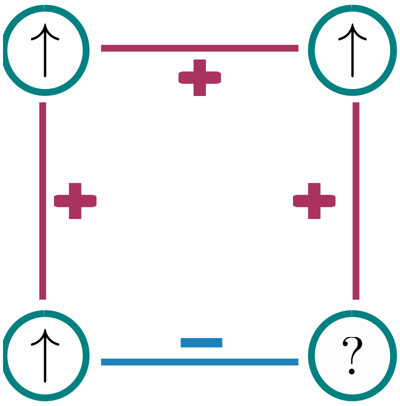

Figure 1.1: Schematic representation of frustration. The positive couplings (red) force the spins in the nodes to be oriented in the same direction, while the negative couplings (blue) force an opposite orientation.

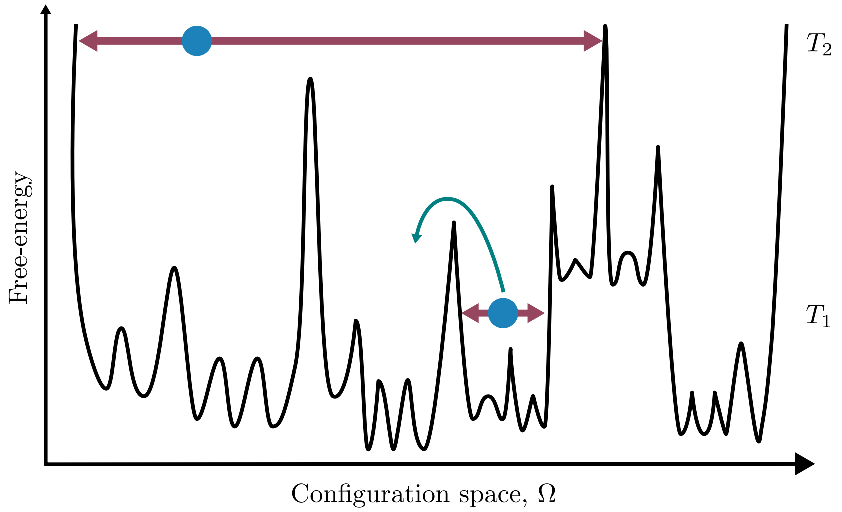

Figure 1.2: **Schematic representation of the free-energy landscape.** The different stable states of the system (the minimums) are separated by high energy barriers. The system (represented by a blue circle) at some temperature T field the free-energy landscape and must overcome the energy barrier in order to explore the configuration spaces. This scenario will explain the extremely slow glassy dynamics.

As the reader will notice, in the situation represented in Fig. 1.1 there are many different configurations of the spins that produce the same energy [recall the Edwards-Anderson Hamiltonian (1.1)]. When we consider a larguer system, the frustration introduced by the disorder produces a rugged free-energy landscape, with a very high energy barriers separating the states of the system (see Fig. 1.2). In spin glasses, these states are organized ultrametricaly [MPS$^+$84b]. Then, going from one state to another would be very difficult despite the energy barriers. Thus, the system cannot travel for the whole configuration or needs a very long time (*non-ergodicity*), producing the usual extremely slow glassy dynamics.

1.1.2 Experimental results

At the beginning of this chapter, we made a brief historical review of the various experimental results that gave rise to the theory of spin glasses. We elaborate on this topic now.

The specific heat and the magnetic susceptibility

One of the first experiments that showed anomalous behavior when including magnetic impurities in a noble metal (for example CuMn) is [Zim60]. In this work, the authors found that by introducing a few impurities, the specific heat increases drastically, as shown in Fig. 1.3. In addition, using the usual representation of C/T vs T^2 (see Fig. 1.3), they were able to verify that temperature dependence of their results could be described by a straight line with a greater slope than the results for pure metal. Moreover, at low temperatures, the specific heat appears to have a linear behavior with T, being almost independent of impurity concentration.

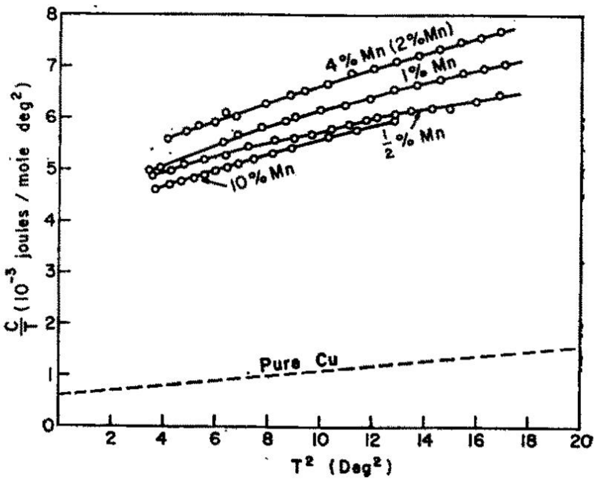

Figure 1.3: Specific heat of CuMn alloys at liquid helium temperatures. Data for different concentrations of Mn. The dashed line is the reference specific heat for the pure copper. Figure from [Zim60].

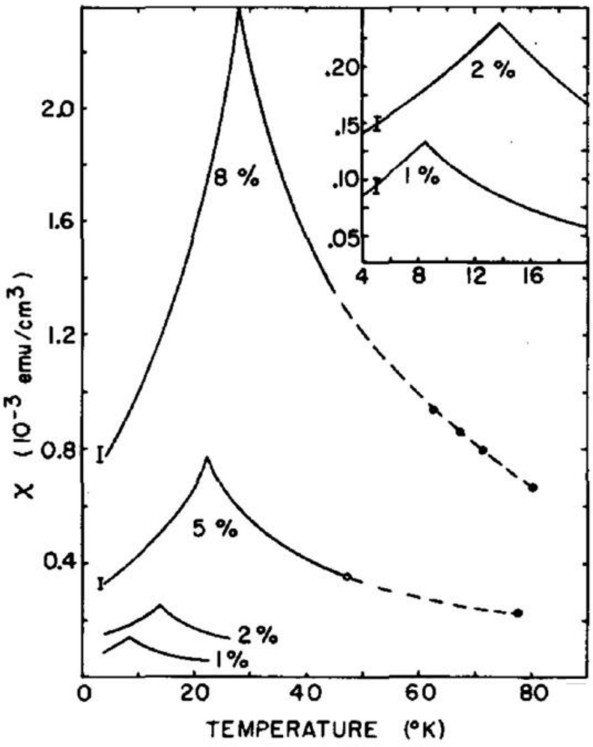

Figure 1.4: The magnetic susceptibility of spin glasses: the results for Au-Fe alloys in the region of low Fe concentration. Figure from [CMB71].

The other result that seemed to indicate the existence of a critical phenomenon for these magnetic alloys was the behavior of the magnetic susceptibility, χ. As shown in Fig. 1.4, $\chi(T)$ exhibited a sharp peak at some temperature T_0. In addition, they observed that the susceptibility appeared to follow a Curie law, i.e., $1/T$, which seemed to indicate that the system went from a disordered phase at high temperatures to a phase with some antiferromagnetic order for low temperatures.

Although the results given in Ref. [CMB71] clearly show the existence of a critical phenomenon (see Fig. 1.4), it took some years to close the debate on the presence of the phase transition. Refs. [BMdPSFdsdE86, GSN+91] provided the first attempts of estimating the critical temperature and the critical exponents for different alloys through a scaling analysis of the in-phase susceptibility when a sinusoidal external field is applied [see Fig. 1.5, see also Eq. (1.2)].

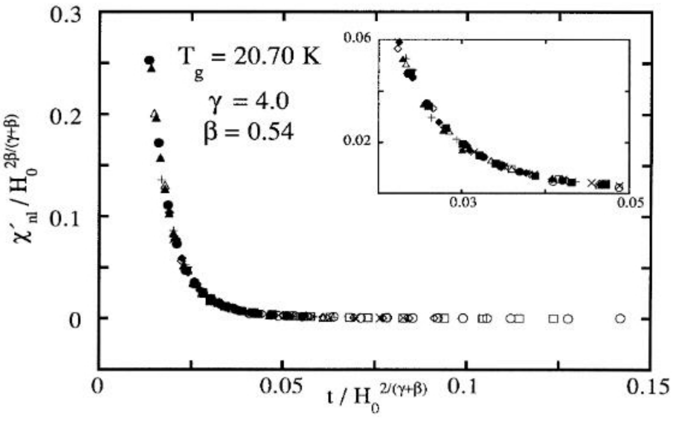

Figure 1.5: Static scaling for the in-phase susceptibility χ' time evolution for Ising spin glass $Fe_{0.5}Mn_{0.5}TiO_3$. The collapsing of the data is obtained using $T_g = 20.70$ K, and the critical exponents $\gamma = 4.0$ and $\beta = 0.54$. The inset shows a magnified part of the plot. Figure from [GSN+91].

Aging

Another of the most representative phenomena of the glass phase is the so-called aging phenomenon. Let us consider the experiment performed by [VHO+97], the so-called thermo-remanent magnetization (TRM). A sample is taken at temperature T_0 above the critical one T_c and cooled in the presence of a field at temperature $T_1 < T_g$ (the sub-index g stands for the glassy transition point). The system is allowed to mature at temperature T_1. After a time t_w, the field is turned off, and the evolution of the magnetization M with time t is measured. Note that the moment of turning off the field corresponds to $t = 0$. As shown in Fig. 1.6, the evolution of the magnetization with time depends on how much time t_w the system has spent in the presence of the external field. In addition, for all the curves in Fig. 1.6, it is possible to observe an inflection point close to $t = t_\mathrm{w}$. Similar experiments are performed in Refs. [Cha84, OAH85, NSLS86, AOH86].

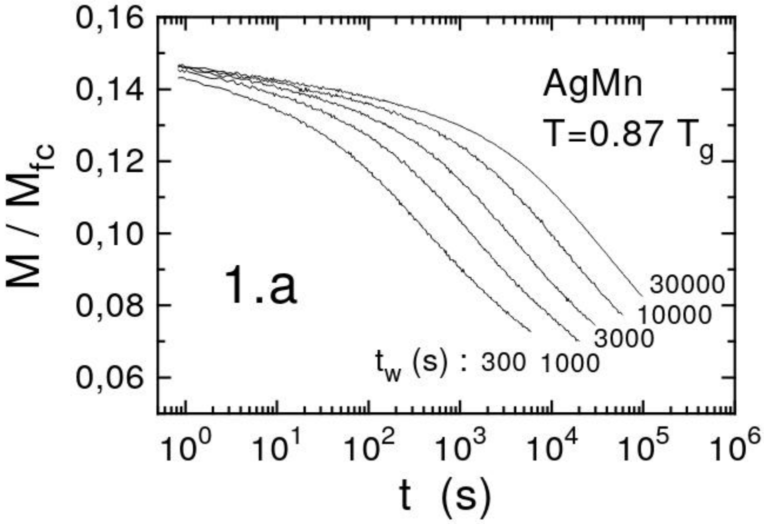

Figure 1.6: Thermo-remanent magnetization M, normalized by the field-cooled value M_{fc}, vs. $t(s)$ (log_{10} scale) for the Ag : Mn$_{2.6\%}$ sample, at $T = 9\mathrm{K} = 0.87T_\mathrm{g}$. The sample has been cooled in a 0.1 Oe field from above $T_\mathrm{g} = 10.4\mathrm{K}$ to 9K; after waiting t_w, the field has been cut at $t = 0$, and the decaying magnetization recorded. Figure from [VHO$^+$97].

In addition to TRM experiments, one can also measure the co-called zero-field cooled (ZFC) magnetization. In this type of experiment, the system is cooled without an external field. After some time, the field is turned on, and the evolution of the magnetization of the system is studied. In Refs. [LSB83, NSLS86], the reader will find experimental results for ZFC protocols.

Both the ZFC and the TRM magnetizations turn out to be (approximately) a function of the ratio t/t_w. Hence, t_w is the most important time scale in the problem. It has been argued that the crucial role is played by the coherence length $\xi(t)$ [MG21]. In Chapter 3, we will recover this idea, not in the context of aging, but in accelerating out-off-equilibrium dynamics.

Memory and rejuvenation

In the previous examples, when we applied an external field, it was constant in time. However, we can consider using a sinusoidal field, $H_\mathrm{ac} = H_0 \cos\phi$. In this situation, we would measure the so-called *ac-susceptibility*, χ_ac. In this situation, as a response to the sinusoidal field, the susceptibility has a sinusoidal behavior, but with a phase-delay ϕ with respect to concerning the field H_ac. This delay allows us to define the so-called in-phase susceptibility χ' and the out-of-phase susceptibility χ''.

$$\chi' = \chi \cos\phi \quad , \quad \chi'' = \chi \sin\phi \,. \tag{1.2}$$

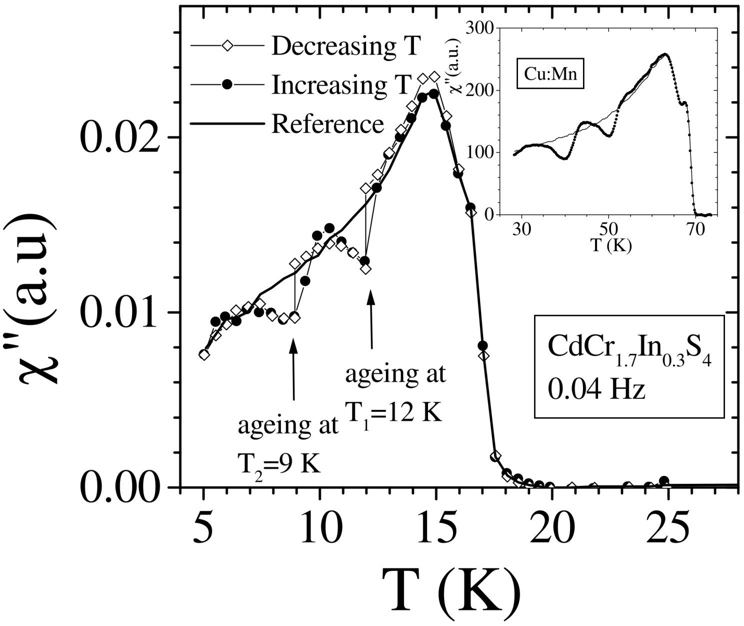

Figure 1.7: Out-of-phase susceptibility χ'' of the $CdCr_{1.7}In_{0.3}S_4$ spin glass as function of the temperature T in presence of a sinusoidal field H_{ac} of frequency $f = 0.04\,$Hz. The solid line is measured upon heating the sample at a constant rate of 0.1K/min (reference curve). The cooling procedure has been stopped during 7h at 12K and then 40h at 9K. The inset shows a similar "double memory" experiment performed on the Cu:Mn metallic SG. Figure from [JVH+98].

Fig. 1.7 shows experimental results (from Ref. [JVH+98]) for χ'' in two protocols: In the first protocol, continuous line in Fig. 1.7, the system was cooled at a constant cooling-rate. After reaching the lowest temperature of 5 K, the system was heated back continuously at the same rate. The results from the cooling and heating process result in very close curves. Then, only the heating process is shown in Fig. 1.7.

In the second protocol, the process was repeated, but including two stops in the cooling process at temperatures T_1 and T_2 below the critical temperature T_{c} (which correspond with the peak in Fig. 1.7). At these temperatures the system was let to age for $t_{\mathrm{w}} = 7$ h for T_1 and $t_{\mathrm{w}} = 40$ h for T_2. The results of the cooling process are shown with white circles in Fig. 1.7. Last, after reaching 5 K, the system is reheated at a constant heating rate (black dots in Fig. 1.7).

As the reader will notice, we can extract two prominent conclusions from the results in Fig. 1.7: In the cooling process, at T_1 and T_2 makes aging, χ'' diminish, as evidenced by the separation from the reference curve. However, when the cooling is resumed again, the susceptibility merges back with the reference curve. This phenomenon is the so-called *rejuvenation*. As for the heating process, when approaching the aging temperatures T_1 and T_2, the system separates from the reference results, following the data of the cooling process. In this sense, we say that the system has *memory* so that it *remembers* the aging process and follows the susceptibility curve.

These experimental results imply that the aging process at temperature T does not affect susceptibility values at lower temperatures. This independence is usually related to the so-called *temperature chaos*. The interested reader can find more information on temperature chaos in [MG21].

To conclude this paragraph, let us mention that although rejuvenation and memory effects in spin glasses have been observed experimentally for more than 25 years, obtaining results by simulation has only been possible very recently [BJCC+23]. Thanks to the dedicated computer Janus II [BJBnC+14c], the prominent role of temperature chaos in producing rejuvenation was confirmed.

1.1.3 Beyond physics

It is not always easy to find a clear example of how a theoretical physics work would transcend to other fields or the possible relevance in everyday life. However, the spin glass theory and the different tools developed for its study (including computational ones) are one of those examples. To enumerate some of the different applications of the spin glass model (without trying to be exhaustive): [Hop82] found that a neural network modeled by a spin glass will reproduce a "content-addressable" memory, a memory that can recover full details from a fragment of information (and correct errors); [RAS86] demonstrated that the origin of biological information could be modeled by a frustrated and quenched random model of spins; different computational problems, like the traveling salesman problem (where one needs to connect N cities —or electronic devices, delivery spots, etc. — using the shortest path) among others, can be modeled by a spin glass (see below); and so on.

The computational complexity theory gives a better understanding of the relevance of the SG model. Consider N agents in some problems, for example, cities that must be visited, electronic elements to connect, people to arrange in working groups, or elements in a database to sort. The computational complexity theory classifies this problem according to the "difficulty" of solving these problems in a computer (measured in time, or amount of memory) scales with the number N of agents involve [Pap94]. According to this, there are tractable problems, for which the resources scale polynomially with the agents (P problems), and untractable problems, for which the needed resources scale faster than any polynomial in N. These are called NP problems. A subset of the NP problems are known as NP-complete problems. Their interest lies in the fact that any NP problem can be transformed into one of the NP-complete problems using a polynomial-time algorithm. This implies that developing an algorithm that efficiently solves one of the NP-complete problems (i.e., an algorithm in which the needed resources scale polynomially on N) means solving all NP problems efficiently [Pap94].

In such a framework, the relevance of the spin glass model is clear thanks to the fact that Refs. [Bar82, Ist00] demonstrated that finding the ground state of a spin glass in a non-planar interacting graph is an NP-complete problem. Then, other NP problems like the salesman problem mentioned above, the graph coloring problem, or the task assignment problem can be solved using an algorithm that minimizes the energy in a spin glass.

The particular NP-complete problem posed by SG allows us to employ physical intuition. The introduction of the notion of temperature, alien to optimization theory, led to the simulated annealing algorithm. For instance, physics can provide powerful insights in this context.

1.2 Theory

As it was explained at the beginning of this chapter, the first tentatives to explain the linear dependence of the specific heat in the low-temperature regime and the sharp cusp in the magnetic susceptibility presented in the alloys considered the interaction between the magnetic moments (located over the diluted Mn) via free electrons in the conduction band [Kas56, Yos57, Mar60]. This description uses the Ruderman-Kittel-Kasuya-Yosida law for the coupling,

$$J_{\vec{x},\vec{y}}^{\mathrm{RKKY}} \simeq J_0 \frac{\cos(2k_{\mathrm{F}}\|\vec{x}-\vec{y}\|)}{\|\vec{x}-\vec{y}\|^3}\,, \tag{1.3}$$

between two magnetic moments at sites $\vec{x}$ and $\vec{y}$, respectively. Notice that the interaction decreases and oscillates with the distance. In addition, due to the Fermi momentum k_{F} is of the order of an Armstrong to the minus one, the interaction changes in sign very fast. These features, combined with the random distribution of the impurities in space, suggest that the couplings would be treated as random variables [Bro59], which depend only on the single realization of the alloy.

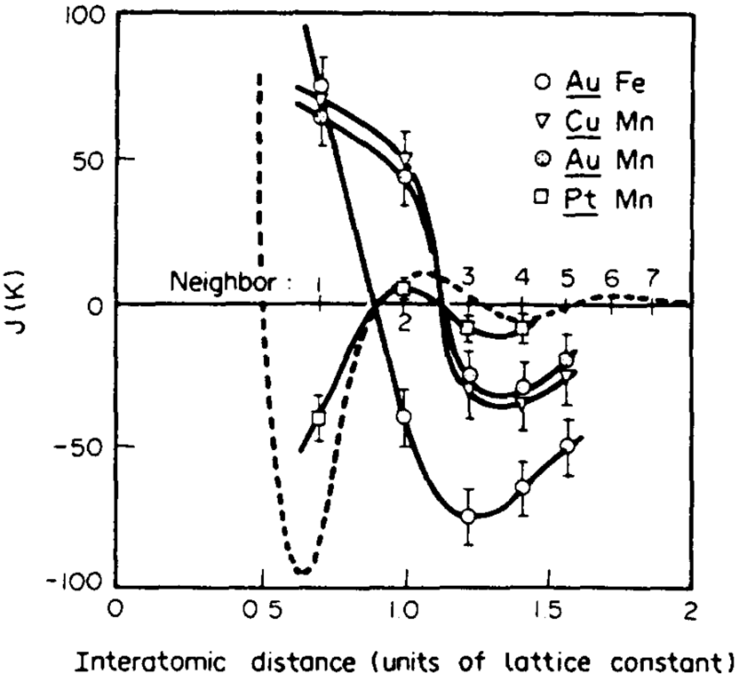

Figure 1.8: Exchange parameters J (couplings) as a function of neighbor distance. The dashed line represents the RKKY-conduction electron polarization [cf. Eq. (1.3)]. Figure from [MM83].

The revolutionary change introduced by [And70] was considering a random matrix $J_{\vec{x},\vec{y}}$ instead of the "real" RKKY interaction and proposed an easier model given by Eq.(1.1). Notice that this model captures the essential features of the phenomena (randomness of the couplings and frustration due to the possible negative values of the couplings). Each realization of the matrix $J_{\vec{x},\vec{y}}$ corresponds to the disorder present in the alloy (i.e., the random positions taken by the Mn ions). Note that Mn ions do not migrate in experimental times, which justifies considering $J_{\vec{x},\vec{y}}$ as time independent. We name this property as quenched disorder. A realization of the disorder is called a sample. The two usual elections for the distribution of the couplings are (i) a normal distribution with zero mean and variance one, or (ii) $J_{\vec{x},\vec{y}} = \pm 1$ with 50% probability.

In this dissertation, we have specialized Eq. (1.1) to spins restricted to $s_{\vec{r}} = \pm 1$ (known as Ising spin glass model, or Edwards-Anderson model [EA75]) and constant external field for the whole sample, i.e. $\vec{h}_{\vec{x}} = \vec{h}$ oriented in the same direction as the spins (only in Chapter 6 we have considered a transverse field to drive quantum fluctuations). Under this consideration Eq. (1.1) is written as

$$\mathcal{H} = -\sum_{\langle i,j \rangle} J_{i,j} s_i s_j - h \sum_i s_i \,, \tag{1.4}$$

where the subindex i and j identified the spin in a regular lattice in D dimensions, and $\langle i, j \rangle$ restricts the sum over nearest-neighbors.

[EA75] noticed that some preferred orientation for the spins (system configurations) must exist that give the minimum of the energy. For temperatures above the critical one, T_c, the spins are blind to the energy minima, causing an expected value $\langle s_i \rangle = 0$. However, below T_c, the spins feel the existence of the energy minima, and some order appears in the system [recall Fig. 1.2]. specifically, if we consider spin s_i, there exists a non-vanishing probability that the spin has the same orientation at later times, which could be measured through the local order parameter of the system, the so-called *overlap*,

$$q = \lim_{t \to \infty} \left[\lim_{N \to \infty} \frac{1}{N} \sum_i \langle s_i(0) s_i(t) \rangle_t \right] , \tag{1.5}$$

where N is the number of spins in the system and $\langle \mathcal{O}(t) \rangle_t$ is the time average of an observable $\mathcal{O}$, i.e.

$$\langle \mathcal{O}(t) \rangle_t \equiv \lim_{t \to \infty} \frac{1}{t} \int_0^t d\tau \mathcal{O}(\tau) \,. \tag{1.6}$$

As the reader will notice, there is no preferred direction at a high temperature (in equilibrium), so $q = 0$, and the system is in the paramagnetic phase. However, in the spin-glass phase, the spins feel the minimum-energy states, and some order arises. Then, the overlap differs from zero, i.e., $q \neq 0$.

Now, the problem is obvious: to compute the average in Eq. (1.6), we need to know the time evolution of the considered observable. The formalism of statistical mechanics was invented to address this problem, specializing in the SG case. As usual, one needs to compute the partition function

$$Z \equiv \mathrm{Tr} \mathrm{e}^{-\beta \mathcal{H}} = \sum_{\{s_i\}} \mathrm{e}^{-\beta \mathcal{H}(\{s_i\})} \,, \tag{1.7}$$

where β is the inverse temperature of the system in units such that the *Boltzmann constant* $k_\mathrm{B} = 1$, and $\{s_i\}$ refers to the configuration of the system. Then, we can define the probability distribution function (pdf) of the configuration $\{s_i\}$ as

$$P(\{s_i\}) = \frac{\mathrm{e}^{-\beta \mathcal{H}(\{s_i\})}}{Z} \,. \tag{1.8}$$

Now, consider that the system will reach every possible configuration in equilibrium. In this situation, we can trade the integral over time in Eq. (1.6) with an average over the configuration of the system weighted with (1.8). Then, we have that

$$\langle \mathcal{O} \rangle = \frac{\sum\limits_{\{s_i\}} \mathcal{O}(\{s_i\}) \mathrm{e}^{-\beta \mathcal{H}(\{s_i\})}}{Z} \,. \tag{1.9}$$

Then, from now on, $\langle \cdot \rangle$ will represent the thermal average over system configurations.

A special case is the free energy, which can be computed directly from the partition function as

$$F = -\frac{1}{\beta} \log Z \,, \tag{1.10}$$

from which we can obtain all the fundamental thermodynamics quantities, such as the energy or the magnetization. However, Eq. (1.10) hides the fundamental difficulty of spin-glass systems: The disorder variables $J_{i,j}$ are fixed (that are quenched variables). Then, we have to average over the disorder to compute the real free energy (notice that a macroscopic system can be considered a sum of smaller parts, each with its own $J_{i,j}$). Then, we have

$$F = -\frac{1}{\beta} \overline{\log Z_{J_{i,j}}} \,, \tag{1.11}$$

where the $\overline{(\cdot)}$ operator stands for the average over the disorder (or quenched average).

1.2.1 Replica trick

In order to compute the quenched average in Eq. (1.11), [EA75] proposed the so-called replica trick, that uses the fact that

$$\log(x) = \lim_{m \to 0} \frac{x^m - 1}{m} \,. \tag{1.12}$$

Then, Eq. (1.11) can be written as

$$F = \lim_{m \to 0} -\frac{1}{\beta} \frac{\overline{Z^m} - 1}{m} \,. \tag{1.13}$$

Assuming that m is an integer, when we take the average over disorder for Z^m, we can consider an average over m identical copies (or replicas) of the system that share the couplings $J_{i,j}$.

In the new replica formalism, the order parameter, see Eq (1.5), is written as

$$q^{ab} = \langle s_i^{(a)} s_i^{(b)} \rangle \,, \tag{1.14}$$

where the super-index refer to the replica identifier. In this sense, we can think of the replicas as a very separated time configuration of the system [cf. Eq. (1.6)]. Then, it is natural to assume that all the replicas are equivalent, the so-called replica symmetric ansatz. This implies that the overlap between replicas is always the same, i.e.

$$q^{ab} = q(1 - \delta_{ab}) \,, \tag{1.15}$$

with δ_{ab} the Kronecker delta.

1.2.2 Replica Symmetry Breaking

As briefly discussed at the beginning of this chapter, the replica trick with the replica symmetry assumption produces a negative entropy for the SK model [SK75]. The first sign of the solution was provided in Refs. [dAT78], which showed that the the replica symmetric ansatz is not valid under the critical temperature.

This is the so-called replica symmetry breaking (RSB), implying that below the critical temperature, there are replicas more correlated than others. Then, a different than Eq. (1.15) form for the q^{ab} is needed to represent the situation. Rather than delving into intricate details, we aim to provide a concise exploration of the essential conceptual foundations that underlie this theory introduced by [Par79a] (the interested reader will see, e.g., [CMM+23]).

The RSB can be interpreted in terms of the complex free energy landscape of the system, which characterizes the system states: Let us assume that the system is at high temperature (high energy). The system is insensible to the free energy local details, so all the replicas are equivalent. Then, we initially have a replica symmetric, represented in terms of the order parameter [cf. Eq.(1.15)]

$$(q^{ab}) = \begin{pmatrix} 0 & & & & & & & \\ & 0 & & & & & & \\ & & 0 & & & q_0 & & \\ & & & \ddots & & & & \\ & & & & \ddots & & & \\ & q_0 & & & & 0 & & \\ & & & & & & 0 & \\ & & & & & & & 0 \end{pmatrix} \tag{1.16}$$

By reducing the temperature, at some point, the system is trapped in different regions, thanks to the free-energy barriers. Then, different replicas fell different states, which produced the first RSB. In order to represent this effect, the original $n \times n$ matrix is divided into n/m_1 blocks of size $m_1 \times m_1$. The blocks represent the overlap of the new groups of configuration. Then, the off-diagonal blocks are the overlap between different groups of samples and remain unchanged. In contrast, the diagonal blocks are the overlap inside the same group of configurations, which have a different overlap $q_1 > q_0$ (it is natural to think that configurations in the same group are more correlated). This behavior is well represented by the overlap matrix

$$(q^{ab}) = \left(\begin{array}{cccc|cccc} 0 & & q_1 & & & & & \\ & \ddots & & & & & q_0 & \\ q_1 & & \ddots & & & & & \\ & & & 0 & & & & \\ \hline & & & & 0 & & q_1 & \\ & & & & & \ddots & & \\ & q_0 & & & & & \ddots & \\ & & & & q_1 & & & 0 \end{array}\right) \tag{1.17}$$

By lowering the temperature, this process continues, breaking the q^{ab} matrix in smaller blocks, representing the RSB process each time. Thus, there is a hierarchy of overlaps, which can be represented with an ultrametric tree. The bigger the value of q, the closer in the tree are the replica configurations.

$$(q^{ab}) = \left(\begin{array}{c|c} \begin{array}{c|c} \begin{smallmatrix}0 & q_2\\ q_2 & 0\end{smallmatrix} & q_1 \\ \hline q_1 & \begin{smallmatrix}0 & q_2\\ q_2 & 0\end{smallmatrix} \end{array} & q_0 \\ \hline q_0 & \begin{array}{c|c} \begin{smallmatrix}0 & q_2\\ q_2 & 0\end{smallmatrix} & q_1 \\ \hline q_1 & \begin{smallmatrix}0 & q_2\\ q_2 & 0\end{smallmatrix} \end{array} \end{array}\right) \tag{1.18}$$

Let us remark that we can continue this process to infinity by dividing the matrix into smaller blocks of size m_i. Obviously, $n \equiv m_0 > m_1 > \cdot > m_\infty = 1$. In addition, in the replica trick, we must take the $n \to 0$ limit [cf. Eq. (1.13)], so there is no reason to still consider m_k with $k = 0, 1, 2, \cdots$ to be integers. Therefore, we can consider $m_k \in [0, 1]$. Moreover, when $k \to \infty$ the q_{ab} matrix becomes a continuous function $q(x)$, where $x \in [0, 1]$. By this process, Refs. [Par79a, Par79b, Par80] correctly solved the SK model.

The hierarchic of states explains the very slow glassy dynamics: when the system is in the RSB phase, the system gets trapped in some group of the infinitely large number of states. Moving inside a group is easy, but the system must overcome a big free-energy barrier to go from one group to another, making the dynamics slow. As the reader will notice, this idea is connected with the non-ergodicity property discussed in Sect. 1.1.1.

Finally, let us remark that, despite the RSB theory being proved correct for infinite dimension [Dot01, dDG06, CMM$^+$23], it is under discussion whether or not it is suitable for describing the Edwards-Anderson model in finite dimensions. Results related to this topic will be found in Chapter 4, where we compare the numerical result with the RSB predictions for the EA in dimension $D = 4$.

1.2.3 Droplets

Let us conclude this section with a brief explanation of the main ideas of the droplet picture proposed by [McM84, FH86, BM87b].

In the droplet viewpoint, the SG phase is understood from its ground state. The basic object, the *droplet*, consists of a *compact* magnetic domain of linear size ℓ of coherently flipped spins concerning the ground state [FH86, BM87a, FH88b, FH88a]. The droplets are expected to have fractal boundaries with a surface area of order ℓ^{d_s}, $d - 1 \le d_s < d$.

The main results predicted for the droplet theory are: i) the spatial correlation function [see Eq. (1.31)] decays with exponent α (the so-called *stiffness exponent*), i.e

$$C(r) \propto \frac{1}{r^\alpha}\,, \tag{1.19}$$

with r the spatial distance. ii) as a consequence of the long-distance vanishing limit of the correlation function [FH86], the overlap distribution function of the overlap is a delta function, $P(q) = \delta(q^2 - q_{\mathrm{EA}}^2)$. iii) An external magnetic field suppresses the SG phase.

1.3 Methodology

As it was mentioned briefly in Sect. 1.1.1, SGs have a very large number of possible configurations. These configurations are grouped (recall the discussion in Sect. 1.2.2) in such a way that it is easy to explore neighboring configurations, but going from one group to another is very difficult (non-ergodicity). This makes it very difficult to reach equilibrium in SGs, forcing researchers to design new numerical methods to help connect theory with experiments. In this section, we will briefly discuss some of these techniques.

1.3.1 Numerical methods

In order to reach comparable situations to those of an experimental system (see, e.g., Refs. [ZPBJ+20, PZBJ+21, PZBJ+23]), the scientific community has been forced to develop algorithms based on unnatural dynamics to accelerate the thermalization process such as Parallel Tempering (see below), to create specially dedicated computers such as Janus I and II [BMP+06, BJBnC+14c], to develop algorithms with a very high level of parallelization to take full advantage of the computational capabilities of the moment [RSS94, BPMMP23], or a combination of all these strategies.

Without the intention of being exhaustive, we will mention here the main numerical techniques used to obtain the results reported in this dissertation (the interested reader can find more information in Appendices D, F and E). In particular, in this thesis, we use dynamical Monte Carlo (MC) methods, which allow us to sample configurations according to the correct probability density function: the Boltzmann distribution. Using this technique, we can explore the configuration space, reaching the equilibrium. In the following paragraph, we will introduce the fundamental properties of our Monte Carlo method.

Markov chain

In order to explore the configuration space, we consider a random walk. The main idea is that, at some temperature $T = 1/\beta$, the random walk allows us to reach the relevant configurations at that temperature (i.e., thermalize the system) according to the Boltzmann-Gibbs distribution

$$\pi(\{s_i\}) = \frac{\mathrm{e}^{-\beta\mathcal{H}(\{s_i\})}}{Z} \,, \tag{1.20}$$

where Z is the partition function. Our random walk should be Markovian, i.e., the next state depends only on the actual state, not on the history of the random walker [Sok97], and it will be represented by a transition matrix W. Each element $W_{X,Y}$ represents the probability of moving from configuration X to another configuration Y in one step. Thus, $W_{Y,X} \geq 0 \, \forall \, X, \, Y$ and $\sum_Y W_{X,Y} = 1$. The completeness condition $\sum_Y W_{X,Y} = 1$ means that our walker must reach some state. We name *stationary* those Markov chains where the transition probability is time-independent. Here, time is a synonym for MC step, and hence, when we say that the Markov chain is stationary, we mean that W is the same for all MC steps.

As the reader will notice, thanks to the Markovian property, the probability of going from one configuration X_{n_0} to one configuration X_n in $n > 1$ steps is the sum of the probabilities of each path that connects both configurations in n steps:

$$[W^n]_{X_{n_0},X_n} = \sum_{X_1,X_2,\cdots,X_{n-1}} W_{X_{n_0},X_1} W_{X_1,X_2} \cdots W_{X_{n-1},X_n} \,. \tag{1.21}$$

There are two essential features of our Markov chain, one related to the *ergodicity*, and the other refers to the existence of a stationary distribution. Let us start by briefly reviewing the basic concepts related to ergodicity. After that, we will discuss the *stationarity of the distribution* π for a Markov chain.

We shall consider concepts related to ergodicity, namely irreducibility and aperiodicity. *Irreducibility* guarantees that all the configurations Y are accessible from any configuration, i.e.

$$\forall\, X,\, Y\, \exists\, n_{X,Y} > 0 : \quad [W^{n_{X,Y}}]_{X,Y} > 0 \,. \tag{1.22}$$

Next, we need to define the concept of *period* in a Markov chain. We call period d_X of the state X the maximum common divisor of the length of all the paths that start and end at the configuration X. A Markov chain is *aperiodic* if $d_X = 1$ for all states. In the following, we impose irreducibility and aperiodicity properties on the Markov chain.

We say that π is a *stationary distribution* if it satisfies

$$\pi(Y) = \sum_X \pi(X) W_{X,Y} \,. \tag{1.23}$$

Note that the above is equivalent to saying that π is a left-eigenvector with eigenvalue one for matrix W. A stronger condition can be imposed if we consider a *time-reversability* property of the Markov chain. This condition is known as *detailed balance* condition, and it can be expressed as follows:

$$\pi(X) W_{X,Y} = \pi(Y) W_{Y,X} \,. \tag{1.24}$$

Notice that summing over X in Eq. (1.24) we recover Eq. (1.23).

The crucial point is that, for a Markov chain that is irreducible, aperiodic, and that satisfies the stationarity condition of π, we can resort to a useful theorem (see Ref. [Sok97]) that guarantees that the transition probability $[W^n]_{XY}$ satisfies

$$\lim_{n\to\infty} [W^n]_{XY} = \pi(Y) \,. \tag{1.25}$$

As the reader will notice, Eq. (1.25) implies that our random walk will eventually sample the desired Boltzmann-Gibbs distribution and then converge to equilibrium.

Metropolis and Heat Bath dynamics

Both the Metropolis (MET) (Metropolis-Hastings) and the Heat Bath (HB) algorithms are nothing more than concrete dynamics to obtain the sampling of distributed configurations according to the Boltzmann distribution function of the system under consideration. Both dynamics fulfill the properties of Markov chains described above. Despite their more general validity, let us consider the case we are interested in here: moving the system from configuration X to a different one Y.

To carry out this change, we can proceed in many ways. The most widespread way consists of considering the change of a spin individually, trying to change its orientation (spin-flip). The way we choose the individual spin will affect the performance, but the most extended way is to consider a sequential process over the lattice.

In this way, the dynamics of both Metropolis and Heat Bath are very similar. Let us consider temperature $T = 1/\beta$, so the dynamic process is

1. Compute the energy of the configuration X, namely $\mathcal{H}(X)$.
2. Flip the spin at site i and compute the new configuration energy Y: $\mathcal{H}(Y)$.
3. The change is accepted according to a probability p, which is dynamic dependent. For example,

$$p_{\mathrm{MET}} = \min\{1, \mathrm{e}^{-\beta[\mathcal{H}(Y)-\mathcal{H}(Y)]}\}\,, \quad p_{\mathrm{HB}} = \frac{\mathrm{e}^{-\beta[\mathcal{H}(Y)-\mathcal{H}(Y)]}}{1+\mathrm{e}^{-\beta[\mathcal{H}(Y)-\mathcal{H}(Y)]}}\,, \tag{1.26}$$

   represents the probability for the Metropolis and Heat Bath dynamics, respectively.
4. Repeat steps 1 to 3 for all the spins in the lattice. We denote the realization of the complete process for all the lattice a *lattice sweep* or simply a *sweep*.

As the reader will notice, both algorithms favor a decrease in system energy over an increase in system energy. The difference between the two algorithms is that Metropolis always accepts changes that decrease energy, while Heat Bath does so with probability p. Let us remark that allowing the system to increase the energy prevents the system from getting trapped in a local minimum. Thinking in the free-energy landscape, allowing the system to overcome the energy barriers between local minima helps to explore the configuration space.

Multispin coding

Nowadays, many processors can work with 256-bit (even 512-bit) words and perform synchronized Boolean operations on all bits in a computer word. As the reader will have noticed, in the case of Ising SG, we can represent the state of a spin with a single bit. We can use just one bit to code the interaction for $J_{i,j} = \pm 1$ couplings. This, together with the current capabilities of computers, allows us to perform parallel operations with 256 spins (or even 512) since Metropolis and Heat Bath algorithms can be implemented almost entirely with Boolean operations.

This way of working is known as multispin coding and, according to the way of coding the spins, we can define two methods: On one hand, we have the so-called multispin MUlti-SAmple (MUSA) method, in which many different samples are coded in the same computer word. Due to this characteristic, the MUSA multispin coding has no restriction concerning system size, number of temperatures, or dimensionality of the problem. On the other hand, we have the multispin MUlti-SIte (MUSI), in which different sites of the same sample are encoded in the same computer word. Then, this method poses several constraints on the size dimensions. Such restrictions will depend on the number of bits in a word or how the system is encoded.

In this thesis, we have performed Monte Carlo simulations of both MUSA and MUSI multispin types. The reader can find a more detailed description of both ideas in Appendix D.

In addition, these parallel coding techniques can also be used for programs intended to run on graphic processor unit (GPU), as we do in Chapter 6. The implementation of a Monte Carlo algorithm with MUSI coding implemented for GPU is described in more detail in Appendices D and F.

To conclude this paragraph, it is worth mentioning that one of the major difficulties of both methods, MUSA and MUSI, is the generation of random numbers and their implementation in the simulation algorithms. The needs of each problem and coding and other aspects will be reflected in how random numbers are generated and used. More details on this topic can be found in Appendix F.

Parallel Tempering

The slow dynamics exhibited by SGs is the first obstacle for the Monte Carlo methods that mimic natural dynamics, such as the Metropolis and Heat Bath algorithms, because the time to achieve thermalization would be prohibitive. Different algorithms try to mitigate this problem, such as simulated annealing [KGV83]. In this dissertation, we have used Parallel Tempering (PT) [HN96, Mar98].

The main idea of the PT is to thermalize at the same time a set of N identical copies of the system which are at different temperatures $T_1 < T_2 < \cdots < T_N$ (or equivalently $\beta_1 > \beta_2 > \cdots > \beta_N$). For those copies at $T > T_\mathrm{c}$ the evolution to the equilibrium is faster than the evolution for copies at $T < T_\mathrm{c}$, which are almost frozen (recall the discussion in Sect. 1.2.2 about the exploration of the configuration space). Then, the PT alternate two kind of steps:

First, each copy evolves independently through standard Monte Carlo dynamics (for example, Metropolis) at its temperature. We can use $m \geq 1$ Monte Carlo steps in this evolution. Second, after performing these m steps, we try to exchange the temperature of the copies. The exchange rule between two copies labeled α_1 and α_2 with configurations $\{s^{(\alpha_1)}\}$ and $\{s^{(\alpha_2)}\}$ of the systems use a Metropolis for accepting the move:

$$p = \min\{1, \exp\Big(|\beta_{\alpha_1} - \beta_{\alpha_2}|[\mathcal{H}(\{s^{(\alpha_1)}\}) - \mathcal{H}(\{s^{(\alpha_2)}\})]\Big)\} . \tag{1.27}$$

The underlying idea of PT method is very simple: Copies at low temperatures explore nearby local minima in the free-energy landscape. By increasing their temperature, they do not feel the effects of local minima and can move to other regions of the configuration space. Thus, by lowering the temperature again, the copy will explore different local minima in the free-energy landscape. As the reader will notice, for an effective thermalization using the PT algorithm, every copy of the system must spend the same time in all the temperatures: slow temperatures for exploring local minima and high temperatures for moving to far regions in the configuration space.

The PT has been tested and used in various contexts, such as physics, biology, or chemistry, among others. Thus, to obtain better performances, different switching rules have been designed [SO99, Cal05, ED05, BSVI07, BNJ08, MP13], as well as other methods to optimize the choice of temperatures [KTHT06, SMFD08]. The interested reader will find Chapter 6 or Appendix C of Ref. [MG21] useful.

1.3.2 When classical computing is not enough

Perhaps the best way to clearly state the major intrinsic difficulty of studying spin glasses from the computational point of view comes from the computational complexity theory. As already mentioned in the Sect. 1.1.3, finding the fundamental state of a SG in a non-planar graph turns out to be one of the most computationally difficult problems to solve. Specifically, it is an NP-complete problem [BMRU82, Ist00]. Moreover, given the property of these problems to represent the whole class of computational complexity [Pap94], developing new techniques to solve the problem has practical significance.

The difficulty of finding the fundamental state in SGs is related to two of their fundamental properties: the space of possible solutions is exponentially large, and the free energy landscape is very abrupt (recall the discussion in Sect. 1.2.2). Thus, algorithms that mimic physical dynamics have the problem that exploring the configuration space to find the energy minimum requires overcoming large energy barriers, making it very difficult to find the solution to the problem. Parallel Tempering is hampered by the temperature chaos phenomenon [BFM+18].

A possible solution to this problem is by introducing quantum fluctuations, which allow the system to cross the barriers separating the states instead of jumping over them, as is done by the Parallel Tempering algorithm. In Ref. [KN98], the authors proposed a method to find the fundamental state of a SG by introducing quantum fluctuations to the system, the so-called quantum annealing. Putting quantum annealing into practice is not an easy task. However, today, computers implementing this algorithm are a reality[J+11, MF20, KRL+23], although they need to face several problems. One of these problems is the existence of a phase transition that the system must cross in quantum annealing. This problem will be discussed again in Chapter 6.

1.4 Analysis

In order to establish a common notation for this thesis, in this section, we will introduce some of the common concepts that will be used in the subsequent chapters to define the observable magnitudes. However, in each chapter, we will present the corresponding magnitudes of interest in greater detail.

1.4.1 Symmetries

In the case of the Hamiltonian in Eq. (1.4), one of the fundamental symmetries is the so-called gauge symmetry. Specifically, if we implement a random transformation $\epsilon_i = \pm 1$ for each site i, the resulting Hamiltonian is of the same type as the original one but with a new couplings, i.e.

$$s_i \to \epsilon_i s_i , \quad J_{i,j} \to \epsilon_i \epsilon_j J_{i,j} \, , \quad h_i \to \epsilon_i h_i \, .$$

With some work, one can demonstrate that, for symmetric probability distributions over the couplings, i.e. $P(J_{i,j}, h_i) = P(\pm J_{i,j}, \pm h_i)$ (e.g. the normal distribution or the considered in this thesis —$J_{i,j} = \pm 1$ with 50% probability), the average over the quenched disorder of any observable $\mathcal{O}$ in the original system and the transformed system satisfies the relation

$$\overline{\langle \mathcal{O}\left(\{s_i\},\{J\},\{h\}\right)\rangle_{\{J\},\{h\}}} = \overline{\langle \mathcal{O}\left(\{\epsilon_i s_i\},\{\tilde{J}\},\{\tilde{h}\}\right)\rangle_{\{J\},\{h\}}} \, . \tag{1.28}$$

where $\langle\cdot\rangle_{\{J\},\{h\}}$ is the thermal average with couplings $\{J\},\{h\}$. Let us emphasize that we take the thermal average for the same couplings, $\{J\}$ and $\{h\}$, in both sizes of Eq. (1.28).

Eq. (1.28) implies that only the gauge-invariant part of an observable $\mathcal{O}$ survives when we take the quenched average after the thermal average. Therefore, it is convenient to work with gauge invariant observables to avoid losing information upon averaging. For example, the four-body correlation function [cf. Eq. (1.32)] is gauge invariant, because

$$q^{ab}_{\vec{x}} q^{ab}_{\vec{x}+\vec{r}} = s^{(a)}_{\vec{x}} s^{(a)}_{\vec{x}+\vec{r}} s^{(b)}_{\vec{x}} s^{(b)}_{\vec{x}+\vec{r}} \to \epsilon^2_{\vec{x}} \epsilon^2_{\vec{x}+\vec{r}} s^{(a)}_{\vec{x}} s^{(a)}_{\vec{x}+\vec{r}} s^{(b)}_{\vec{x}} s^{(b)}_{\vec{x}+\vec{r}} = q^{ab}_{\vec{x}} q^{ab}_{\vec{x}+\vec{r}} \,. \tag{1.29}$$

1.4.2 Spatial correlation functions

The spatial correlation function in disorder systems, particularly within Ising models and spin glasses, serves as a crucial metric for understanding the spatial arrangement of spins and their interaction. More precisely, this function measures the correlations between the spins of the system. A fundamental aspect must be taken into account when considering its definition, which is related to the nature of the system. Usually, this aspect is not explicitly stated since it is unusual to consider systems that require different definitions of the correlation function. However, since throughout this thesis, we will consider both Ising (Part II) and EA models (Parts III-V), to avoid confusion, we will make the difference explicit.

In general, we can define the n-body correlation function, where n stands for the number of different spins in the expression. In such a way, for a system with N spins $s_{\vec{x}}$ in the nodes of a D-dimensional lattices, we can define the 2-body correlation function as

$$C(\vec{r}, t) = \frac{1}{N} \sum_{\vec{x}} \langle s_{\vec{x}} s_{\vec{x}+\vec{r}} \rangle \,. \tag{1.30}$$

where recall that $\langle\cdot\rangle$ is the thermal average. In systems without quenched averages, like the Ising model, this expression is enough to characterize the correlation of the system.

In contrast, if we consider a system with quenched disorder, like the Edwards-Anderson model, we need to consider the quenched average, $\overline{(\cdots)}$, to study the system behavior. Notice that two spins would be correlated in one sample, i.e. $\langle s_{\vec{x}} s_{\vec{y}} \rangle_{\{J\}_a} = 1$, while they would be anti-correlated in other, i.e. $\langle s_{\vec{x}} s_{\vec{y}} \rangle_{\{J\}_b} = -1$. Then, the quenched average produce that $\overline{\langle s_{\vec{x}} s_{\vec{x}+\vec{r}} \rangle_{\{J\}}} = 0, \forall\, \vec{x}$ and $\vec{r}$. We can avoid this problem by using the four-body correlation function, which has the form

$$C_4(\vec{r}, t) = \frac{1}{N} \sum_{\vec{x}} \overline{\langle s_{\vec{x}} s_{\vec{x}+\vec{r}} \rangle^2_{\{J\}}} \,. \tag{1.31}$$

Note subindex 4 to indicate that this is the four-body correlation function and to avoid confusion with the two-body correlation function defined in Eq. (1.30). Now, let us consider different replicas in Eq. (1.31) to calculate the four-body correlation function

$$C_4(\vec{r}, t) = \frac{1}{N} \sum_{\vec{x}} \overline{\langle s^{(a)}_{\vec{x}} s^{(a)}_{\vec{x}+\vec{r}} s^{(b)}_{\vec{x}} s^{(b)}_{\vec{x}+\vec{r}} \rangle_{\{J\}}} = \frac{1}{N} \sum_{\vec{x}} \overline{\langle q^{ab}_{\vec{x}} q^{ab}_{\vec{x}+\vec{r}} \rangle_{\{J\}}} \,. \tag{1.32}$$

Then, for systems with quenched disorder, the four-body correlation function is equivalent to a two-body correlation function over Edward-Anderson's order parameter, i.e., the replica overlap field $q^{ab}_{\vec{x}}$.

At this point, it is necessary to differentiate between the behavior of the correlation function out of equilibrium and once equilibrium has been reached. In the first case, the relevant length scale is the so-called coherence length, while in equilibrium, it is the correlation length.

Coherence length

As previously mentioned, we can compare the correlation decay with the theoretical predictions. In general, we expect that a system in contact with a thermal bath at temperature T after a time t will exhibit a long-distance decay

$$C(T,\vec{r},t) \sim r^{-\theta} f[r/\xi(t)]\,, \tag{1.33}$$

where $\xi(t)$ is the coherence length, which measures the linear size of domains of correlated spins along the dynamics evolution [notice the explicit time dependency in Eq. (1.33)].

The problem of determining the characteristic coherence length in evolving systems has been widely discussed. Previous works have concluded that a well-behaved estimator of $\xi(t)$, from the numerical point of view, can be computed through the integrals [BGM+09]

$$I_k(t) = \int_0^\infty r^k C(T,r,t)\mathrm{d}r\,. \tag{1.34}$$

By considering the long-distance decay [cf. Eq. (1.33)] in Eq. (1.34), and taking $x = r/\xi$, we would obtain

$$I_k = \int_0^\infty \xi^{k-\theta}(r/\xi)^{k-\theta} f(r/\xi)\xi\frac{\mathrm{d}r}{\xi} = \xi^{k+1-\theta}\int_0^\infty x^{k-\theta} f(x)\mathrm{d}x\,. \tag{1.35}$$

Then, we can estimate the coherence length by

$$\xi_{k,k+1}(t) = \frac{I_{k+1}}{I_k} \propto \xi(t)\,. \tag{1.36}$$

In this thesis, we have followed Ref. [BGM+09] using $k = 1$. The interested reader can find a more detailed explanation of the ξ estimation from the Eq. 1.4.2 in the Appendix G.

Correlation length

In addition to the coherence length, from the correlation function, we can compute the zero and minimal moment $\vec{p}$ susceptibilities

$$\chi(T) = \sum_{\vec{r}} C(T,r)\,, \quad F(T) = \sum_{\vec{r}} C(T,r)\mathrm{e}^{i\vec{p}\cdot\vec{r}}\,, \tag{1.37}$$

where $\vec{p} = (2\pi/L, 0, \cdots, 0)$ is the minimal moment in the D-dimensional space (or permutations) [PC99, BCF+00]. From χ and F, we can calculate the second-moment correlation length (see, e.g., Ref. [AMM05])

$$\xi_{\mathrm{corr}}(T) = \frac{1}{2\sin(\pi/L)}\sqrt{\frac{\chi(T)}{F(T)} - 1}\,. \tag{1.38}$$

Both quantities are usually sensitive to phase transition, so they have been used to study critical behavior. The correlation length measures how far the fluctuations in the system propagate. It is important to notice that they are not the same quantity despite being related and exhibiting a similar value [BCF$^+$09]. The most relevant difference is that the coherence length is an evolving property in the out-of-equilibrium dynamics [which we represent by the explicit time dependence in Eq. (1.33)], while the correlation length is a static property, defined in equilibrium. Along this thesis, we will refer to both coherence and correlation length as $\xi(t)$ and ξ, respectively (notice the explicit time dependence in the coherence length as a reminder of the different nature of both quantities; we will use ξ_{corr} where confusion is possible).

Part II

Counterintuitive dynamics

2

Unifying paradoxical dynamic effects

Shortcuts of freely relaxing systems using equilibrium physical observables

I. González-Adalid Pemartín, E. Mompó,
A. Lasanta, V. Martín-Mayor, J. Salas

Phys. Rev. Lett. (in press)
https://doi.org/10.48550/arXiv.2308.04094

The study of out-of-equilibrium relaxation processes has attracted great interest in recent decades. Much of this interest stems from the desire to find ways to control and predict these relaxation processes [Nyq28, Zwa28, Ons31a, Ons31b, Kub66, MPRV08, ESW08b, ESW08a]. However, we currently lack a general theory that goes beyond linear response theory and fluctuation theorems, which would allow us to control these processes. In particular, this theory could potentially lead to a short duration of relaxation times of freely evolving systems between two desired states [Sei12], which has theoretical and industrial significance.

Recent research focuses on understanding different strange relaxation processes in non-equilibrium systems, for example, the Mpemba effect [Jen06, MO69, BKC21]. Consider two identical systems in equilibrium at different temperatures. Put them in contact with a thermal bath at a temperature lower than that of both systems. The Mpeba effect occurs when the system that starts from a higher temperature reaches equilibrium before the system that was initially closer to equilibrium.

In Markovian systems, the Mpemba effect has been explained through spectral decomposition and decreasing or eliminating the slowest relaxation modes. This has been achieved for both classical [LR17, KRHV19, KB20, WV21, BRP23, SL22, KCB22] and open quantum systems [CLL21, NF19]. On the other hand, in systems where spectral decomposition cannot be applied, different strategies have been used to control dynamics using macroscopic observables. Some of these include energy non-equipartition in water [GLH19], a particular condition in kurtosis in granular gases [LVRPS17, TLCnL$^+$19, MLCL$^+$21], and correlation length in spin glasses [BJCC$^+$19]. In the same way, strategies that use temperatures other than the target temperature show speed-up dynamics. These include preheating protocols [GR20], or precooling protocols to control the size of magnetic domains in systems without temporal scale separation (see Chapter 3), or different control techniques [GOJP$^+$22, CL23].

What is even more surprising is another anomaly that was verified theoretically and experimentally found: far from equilibrium, an asymmetry may appear: equidistant and symmetric heating and cooling processes [LG20, IDL$^+$23] need different time to reach equilibrium. Even more, using reciprocal relaxation processes between two fixed temperatures, asymmetry is also found [IDL$^+$23]. The so-called "thermal kinematics" [IDL$^+$23] has successfully explained the phenomenon through information geometry [Cro07, ID20].

In this chapter, we introduce an unifying framework for several of the above-mentioned phenomena, in the context of Markovian dynamics. We aim to control the out-of-equilibrium evolution of a system. In particular, in this chapter, we *solely* use the system in-equilibrium physical observables and the spectral decomposition of the dynamic-generating matrix introduced in Sect. 2.1. Identifying the slowest-decaying physical observables, we can project the system onto the faster ones to speed up the total relaxation of the system. Choosing the appropriate initial condition for the final relaxation (from equilibrium, or after preheating or cooling) it is possible to obtain faster dynamics. To showcase this, we consider the antiferromagnetic 1D Ising model with a magnetic field.

The remaining part of this chapter is organized as follows. In Sect. 2.1 we introduce the theoretical framework. The explanation of the paradoxical dynamics effects is given in Sect. 2.2. Sect. 2.3 contains a real example to illustrate the surprising phenomena. In particular, we consider in Sect. 2.3 the antiferromagnetic Ising model in 1 dimension. In a first pass, readers may choose to skip Sect. 2.1.2, as well as Sect. 2.3.1, that contains technical information that is not essential for understanding the chapter.

2.1 Theoretical framework

We focus on Markovian dynamics to present strategies for controlling out-of-equilibrium dynamics. This choice is motivated by the well-established theoretical framework for Markovian dynamics. In particular, we focus our attention on modeling the dynamics of a system in contact with a thermal bath at temperature T_b through Markov dynamics with continuous time [LP17]. The continuous-time dynamic is obtained as the limit of some discrete-time Markov chain (in our case, the Heat Bath dynamics [Sok97]), which we explain in Sect. 2.1.2.

There are two possible viewpoints on Markov dynamics. The first one considers the time evolution of the probability distribution function (the so-called *strong form* of the associated stochastic differential equation). The second focuses on the time evolution of the observable magnitudes (*weak form*). These two viewpoints of the problem are connected. This connection is analog to the connection between the Heisenberg and Schrödinger representations in Quantum Mechanics for the time evolution. While recent work [CL23] has emphasized the strong form, we consider the weak-form approach more insightful. Before going into more detail in Sect. 2.1.2, we briefly recall the main ideas of both approach in the following section (see [LP17] for more details).

2.1.1 Strong and Weak Markov Dynamics

Let Ω be the set of all possible states $\boldsymbol{x}$ of the system (for a chain of N Ising spins, the number of states is $|\Omega| = 2^N$). The strong form of the dynamics focuses the attention on the Master equation for $P_{\boldsymbol{y}}^{(t)}$, the probability of finding the system in the microscopic state $\boldsymbol{y}$ at time t:

$$\frac{\mathrm{d}P_{\boldsymbol{y}}^{(t)}}{\mathrm{d}t} = \frac{1}{\tau_0} \sum_{\boldsymbol{x}\in\Omega} P_{\boldsymbol{x}}^{(t)} R_{\boldsymbol{x},\boldsymbol{y}}^{(\mathrm{b})} , \tag{2.1}$$

where $R_{\boldsymbol{x},\boldsymbol{y}}^{(\mathrm{b})}/\tau_0$ is the probability per unit of time for the system to jump from state $\boldsymbol{x}$ to state $\boldsymbol{y}$ when subject to a thermal bath with temperature T_b (notice the use of the label b to recall the temperature dependency and the use of τ_0 as a fixed time unit). Let us remark that the diagonal terms must be set as

$$R^{(\mathrm{b})}_{\boldsymbol{x},\boldsymbol{x}} = - \sum_{\boldsymbol{y}\in\Omega\setminus\{\boldsymbol{x}\}} R^{(\mathrm{b})}_{\boldsymbol{x},\boldsymbol{y}} \tag{2.2}$$

to ensure the total probability conservation. The Master equation (2.1) can be solved by obtaining the left-eigenvectors of the matrix $R^{(\mathrm{b})}$ (see e.g. [LP17], or Sect. 2.1.2 for more details), and expressing the initial probability $\boldsymbol{P}^{(t=0)}$ as a linear combination of these left-eigenvectors (we use $\boldsymbol{P}$ to represent the row vector of components $P_{\boldsymbol{x}}$). Let us remark that diagonalizing $R^{(\mathrm{b})}$ which is a $2^N \times 2^N$ matrix, would be a challenge even for a small system (special methods have been developed to address similar problems, see Chapter 6 for an example).

Let us now focus on the weak form of the dynamics (i.e. in the evolution of the observable magnitudes), which relies on two crucial mathematical ingredients.

First, we need the inner product between two observables $\mathcal{A}$ and $\mathcal{B}$, which are two mappings from the configuration space Ω to real numbers. Let

$$\mathbb{E}^{(\mathrm{b})}[\mathcal{A}] = \sum_{\boldsymbol{x}\in\Omega} \pi^{(\mathrm{b})}_{\boldsymbol{x}}\, \mathcal{A}(\boldsymbol{x}) \tag{2.3}$$

be the *equilibrium* expected value of $\mathcal{A}$ at bath temperature T_b, $\pi^{(\mathrm{b})}_{\boldsymbol{x}}$ being the Boltzmann weight for state $\boldsymbol{x}$, which is given by:

$$\pi^{(\mathrm{b})}_{\boldsymbol{x}} = \frac{\exp\{-\mathcal{H}(\boldsymbol{x})/(k_\mathrm{B}T_\mathrm{b})\}}{Z_N(T_\mathrm{b})}\,, \tag{2.4}$$

where

$$Z_N(T) = \sum_{\boldsymbol{x}\in\Omega} \exp\{-\mathcal{H}(\boldsymbol{x})/(k_\mathrm{B}T)\} \tag{2.5}$$

is the system partition function, and $\mathcal{H}(\boldsymbol{x})$ is the energy of the system at the configuration state $\boldsymbol{x}$. Under these conditions, the inner product of two observables $\mathcal{A}$ and $\mathcal{B}$ is defined as

$$\langle\, \mathcal{A} \,|\, \mathcal{B}\, \rangle \;:=\; \mathbb{E}^{(\mathrm{b})}[\mathcal{A}\,\mathcal{B}] \;=\; \sum_{\boldsymbol{x}\in\Omega} \pi^{(\mathrm{b})}_{\boldsymbol{x}}\, \mathcal{A}(\boldsymbol{x})\, \mathcal{B}(\boldsymbol{x})\,. \tag{2.6}$$

Notice the use of index (b) to refer to the thermal bath temperature. we emphasize the role of the constant observable such that $\mathbf{1}(x) = 1$ for any state $\boldsymbol{x}$, because for any observable $\mathcal{A}$,

$$\langle \mathbf{1} | \mathcal{A} \rangle = \mathbb{E}^{(\mathrm{b})}[\mathcal{A}]\,. \tag{2.7}$$

For any observable $\mathcal{A}$, its component orthogonal to $\mathbf{1}$ represents its *fluctuations*:

$$\mathcal{A}^\perp := \mathcal{A} - \mathbf{1}\mathbb{E}^{(\mathrm{b})}[\mathcal{A}]\,. \tag{2.8}$$

Indeed, the equilibrium fluctuations of $\mathcal{A}$ from its expected value at T are measured by

$$\langle \mathcal{A}^\perp | \mathcal{A}^\perp \rangle = \langle \mathcal{A} | \mathcal{A} \rangle - \mathbb{E}^{(\mathrm{b})}[\mathcal{A}]\langle \mathcal{A} | 1 \rangle = \mathbb{E}^{(\mathrm{b})}[\mathcal{A}^2] - (\mathbb{E}^{(\mathrm{b})}[\mathcal{A}])^2\,. \tag{2.9}$$

The second crucial ingredient is the time-evolution operator $\mathcal{R}$ that acts over the observables to produce time evolution, at bath temperature T_b,

$$\mathcal{R}^{(\mathrm{b})}[\mathcal{A}](\boldsymbol{x}) = \sum_{\boldsymbol{y}\in\Omega} R^{(\mathrm{b})}_{\boldsymbol{x},\boldsymbol{y}} \mathcal{A}(\boldsymbol{y})\,, \tag{2.10}$$

where the matrix $R_{\boldsymbol{x},\boldsymbol{y}}$ is defined in Eq. (2.1) and codifies the dynamics.

2.1.2 From discrete to continuous-time dynamics

Notice that, even though the discrete or continuous-time dynamics do not make a difference in the inner product, $\mathcal{R}$ is not independent of the chosen dynamics. To better understand the effect of the dynamics in the time-evolution operator, we follow the way from the discrete-time to the continuous-time dynamics in the following sections (this process is well-established, and can be found in textbooks, e.g. [LP17]).

Despite this theory being general, we are going to consider the Ising model with N spins in one dimension with coupling J and external field h, which Hamiltonian is

$$\mathcal{H}(\boldsymbol{x}) \ := \ -J\sum_{i=1}^{N} s_i\, s_{i+1} - h\sum_{i=1}^{N} s_i\,, \tag{2.11}$$

as an example for the following discussion.

Discrete time

Let us consider the probability for the system to jump from estate $\boldsymbol{x}$ to state $\boldsymbol{y}$ in a single time-step $W_{\boldsymbol{x},\boldsymbol{y}}$. If there is a finite number $|\Omega|$ of states, $W_{\boldsymbol{x},\boldsymbol{y}}$ can be regarded as an element of an $|\Omega|\times|\Omega|$ matrix W (recall that for infinity number of states, the mathematical framework is functional analysis). Because $W_{\boldsymbol{x},\boldsymbol{y}}$ is a probability, the matrix W must complain with four basic properties: the positivity and completeness

$$W_{\boldsymbol{x},\boldsymbol{y}} \geq 0 \quad , \quad \forall\, \boldsymbol{x},\boldsymbol{y}\ \in \Omega\,, \tag{2.12}$$

$$\sum_{\boldsymbol{y}\in\Omega} W_{\boldsymbol{x},\boldsymbol{y}} = 1 \quad , \quad \forall\, \boldsymbol{x} \in \Omega\,; \tag{2.13}$$

irreducibility,

$$\forall\, \boldsymbol{x},\boldsymbol{y}\ \in \Omega\,,\ \exists n_{\boldsymbol{x},\boldsymbol{y}} > 0 \text{ such that } [W^{n_{\boldsymbol{x},\boldsymbol{y}}}]_{\boldsymbol{x},\boldsymbol{y}}\,, \tag{2.14}$$

i.e. always it is possible going from any state $\boldsymbol{x}$ to any other state $\boldsymbol{y}$; and stationary, which implies that the Boltzmann weight $\boldsymbol{\pi}^{\mathrm{b}}$ is a left-eigenvector of the matrix W:

$$\pi^{\mathrm{b}}_{\boldsymbol{y}} = \sum_{\boldsymbol{x}\in\Omega} \pi^{\mathrm{b}}_{\boldsymbol{x}} W_{\boldsymbol{x},\boldsymbol{y}}\,. \tag{2.15}$$

This implies that a system initially in thermal equilibrium at temperature T_{b} remains in equilibrium forever, see Eq. (2.16).

Now, let denote $P^{(m)}_{\boldsymbol{x}}$ the probability of finding the system in state $\boldsymbol{x}$ at the discrete time-step m. Then, the probability after n further time steps is

$$P^{(m+n)}_{\boldsymbol{y}} = \sum_{\boldsymbol{x}\in\Omega} P^{(m)}_{\boldsymbol{x}} [W^n]_{\boldsymbol{x},\boldsymbol{y}}\,, \tag{2.16}$$

where W^n is the n-th power of the matrix W [Eq. (2.16) is the discrete version of the Master equation (2.1) and encodes the Markov and stationary properties of the dynamics]. Notice that $m=0$ is the case of the time evolution of the probability from the initial condition $P^{(m=0)}_{\boldsymbol{x}}$.

For our example model, the Ising spin chain, the Heat Bath discrete-time dynamics with random access to the chain forbids going from one state $\boldsymbol{x}$ to another state $\boldsymbol{y}$ with more than one different spin (i.e. $W_{\boldsymbol{x},\boldsymbol{y}} = 0$ for states $\boldsymbol{x}$ and $\boldsymbol{y}$ differing in more than one spin). However, if $\boldsymbol{x}$ and $\boldsymbol{y}$ differ in the value of only one spin, then

$$\begin{aligned} W_{\boldsymbol{x},\boldsymbol{y}} &= \frac{1}{N} R^{\mathrm{HB}}_{\boldsymbol{x},\boldsymbol{y}} \,, && (2.17) \\ R^{\mathrm{HB}}_{\boldsymbol{x},\boldsymbol{y}} &= \frac{\exp\{-[\mathcal{H}(\boldsymbol{y}) - \mathcal{H}(\boldsymbol{x})]/(k_{\mathrm{B}} T_{\mathrm{b}})\}}{1 + \exp\{-[\mathcal{H}(\boldsymbol{y}) - \mathcal{H}(\boldsymbol{x})]/(k_{\mathrm{B}} T_{\mathrm{b}})\}} \,. && (2.18) \end{aligned}$$

Remember that diagonal terms are fixed by the completeness condition (2.13). The $1/N$ prefactor in Eq. (2.17) tells that the spin that will be attempted to flip is chosen with uniform probability. These probabilities $R^{\mathrm{HB}}_{\boldsymbol{x},\boldsymbol{y}}$ ensure that W satisfied the detailed balance condition

$$\pi^{\mathrm{b}}_{\boldsymbol{x}} W_{\boldsymbol{x},\boldsymbol{y}} = \pi^{\mathrm{b}}_{\boldsymbol{y}} W_{\boldsymbol{y},\boldsymbol{x}} \,, \tag{2.19}$$

that can be used with the completeness condition to demonstrate that the detailed balance implies stationary (2.15).

For a single spin-flip dynamics, it is common to restrict the number of time steps n in Eq. (2.16) to a multiple of the number of spins N

$$n = kN \,, \; k \in \mathbb{N} \,, \tag{2.20}$$

to guarantee (on average) that every spin has k opportunities to change.

In difference to the strong formalism, where the attention is focused on the probability distributions (i.e. Eqs. (2.1) or (2.16) are solved by finding a base of left-eigenvectors of matrix W), the weak formalism focus on the observable $\mathcal{A}$ evolution, which is driven by the operator $\mathcal{W}$ as

$$\mathcal{W}[\mathcal{A}](\boldsymbol{x}) = \sum_{\boldsymbol{y} \in \Omega} W_{\boldsymbol{x},\boldsymbol{y}} \mathcal{A}(\boldsymbol{y}) \,. \tag{2.21}$$

Notice that $\mathcal{W}[\mathcal{A}]$ is a new observable. In addition, in this formalism, observables are column vectors. In this situation, the operator $\mathcal{W}^n[\mathcal{A}](\boldsymbol{x})$ is the expected value of $\mathcal{A}$ after n steps (where one knows for sure that the initial configuration is $\boldsymbol{x}$). Remark that for $n \to \infty$ the expected value of $\mathcal{A}$ becomes the equilibrium expected value at temperature T_{b}, independently of the initial configuration $\boldsymbol{x}$. The probability conservation [or completeness property (2.13)] implies as well that $\mathbf{1}$ is an eigenfunction of $\mathcal{W}$ with eigenvalue 1, i.e. $\mathcal{W}[\mathbf{1}] = \mathbf{1}$. Detailed balance implies that $\mathcal{W}$ is a self-adjoint operator for the inner product (2.6),†

$$\langle \mathcal{W}[\mathcal{A}] | \mathcal{B} \rangle = \langle \mathcal{A} | \mathcal{W}[\mathcal{B}] \rangle \,. \tag{2.22}$$

Therefore, the spectrum of $\mathcal{W}$ (and hence of W) is real. In addition, the completeness condition (2.13) guarantee that all the eigenvalues Λ belong to the interval $[-1, 1]$. Remember that the constant operator $\mathbf{1}$ has $\Lambda_1 = 1$, being the largest eigenvalue. Moreover, we can find an orthonormal basis of the space of observables with finite variance $(\mathbf{1}, \mathcal{O}^{\mathrm{b}}_2, \mathcal{O}^{\mathrm{b}}_3, \ldots)$, in which the $\mathcal{O}^{\mathrm{b}}_k$ are all eigenfunctions $\mathcal{W}[\mathcal{O}^{\mathrm{b}}_k] = \Lambda_k \mathcal{O}^{\mathrm{b}}_k$. We can order the basis in such a way that $1 = \Lambda_1 > \Lambda_2 \geq \Lambda_3 \geq \ldots \Lambda_{|\Omega|} \geq -1$.

† From inner product definition (2.6) and detailed balance property (2.19)

$$\begin{aligned} \langle \mathcal{W}[\mathcal{A}] | \mathcal{B} \rangle &= \sum_{\boldsymbol{x}} \pi^{(\mathrm{b})}_{\boldsymbol{x}} \mathcal{W}[\mathcal{A}](\boldsymbol{x}) \mathcal{B}(\boldsymbol{x}) \\ &= \sum_{\boldsymbol{x} \in \Omega} \sum_{\boldsymbol{y} \in \Omega} \pi^{(\mathrm{b})}_{\boldsymbol{x}} W_{\boldsymbol{x},\boldsymbol{y}} \mathcal{A}(\boldsymbol{y}) \mathcal{B}(\boldsymbol{x}) \\ &= \sum_{\boldsymbol{x} \in \Omega} \sum_{\boldsymbol{y} \in \Omega} \pi^{(\mathrm{b})}_{\boldsymbol{y}} W_{\boldsymbol{y},\boldsymbol{x}} \mathcal{A}(\boldsymbol{y}) \mathcal{B}(\boldsymbol{x}) \\ &= \sum_{\boldsymbol{y} \in \Omega} \pi^{(\mathrm{b})}_{\boldsymbol{y}} \mathcal{A}((y)) \mathcal{W}[\mathcal{B}](\boldsymbol{y}) \\ &= \langle \mathcal{A} | \mathcal{W}[\mathcal{B}] \rangle \,. \end{aligned}$$

Briefly getting back to the strong viewpoint, if $(\boldsymbol{\pi}^{(\mathrm{b})}, \boldsymbol{v}_2^{(\mathrm{b})}, \ldots)$ is the corresponding basis of left-eigenvectors, the starting probability can be linearly expressed

$$\boldsymbol{P}^{(n=0)} = \boldsymbol{\pi}^{(\mathrm{b})} + \sum_{k\geq 2}^{|\Omega|} \gamma_k \boldsymbol{v}_k^{(\mathrm{b})} \,. \tag{2.23}$$

Hence, the solution of the Master equation (2.16) for the dynamic evolution for the probability is

$$\boldsymbol{P}^{(n)} = \boldsymbol{\pi}^{(\mathrm{b})} + \sum_{k\geq 2}^{|\Omega|} \Lambda_k^n \gamma_k \boldsymbol{v}_k^{(\mathrm{b})} \,. \tag{2.24}$$

Returning to the weak formalism, the discrete-time evolution for the expectation value of an arbitrary magnitude $\mathcal{A}$, with finite variance and after n time steps, can be computed using a linear decomposition over the right-eigenvectors base of the magnitude $\mathcal{A}$,

$$\mathcal{A}(\boldsymbol{x}) = \mathbb{E}^{(\mathrm{b})}[\mathcal{A}]\mathbf{1}(\boldsymbol{x}) + \sum_{k\geq 2}^{|\Omega|} \langle \mathcal{O}_k^{(\mathrm{b})} | \mathcal{A} \rangle \mathcal{O}_k^{(\mathrm{b})}(\boldsymbol{x}) \,, \tag{2.25}$$

and Eq. (2.16) for the probability evolution. The complete computation

$$\begin{aligned}
\mathbb{E}_n[\mathcal{A}] &= \sum_{\boldsymbol{x}\in\Omega} P_{\boldsymbol{x}}^{(n)} \mathcal{A}(\boldsymbol{x}) = \sum_{\boldsymbol{x}\in\Omega} \sum_{\boldsymbol{y}\in\Omega} P_{\boldsymbol{y}}^{(n=0)} [W^n]_{\boldsymbol{y},\boldsymbol{x}} \mathcal{A}(\boldsymbol{x}) \\
&= \mathbb{E}^{(\mathrm{b})}[\mathcal{A}] + \sum_{\boldsymbol{x}\in\Omega} \sum_{\boldsymbol{y}\in\Omega} \sum_{k\geq 2}^{|\Omega|} P_{\boldsymbol{y}}^{(n=0)} \langle \mathcal{O}_k^{(\mathrm{b})} | \mathcal{A} \rangle [W^n]_{\boldsymbol{y},\boldsymbol{x}} \mathcal{O}_k^{(\mathrm{b})}(\boldsymbol{x}) \\
&= \mathbb{E}^{(\mathrm{b})}[\mathcal{A}] + \sum_{\boldsymbol{x}\in\Omega} \sum_{\boldsymbol{y}\in\Omega} \sum_{k\geq 2}^{|\Omega|} P_{\boldsymbol{y}}^{(n=0)} \langle \mathcal{O}_k^{(\mathrm{b})} | \mathcal{A} \rangle \Lambda_k^n \mathcal{O}_k^{(\mathrm{b})}(\boldsymbol{x}) \,,
\end{aligned}$$

can be written as

$$\begin{aligned}
\mathbb{E}_n[\mathcal{A}] &= \mathbb{E}^{(\mathrm{b})}[\mathcal{A}] + \sum_{k\geq 2} \alpha_k^{(n=0)} \beta_k^{\mathcal{A}} \Lambda_k^n \,, && (2.26) \\
\beta_k^{\mathcal{A}} &= \langle\, \mathcal{O}_k^{\mathrm{b}} \,|\, \mathcal{A} \,\rangle \,, && (2.27) \\
\alpha_k^{(n=0)} &= \sum_{\boldsymbol{x}\in\Omega} P_{\boldsymbol{x}}^{(n=0)} \, \mathcal{O}_k^{\mathrm{b}}(\boldsymbol{x}) \,. && (2.28)
\end{aligned}$$

Introducing small time step

Consider a modification of the previous discrete-time dynamics encoded in the matrix W: at each time step, with probability ϵ, we evolve the system using the discrete-time dynamics introduced in the previous section, while with probability $1-\epsilon$, we do nothing. The main idea of introducing the probability ϵ is to represent a tiny time step. Explicitly, we can represent this dynamics though a new W_ϵ matrix defined as

$$W_\epsilon = (1-\epsilon)\mathbb{I} + \epsilon W \,, \tag{2.29}$$

or, better,

$$W_\epsilon = \mathbb{I} + \epsilon \tilde{R}, \;\; \tilde{R} = W - \mathbb{I} \,. \tag{2.30}$$

Bear in mind that matrices W and $\tilde{R}$ have the same off-diagonal terms, while the completeness relation (2.13) for $\tilde{R}$ is

$$\tilde{R}_{\boldsymbol{x},\boldsymbol{x}} = - \sum_{\boldsymbol{y}\in\Omega\setminus\{\boldsymbol{x}\}} \tilde{R}_{\boldsymbol{x},\boldsymbol{y}} \,, \; \forall\, \boldsymbol{x} \in \Omega \,. \tag{2.31}$$

It is also crucial that $\tilde{R}$ and W share the basis of observables $(\mathbf{1}, \mathcal{O}_2^{\mathrm{b}}, \ldots)$, which is orthogonal with respect to the inner product defined in terms of the Boltzmann weight [recall Eq. (2.6)],[†] as well as the basis of probabilities $(\boldsymbol{\pi}^{(\mathrm{b})}, \boldsymbol{v}_2^{(\mathrm{b})}, \ldots)$. So Eqs. (2.24)-(2.26) are valid for the new dynamics with the replacement of the Λ_k eigenvalues of the matrix W by the $\Lambda_{k,\epsilon}$ eigenvalues of the matrix W_ϵ. Notice that both sets of eigenvalues are related by the eigenvalues $\tilde{\lambda}_k$ of the matrix $\tilde{R}$ (remember that these three matrices, W, W_ϵ, and $\tilde{R}$ have the same left- and right-eigenvectors):

$$\tilde{\lambda}_k = \Lambda - 1, \tag{2.32}$$

$$\Lambda_{k,\epsilon} = 1 + \epsilon\tilde{\lambda}_k\,, \tag{2.33}$$

where

$$0 = \tilde{\lambda}_1 > \tilde{\lambda}_1 \geq \ldots \geq \tilde{\lambda}_{|\Omega|} \geq -2\,. \tag{2.34}$$

Hence, for $\epsilon \leq 1/2$, all the eigenvalues of W_ϵ are guaranteed to be positive.

[†] Detailed balance implies that $\tilde{R}$ and W are self-adjoint operators with respect to the scalar product (2.6). However, if one prefers using the standard $\mathbb{R}^{|\Omega|}$ scalar product, it is possible to transform $\tilde{R}$ and W into real, symmetric matrices through a similarity transformation D, with matrix elements $D_{\boldsymbol{x},\boldsymbol{y}} = \pi_{\boldsymbol{x}}^{(\mathrm{b})}\delta_{\boldsymbol{x},\boldsymbol{y}}$. In this way, the left and right eigenvectors for $\tilde{R}$ and W can be simply put into correspondence with the corresponding eigenvectors $\Psi_k^{(b)}$ of the (similarity transformed) symmetric matrices $D^{-1}\tilde{R}D$ and $D^{-1}WD$. Of course, the set of all the $\Psi_k^{(b)}$ provides an orthonormal basis of $\mathbb{R}^{|\Omega|}$ (we mean orthonormal with respect to the standard scalar product). The correspondence between the different eigenvectors goes as follows:

$$\boldsymbol{v}_{k,\boldsymbol{x}}^{(\mathrm{b})} = \Psi_{k,\boldsymbol{x}}^{(\mathrm{b})}\sqrt{\pi_{\boldsymbol{x}}^{(\mathrm{b})}} \text{ and } \mathcal{O}_{k,\boldsymbol{x}}^{(\mathrm{b})} = \frac{\Psi_{k,\boldsymbol{x}}^{(\mathrm{b})}}{\sqrt{\pi_{\boldsymbol{x}}^{(\mathrm{b})}}}\,.$$

Continuous-time dynamics

In order to reach the continuous-time limit we need to make the parameter ϵ in Eq. (2.29) arbitrarily small. The first step is to take the limit in such a way that t/τ_0 is a rational number (remember that τ_0 defines our time unit)

$$\frac{t}{\tau_0} = \frac{p}{q} \in \mathbb{Q}\,, \tag{2.35}$$

where p/q is an irreducible fraction (the irrational value of t/τ_0 will be directly solved by continuity in our final formulation). Consider a sequence of ϵ_r going to zero as

$$\epsilon_r = \frac{1}{qr}\,, \quad r \in \mathbb{N}\,. \tag{2.36}$$

If we fix the number of time steps n_r as

$$n_r = Npr\,, \tag{2.37}$$

we obtain that $n_r\epsilon_r = Nt/\tau_0$, independently of r. The factor N is introduced because we are interested in a single spin-flip dynamics, so we want to work with an extensive number of spin-flip attempts.

Notices that Eqs. (2.27) and (2.28) are independent of n_r and ϵ_r. However, Eqs. (2.24) and (2.26) take the form

$$\boldsymbol{P}^{(n_r)} = \boldsymbol{\pi}^{(\mathrm{b})} + \sum_{k\geq 2}^{|\Omega|}(1 + \epsilon_r\tilde{\lambda}_k)^{n_r}\gamma_k\boldsymbol{v}_k^{(\mathrm{b})}\,, \tag{2.38}$$

$$\mathbb{E}_n[\mathcal{A}] = \mathbb{E}^{(\mathrm{b})}[\mathcal{A}] + \sum_{k\geq 2}\alpha_k^{(n=0)}\beta_k^{\mathcal{A}}\,(1 + \epsilon_r\tilde{\lambda}_k)^{n_r}\,. \tag{2.39}$$

The continuous time limit is reached by letting r go to infinity, so that ϵ_r goes to zero:

$$\lim_{r\to\infty}(1+\epsilon_r\tilde{\lambda}_r)^{n_r} = e^{-N|\tilde{\lambda}_k|t/\tau_0}\,, \tag{2.40}$$

where we have taken care of the fact that the eigenvalues $\tilde{\lambda}_k$ are non-positive numbers. Finally, making the connection between $\tilde{R}$ and R^{HB} (and their respective for the eigenvalues), we obtain

$$\begin{aligned} R^{\text{HB}} &= N\tilde{R}\,, && (2.41)\\ \lambda_k &= N\tilde{\lambda}_k\,. && (2.42)\end{aligned}$$

The final expressions for the probability or observable expectation value are

$$\begin{aligned} \boldsymbol{P}^{(t)} &= \boldsymbol{\pi}^{(\text{b})} + \sum_{k\geq 2}^{|\Omega|} e^{-|\lambda_k|t/\tau_0}\gamma_k \boldsymbol{v}_k^{(\text{b})}\,, && (2.43)\\ \mathbb{E}_t[\mathcal{A}] &= \mathbb{E}^{(\text{b})}[\mathcal{A}] + \sum_{k\geq 2}\alpha_k^{(t=0)}\beta_k^{\mathcal{A}}\, e^{-|\lambda_k|t/\tau_0}\,, && (2.44)\end{aligned}$$

where, recalling Eqs. (2.27) and (2.28),

$$\begin{aligned} \beta_k^{\mathcal{A}} &= \langle\, \mathcal{O}_k^{\text{b}}\,|\,\mathcal{A}\,\rangle\,,\\ \alpha_k^{(n=0)} &= \sum_{\boldsymbol{x}\in\Omega} P_{\boldsymbol{x}}^{(n=0)}\,\mathcal{O}_k^{\text{b}}(\boldsymbol{x})\,.\end{aligned}$$

2.1.3 Understanding the observables evolution

Regarding Eq. (2.28), in situations where the system shows a separation of time scales (i.e. $|\lambda_2| < |\lambda_3|$), Eq. (2.44) gives rise to a hierarchy of physical magnitudes, with $\mathcal{O}_2^{\text{b}}$ having the slowest decay. If we find an initial setup such that $\alpha_2^{(t=0)} = 0$ —all $\alpha_k^{(t=0)}$ are independent of the observable $\mathcal{A}$ under consideration— then, provided that $\beta_2^{\mathcal{A}} \neq 0$, the time evolution to the equilibrium of the expected value will show an exponential speed-up (for an example of how to obtain an exponential speed-up in system without separation of time scales see Chapter 3).

Notice that the starting probability $\boldsymbol{P}^{(t=0)}$ codes the initial setup. This setup is not restricted to an equilibrium state. Nevertheless, equilibrium states are easier to control (e.g. experimentally), making them simpler to control. For instance, using an equilibrium initial condition, the requirement for a speed-up would be met if we can find a temperature $T \neq T_{\text{b}}$ (at which we previously equilibrate the system) such that $\alpha_2^{(t=0)} \equiv \mathbb{E}^T[\mathcal{O}_2^{\text{b}}] = 0$.

To make it explicit, consider the system at temperature T. After a long enough time, the system is at equilibrium (this reasoning can also be applied to situations where the first temperature does not reach equilibrium), so $\boldsymbol{P}^{(t=0)} = \boldsymbol{\pi}^T$. When the thermal bath temperature is changed to T_{b}, for any observable $\mathcal{A}$, the time evolution of the expected value can be written (in the presence of time-scale separation) as

$$\mathbb{E}_t^{T_{\text{b}}}[\mathcal{A}] \simeq \mathbb{E}^{(\text{b})}[\mathcal{A}] + \alpha_2^{(t=0)}\beta_2^{\mathcal{A}} e^{-|\lambda_k|t/\tau_0}\,, \tag{2.45}$$

where

$$\alpha_2^{(t=0)} = \sum_{\boldsymbol{x}\in\Omega} \pi_{\boldsymbol{x}}^T \mathcal{O}_2^{(\text{b})}(\boldsymbol{x}) \equiv \mathbb{E}^T[\mathcal{O}_2^{(\text{b})}]\,. \tag{2.46}$$

Notice that a prior knowledge of $\mathbb{E}^T[\mathcal{O}_2^{(\mathrm{b})}]$ is not accessible, so determining the value of T that guarantees $\alpha_2^{(t=0)} = 0$ is not an easy task. However, as it is detailed in Sect. 2.2, in some situations, it is possible to force this behavior.

2.2 Experimental suitability

As the reader will have noticed, for a large number of states, the spectral decomposition (2.25) is not practical. In particular, identifying the slowest observable, $\mathcal{O}_2^{\mathrm{b}}$, may not be feasible, or its experimental measurement may be difficult. Nevertheless, there are more favorable situations.

Specifically, let us consider the neighborhood of a first-order phase transition at zero temperature separating two ground states with different symmetries (see Sect. 2.3 for a specific example). Let $\mathcal{M}_{\mathrm{w}}$ be the order parameter of the unstable phase (the suffix w stands for *wrong*). If symmetries are such that $\mathbb{E}^T[\mathcal{M}_{\mathrm{w}}] = 0$ for all T, then there are good chances that $(\mathcal{M}_{\mathrm{w}}^2)^{\perp}$ [remember definition (2.8)] will be a nice proxy for $\mathcal{O}_2^{\mathrm{b}}$. Indeed, at phase coexistence, slow dynamics are often caused by metastability [Par88]. Notice that $(\mathcal{M}_{\mathrm{w}}^2)^{\perp}$ is the fluctuating part of $\mathcal{M}_{\mathrm{w}}^2$ [see Eq. (2.9)], so it will have a zero expectation value at equilibrium in the thermal bath temperature. Therefore, $(\mathcal{M}_{\mathrm{w}}^2)^{\perp}$ agrees with the behavior of $\mathcal{O}_2^{\mathrm{b}}$: $\mathbb{E}^{T_{\mathrm{b}}}[\mathcal{O}_2^{\mathrm{b}}] = \langle \mathbf{1} | \mathcal{O}_2^{\mathrm{b}} \rangle = 0$. In other words, we expect that $(\mathcal{M}_{\mathrm{w}}^2)^{\perp}$ is parallel, or close to parallel, to $\mathcal{O}_2^{\mathrm{b}}$:

$$\frac{\langle (\mathcal{M}_{\mathrm{w}}^2)^{\perp} | \mathcal{O}_2^{\mathrm{b}} \rangle}{\langle (\mathcal{M}_{\mathrm{w}}^2)^{\perp} | (\mathcal{M}_{\mathrm{w}}^2)^{\perp} \rangle^{1/2}} \approx 1 \,, \tag{2.47}$$

with the scalar product defined in Eq. (2.6).

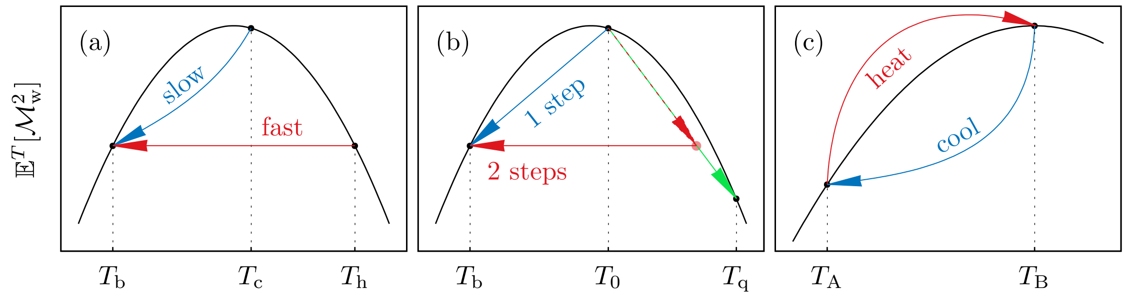

Figure 2.1: Graphical explanation of the anomalous effects. (a) The Mpemba effect. (b) Preheating for fast cooling. (c) Asymmetry of heating and cooling processes.

The key property to produce unconventional dynamics effects is that $\mathbb{E}^T[\mathcal{M}_{\mathrm{w}}^2]$ is a non-monotonic function of T, and there is a bath temperature T_{b}^* such that $\mathbb{E}^T[\mathcal{M}_{\mathrm{w}}^2]$ has a local maximum(see Figs. 2.1 and 2.2).† Notice that the behavior in Figs. 2.1 and 2.2 is general because $\mathbb{E}^T[\mathcal{M}_{\mathrm{w}}^2]$ is proportional to the susceptibility of $\mathcal{M}_{\mathrm{w}}$ with respect to its conjugate field. This susceptibility goes to zero when $T \to 0$ because M_{w} is the order parameter for the unstable phase. On the other side, when the temperature increases, all susceptibilities decrease. These imply that there is at least one local maximum of $\mathbb{E}^T[\mathcal{M}_{\mathrm{w}}^2]$.

† If there were a physical argument justifying the existence of a local minimum, the argument would remain valid.

2.2.1 Our basic observation

Take the spectral decomposition (2.25) for $\mathcal{M}_{\mathrm{w}}^2$ when the starting distribution $\boldsymbol{P}^{(t=0)}$ is the Boltzmann weight for some temperature $T^* \neq T_{\mathrm{b}}$. Under the just discussed conditions, we can approximate the coefficient $\alpha_2^{(t=0)}$ as

$$\alpha_2^{(t=0)} \approx \frac{\mathbb{E}^{T^*}[\mathcal{M}_{\mathrm{w}}^2] - \mathbb{E}^{(\mathrm{b})}[\mathcal{M}_{\mathrm{w}}^2]}{\sqrt{\langle (\mathcal{M}_{\mathrm{w}}^2)^{\perp} | (\mathcal{M}_{\mathrm{w}}^2)^{\perp} \rangle}} \,, \tag{2.48}$$

where the denominator is only a constant fixed by the bath temperature.

Indeed, Eq. (2.48) is more general than it seems at first sight. In particular, it is not necessary to achieve equilibrium at temperature T^*. In those situations, we can replace $\mathbb{E}^{T^*}[\mathcal{M}_{\mathrm{w}}^2]$ by the expected value of $\mathcal{M}_{\mathrm{w}}^2$ after evolving the system any time at temperature T^*, $\mathbb{E}_{t=0}[\mathcal{M}_{\mathrm{w}}^2]$ (we shall be changing the temperature of the thermal bath at time $t = 0$). This expected value is given by the probability distribution, $\boldsymbol{P}^{(t=0)}$, before changing the temperature from T^* to T_{b}. This probability distribution $P^{(t=0)}$ may differ from the equilibrium distribution, $\boldsymbol{\pi}^{T^*}$.

2.2.2 Markovian Mpemba effect

Consider a thermal bath at temperature T_{b} and two others temperatures, T_{c} (c from *cold*) and T_{h} (h from *hot*) such that $T_{\mathrm{b}} < T_{\mathrm{c}} < T_{\mathrm{h}}$. These temperatures have been chosen to have expectation values of $\mathcal{M}_{\mathrm{w}}^2$ as shown in Fig. 2.1-(a). This situation forces that $\alpha_2^{\mathrm{h}} = 0$ despite $\alpha_2^{\mathrm{c}} > 0$ [remember Eq. (2.48)]. In this situation, we take two systems at equilibrium at temperatures T_{h} and T_{c} and put them in contact with a thermal bath at temperature T_{b}. For any observable $\mathcal{A}$ with $\beta_2^{\mathcal{A}} \neq 0$ [see Eq. (2.27)] in the system originally in equilibrium at $T = T_{\mathrm{h}}$ will experiment an exponential dynamic speed-up. Instead, the system equilibrated at $T = T_{\mathrm{c}}$ will display a slower relaxation. In general, T_{h} will not be such that α_2^{h} will exactly by $\alpha_2^{\mathrm{h}} = 0$, but T_{h} will be close to the temperature where exact equality is achieved.

Remark that situations where $\mathbb{E}^{(\mathrm{c})}[\mathcal{A}]$ is closer to $\mathbb{E}^{(\mathrm{b})}[\mathcal{A}]$ than $\mathbb{E}^{(\mathrm{h})}[\mathcal{A}]$ will produce a most spectacular Mpemba effect because the difference

$$\Delta_t[\mathcal{A}] = \frac{1}{N}(\mathbb{E}_t^{(\mathrm{h})}[\mathcal{A}] - \mathbb{E}_t^{(\mathrm{c})}[\mathcal{A}]) \tag{2.49}$$

will change sign.

Let us finally mention that the above explanation is also valid for the *inverse* Mpemba effect [LR17]. This phenomenon refers to situations where two identical systems in equilibrium at temperatures T_{cold} and T_{hot}, such that $T_{\mathrm{c}} < T_{\mathrm{h}}$, are putting in contact with a hotter than both thermal bath at temperature T_{b}. The inverse Mpemba effect occurs when the system at temperature T_{cold} reaches equilibrium before the system at T_{hot}. However, due to the rapid thermalization at high temperatures, the relaxation times are shortened and become similar to each other. This makes it difficult to observe the inverse Mpemba phenomenon, as it requires a higher degree of precision.

2.2.3 Preheating for a faster cooling

Previous works, such as those of [LR17, GR20] for systems with separation of time scales, or the one explained in Chapter 3 for systems without time scale separation, propose pre-cooling protocols to produce faster thermalization at high temperatures. Specifically, take a system from equilibrium at temperature T_0 and cool it down to a temperature $T_q < T_0$. After some time t', put it in contact with a thermal bath at temperature $T_\mathrm{b} > T_0$. This evolution can make it thermalize faster than a system that evolves freely from T_0 to T_b directly (see Chapter 3 or reference [LR17]). We shall consider, instead, the inverse situation, i.e., whether pre-heating a system to a temperature $T_q > T_0$ [as shown in Fig. 2.1-(b)] can be used to accelerate the dynamics to equilibrium at temperature T_b (as compared to a system originally equilibrated at temperature T_0, that is suddenly placed in a thermal bath at T_b).

Notice that, for both protocols (pre-cooling and pre-heating), the exponential acceleration is achieved by setting the $\alpha_0^{(t=0)}$ term to zero. Eq. (2.48) gives us a direct way to do so, independently of the protocol considered.

As said above in this chapter, we focus on a pre-heating protocol. To amplify the effect, we chose T_0 close to the maximum of $\mathbb{E}^T[\mathcal{M}_\mathrm{w}^2]$, so that $\alpha_2^{T_0\to T_\mathrm{b}}$ will be as large as possible, cf. Eq. (2.48). In addition, we chose $T_\mathrm{q} \gg T_0$ so that $\mathbb{E}^{(\mathrm{h})}[\mathcal{M}_\mathrm{w}^2] > \mathbb{E}^{(\mathrm{q})}[\mathcal{M}_\mathrm{w}^2]$, see Fig. 2.1-(b). In this situation, after changing the bath temperature from T_0 to T_q the expected value of $\mathcal{M}_\mathrm{w}^2$ decreases from its initial value $\mathbb{E}^{T_0}[\mathcal{M}_\mathrm{w}^2]$ and, at some time t', crosses $\mathbb{E}^{(\mathrm{b})}[\mathcal{M}_\mathrm{w}^2]$. From Eq. (2.48) it follows that if we instantaneously lower the bath temperature from T_q to T_b at time $t_\mathrm{p} \approx t'$ (where p comes from pre-heating), the relaxation at T_b will start with $\alpha_2^{t_\mathrm{p}} = 0$. This t_p time overhead is compensated by the exponential speed-up at T_b.

For a better illustration of the phenomena, see Sect. 2.3.2, we introduce the convenient estimator

$$\delta_t[\mathcal{A}] = \frac{1}{N}(\mathbb{E}_t[\mathcal{A}] - \mathbb{E}_t^{(\mathrm{b})}[\mathcal{A}]) \tag{2.50}$$

what quantifies how far from the equilibrium is the system at time t.

2.2.4 Heating and cooling may be asymmetric processes

Naively one would think that two systems at temperatures T_A and T_B, equidistant from a third temperature T_C, should need the same time to equilibrate at T_C. Another situation where it is normal to expect to the same equilibration time for different processes is the thermalization of a system that goes from T_A to T_B and the inverse process, i.e. going from T_B to T_A. However, recent works [LG20, IDL+23] have shown that these expectations do not hold for out-of-equilibrium dynamics.

In order to explain these surprising effects, we focus on the second example, where process $T_B \to T_A$ is *faster* than its counterpart $T_A \to T_B$ [see Fig. 2.1-(c)]. Unlike previous cases, where the value of $\alpha_2^{(t=0)}$ is the key for explaining the behavior, here the values of $\alpha_2^{T_B\to T_A}$ and $\alpha_2^{T_A\to T_B}$ are numbers of similar magnitude but opposite signs. Hence, the main open possibility to obtain a different equilibration speed in the relaxation process is the largest relaxation time $1/|\lambda_2|$ in the system. Notice that the value of the eigenvalues λ_k of the evolution matrix R^{HB} are dependent on the bath temperature [see Eq. (2.18)]. Therefore, the values of $\lambda_2^{(T_A)}$ and $\lambda_2^{(T_B)}$, which dominate the relaxation process, will be different in general. This is the origin of the asymmetry as we explain next.

To amplify the effect, let us consider the maximum of $\mathbb{E}^{(B)}[\mathcal{M}_{\mathrm{w}}^2]$ at temperature T_B in Fig. 2.1. In this situation, it is natural to expect that the relaxation time $1/|\lambda_2|$ will also attain its maximum value (remark the relation between slow dynamics a metastability exhibit at phase coexistence [Par88]). Under these conditions [recall Eq. (2.45)] and because λ_2 is independent of the observable under consideration, it is faster to reach the equilibrium expected value when the system goes from T_B to T_A than when the temperature is changed from T_A to T_B.

However, the energy is an important exception. But the underlying reason is the fluctuation-dissipation theorem, that can be written as

$$T^2 \frac{\mathrm{d}\mathbb{E}^T[\mathcal{M}_{\mathrm{w}}^2]}{\mathrm{d}T}\bigg|_{T=T_{\mathrm{b}}} = \langle (\mathcal{M}_{\mathrm{w}}^2)^{\perp} | \mathcal{E} \rangle \,, \tag{2.51}$$

where $\mathcal{E}$ is the energy operator. On the one hand, the l.h.s of Eq. (2.51) is zero for $T_{\mathrm{b}} = T_B$ because there is a local maximum of $\mathbb{E}^T[\mathcal{M}_{\mathrm{w}}^2]$ at that temperature. On the other hand, the r.h.s term in Eq. (2.51) is approximately equal to $\beta_2^{\mathcal{E}}$ [recall that $(M_{\mathrm{w}}^2)^{\perp} \approx \mathcal{O}_2^{(\mathrm{b})}$]. Thus, the approach to equilibrium of $\mathcal{E}$ at T_B is ruled by λ_3 rather than λ_2, which makes it very difficult to predict which will be the fastest process for the energy.

2.3 The antiferromagnetic 1D Ising model

This section provides a working example that illustrates the surprising phenomena that have been explained in Sect. 2.2. The model we consider is the antiferromagnetic 1D Ising model with N spins $s_i = \pm 1$, $1 \leq i \leq N$, and periodic boundary conditions $s_{N+1} := s_1$. The configuration space is given by $\Omega = \{-1, 1\}^N$. The energy for a given spin configuration $\boldsymbol{x} = (s_1, s_2, s_3, \ldots, s_N)$ is given by the Hamiltonian (1.4) with coupling constants $J_{i,j} = J < 0$ and external field $h > 0$

$$\mathcal{H}(\boldsymbol{x}) = -J \sum_{k=1}^{N} s_k s_{k+1} - h \sum_{k=1} s_k \,. \tag{2.52}$$

We take N even to avoid frustration in the system. The line $2J + h = 0$ separates two different minimum-energy configurations. If $J > -h/2$, the ground state (GS) is the uniform configuration $\{s_i = 1\}$. Instead, if $j < -h/2$, the GS is one of the two ordered staggered configurations $\{s_i = (-1)^i\}$ or $\{s_i = (-1)^{i+1}\}$. We see that this model realizes the first-order transition at T=0 required to demonstrate exotic dynamics.

The order parameters that discriminates our GS are the uniform ($\mathcal{M}_{\mathrm{u}}$) and the staggered ($\mathcal{M}_{\mathrm{st}}$) magnetizations:

$$\mathcal{M}_{\mathrm{u}}(\boldsymbol{x}) = \sum_{k=1}^{N} s_k \,, \tag{2.53}$$

$$\mathcal{M}_{\mathrm{st}}(\boldsymbol{x}) = \sum_{k=1}^{N} (-1)^k s_k \,. \tag{2.54}$$

In the uniform GS, $\mathcal{M}_\mathrm{u} = N$ and $\mathcal{M}_\mathrm{st} = 0$, while for the staggered GSs one finds $\mathcal{M}_\mathrm{u} = 0$ and $\mathcal{M}_\mathrm{st} = \pm N$. The energy $\mathcal{E}$, which is given by the Hamiltonian (2.52), is invariant under spatial translations ($s_i \to s_{i+1}$) which ensures that $\mathbb{E}^T[\mathcal{M}_\mathrm{st}] = 0$ for all temperatures. This is the preferred situation explained in Sect. 2.2. Therefore, we make stable the uniform GS by choosing $(J, h) = (-4, 8.2)$ in order to use as our *wrong* order parameter the staggered magnetization, i.e. $\mathcal{M}_\mathrm{w} \equiv \mathcal{M}_\mathrm{st}$. Other magnitudes of interest will be the staggered susceptibility

$$\chi_\mathrm{st} = \frac{1}{N}\mathbb{E}^T[\mathcal{M}_\mathrm{st}^2]\,, \tag{2.55}$$

and the spin-spin interaction

$$\mathcal{C}_1(\boldsymbol{x}) = \sum_{k=1}^{N} s_k s_{k+1}\,. \tag{2.56}$$

Notice that all the observable magnitudes considered here are invariant under spatial translations. Also our dynamics, see Eq. (2.1), preserves the translational symmetry of the starting probability $\boldsymbol{P}^{(t=0)}$. Therefore, the spectral decomposition in Eq. (2.25) can be restricted to the subspace of magnitudes $\mathcal{O}_k^\mathrm{b}$ that are themselves invariant under translations.

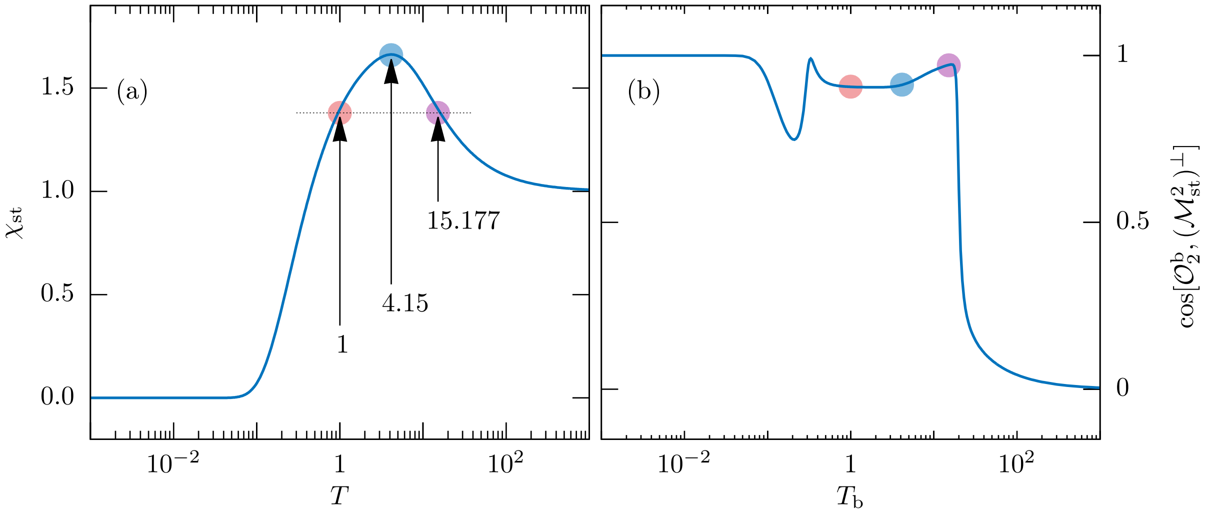

Figure 2.2: **Validation of $(\mathcal{M}_\mathrm{w}^2)^\perp$ as a proxy for the slowest decaying observable $\mathcal{O}_2^\mathrm{b}$.** (a) χ_st as computed for $N \to \infty$ as function of the thermal bath temperature T, see Eq. (2.62). The susceptibility has a maximim at $T_\mathrm{b}^* \approx 4.15$. The curves for $N = 8$ and $N \to \infty$ are hardly distinguishable at this scale. (b) For $N = 8$, the cosine of the angle between $(\mathcal{M}_\mathrm{w}^2)^\perp$ and $\mathcal{O}_2^\mathrm{b}$ is close to 1 for a wide range of bath temperatures. $\mathcal{O}_2^\mathrm{b}$ is obtained by exact diagonalization (see Appendix C). The colored dots in (a) and (b) indicate the three temperatures that we mostly use to demonstrate unconventional dynamics.

In Fig. 2.2(a) we show the temperature evolution of χ_st. As we expect from the general discussion, we can confirm that the staggered susceptibility is non-monotonic. Moreover, Fig. 2.2(b) shows that that the angle (defined by Eq. 2.6) between the slowest decay observable $\mathcal{O}_2^\mathrm{b}$ and the fluctuations of $\mathcal{M}_\mathrm{st}^2$, namely $(\mathcal{M}_\mathrm{st}^2)^\perp$, is small. Therefore, the conditions necessary for the existence of exotic dynamics are met with our working parameters.

2.3.1 Exact expectation values

One of the reasons for considering the one-dimensional Ising model with external magnetic field is that it allows us to obtain analytically the temperature dependence of the different observables studied in this chapter, see Eqs. (2.52)-(2.56), for a system of N spins. In particular, using the transfer matrix formalism (see Appendix B for details) it is possible to derive the free density energy (for N even):

$$F_N = \log \lambda_+ + \frac{1}{N} \log \left[1 + \left(\frac{\lambda_-}{\lambda_+} \right) \right] \tag{2.57}$$

where $\lambda_\pm$ are the respective eigenvalues of the transfer matrix (see Appendix B). Now, introducing the notation $K = J/(k_\mathrm{B}T)$ and $H = h/(k_\mathrm{B}T)$, and the ratio

$$\psi(K,H) \ = \ \frac{\lambda_-}{\lambda_+} = \frac{\cosh(H) - \sqrt{e^{-4K} + \sinh^2(H)}}{\cosh(H) + \sqrt{e^{-4K} + \sinh^2(H)}} \,, \tag{2.58}$$

we can calculate the temperature dependence of any observable from the free density energy. In particular, the uniform magnetization

$$\mathcal{M}_\mathrm{u} = \frac{\sinh(H)}{\sqrt{e^{-4K} + \sinh^2(H)}} \, \frac{1 - \psi^N}{1 + \psi^N} \,, \tag{2.59}$$

and the spin-spin interaction is

$$\mathcal{C}_1 = \frac{\sinh^2(H)}{e^{-4K} + \sinh^2(H)} + \frac{1 + \psi^{N-2}}{1 + \psi^N} \, \frac{\psi}{1 + e^{4K} \sinh^2(H)} \,. \tag{2.60}$$

From these results, we can calculate the system energy as

$$\mathcal{E} = -J\mathcal{C}_1 - h\mathcal{M}_\mathrm{u} \,. \tag{2.61}$$

Finally, the staggered susceptibility has the expression

$$\chi_\mathrm{st} = \frac{e^{-4K}}{\cosh(H) \sqrt{e^{-4K} + \sinh^2(H)}} \, \frac{1 - 2\psi^N}{1 + \psi^N} \,. \tag{2.62}$$

2.3.2 Results

We have studied single-site dynamics (Heat Bath dynamics or Gibbs sampler [LP17, Sok97]). For short chains ($N = 8, 12$), we solved the Master equation (2.1) in two ways: through Monte Carlo (MC) simulations, and by finding the “exact” spectral decomposition of the operator R (strictly speaking, we compute the spectral decomposition of R using 300-digit arithmetic). Both computational methods are explained in detail in Appendix E. The results support the proposed approach for small N with a full agreement between both methods. However, for larger chains ($N = 32$) we have only used a MC method (because the numerical diagonalization is hardly accesable —see Appendix C for a discussion), which validates our proposal as well. Let us mention that we have found statistical compatibility for $N = 12$ and $N = 32$.

Our simulation setup

In our MC simulations we generate a large number of statistically independent replicas, $S = 2.4 \times 10^9$. Along each trajectory we consider $\mathcal{M}_\mathrm{u}$, χ_st, and $\mathcal{C}_1$. We select a priori a mesh of measuring times $\{t^{(1)}, \dots, t^{(M)}\}$. For each of this times $t^{(k)}$, and for each trajectory r, we obtain the corresponding value

$$\mathcal{A}_{k,r} \equiv \mathcal{A}[\boldsymbol{x}^{(r)}(t^{(k)})] \,. \tag{2.63}$$

$\boldsymbol{x}^{(r)}(t^{(k)})$ is the configuration of the r-trajectory at time $t^{(k)}$. The expected value $\mathbb{E}_{t^{(k)}}[\mathcal{A}]$ is estimated as

$$\mathbb{E}_{t^{(k)}}[\mathcal{A}] = \frac{1}{S}\sum_{r=1}^{S} \mathcal{A}_{k,r} \,, \tag{2.64}$$

while the errors for these expected values are computed in the standard way

$$\Delta\mathbb{E}_{t^{(k)}}[\mathcal{A}] = \sqrt{\frac{1}{S(S-1)}\sum_{r=1}^{S}\left(\mathcal{A}_{k,r} - \mathbb{E}_{t^{(k)}}[\mathcal{A}]\right)^2} \,. \tag{2.65}$$

All our replicas contain a preparation step and a measuring step. In the preparation, the initial configurations are chosen randomly with uniform probability (equivalent to infinite temperature). Hence, the dynamics explained in Appendix E is followed at the initial temperature for a time long enough to ensure equilibration. Then, one (or more) temperature jumps are performed by changing the thermal bath temperature in Eq. (2.18), while taking as the initial configuration the final configuration at the previous temperature. Table 2.1 summarizes relevant details about our simulations.

Simulation T_b, (T_q)	Size	Trajectories	Time
$15.177 \to 1$	8, 12, 32	2.4×10^9	10
$4.15 \to 1$	8, 12, 32	2.4×10^9	10
$1 \to 15.177$	8, 12, 32	2.4×10^9	10
$4.15 \to 15.177$	8, 12, 32	2.4×10^9	10
$15.177 \to 4.15$	8, 12, 32	2.4×10^9	8
$1 \to 4.15$	8, 12, 32	2.4×10^9	8
$4.15 \to (2000) \to 1$	8,12, 32	2.4×10^9	10 (0.156)

Table 2.1: List of simulations. Columns: (I) Bath temperatures used in each case simulated. Parentheses indicate the temperature used during the first step in the preheating protocol. (II) Number of spins in the chain. (III) Number of independent trajectories, or replicas. (IV) Time length in units such that $\tau_0 = 1$. Parentheses indicate the time in contact with the first thermal bath during the preheating protocol.

Markovian Mpemba effect

Fig. 2.3 illustrate the Mpemba effect for all the observables introduced above (i.e. $\mathcal{E}$, $\mathcal{C}_1$, $\mathcal{M}^2_\mathrm{st}$, and $\mathcal{M}_\mathrm{u}$). We have obtained the result with $T_\mathrm{b} = 1$, $T_\mathrm{c} = 4.15$, and $T_\mathrm{h} = 15.177$, for $N = 8, 12$, (data from exact diagonalization) and 32 (data from MC). We represent the time evolution of $\Delta_t[\mathcal{A}]$ [cf. Eq. (2.49)]. Notice that a change in sign on $\Delta_t[\mathcal{A}]$ (marked by a dot in Fig 2.3) implies a crossing between $\mathbb{E}^{\mathrm{h}}[\mathcal{A}]$ and $\mathbb{E}^{\mathrm{c}}[\mathcal{A}]$. Remark, there is no crossing for $\mathcal{M}^2_{\mathrm{st}}$, which is expected because we prepared our system so that $\mathbb{E}^{\mathrm{h}}_t[\mathcal{M}^2_{\mathrm{st}}]$ goes exponentially fast w.r.t. $\mathbb{E}^{\mathrm{c}}_t[\mathcal{M}^2_{\mathrm{st}}]$. Hence, the negative sign in Fig. 2.3(a).

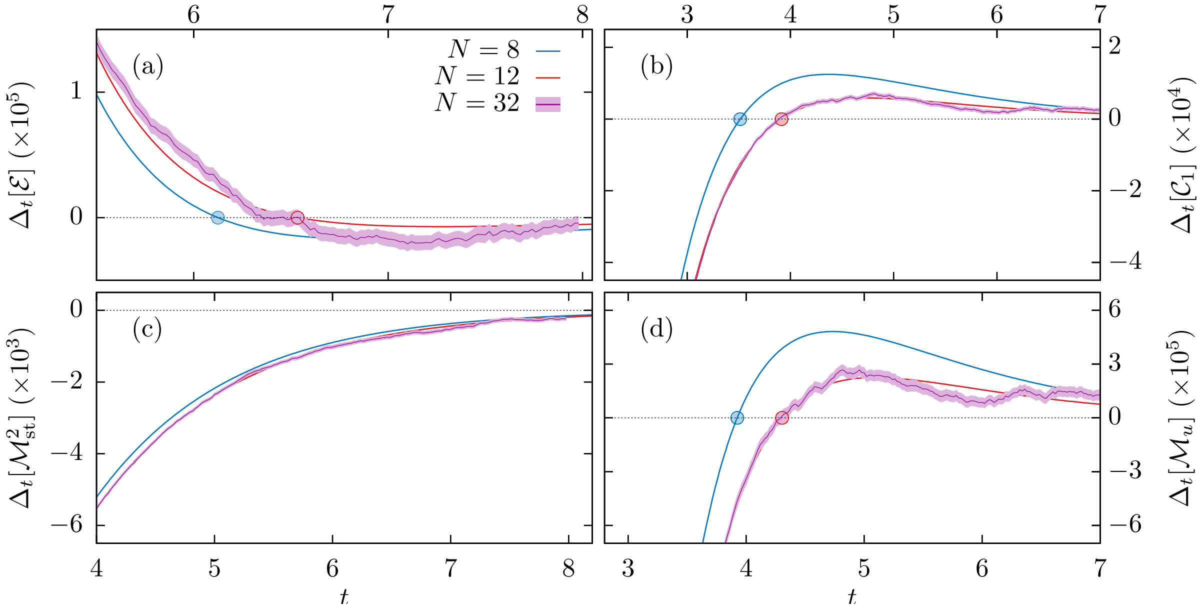

Figure 2.3: Mpemba effect as obtained with $T_{\mathrm{b}} = 1$, $T_{\mathrm{c}} = 4.14$, and $T_{\mathrm{h}} = 15.177$. Evolution of $\Delta_t[\mathcal{A}]$ [cf. Eq. (2.49)] for the observables $\mathcal{A} = \mathcal{E}$ (a), $\mathcal{A} = \mathcal{C}_1$ (b), $\mathcal{A} = \mathcal{M}^2_{\mathrm{st}}$ (c), and $\mathcal{A} = \mathcal{M}_{\mathrm{u}}$ (d). We show the results for $N = 8$ (blue), $N = 12$ (red), and $N = 32$ (purple, with a lighter shade representing the error bars of the MC data). The time at which $\Delta_t[\mathcal{A}]$ changes sign is marked by a colored dot.

Preheating for faster cooling

We compare the usual protocol (blue and green in Fig. 2.4) against a preheating protocol (red and purple in Fig. 2.4). In the former, we start with a system in equilibrium at temperature $T_0 = 4.15$, and we let this system evolve with a bath temperature $T_{\mathrm{b}} = 1$. In the two-step protocol, we start again at T_0, but we first let the system evolve with a bath at temperature $T_q = 2000$ up to $t = t_{\mathrm{p}} = 0.156$. At this time we put the system in contact with the bath at temperature T_{b}. All the panels in Fig. 2.4 show the expected speed-up for the preheating protocol, although in the case of the energy [see Fig. 2.4(c)] the error bars for $N = 32$ are probably too large to draw a definitive conclusion.

Heating and cooling may be asymmetric processes

Finally, we have the asymmetry between cooling and heating. We have chosen $T_A = 1$ and $T_B = 4.15 \approx T^*$ (left panels in Fig. 2.5) for a first experiment, and $T_A = 15.177$ and $T_B = 4.15$ (right panels in Fig. 2.5) for a second experiment. Notice, that T^* is the temperature at which the staggered susceptibility χ_{st} attains a maximum [see Fig. 2.2(a)]. Therefore, since $1/|\lambda_2|$ reaches its maximum value at this point, it will always be slower to reach equilibrium for T^* than other temperatures. This phenomenon can be seen for the $\mathcal{M}_{\mathrm{u}}$, $\mathcal{M}_{\mathrm{st}}$, and $\mathcal{C}_1$ in Fig. 2.5. However, the behavior of the energy is the opposite: it is faster to equilibrate at temperature $T_B = T^*$. This phenomenon, as explained in Sect. 2.2.4, is due to the fact that $\beta_2^{\mathcal{E}} \approx 0$.

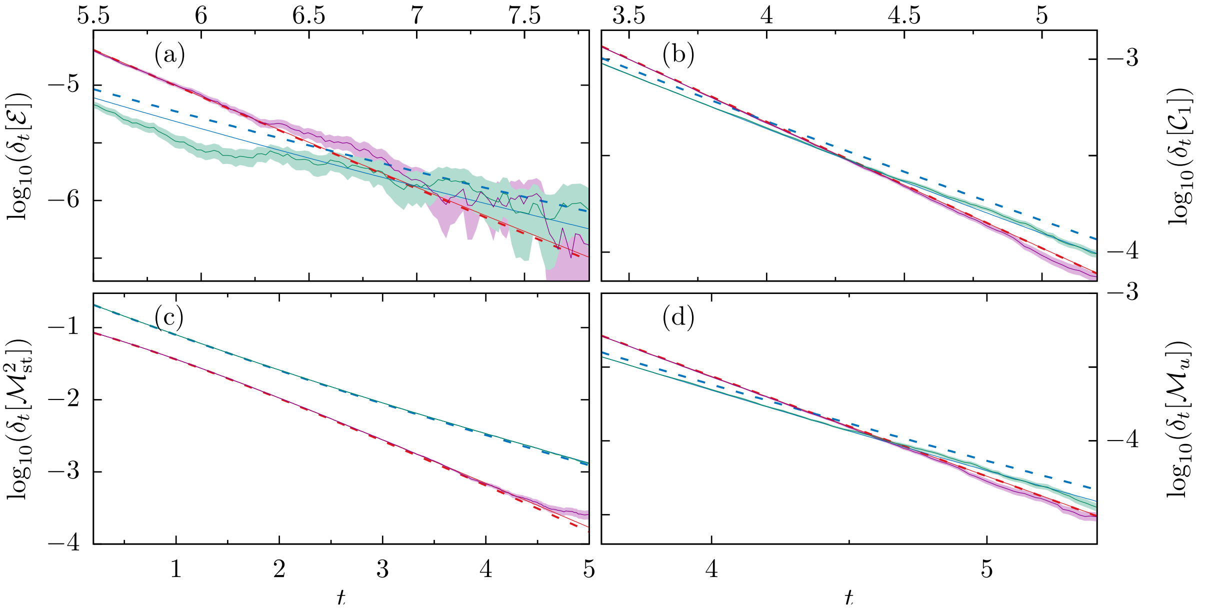

Figure 2.4: Preheating strategy for faster cooling with $T_{\mathbf{b}} = 1$, $T_0 = 4.14$, and $T_q = 2000$. Evolution of $\delta_t[\mathcal{A}$ [cf. Eq. (2.50)] for the observables $\mathcal{A} = \mathcal{E}$ (a), $\mathcal{A} = \mathcal{C}_1$ (b), $\mathcal{A} = \mathcal{M}_{\rm st}^2$ (c), and $\mathcal{A} = \mathcal{M}_{\rm u}$ (d). Colors red and purple (resp. blue and green) denote that the protocol includes (resp. does not include) an initial quench at temperature T_q. We show data for $N = 8$ (dashed lines), $N = 12$ (solid lines), and $N = 32$ (solid lines width lighter shade representing the error bars of the MC data).

2.4 Conclusions

We have demonstrated that the “weak form” of Markov dynamics provides a unified geometric framework for understanding and controlling various exotic dynamic effects in the realm of the Mpemba effect. Our approach differs from prior work, which typically prioritizes the “strong form” of the dynamics by tracking the evolution of the entropy of the system (or, more precisely, some type of entropic “distance” such as the Kullback-Leibler divergence [KL51]). We consider, instead, different physical observables, some of which can be measured at the mesoscopic level.

Our geometric approach has not only allowed us to explain the Mpemba effect, but our formalism has also allowed us to propose (and test) a protocol to accelerate the dynamics through preheating. In the same way, we could verify that it is possible to find observables that are unaffected by this acceleration due to an orthogonality phenomenon. Hence, one cannot have too short a spectrum of observables when investigating the Mpemba effect.

Finite-size effects on the separation of time scales are also of concern because it is this separation that determines the attainable exponential speed-up. Fortunately, we have found that the speed-up depends very mildly (if at all) on the system size. However, in the following chapter, we consider the case of a system without scale separation, studying the possibility of obtaining an exponential acceleration through a protocol that exploits a different physical mechanism.

Finally, we emphasize that our novel method can also be applied to other systems where anomalous relaxation and non-monotonicity of equilibrium thermodynamic observables have been observed, as reported in previous studies [IDL$^+$23, GR20, KB20].

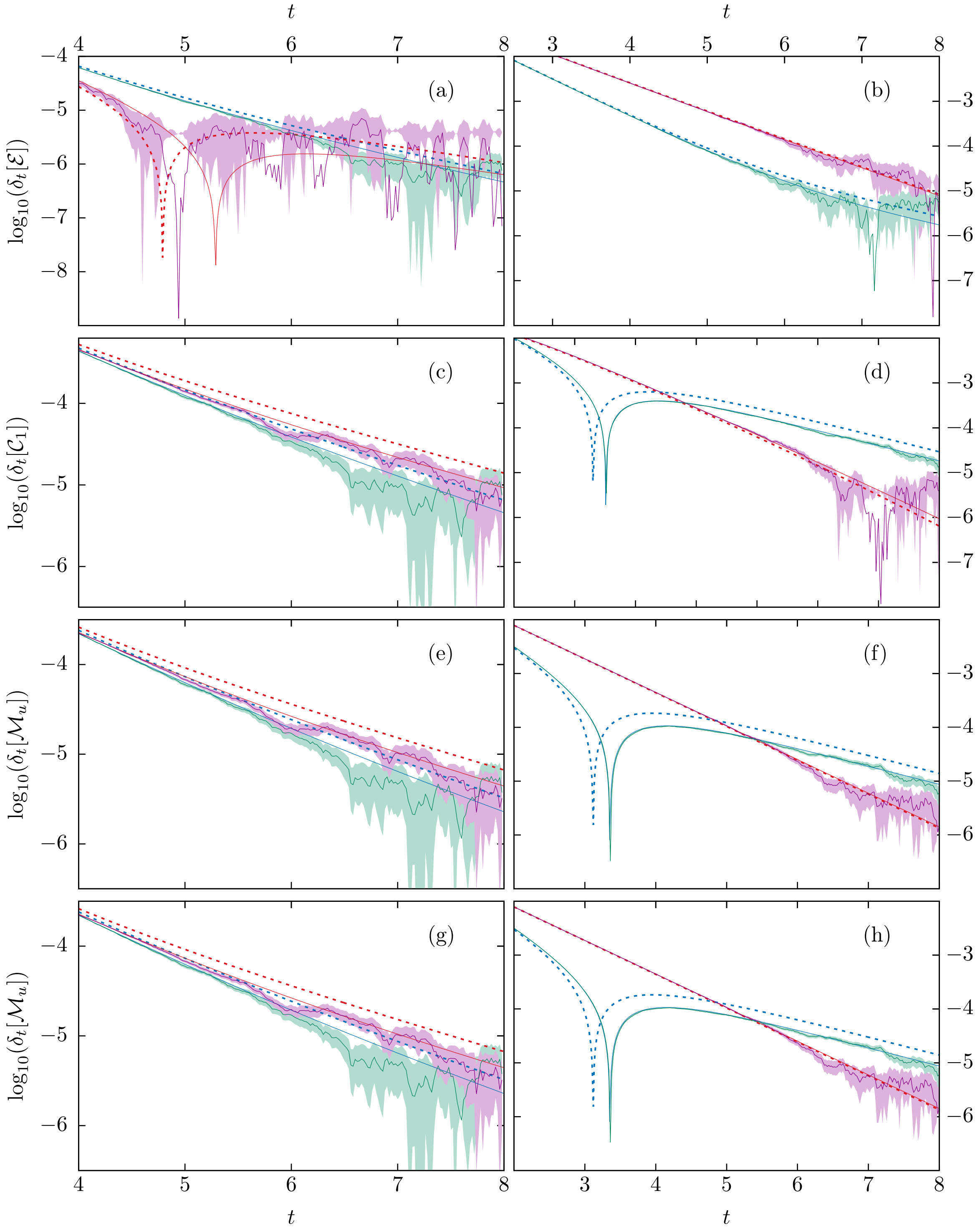

Figure 2.5: **(A)symmetry in heating and cooling.** Evolution of $\delta_t[\mathcal{A}$ [cf. Eq. (2.50)] for the observables $\mathcal{A} = \mathcal{E}$ (a, b), $\mathcal{A} = \mathcal{C}_1$ (c, d), $\mathcal{A} = \mathcal{M}^2_{\mathrm{st}}$ (e, f), and $\mathcal{A} = \mathcal{M}_{\mathrm{u}}$ (g, h). In each panel, we depict cooling (blue and green) and heating (red and purple) processes. We show the results for $N = 8$ (dashed lines), $N = 12$ (solid lines), and $N = 32$ (solid lines, with a lighter shade representing the error bars of the MC data). The cooling and heating processes were carried out between: (a, c, e, g) $T_A = 1$ and $T_B = 4.15$; and (b, d, f, h) $T_A = 15.177$ and $T_B = 4.15$.

3

Accelerating out-of-equilibrium dynamics

Slow growth of magnetic domains helps fast evolution routes for out-of-equilibrium dynamics

I. González-Adalid Pemartín, E. Mompó, A. Lasanta, V. Martín-Mayor, J. Salas

Phys. Rev. E **104**, 044114

https://doi.org/10.1103/PhysRevE.104.044114

As it is mentioned in Chapter 2, nonequilirbium relaxation processes have generated great interest in the last decades, where the promise of reducing the relaxation times has been the main objective. In this scenario, it is normal that the counterintuitive phenomenon such as the Mpemba effect [MO69] have stirred considerable attention. Indeed, we now understand which are the general conditions allowing for faster cooling , or heating, in Markovian system [LR17, KRHV19] —such as the considered in Chapter 2—, granular matter [LVRPS17, TLCnL+19], spin glasses [BJCC+19], water [GLH19], quantum Ising spin model [NF19], and very recentrly the generalization to Markovian open quantum systems [CLL21].

On this line, [GR20] have designed a new strategy for systems with timescale separation, in which precooling the system results in a faster heating. On the other hand, in Chapter 2 we develop a similar strategy to obtain a faster cooling process through an excursion to high temperatures. However, the success of this protocol is based on the capacity to cancel the slowest-decay relaxation modes, which is only possible for system with timescale separation. Yet, for some systems timescale separation is not possible, think of a second-order phase transition where critical slowing down [Par88, ZJ05] evidences a continuum of timescales [see e.g., Eq. (3.2) below]. Under these circumstances, unraveling the machanism that drives the dynamics is the key to potentially control the evolution.

In this chapter we show that growth of the ordered magnetic domains when the system enters the symmetry-broken phase [Bra94, ABCS07, Bin87] allows to control the relaxation time. In particular, the relevance of the domain growth for the dynamics slowdown in spin glasses is now clear [MPRLR96, BB02, BCC+08a, BJCC+17b, BJCC+17a, BJCC+18, ZPBJ+20, PZBJ+21, BJCC+23, PZBJ+23]. Here, we study the ferromagnetic two-dimensional Ising spin model through numerical simulations. We develop an unexplored out-of-equilibrium heating protocol, in which the bath temperature starts below the critical temperature and is later heated above the critical point. We find that this excursion to the ordered phase induces a speed-up in the energy evolution of the system, which is due to an acceleration of slow domain-growth process.

The rest of the following chapter is organize as follows: In Sect. 3.1 we discuss the model and the basic parameters of our simulation setup. Sect.3.2 we study the isothermal equilibration protocol, while in Sect. 3.3 we consider a two-steps protocol to accelarate the thermalization. We measure and compare the real speed-up for different two-steps protocol setup. Finally, in Sect. 3.5 we summarize the main results of this chapter.

3.1 Model

In this work, we consider the well-known ferromagnetic Ising model in two dimensions [MW73], defined by the Hamiltonian

$$\mathcal{H} = -J \sum_{\langle i,j \rangle} s_i s_j \,, \tag{3.1}$$

where the spins $s_i = \pm 1$ occupy the nodes i of a square lattice of linear size $L \times L$ with PBC. The system is in contact with a thermal bath described by the (dimensionless) inverse-temperature $\beta = J/(K_\mathrm{B}T)$, with $J\!=\!1$ energy units. As demonstrated by [Ons44], a second-order phase transition at $\beta_\mathrm{c} = \log(1+\sqrt{2})/2$ separates the paramagnetic phase at $\beta < \beta_\mathrm{c}$, from the ferromagnetic phase at $\beta > \beta_\mathrm{c}$.

As it was demonstrated by [Ons44], the system correlation function, $C(\vec{r};t)$ (as defined in Eq. (1.38)), gives the relevant information —for our purpose— of the system. In particular, we focus our attention on the energy density $E(t)$ —accessible through the relation $E(t) = -2C(\vec{r}_\mathrm{min};t)$, where $\vec{r}_\mathrm{min} = (0,1)$ [or $(1,0)$]— and the coherence length $\xi(t)$, computed from space integrals of $C(\vec{r};t)$ [BCC$^+$08b] [see Sect. 1.4.2, and Appendix G for more details about the space integrals of $C(\vec{r};t)$]. We have used $N_\mathrm{R} = 256$ independent trajectories or replicas —except for a few exceptions collected in Table 3.1— for the thermal average used in the correlation function estimation (see Sect. 1.4.2 for more information about the computation of thermal averages).

We use the energy density as a thermometric quantity [BJCC$^+$19] (i. e. as a measure of how far the system is from equilibration) for which the equilibrium values $E_\mathrm{eq} \equiv E(t\to\infty)$ is given by the exact result [Ons44]. On the other hand, the coherence length, which corresponds with the typical linear size of the ferromagnetic domains (it should not be confused with the correlation-length ξ_corr related to the spatial range of the correlations in a domain —see Sect.1.4.2 for a extended discussion about both quantities), is the quantity used to understand and drive the dynamic acceleration in the proposed *two-steps* protocol, explained in Sec. 3.3.

Remember that Metropolis and Heat Bath dynamics are characterized by the probability, p, to allow a spin-flip with an energy change ΔE:

$$\begin{aligned} p_\mathrm{MET}(\Delta E) &= \min\{1, \mathrm{e}^{-\Delta E/T}\}\,, \\ p_\mathrm{HB}(\Delta E) &= \frac{\mathrm{e}^{-\Delta E/T}}{1+\mathrm{e}^{-\Delta E/T}}\,. \end{aligned}$$

Finally, we consider simulating two dynamical rules for the model: Metropolis (MET) and Heat Bath (HB) algorithms (see, e.g., [Sok97, LB05] for more details). Both dynamical rules are described by the so-called *model* A dynamic universality class [HH77], which is characterized by the absence of conserved quantities. The system size in our simulations, $L = 4096$, is large enough to ensure the thermodynamic limit has been reached. We consider the usual time step definition as a full-lattice sweep [Sok97]. We implement a multispin MUlti-SIte coding [FMM15], for the square lattice [FMMM$^+$19] (see Appendix D for a complete description), as well as an efficient way, adapted to the high temperatures of this work, for generating the random numbers needed in the simulation (see Appendix F for a detailed description).

β	Protocol information	N_R
0.435	Isothermal	1536
0.4378	Isothermal	4096
0.4378	from $\beta_\mathrm{start} = 0.46$ with $\xi_\mathrm{start} = 120$	1024

Table 3.1: Number of independent trajectories, or replicas, simulated for each thermal bath and protocol. The data not contained in the table uses $N_\mathrm{R} = 256$. The first column summarizes the target inverse-temperature where the equilibration is wanted. The second column contains the relevant information on the thermalization protocol used for thermalization. In particular, only the last row corresponds to a *two-steps* suggested protocol.

3.2 Isothermal equilibration

As was mentioned in the introduction of this chapter, this work tries to unravel the mechanism that drives the dynamics. In addition, we want to develop a thermalization protocol that exploits this mechanism to reach the equilibrium faster. Particularly, we center our attention on the paramagnetic phase. To achieve these objectives, we first need to study the isothermal (usual or natural) equilibration. Thus, we consider a *one-step* thermalization protocol, where a fully disordered spin configuration (corresponding to infinite temperature) is put in contact with a thermal bath at inverse-temperature β, at the initial time $t = 0$.

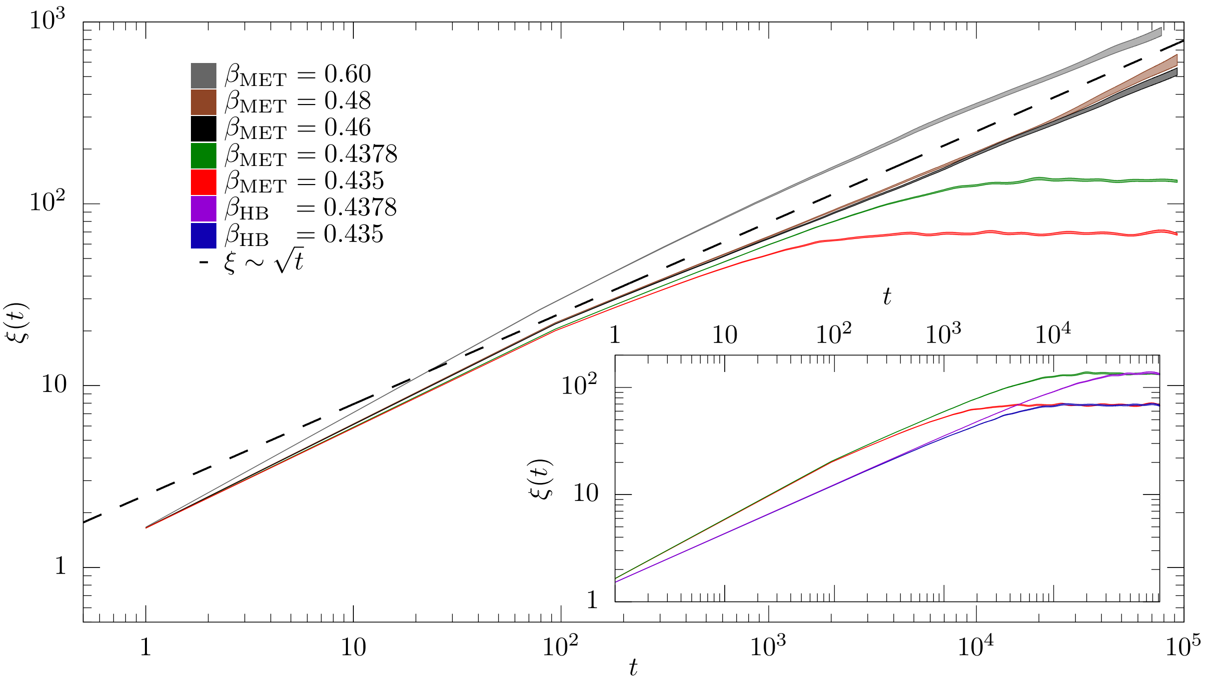

Figure 3.1: Coherence length ξ as a function of the time t, as computed with Metropolis (MET) and Heat Bath (HB) algorithms for an isothermal protocol and several values of β (the width of the curves is twice the statistical error; β increases from bottom to top).Only in the paramagnetic phase, $\beta < \beta_\mathrm{c} \approx 0.44068679$, the coherence length reaches its equilibrium value at long times. In the ferromagnetic phase $\xi(t) \propto \sqrt{t}$ at long times (dashed line). **Inset:** Comparison of the HB and MET dynamics in the paramagnetic phase. Although $\xi(t)$ grows significantly faster for MET, the equilibrium limit at long times is the same for both dynamics.

Under these conditions, the behavior of the system in the two phases is very different, see Fig. 3.1. On the one hand, in the paramagnetic phase ($\beta < \beta_c$) both $\xi(t)$ and $E(t)$ approach exponentially their equilibrium value [Par88, FMMM⁺19]:

$$O(t;\beta) = O_{t\to\infty}(\beta)\left[1 \; - \; \int_1^{\tau_\beta} \rho_O(\tau,\beta)\, \mathrm{e}^{-t/\tau}\, \mathrm{d}\tau\right], \tag{3.2}$$

where $O(t;\beta)$ refers to $E(t;\beta)$ or $\xi(t;\beta)$ and $\rho_O(\tau,\beta)$ is a continuous distribution of autocorrelation times τ (remember that time scale separation is not possible at a second-order phase transition due to the critical slowing down [Par88, ZJ05]).† The cut-off τ_β (which corresponds to the largest timescale that diverges at the critical point) guarantees an exponential decay, $\exp(-t/\tau_\beta)$, for the finite-time corrections. On the other hand, in the ferromagnetic phase, the domains grow as $\xi \sim \sqrt{t}$ [Bra94] until $\xi \sim L$ (dashed line in Fig. 3.1), so the largest timescale exists in the ferromagnetic phase only as a finite-size effect.

† Near a critical point, fluctuations become very large. This slows down the rate at which the system relaxes to equilibrium because even small changes in the system remain for a long time. As a result, the different relaxation time scales approach a continuum.

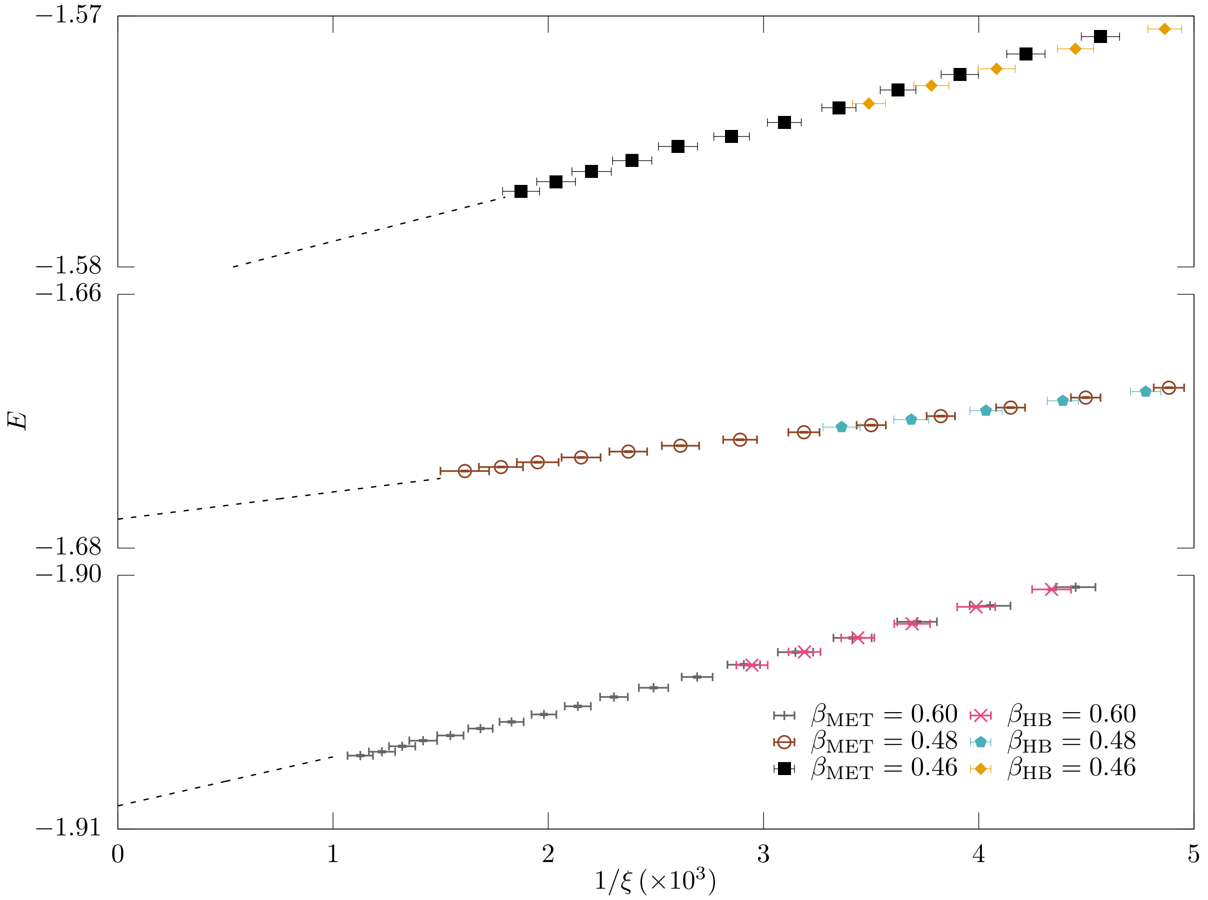

Figure 3.2: Energy density $E(t)$ from our isothermal protocol as a function of $1/\xi(t)$ in the ferromagnetic phase, as computed for $\beta = 0.6$, 0.48, and 0.46. In this representation, and for a given β, our Metropolis (MET) and Heat Bath (HB) data fall on the same curve. The dashed lines are fitted to $E(t;\beta) = E_{\mathrm{eq}}(\beta) + b_\beta/\xi(t;\beta)$ (the only fitting free parameters are the slopes b_β, remember that $E_{\mathrm{eq}}(\beta)$ is given by the Onsager solution) [Ons44]). We only show the fits for $\xi(t)$ larger than the maximum value reached in each simulation. Error bars in the y-axes are smaller than the symbols.

Concerning to the energy evolution, in the ferromagnetic phase (excluding fast initial relaxations) its relation with $\xi(t)$ is well known [Par88]. This relation can be directly shown if we consider the space divided in $(L/\xi)^D$ magnetic domains (notices this assume a non-fractal surface of the magnetic domains). Each magnetic domain while have, on average, an energy

$$E_{\mathrm{d}} = E_{\mathrm{eq}}(T)\xi^D + A(T)\xi^{D-1}\,, \tag{3.3}$$

where the first term is the internal energy, and the second is a boundary term, which represent the energy accumulation at the boundaries of the magnetic domains. Therefore, the total energy of the system is

$$E(\xi) = E_{\mathrm{eq}}(T) + \frac{A(T)}{\xi}\,. \tag{3.4}$$

This behavior is shown in Fig. 3.2. Surprisingly, the results for the paramagnetic phase reveal that this relation extends to the paramagnetic phase (see Fig. 3.3), with an important exception. Close to equilibrium, the energy is not affected by the magnetic domain growth, which is shown by the null slope at the equilibrium limit.

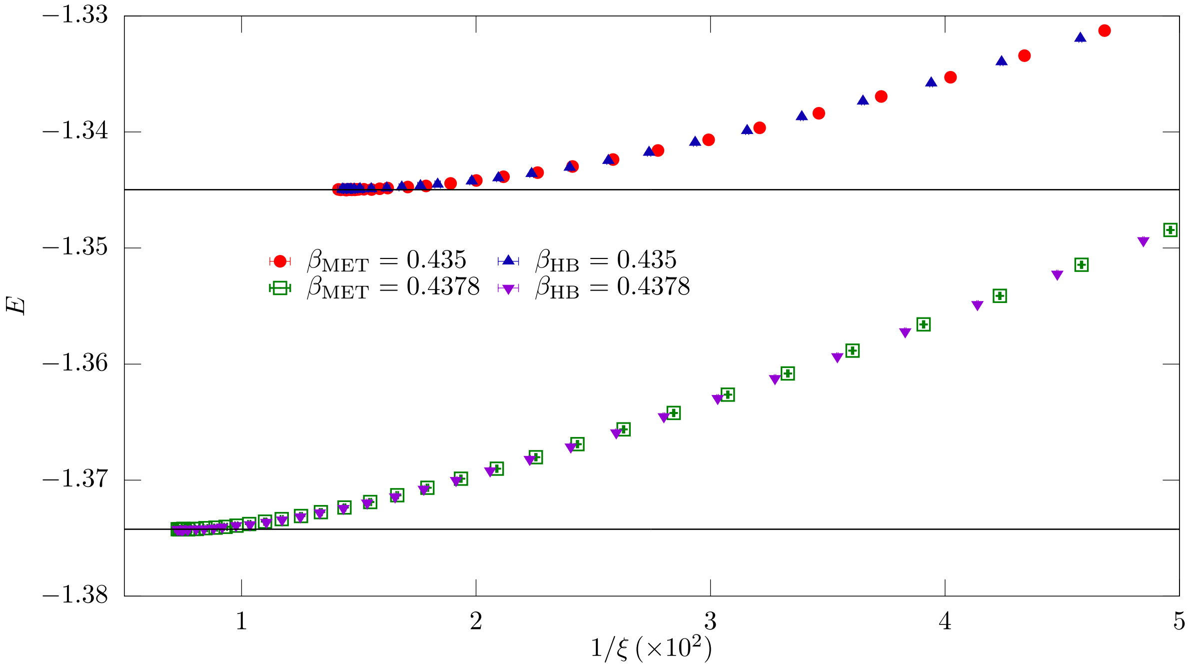

Figure 3.3: Energy density $E(t)$ from our isothermal protocol as a function of $1/\xi(t)$ in the paramagnetic phase, as computed for $\beta = 0.4378$, and 0.435. In this representation, and for a given β, our Metropolis (MET) and Heat Bath (HB) data fall on the same curve. The solid horizontal lines are the exact Onsager solution [Ons44]. Error bars are smaller than the symbols. The null slope at equilibrium implies that the growth of the magnetic domains does not modify the energy.

The clear relation between the density energy $E(t)$ and the coherence length $\xi(t)$ suggests that this relation could be exploited as a way to achieve faster equilibration. To obtain this speed-up, we propose to use the faster growth of the magnetic domains in the ferromagnetic phase (see Fig. 3.1) to drive the energy equilibration in the paramagnetic phase. This idea corresponds to a *two-step* protocol, in which the system is in contact with a thermal bath at inverse-temperature $\beta > \beta_{\mathrm{c}}$ (in the ferromagnetic phase) before the thermal bath is changed to the paramagnetic phase ($\beta < \beta_c$). The complete analysis of this protocol is explained in Sect. 3.3.

3.3 Two steps protocol: Canceling largest time corrections

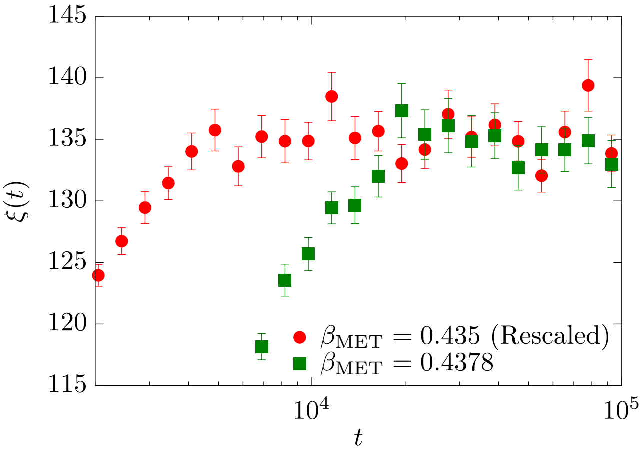

Figure 3.4: Time evolution of the coherence length in the paramagnetic phase for an isothermal protocol for Metropolis (MET) dynamics. Data for $\beta = 0.435$ are multiplied by the scale factor $(\beta_c - 0.435)/(\beta_c - 0.4378)$ to show the compatibility of both equilibrium data, showing that we are in the scaling region. Let us remark, for late reference, the value $\xi_{\mathrm{end}} = 135(2)$ for the long-time limit at $\beta = 0.4378$.

In contrast with the isothermal evolution (*one-step* protocol) studied in Sect. 3.2, our *two-step* protocol uses an excursion to the ferromagnetic phase to control, in some way, the speed of the equilibration in the paramagnetic phase. The complete protocol consists of introducing a fully disordered spin configuration (equivalent to infinite temperature) in a thermal bath in the ferromagnetic phase, $\beta_{\mathrm{start}} > \beta_c$. When the coherence length $\xi(t)$ (which is the driver of the speed-up) reaches a target value ξ_{start}, the bath temperature is instantaneously raised to enter the paramagnetic phase β_{end}. This moment corresponds with our initial time $t = 0$. Notice that it is acceptable that ξ_{start} may be larger than $\xi_{\mathrm{end}} \equiv \xi(\to \infty; \beta_{\mathrm{end}})$. Let us remark as well that a *one-step* protocol with $\beta < \beta_c$ is a particular case of a *two-step* protocol with $\xi_{\mathrm{start}} = 0$ and $\beta_{\mathrm{end}} = \beta$.

We take $\beta_{\mathrm{end}} = 0.435$ and 0.4378, where ξ_{end} is very large, but the equilibrium limit is still reachable for us (remember the horizontal line for both dynamics in the inset of Fig. 3.1). The two β_{end} are close enough to the critical point to be in the so-called scaling region as it is shown in Fig. 3.4. Under these conditions, the product $(\beta_c - \beta_{\mathrm{end}})\xi_{\mathrm{end}}$ remains constant as β_{end} approach the critical point [MW73] (see Fig. 3.4). This behavior holds because the coherence length and the correlation-length coincide in the paramagnetic phase, and the value of thermal critical exponent, $\nu = 1$.† In addition, this result assures the scale independence of the following discussion and supports the universality hypothesis for the whole *model A* dynamics.

Based on Eq. 3.2, it is straightforward to show that once the system is introduced into the paramagnetic phase, the difference in energy density to the equilibrium value must evolve at long times as

$$E(t) - E_{\mathrm{eq}} = \mathcal{A}(\xi_{\mathrm{start}}) e^{-t/\tau_\beta} \,, \tag{3.5}$$

where the amplitude $\mathcal{A}$ depends on the initial value of the coherence length (the isothermal evolution is recovered for $\xi_{\mathrm{start}} = 0$), as seen in Fig. 3.5. The most remarkable result shown in Fig. 3.5 is that $\mathcal{A}$ decreases until it changes sign as the initial coherence length of the system increases. This suggests that there must

† In the paramagnetic phase, and close enough to the critical point, the theory preditcs

$$\xi_{L\to\infty}(\beta) \propto \frac{1}{|\beta - \beta_c|^{\nu}} \,,$$

with critical exponement $\nu = 1$ for the 2D Ising model.

be a value of the coherence length, ξ^*_{start}, for which $\mathcal{A}(\xi^*_{\text{start}}) = 0$, which would result in an exponential acceleration of the thermalization process of the system. Notices the independence of β_{start} for ξ^*_{start} shown in Fig. 3.5 However, due to statistical errors, it has not been possible to determine this value of ξ^*_{start} with high accuracy.

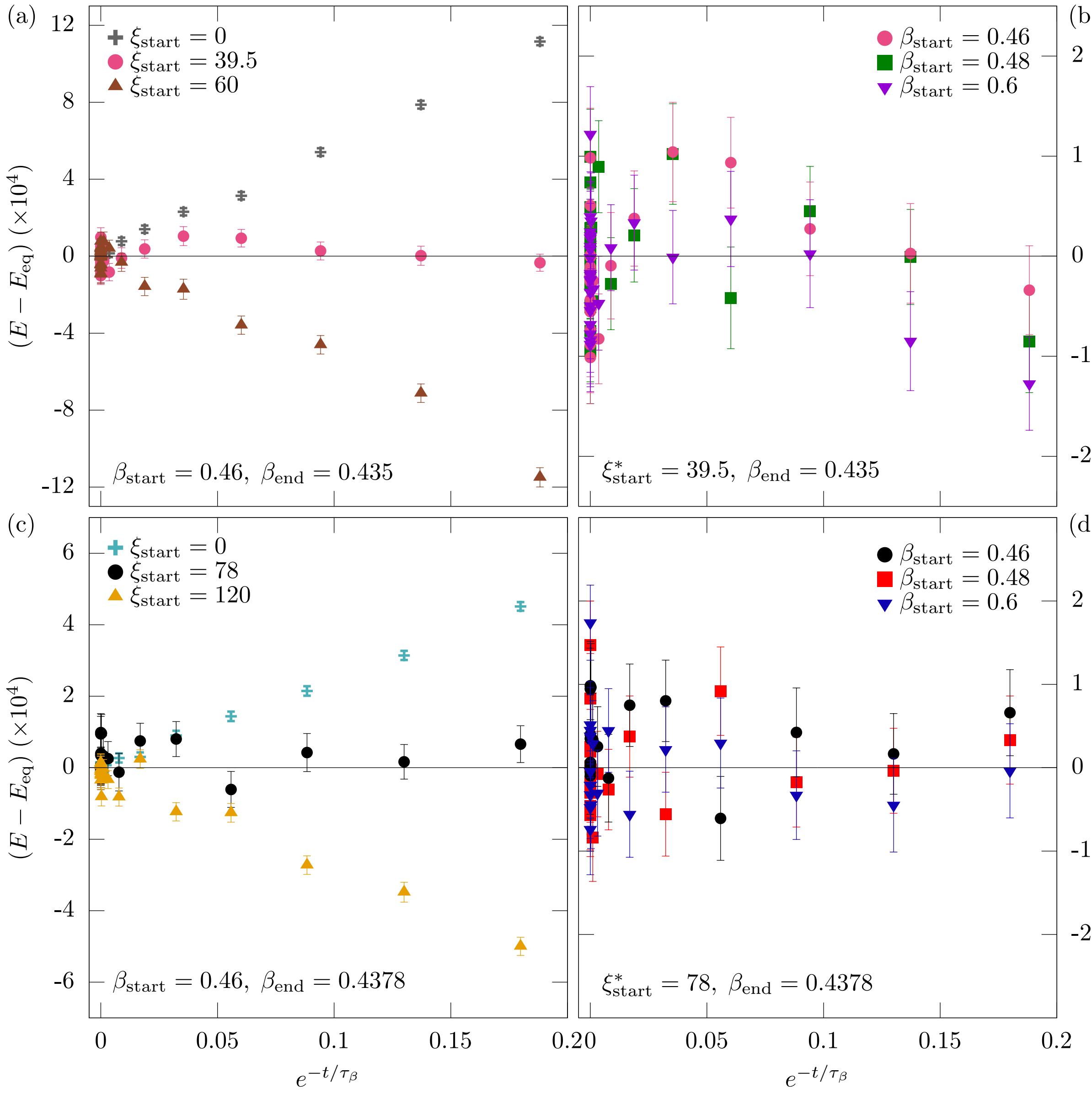

Figure 3.5: Excess energy $E(t) - E_{\text{eq}}$ vs $\exp(-t/\tau_\beta)$, as obtained with Metropolis dynamics. (a) Data for βstart $= 0.46$ and $\beta_{\text{end}} = 0.435$, as computed for several values of ξ_{start}. (b) Data for $\xi^*_{\text{start}} = 39.5$ and $\beta_{\text{end}} = 0.435$, as computed for several values of β_{start}. (c) As in panel (a), for $\beta_{\text{start}} = 0.46$ and $\beta_{\text{end}} = 0.4378$. (d) As in panel (b), for $\xi^*_{\text{start}} = 78$ and $\beta_{\text{end}} = 0.4378$. The equivalent results for the Heat Bath dynamics are available in [GAPML+21].

Our strategy to estimate ξ^*_{start} consists of taking different values of ξ_{start} close to our initial guess for ξ^*_{start}, obtained from Fig. 3.5 (MET). After that, using the *Ansatz* in Eq. (3.5), we estimate $\mathcal{A}(\xi_{\text{start}})$ through a fit with τ_β fixed. We obtain previuosly the value of τ_β by fitting our most precise data, namely, that with $\xi_{\text{start}} = 0$ (i. e. data from the isothermal evolution with $\beta = 0.4378$), to the same *Ansatz* in Eq. (3.5). We use as a fitting window the interval $0 \leq \exp(-t/\tau_\beta) \leq 0.2$.

With these results, we find an interval $(\xi^+_{\text{start}}, \xi^-_{\text{start}})$ where ξ^*_{start} is contained (see Tables 3.2 and 3.3). In order to determine the value of ξ^+_{start} (resp. ξ^-_{start}) we impose $\mathcal{A}$ to be the closest to zero positive (resp. negative) value, clearly bigger (resp. smaller) than zero (i. e. larger in absolute value than twice its statistical error).

(a) Metropolis			(b) Heat Bath		
ξ_{start}	$\mathcal{A}\times 10^4$	$\lvert\mathcal{A}\rvert/\Delta\mathcal{A}$	ξ_{start}	$\mathcal{A}\times 10^4$	$\lvert\mathcal{A}\rvert/\Delta\mathcal{A}$
37	10.6(18)	5.9	36	13(2)	6.5
39.5	0.8(20)	0.4	39.5	3(2)	1.5
42	−4.6(18)	2.6	50	−26.3(19)	13.8

Table 3.2: Values of $\mathcal{A}(\xi_{\text{start}})$ obtained with $\beta_{\text{start}} = 0.46$ and $\beta_{\text{end}} = 0.435$ form the Metropolis (a) and Heat Bath (b) dynamics. $\Delta\mathcal{A}$ is the statistical error obtained from the fit to Eq. (3.5). The value of τ_β used to fit these data are 433(14) for Metropolis, and 1470(50) for Heat Bath.

(a) Metropolis			(b) Heat Bath		
ξ_{start}	$\mathcal{A}\times 10^4$	$\lvert\mathcal{A}\rvert/\Delta\mathcal{A}$	ξ_{start}	$\mathcal{A}\times 10^4$	$\lvert\mathcal{A}\rvert/\Delta\mathcal{A}$
70	5(2)	2.5	70	9(2)	4.5
79	−2(2)	1	81.5	−1(3)	0.3
87	−5.0(19)	2.6	92	−8(3)	2.7

Table 3.3: Values of $\mathcal{A}(\xi_{\text{start}})$ obtained with $\beta_{\text{start}} = 0.46$ and $\beta_{\text{end}} = 0.4378$ form the Metropolis (a) and Heat Bath (b) dynamics. $\Delta\mathcal{A}$ is the statistical error obtained from the fit to Eq. (3.5). The value of τ_β used to fit these data are 2000(100) for Metropolis, and 6500(300) for Heat Bath.

$\beta_{\text{end}} = 0.435$		$\beta_{\text{end}} = 0.4378$	
MET	HB	MET	HB
40(3)	43(7)	79(9)	81(11)

Table 3.4: Values of ξ^*_{start} estimate for the Metropolis (MET) and Heat Bath (HB) dynamics. We use $\beta_{\text{start}} = 0.46$, but as it expected, the behavior in the paramagnetic phase is independent of how deep in the ferromagnetic phase the system is prepared (i. e. independent of β_{start}, see Fig. 3.5). The center value and its error are obtained from the semi-sum and the semi-difference of the extreme values from Tables 3.2 and 3.3.

We determine ξ^*_{start} as the average of ξ^+_{start} and ξ^-_{start}, and its error as the semi-difference (see Table 3.4). As expected, the results are independent of the inverse-temperature β_{start} of the preparation bath in the ferromagnetic phase (see Fig. 3.5). The final results for ξ^*_{start} are statistically compatible for both dynamics (see Table. 3.4).

Notice that these results for ξ^*_{start} scales as the equilibrium coherence length ξ_{end} [$\xi_{\text{end}}(0.435) = 69(1)$ and $\xi_{\text{end}}(0.4378) = 135(2)$], i.e. as $1/(\beta_c - \beta_{\text{end}})$. This correct scaling and the independence of β_{start} for ξ^*_{start}, are distinctive features of universality. In fact, we speculate that the scale-invariant ratio that we find for the Metropolis dynamics,

$$\lim_{\beta\to\beta_c^-} \frac{\xi^*_{\text{start}}}{\xi_{\text{end}}} = 0.59(7) \tag{3.6}$$

will be common to all models with scalar order parameter in the *model-A* dynamic universality class [HH77]. Our results for the Heat Bath dynamics are consistent with this speculation.

3.4 Measuring real speed-up

We have verified the possibility of obtaining an exponential acceleration by forcing the system to reach a value ξ^*_{start} by entering the ferromagnetic phase. In order to compare both processes (i. e. the isothermal and two-step protocols), we need to consider the total time, t_{total}: the time that the system spends at both inverse-temperatures β_{start} and β_{end}. On the other hand, in order to adjust the parameters of the protocol, we need to define the time it takes the system to reach equilibrium we need an operational definition because strictly speaking, recall Eq. (3.2), equilibrium is never reached]. To do this, we have defined the equilibrium time, $t_{\text{eq}}^{0.1\%}$, as the last instant at which the energy density of the system is not within 0.1% of the equilibrium value. This definition corresponds to the last time the energy density goes inside the interval $[1.0001E_{\text{eq}},\, 0.999E_{\text{eq}}]$ (see Fig. 3.5).

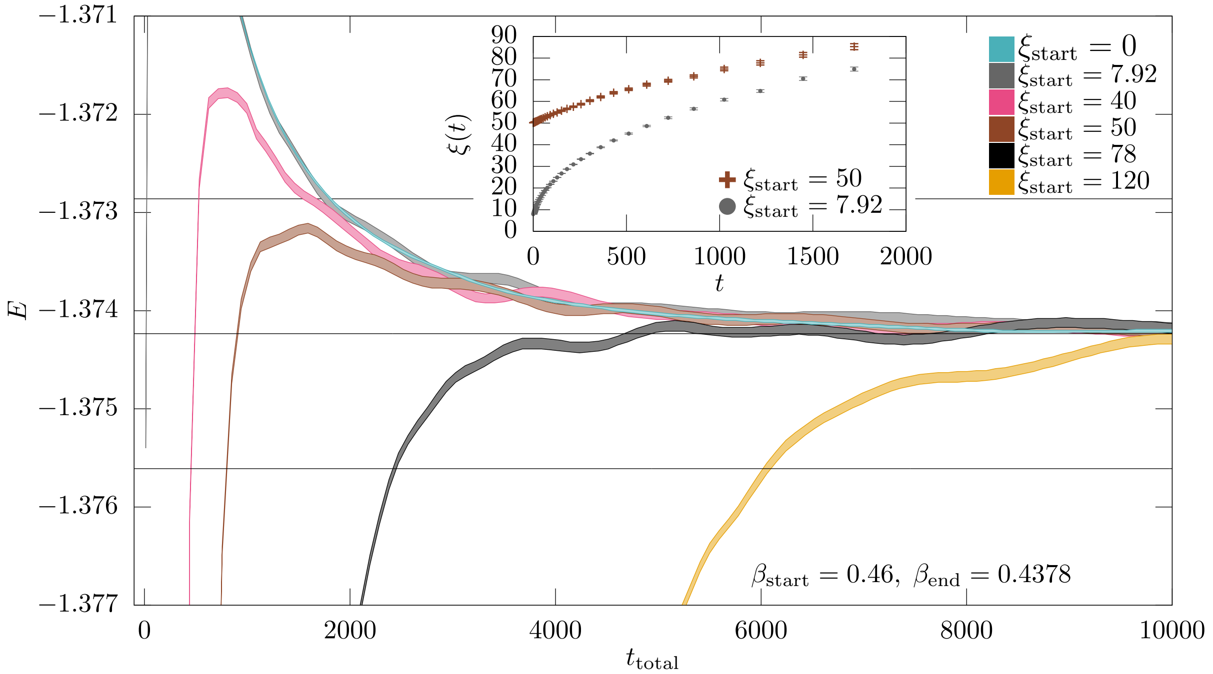

Figure 3.6: Energy density as a function of the total time t_{total} elapsed since the beginning of the two-step protocol. Data computed with the Metropolis dynamics for βstart = 0.46 and βend = 0.4378. We represent different values of ξ_{start}, increasing from top to bottom. The width of the curves is twice the statistical error. The horizontal lines correspond to E_{eq} and the 0.1% band. Inset: Coherence length during the two-step protocol ($\beta_{\text{start}} = 0.46$, $\beta_{\text{end}} = 0.4378$) as a function of the time t elapsed since the temperature changed. We show data for $\xi^{\text{Kovacs}}_{\text{start}} \approx 7.92$ (lower curve), as well as for $\xi_{\text{start}} = 50$ (upper curve; this value yields the minimum equilibration time; see Fig. 3.7. The equivalent results for the Heat Bath dynamics, which are very similar except for the time scale, are available in [GAPML+21].

Consider the situation with $\xi_{\text{start}} > \xi^*_{\text{start}}$ and where $\mathcal{A}(\xi_{\text{start}}) < 0$. The energy density tends to equilibrium from *below*. Nevertheless, with $\xi_{\text{start}} < \xi^*_{\text{start}}$ the value of $\mathcal{A}(\xi_{\text{start}}) > 0$, and the equilibrium is reached from *above*. In this range, the value $\xi_{\text{start}} = \xi^{\text{Kovacs}}_{\text{start}}$, defined as the coherence length at β_{start} that produce $E(\xi^{\text{Kovacs}}; \beta_{\text{start}}) = E_{\text{eq}}(\beta_{\text{end}})$ (recall Eq. 3.4 —this is the situation to study the Kovaks effect [BB02, KAHR79]), has an important role: if $\xi^{\text{Kovacs}}_{\text{start}} < \xi_{\text{start}} < \xi^{*}_{\text{start}}$, the energy of the system at the change in temperature is lower than E_{eq} (because the larger coherence length, the lower energy, as it is shown in Fig. 3.2). In this situation (initial energy smaller than E_{eq} and approximating equilibrium from above) $E(t_{\text{total}})$ cannot be a monotonic function of the t_{total}. In fact (see Fig. 3.5), the energy density for $\xi^{\text{Kovacs}}_{\text{start}} \lesssim \xi_{\text{start}} < \xi^{*}_{\text{start}}$ presents a local maximum before a decrease towards E_{eq}. We suggest that this phenomenon is a consequence of a reconfiguration of the magnetic domains created in the excursion to the ferromagnetic phase. Specifically, the magnetic domains must be broken, producing an increase in the system energy due to the appearance of more domain walls. When the domains are huge (i. e. $\xi_{\text{start}} > \xi^{*}_{\text{start}}$) the energy is much lower than E_{eq} and the effect produces only the approximation to equilibrium from *below*. However, small domains (i. e. $\xi_{\text{start}} < \xi^{*}_{\text{start}}$), with a very small internal energy, cause two contradictory effects: at short time the internal domain-energy raises, but, at long times the domain excess energy is the time decreasing boundary contribution.

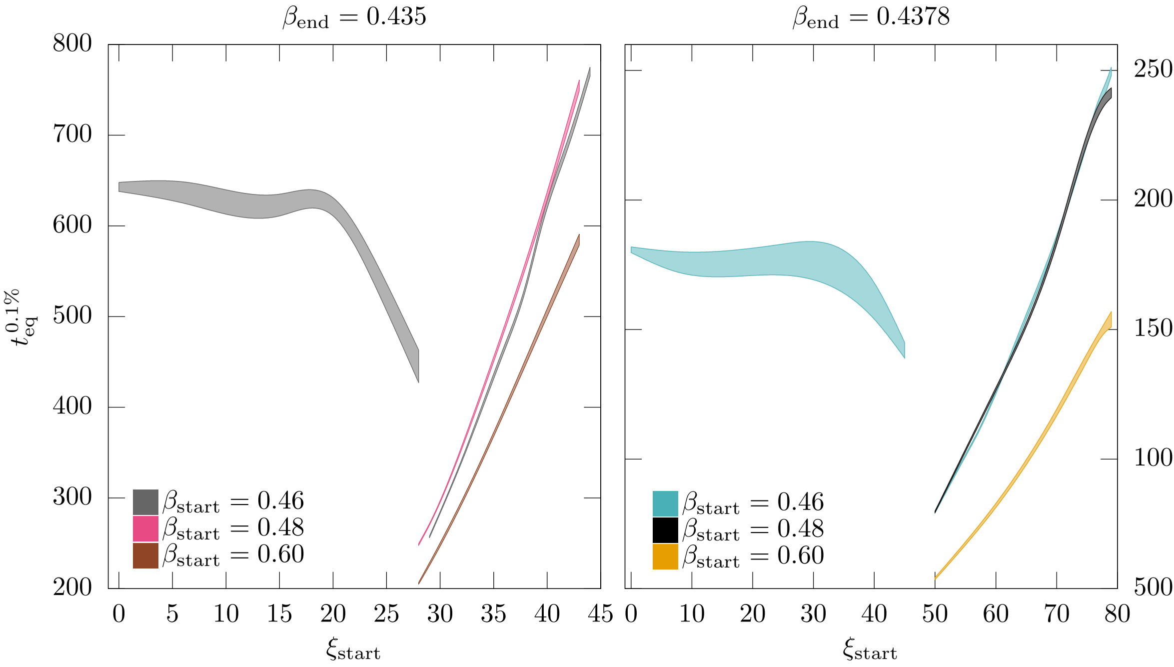

Figure 3.7: Equilibration time $t^{0.1\%}_{\text{eq}}$ as a function of ξ_{start} for the two-step protocol with $\beta_{\text{end}} = 0.435$ (a) and $\beta_{\text{end}} = 0.4378$ (b). Data from the Metropolis dynamics. The width of the curves is twice the statistical error. the nonmonotonic time behavior of $E(t_{\text{total}})$ produces a discontinuity; see Fig. 3.5. Notice how close the curves for $\beta_{\text{start}} = 0.46$ and $\beta_{\text{start}} = 0.48$ are after the discontinuity. The equivalent results for the Heat Bath dynamics are available in [GAPML+21].

The presence of this local maximum of $E(t_{\text{total}})$ entails a discontinuity in the equilibration time $t^{0.1\%}_{\text{eq}}$ as a function of ξ_{start} (see Fig 3.7). The discontinuity appears for a value of ξ_{start} such that the maximum value of $E(t_{\text{total}})$ coincides with the upper limit of the 0.1% band around the equilibration value. Note that for larger ξ_{start}, equilibrium is reached from below, and there is only one entrance in the 0.1% band. However, for smaller ξ_{start}, despite the initial energy being smaller than the equilibrium one, the maximum value is higher than the upper limit (see Figs. 3.6). This produces a second entrance from above to the 0.1% band (whuch provides our operational definition of equilibrium). Thus, just after the discontinuity, the proposed two-step protocol could be shorter than its isothermal counterpart by a factor of three (see Fig. 3.7).

Let us recall that data for Heat Bath dynamics are available at [GAPML+21], and present the same behavior we found for Metropolis dynamics. The main difference is in the time scale. This, it is not surprising because Metropolis dynamics approaches the equilibrium faster than Heat Bath dynamics (see Inset in Fig. 3.1).

3.5 Conclusions

In the present chapter, we have found that precooling a system may produce a faster equilibration at high temperatures in a prototypical system without timescale separation (namely, the ferromagnetic two-dimensional Ising model close to its critical point).

The mechanism that drives this phenomenon is the connection between the internal energy and the size of the ferromagnetic domains, characteristic of a broken symmetry phase [Par88]. Our results suggest that this connection, surprisingly, extends to the paramagnetic phase, which entails a way to easily control the equilibration speed-up.

In particular, the manipulation of the size of the domains can be used in a nonequilibrium protocol to obtain an exponential speed-up in the equilibration process. The speed-up emerges when the size of the magnetic domains produced in the low-temperature phase is a well-defined fraction of the *equilibrium* correlation length at the higher temperature. We numerically obtain evidence for a universality of this fraction (restricted to *model-A* dynamics with scalar order parameter [HH77]). Finally, we explain how to develop and tune a useful protocol that benefits from this universal mechanism.

Part III

Divergences in spin glasses

4

Large correlations in spin glasses in a field

Numerical test of the replica-symmetric Hamiltonian for the correlations of the critical state of spin glasses in a field

L. A. Fernández, I. González-Adalid Pemartın, V. Martín-Mayor, G. Parisi, F. Ricci-Tersenghi, T. Rizzo, J. J. Ruiz-Lorenzo, and M. Veca

Phys. Rev. E **105**, 054106

https://doi.org/10.1103/PhysRevE.105.054106

At the beginning of this thesis, in Chapter 1, we provided a brief overview of the problems that motivated the development of the theory of [EA75] and the consequent theoretical field. One of these problems is the divergence of the susceptibility and the appearance of large correlation lengths and slow relaxations [MPV87, Myd93, You98] in spin glasses in a magnetic field, above the la so-called de Almeida-Thouless (dAT) line [dAT78].

This behavior appears in a huge variety of systems, for instance, structural glasses close to their mode coupling temperature [Cav09], or hard spheres above the Garner transition [Gar85]. All of these phenomena can probably be explained by the same (or similar) field theory. Nevertheless, despite this behavior is predicted by mean-field (MF) [MPV87] and it has been identified both in experiments [BMdPSFdsdE86, GSN$^+$91] and in numerical simulations [SGSN90, DD91, SGSN91, JGFJ93, PRTRL98, MPZ98, MPRL98, MNZ$^+$98, HM99, MPZ00, HM00, CFJ$^+$03, YK04, LPRTRL08, LKMY13, BJBnC$^+$14a, BJBnC$^+$14b, BnCF$^+$12, LPRTRL09, LPRTRL11, GLL18, BBB$^+$05, ABM$^+$16, HC20, DLP$^+$20, ABL$^+$21], the theory for finite space dimensions below the upper critical dimension $D_\mathrm{u} = 6$ is still not fully understood [BR80, TDD02, CY17, ALP$^+$22].

Different viewpoints try to explain the behavior mentioned above. Some believe that these features might be related with a *crossover*, rather than to a phase transition [FS85, FH86, BM87b, BM87a, FH88b, FH88a, FH93]: the corrections to MF theory would destroy the transition, or move it to zero temperature. Another possibility, suggested by [HR20], is the appearance of a first-order phase transition without critical behavior, i.e., with a large but finite correlation length. However, the possibility of having an actual critical behavior is still open, so the existence of a second-order phase transition as an explanation for these phenomena is another possibility.

In this thesis, we will not engage in the debate on whether or not a phase transition exists (nor about its nature). Instead, we focus on studying and understanding the properties of correlations in the region where susceptibilities become enormous. We decided to work with the 4-dimensional spin glasses in a magnetic field to achieve this. The main reasons behind our choice are two: On the one hand, despite its complexity, there is a well-known field-theory framework for $D \geq 6$ [PR13]. It is thus essential to check the behavior below six spatial dimensions. On the other hand, we have the possibility of analyzing equilibrated configurations generated with Janus I [BMP$^+$06] for a large number of samples in a big lattice, which reach large values of the correlation length [BnCF$^+$12], for a $D = 4$ system (which has allowed us to compare the results with theoretical predictions).

The main theoretical predictions to be checked are the existence of three different two-point correlators (with their associated susceptibilities) that become critical and eight non-linear susceptibilities related to the eight three-point correlators (with their corresponding eight different coupling constants). Nevertheless, expanding around the MF solution, it is possible to obtain a transformation such that only one of the three susceptibilities is divergent at the critical temperature T_c. This susceptibility is the so-called replicon. Equivalently, two non-linear susceptibilities present a more violent divergence close to T_c. In particular, at first-order in perturbation theory, they scale as $1/(T - T_\mathrm{c})^3$. For the rest of the non-linear susceptibility, two of them diverge as $1/(T - T_\mathrm{c})^2$, another one as $1/(T - T_\mathrm{c})$, and the last three remain finite at the critical point. Notice that only the couplings corresponding to the most divergent non-linear susceptibilities are relevant near the transition.

The mentioned linear transformation that *diagonalizes* the singularity structure is well known and has a physical meaning. However, corrections to MF could destroy the MF structure of divergences (or they could modify the critical exponents). There is no record of a systematic study of this behavior using numerical simulations. In this chapter, we carry out this study for spin glasses. We verify in this way that the predictions made by the theory are fulfilled in the region where the susceptibilities become very large, making it plausible that (as we explained above) this situation carries over to other systems.

The remaining part of this chapter is organized as follows. In Sect. 4.1, we introduce the main theoretical ideas, focusing on the replicon susceptibility and the most divergent non-linear susceptibilities. We also explain how to estimate these quantities from numerical data. In Sect. 4.2, we show the results for a Bethe lattice and the Edwards-Anderson model (EA) on a four-dimensional hypercubic lattice. Finally, in Sect. 4.3, we summarize the results obtained throughout the chapter and their implications.

4.1 Theoretical framework

Due to the complexity of the theory developed by [PR13], the following section has been divided as follows to present the main points of the theory: in Sect. 4.1.1, we introduce the general situation suggested by the theory. Next, in Sect. 4.1.2, we address the definition of the replicon and longitudinal susceptibilities, while in Sect. 4.1.3 we focus on the couplings of the theory that play a fundamental role in the theoretical predictions. Finally, in Sect. 4.1.4, we present the approximations we need to make in order to study the couplings from the Janus II configurations [BnCF$^+$12].

4.1.1 The scenarios suggested by field theory

The Wilsonian Renormalization Group (RG) [WK74] is the usual theory to study transitions in finite spatial dimension. However, the standard perturbative construction fails in spin glass models: the relevant corrections to MF theory come from a cubic term in the effective Landau-Ginsburg theory (LGT). Just as a reminder, the D-dimensional Ising spin glass with an external magnetic field h is described by a Hamiltonian

$$\mathcal{H} = -\sum_{\langle i,j \rangle} J_{i,j} s_i s_j + h \sum_i s_i \,, \tag{4.1}$$

where, as we introduced in Chapter 1, the spin at the node i, s_i would be $+1, -1$ and the coupling constant J_{ij} are $\{\pm 1\}$ with 50% probability. However, in the critical region, Hamiltonian (4.1) can be expressed as a replica symmetric (RS) Hamiltonian for the replicated overlap field $\psi_{ab}(x)$ ($\psi_{aa}(x) = 0$) [BR80, TDD02]:

$$\begin{aligned}\mathcal{H}_{\mathrm{RS}} = \frac{1}{2} \int \mathrm{d}^D x \biggl[& m_1 \sum_{ab} \psi_{ab}^2 + \frac{1}{2} \sum_{ab} (\nabla \psi_{ab})^2 + m_2 \sum_{abc} \psi_{ab}\psi_{bc} + \\ & + m_3 \sum_{abcd} \psi_{ab}\psi_{cd} - \frac{1}{6}\tilde{w}_1 \sum_{abc} \psi_{ab}\psi_{bc}\psi_{cd} - \frac{1}{6}\tilde{w}_2 \sum_{ab} \psi_{ab}^3 \biggr] \,.\end{aligned} \tag{4.2}$$

In the above expression, m_i are the so-called masses terms. More interesting are the cubic couplings $\tilde{w}_1$ and $\tilde{w}_2$ in Eq. (4.2), which have a special role for $D \lesssim 6$. In general, these *bare* couplings differ from the corresponding *dressed* couplings w_1 and w_2 of the Gibbs Free energy [PR13] (that are named the vertices in the field theoretical language). Let us remark that the coincidence of both coefficients $\tilde{w}_i$ and w_i arises only at the tree-level approximation in field theory.

At the MF level (where $\tilde{w}_i = w_i$), m_1 vanishes linearly in $T - T_{\mathrm{c}}(h)$ upon approaching the dAT line, $T = T_{\mathrm{c}}(h)$. In addition, the solution displays RSB with a breaking point at a value equal to the ratio $\lambda = w_2/w_1$ [GKS85, Riz13]. Notice that the parameter λ controls the MF values of equilibrium, as well as the out-of-equilibrium dynamical exponents in different contexts [PR13, CFL$^+$12, CPR13].

However, in spin glasses and also in other models with the same LGT, the construction of the $D = 6 - \epsilon$ expansion fails because there is not a fixed point in the weak-coupling region [BR80]. In order to solve this problem, following the result of [MR18], [HR20] applied the Renormalization Group (RG) to the Hamiltonian (4.2) until the mass term m_1 (which is initially small because they start close to the dAT line) becomes equal to one. At this point, they analyzed the resulting Hamiltonian at the MF level, following [BR80] and projecting on the replicon subspace (see Sect. 4.1.2 for a non-exhaustive discussion on the replicon). After taking care of the finiteness of the massive modes, [HR20] suggest that below the upper critical dimension, the renormalized coupling λ_{r} (we use the sub-index r as a reminder of the RG flow) becomes larger than one. Therefore, the transition becomes of the first order, in close analogy with the calorimetric transition of glasses (see e.g. [Cav09]). This scenario coincides with the ones obtained by [GKS85] and is in contrast with the mode coupling theory, where λ_{r} must be smaller than one for consistency [GKS85, Riz13].

4.1.2 Replicon and longitudinal susceptibilities

As we have commented at the beginning of this chapter, we want to study the behavior of the correlation functions close to the critical point. Notice that the correlation functions can be computed in numerical simulations. Consider the two points correlation functions. For a system of linear size L, with $N = L^D$ spins $s_i = \pm 1$ we have three relevant susceptibilities:

$$\chi_1 \equiv \frac{1}{N}\sum_{ij}\overline{\langle s_i s_j\rangle^2} - q^2\,, \tag{4.3}$$

$$\chi_2 \equiv \frac{1}{N}\sum_{ij}\overline{\langle s_i s_j\rangle\langle s_i\rangle\langle s_j\rangle} - q^2\,, \tag{4.4}$$

$$\chi_3 \equiv \frac{1}{N}\sum_{ij}\overline{\langle s_i\rangle^2\langle s_j\rangle^2} - q^2\,, \tag{4.5}$$

where $q \equiv \overline{\langle s_i\rangle^2}$ is the average overlap [recall Eq. 1.5], $\langle(\cdots)\rangle$ is the thermal average, and $\overline{(\cdots)}$ is the average over the disorder [recall discussion on Sect. 1.2]. The expansion around the MF solution (at all orders of the perturbation theory) demonstrates the divergence of the so-called replicon susceptibility near the critical point:

$$\chi_{\mathrm{R}} \equiv \chi_{\mathrm{SG}} \equiv \frac{1}{N}\sum_{ij}\overline{\langle s_i s_j\rangle_{\mathrm{c}}^2} = \chi_1 - 2\chi_2 + \chi_3\,, \tag{4.6}$$

where we denoted the connected correlation function as $\langle(\cdots)\rangle_{\mathrm{c}}$ (e.g. $\langle s_i s_j\rangle_{\mathrm{c}} = \langle s_i s_j\rangle - \langle s_i\rangle\langle s_j\rangle$, see for instance [Par88]). On the other hand, the longitudinal and anomalous susceptibilities. χ_{L} and χ_{A}, which are degenerated in presence of a magnetic field,

$$\chi_{\mathrm{L}} = \chi_{\mathrm{A}} = \chi_1 - 4\chi_2 + 3\chi_3\,, \tag{4.7}$$

are not divergent. To understand these results, let us consider a Gaussian magnetic field, included in the Hamiltonian (4.1) through the term $+h_o\sum_i h_i s_i$, where h_i are independent Gaussian variables with zero mean and unit variance. We can then define the staggered magnetization

$$m_{\mathrm{st}} \equiv \overline{\overline{\langle h_i s_i\rangle}}\,, \tag{4.8}$$

where $\overline{\overline{(\cdots)}}$ is the joint average over the couplings and the Gaussian magnetic field, and the corresponding susceptibility

$$\chi_{\mathrm{st}} = \frac{\partial m_{\mathrm{st}}}{\partial h_0} = -\beta\sum_j\left(\overline{\overline{\langle h_i s_i h_j s_j\rangle - \langle h_i s_i\rangle\langle h_j s_j\rangle}}\right)\,. \tag{4.9}$$

Integrating by parts Eq. (4.9) one obtain that $\chi_{\mathrm{st}} = 2\beta\chi_{\mathrm{L}}$. Notice that this connection implies that, if the magnetic susceptibility is not critical, the longitudinal one, χ_{L} is not critical either. Only the average (squared) connected correlator becomes critical. This is in sharp contrast with the $h = 0$ case, where $\chi_2 = \chi_3 = 0$ and $\chi_{\mathrm{A}} = \chi_{\mathrm{L}} = \chi_{\mathrm{R}}$. We anticipate a crossover region for small L and h, where both χ_{L} and χ_{A} seem critical (because χ_{L} and χ_{A} are critical at the $h = 0$ transition).

4.1.3 The cubic couplings and their ratio

As we mentioned previously, the cubic couplings $\tilde{w}_i$ in Wilson's Hamiltonian (4.2) are bare parameters, so they cannot be measured. However, the corresponding coefficients of the Gibbs free energy, w_i, can be obtained through their connection to physical observables [Par88, ZJ05, AMM05]. In particular, because the Gibbs free energy is the Legendre transformation of the free energy [Par88], the dressed couplings w_i can be expressed in terms of the corresponding non-linear susceptibility ω_i as $w_i = \omega_i/\chi_{\mathrm{R}}^3$. These susceptibilities can be calculated in terms of the connected-correlations at zero external momentum [PR13],

$$\omega_1 \equiv \frac{1}{N}\sum_{ijk} \overline{\langle s_i s_j\rangle_{\mathrm{c}}\langle s_j s_k\rangle_{\mathrm{c}}\langle s_k s_j\rangle_{\mathrm{c}}}\,, \tag{4.10}$$

$$\omega_2 \equiv \frac{1}{2N}\sum_{ijk} \overline{\langle s_i s_j s_k\rangle_{\mathrm{c}}^2}\,. \tag{4.11}$$

Under the RG flow, the coupling constants w_1 and w_2 diverge at the transition, while the renormalized coupling constants remain finite. These renormalized couplings are obtained by renormalizing the lengths and the overlap fields

$$w_{i,\mathrm{r}} = \frac{\omega_i}{\chi_{\mathrm{R}}^{3/2}\xi_2^{D/2}}\,, \tag{4.12}$$

where ξ_2 is the second-moment correlation length. Note that these renormalized couplings have finite and model-dependent values except at the critical temperature. Therefore, if scaling holds, there are *finite* universal values $w_{1,\mathrm{r}}^*$ and $w_{2,\mathrm{r}}^*$, so, from definition (4.12), $\chi_{\mathrm{R}} \propto |T-T_{\mathrm{c}}|^{-\gamma}$ and $\xi_2 \propto |T-T_{\mathrm{c}}|^{-\nu}$, one can check that

$$\omega_i \propto |T-T_{\mathrm{c}}|^{-\gamma_3}\,, \quad \gamma_3 = 3\nu - \frac{3}{2}\nu\eta + \frac{D}{2}\nu\,. \tag{4.13}$$

Notice that the renormalized coupling constants $w_{i,\mathrm{r}}^*$ play an important role in the computation of the critical exponents [Par88, ZJ05, AMM05], being the zeroes of the β-functions in the fixed-dimension scheme [Par88].

Returning to the ratio λ, it follows that

$$\lambda_{\mathrm{r}} = \frac{w_{2,\mathrm{r}}}{w_{2,\mathrm{r}}} = \frac{\omega_2}{\omega_1}\,, \tag{4.14}$$

so $\lambda_{\mathrm{r}} = w_2/w_1$: hence, λ remains finite at the critical point (and it is universal for the EA model), thus, we will drop thereafter the sub-index r. We also consider the dimensionless quantities

$$\mathit{\Lambda}_i = \frac{\omega_i}{\chi_{\mathrm{R}}^{3/2}L^{D/2}}\,, \tag{4.15}$$

that should scale with L as a Binder's cumulant [Bin81]. Note that, at the critical temperature, $\mathit{\Lambda}_i \propto w_{i,\mathrm{r}}$.

Finally, it is important to remark that there are nonequivalent ways of taking the relevant limits for $\lambda(L,T)$ in the onset of a second-order phase transition at T_{c}:

$$\lambda^* = \lim_{L\to\infty}\lim_{T\to T_{\mathrm{c}}} \lambda(L,T)\,, \tag{4.16}$$

$$\lambda(T_{\mathrm{c}}^+) = \lim_{T\to T_{\mathrm{c}}}\lim_{L\to\infty} \lambda(L,T)\,. \tag{4.17}$$

It is hardly surprising that $\lambda^* \neq \lambda(T_{\mathrm{c}}^+)$ [SS00]. $\lambda(T_{\mathrm{c}}^+)$ is, in general, more difficult to estimate than λ^*. Still, it could be more desirable given that RG β-functions in the fixed-dimension scheme (see e.g. [Par88]) are expressed in terms of the thermodynamic quantities in analytical computations.

4.1.4 Approximating the divergent non-linear susceptibilities from three and four replicas

In order to calculate the parameter λ_r, we need to compute ω_1 and ω_2 [cf. Eqs. (4.10) and (4.11)]. These couplings are related with quantities like

$$m_i^2 \equiv \overline{\langle s_i \rangle^2}, \quad m_i^4 \equiv \overline{\langle s_i \rangle^4}, \quad m_i^6 \equiv \overline{\langle s_i \rangle^6}. \tag{4.18}$$

The usual approach consists in introduce K independent replicas of the system with the same disorder ($s^{(i)}$, $i = 1, \dots, K$ — remember the replica trick in Sect. 1.2.1) obtaining

$$m_i^2 = \overline{\langle s_i^{(1)} s_i^{(2)} \rangle}, \quad m_i^4 = \overline{\langle s_i^{(1)} s_i^{(2)} s_i^{(3)} s_i^{(4)} \rangle}, \quad m_i^6 = \overline{\langle s_i^{(1)} s_i^{(2)} s_i^{(3)} s_i^{(4)} s_i^{(5)} s_i^{(6)} \rangle}. \tag{4.19}$$

Both couplings, ω_1 and ω_2, can be numerically evaluated once expressed as [PR13]

$$\begin{aligned} \omega_1 &= \mathcal{W}_1 - 3\mathcal{W}_5 + 3\mathcal{W}_7 - \mathcal{W}_8, && (4.20) \\ \omega_2 &= \frac{1}{2}\mathcal{W}_2 - 3\mathcal{W}_3 + \frac{3}{2}\mathcal{W}_4 + 3\mathcal{W}_5 + 2\mathcal{W}_6 - 6\mathcal{W}_7 + 2\mathcal{W}_8, && (4.21) \end{aligned}$$

with

$$\begin{aligned} \mathcal{W}_1 &\equiv N^2 \overline{\langle \delta Q_{12} \delta Q_{23} \delta Q_{31} \rangle}, & \mathcal{W}_5 &\equiv N^2 \overline{\langle \delta Q_{12} \delta Q_{13} \delta Q_{21} \rangle}, \\ \mathcal{W}_2 &\equiv N^2 \overline{\langle \delta Q_{12}^3 \rangle}, & \mathcal{W}_6 &\equiv N^2 \overline{\langle \delta Q_{12} \delta Q_{13} \delta Q_{14} \rangle}, \\ \mathcal{W}_3 &\equiv N^2 \overline{\langle \delta Q_{12}^2 \delta Q_{13} \rangle}, & \mathcal{W}_7 &\equiv N^2 \overline{\langle \delta Q_{12} \delta Q_{13} \delta Q_{45} \rangle}, \\ \mathcal{W}_4 &\equiv N^2 \overline{\langle \delta Q_{12}^2 \delta Q_{34} \rangle}, & \mathcal{W}_8 &\equiv N^2 \overline{\langle \delta Q_{12} \delta Q_{34} \delta Q_{56} \rangle}. \end{aligned}$$

The overlap fluctuations, δQ_{ab}, can be written in terms of independent real replicas with the same quenched disorder

$$\delta Q_{ab} \equiv \frac{1}{N} \sum_i s_i^{(a)} s_i^{(b)} - \frac{1}{N} \sum_i \overline{\langle s_i \rangle^2}. \tag{4.22}$$

In the same way, each correlator $\mathcal{W}_i$ requires a number of different real replicas that is equal to the largest replica index in its definition that appears in its definition. Hence, we need six replicas to compute ω_1 and ω_2.

Nevertheless, the theory predicts that six linear combinations of the $\mathcal{W}_i$'s are less divergent than the $\mathcal{W}_i$ separately. Using these linear relationships one can use only three replicas to estimate the couplings [PR13]

$$\begin{aligned} \omega_1^{(3)} &\equiv \frac{11}{30}\mathcal{W}_1 - \frac{2}{15}\mathcal{W}_2 && (4.23) \\ \omega_2^{(3)} &\equiv \frac{4}{15}\mathcal{W}_1 - \frac{1}{15}\mathcal{W}_2. && (4.24) \end{aligned}$$

Notice the super-index to refer to using only three replicas. On the other hand, the theory predicts that three linear combinations of the $\mathcal{W}$'s remain finite at the critical point. Therefore, it is possible to express $\mathcal{W}_7$ and $\mathcal{W}_8$ as a function of the remaining cumulants. Notice that this allows us to estimate the couplings using only four replicas [Vec21]:

$$\begin{aligned} \omega_1^{(4)} &\equiv \frac{23\mathcal{W}_1}{30} + \frac{\mathcal{W}_2}{20} - \frac{3\mathcal{W}_3}{5} + \frac{9\mathcal{W}_4}{20} - \frac{6\mathcal{W}_6}{5} + \frac{\mathcal{W}_6}{2}, && (4.25) \\ \omega_2^{(4)} &\equiv \frac{7\mathcal{W}_1}{15} + \frac{2\mathcal{W}_2}{5} - \frac{9\mathcal{W}_3}{5} + \frac{3\mathcal{W}_4}{5} - \frac{3\mathcal{W}_5}{5} + \mathcal{W}_6. && (4.26) \end{aligned}$$

Appendix I shows the expressions we have used to calculate the coupling constants from our numerical results.

Let us remark that the three- and four-replica estimators only *coincide* with the true susceptibilities ω_1 and ω_2 at the critical point. For other temperatures, $\omega_{1,\mathrm{r}}$, $\omega_{2,\mathrm{r}}$ and λ_r are model-dependent. In particular, close to the critical temperature

$$\omega_i - \omega_i^{(3)} = O(|T-T_\mathrm{c}|^{\gamma_\Delta})\,, \tag{4.27}$$

$$\omega_i - \omega_i^{(4)} = O(|T-T_\mathrm{c}|^{\gamma_3})\,. \tag{4.28}$$

where the exponents γ_Δ is expected to be smaller than γ_3 (e.g. in MF one finds $\gamma_\Delta = 1$ and $\gamma_3 = 3$). Nevertheless, we are only interested in the universal value the susceptibilities ω_i and parameter λ take at the critical point.

4.2 Numerical results

The different correlation functions, susceptibilities, and coupling constants discussed in Sect. 4.1 can be obtained from simulations using real replicas. As we explain in Chapter 1, from *two* real replicas, one can compute the overlap q [cf. Eq. 4.19]. Using *four* replicas, it is possible to calculate the three susceptibilities under consideration in this chapter (χ_1, χ_2 and χ_3), and with *six* replicas the coupling constants $\omega_{i=1,2}$ in Eqs. (4.10) and (4.11). However, as we detail in subsection 4.1.4, it is possible to compute both ω_i using only three and four replicas at the critical point. Appendix D contains a detailed explanation of the computation of both ω_i from three and four replicas (including the combinatorics).

This section shows the results obtained for the Bethe lattice and the Edwards-Anderson model in 4 dimensions with an external field. We compare our results close to the critical point to test the theoretical predictions.

4.2.1 The Bethe lattice

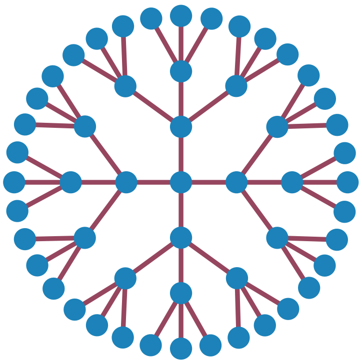

Figure 4.1: Schematic Bethe lattice with fixed-degree 4.

We first study our proposal for three- and four-replica estimators in the Bethe lattice because it is a controlled setting. In particular, the Ising spin glass model in a magnetic field on Bethe lattice can be analytically solved [MP01, PT02]. The existence of a true de Almeida-Thouless (dAT) transition is certain in this model. Furthermore, the divergence of the susceptibilities under consideration (i.e., linear and non-linear) closely matches the description in Sect. 4.1.

The results for λ presented in Fig. 4.2 are obtained using a four fixed-degree random regular graph (see Fig. 4.1 for an example). We show the exact expression (using six replicas) and the three- and four-replica estimators $\lambda^{(3)} \equiv \omega_2^{(3)}/\omega_1^{(3)}$ and $\lambda^{(4)} \equiv \omega_2^{(4)}/\omega_1^{(4)}$. Notice that T_c and $\lambda(T_\mathrm{c}^+)$ are known analytically [PRTR14]. The estimators extrapolate to the correct value at the critical point [taking the limits correctly, cf. Eq. (4.16)], although finite-size corrections are present in the critical region. Let us remark that the finite-size corrections for the true λ (i.e., the six-replica estimator) and the four-replica estimator coincide close to the critical point. We expect the same effect for the three-replica estimator, but the pre-asymptotic corrections at the sizes considered mask the effect. However, all three estimators take the same value $\lambda^* \approx 0.55$.

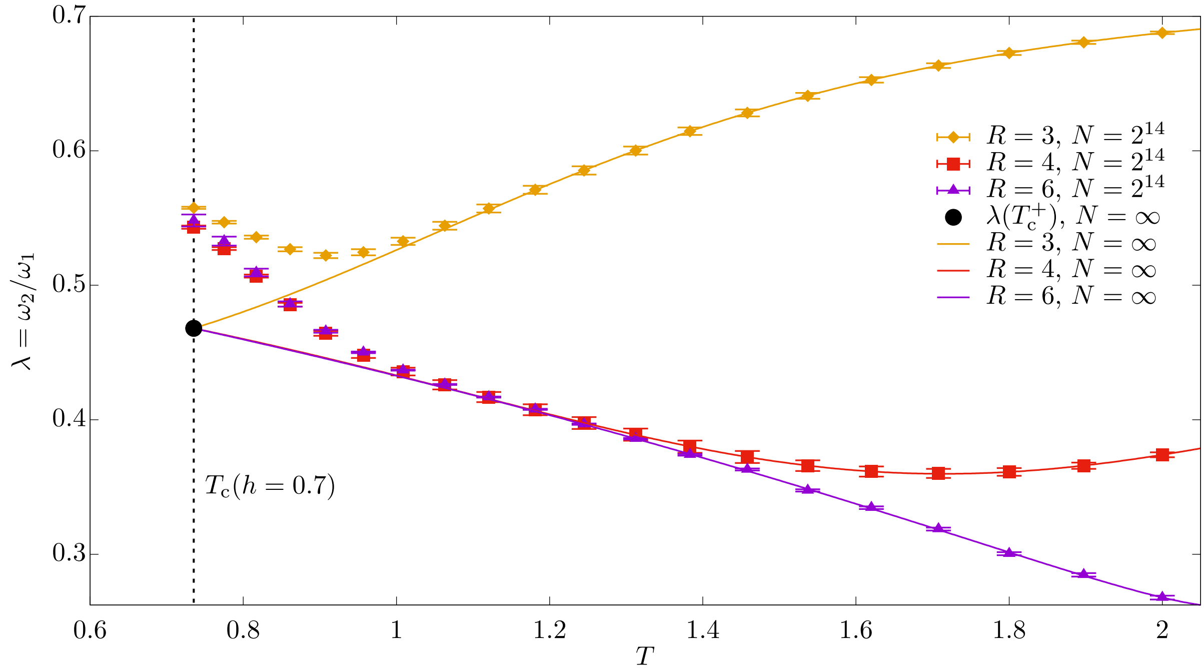

Figure 4.2: Temperature dependence of the ratio of renormalized couplings λ, see Eq. (4.14), computed with a magnetic field $h = 0.7$ on a Bethe lattice. We show data from the three-, four- and six-replica estimators. The critical temperature (vertical dashed line) and the value of $\lambda(T_c^+) \simeq 0.47$ (black dot), see Eq. (4.16), have been extracted from the analytical calculation presented in [PRTR14]. The thermodynamic limit, continuous lines marked as $N = \infty$, are extrapolations considering scaling corrections detailed in [Vec21].

4.2.2 4-dimensional Edward-Anderson model in field.

At variance with the case of the Bethe lattice, it is not certain that the phase transition is described by the theory presented in Sect. 4.1. As we mentioned at the beginning of this chapter, there are several theories to explain the behavior of the susceptibility and the correlation length: a crossover (so there would be no phase transition, or it would be at zero temperature [FS85, FH86, BM87b, BM87a, FH88b, FH88a, FH93]), a discontinuous phase transition at which the correlation length remains finite [HR20], or a second-order transition with critical behavior [BR80, TDD02, CY17, ALP+22]. This would imply that the three- and four-replica estimators could produce different results, thus indicating that the chosen theory is incorrect. Furthermore, the existence of such a theory for D< 6 could even be questioned because there is not a fixed point in the perturbative RG flow below six dimensions. Therefore, the consistency of the results obtained by the three- and four-replica estimators is a non-trivial test for the Replica-Symmetric field theory proposed by [BR80] as applied in the region of large susceptibilities.

In order to study the EA model in 4 dimension, we have re-analyzed equilibrium configurations obtained by the Janus Collaboration [BnCF+12] using the Janus-I supercomputer [BCC+08a]. These configurations were generated for the four-dimensional Ising spin

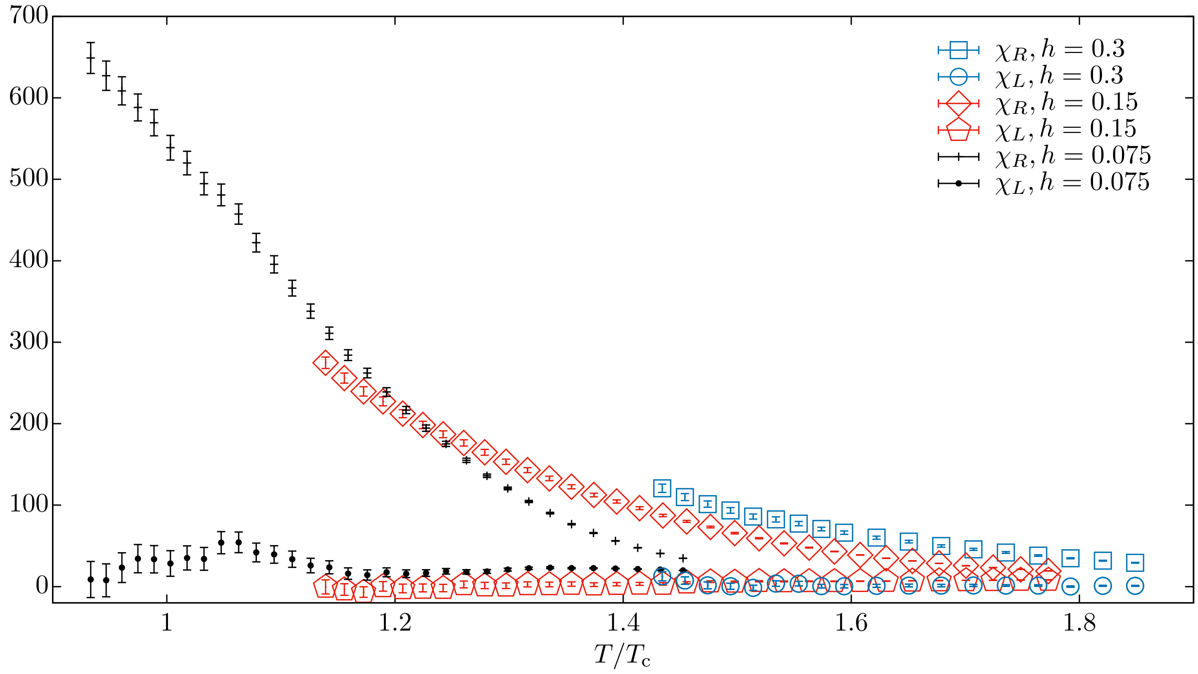

Figure 4.3: Replicon (χ_R) and longitudinal (χ_L) susceptibility, Eqs. (4.6) and (4.7) versus the temperature. The data are obtained for the $D = 4$ Edwards-Anderson model at magnetic fields $h = 0.075$, 0.15, and 0.3. For each h, the temperature is rescaled by the corresponding best estimate for T_c [BnCF+12]. We show data for our largest system, $L = 16$.

glass given by the Hamiltonian in Eq. (4.1). These data were obtained only for four real replicas, which forces us to estimate λ only through the three- and four-replica estimators. The computation of [BnCF+12] was carried out near to (but not exactly) at the dAT line.

We have studied the three values of the external magnetic field ($h = 0.075$, 0.15, and 0.3) that have been used to obtain the critical temperatures and critical exponents in [BnCF+12]. However, in addition to studying the replicon susceptibility χ_R as done in [BnCF+12], we have also analyzed the behavior of the longitudinal susceptibility χ_L, recall Eqs. (4.6) and (4.7). The results are shown in Fig. 4.3, where it can be seen that χ_R becomes very large as the temperature decreases. At the same time, the longitudinal susceptibility saturates to a much smaller plateau. The plateau value of χ_L in Fig. 4.3 approximately scale as h^{-x}, with x between 2 and 3. In MF, χ_L near the critical temperature is proportional to $h^{-2/3}$ [TDD02]. Notice that Fig. 4.3 implies that the correlations extend to much larger distances for the replicon mode than for the longitudinal ones, which is in agreement with our MF-based expectations and with previous dynamic investigations in $D = 3$ [BJBnC+14b]. In particular, the difference between χ_R and χ_L excludes the possibility that the critical behavior in χ_R is due to the $h = 0$ fixed point.

Before studying λ, we considered the behavior of the most divergent nonlinear susceptibilities, ω_1 and ω_2, see Eqs. (4.10) and (4.11). The results presented in Fig. 4.4 show how ω_1 grows as T approaches T_c, or the system size L increases. The divergence suggested by these results led us to consider the dimensionless magnitude Λ_1, see Eq. (4.15). At the critical point, the Λ_1 curves as a function of T for the different sizes should intersect or converge at the critical point T_c. Our data in Fig. 4.4-Right do not seem to behave in this way, making it difficult to calculate T_c (indeed, the authors of Ref. [BnCF+12] could

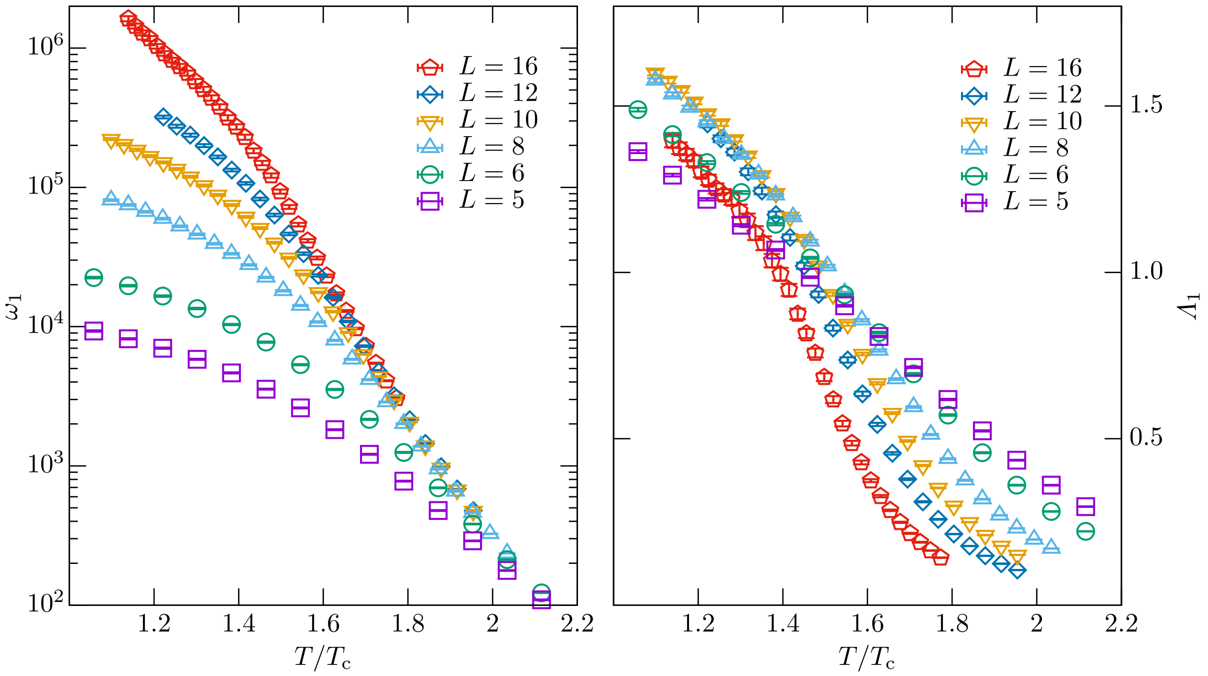

Figure 4.4: Non-linear susceptibility for the Edwards-Anderson model with magnetic field $h = 0.15$ in $D = 4$. Left: Four-replica estimate, $\omega_1^{(4)}$, for the non-linear susceptibility in Eq. (4.25). vs. temperature. **Right:** Four-replica estimate of the dimensionless quantity Λ_1, recall Eq. (4.15) vs. temperature. T is rescaled by the critical temperature T_c [BnCF+12].

locate T_c only by considering quantities at non-zero external momentum). However, in the present thesis, we are more interested in the fact that the results do not seem to show any evidence of an uncontrolled increase in Λ_1 as the system size L increases. This result essentially rules out the scenario of a first-order phase transition [HR20]. It is important to note that data for $L = 16$ possess a smaller statistic sample (see Table II in [BnCF+12]), so its results should be taken as a qualitative confirmation that there is not a divergent behavior in Λ_1 when increasing L.

After verifying that the behavior of ω_1 is consistent with the theoretical predictions, we consider the ratio λ for the case of the EA in 4D. Fig. 4.5 shows the results for the three- and four-replica estimators for the different external magnetic field values. It can be seen from Fig. 4.5 that the results do not show large finite-size corrections as we approach the critical point. Furthermore, the data barely depends on temperature for $T < T_c\,(h = 0.075)$, which suggests that λ^* and $\lambda(T_c^+)$ should take on close values. This result contrasts with those of the Bethe lattice, where a clear difference could be seen between both results, see Fig. 4.2. In addition, given that the only finite-size corrections are a monotonic decrease with increasing L for the three-replica estimator, as opposed to a monotonic increase for the four-replica estimator, it is easy to obtain an interval that encompasses the value of λ^* from the results for the largest size $L = 16$. Our results are consistent with a universal value of $\lambda^* \approx 0.55$ at the critical temperature. Note that our results for both approximations verify a value of $\lambda(L, T) < 1$, so we conclude that $\lambda(T_c^+) < 1$: the first-order phase transition scenarios has been ruled out.

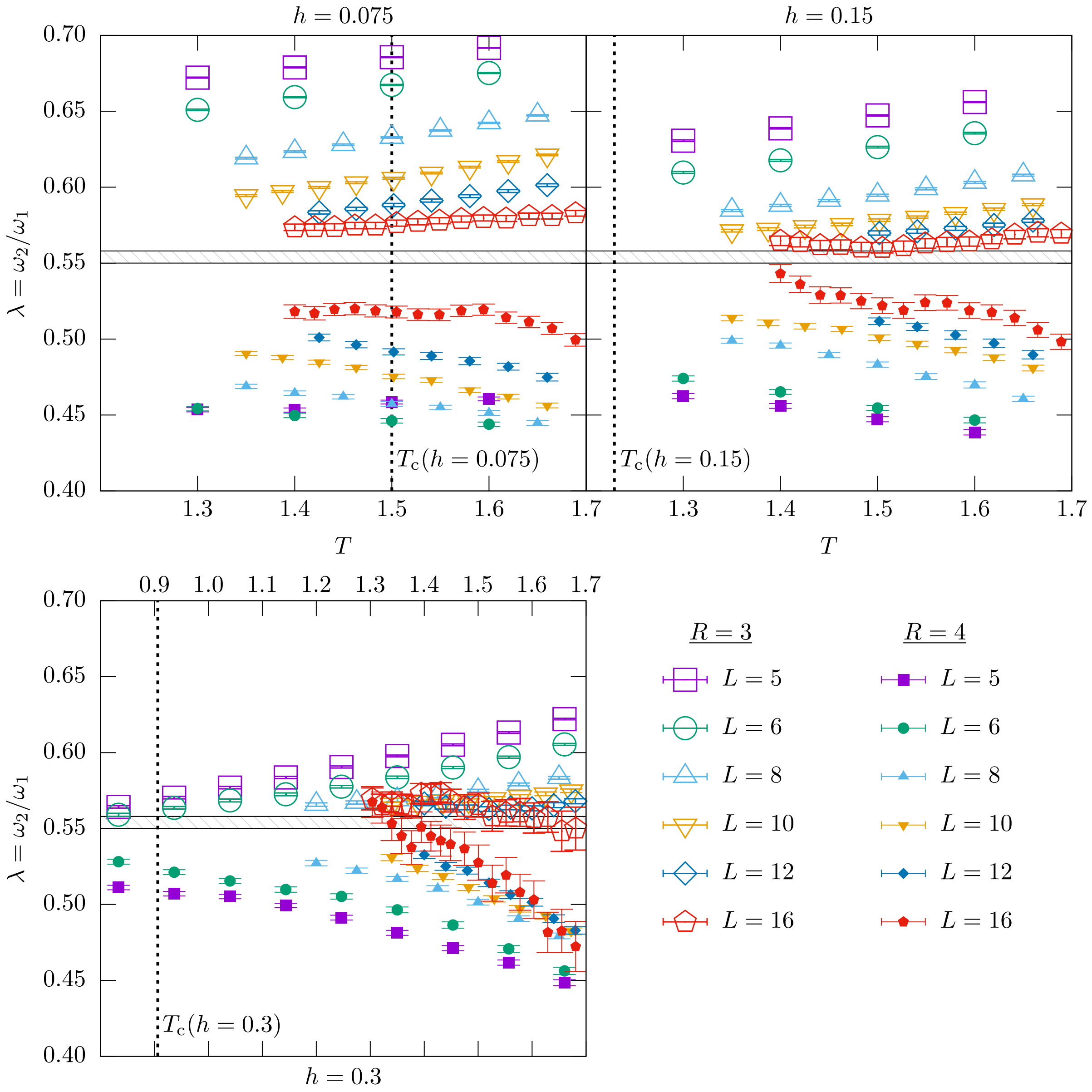

Figure 4.5: Three- and four-replica estimators for λ as a function of the temperature in the $d = 4$ Ising spin glass. Each panel corresponds to one of the values of the external magnetic field studied, from left to right $h = 0.075$, 0.15, and 0.3, respectively. The vertical lines correspond to the three critical temperatures taken from [BnCF⁺12]. The band around $\lambda^* \simeq 0.55$ is our extrapolation to $L \to \infty$, assuming that the three- and four-replica estimators converge to a common value for the three fields considered. The width of the band represents the uncertainty in our extrapolation $\lambda(L) = \lambda^* + A/L^b$ (λ^*, A and b are the fit parameters) for $h = 0.075$.

4.3 Conclusion

Letting aside the debate about the existence or lack thereof of a true glass transition, it is universally accepted that glass formers display slow dynamics and large correlations. When the length scale for fluctuations becomes large, the usual framework to study the problem is a Field Theory. However, the Hamiltonian is not constrained by symmetries: in particular, for spin glasses in a magnetic field, we have a very complex theory with eight different coupling constants.

The theory can be simplified thanks to the work of [BR80]. Indeed, their so-called replica symmetric Hamiltonian is the basis of many analyses. Nevertheless, up to now, it has been impossible to test the basic hypothesis underlying the theory in a non-trivial problem. In this chapter, we overcome this challenge thanks to the detailed scaling description for the many linear and non-linear susceptibilities in the problem provided by [PR13]. We apply this description to re-analyses the equilibration configurations obtained with the Janus I supercomputer for a $D = 4$ spin glass [BnCF^{+}12].

Our results suggest that the crucial scaling relations are fulfilled beyond mean-field approximation, close to (but above) the de Almeida-Thouless line. Furthermore, it is plausible that our approach will be helpful for studying other physical systems (e.g., glass-forming liquids). Finally, let us emphasize that our results for the renormalized coupling λ seem to exclude the suggested scenario of a first-order transition [HR20].

Part IV

Correlation function in spin glasses

5

Multifractal behavior of spin-glass correlations

Multifractality in spin glasses

M. Baity-Jesi, E. Calore, A. Cruz L. A. Fernández, J. M. Gil-Narvión, I. González-Adalid Pemartín, A. Gordillo-Guerrero, D. Iñiguez, A. Maiorano, E. Marinari, V. Martín-Mayor, J. Moreno-Gordo, A. Muñoz Sudupe, D. Navarro, I. Paga,G. Parisi, S. Pérez-Gaviro, F. Ricci-Tersenghi, J. J. Ruiz-Lorenzo, S. F. Schifano, B. Seoane, A. Tarancón, D. Yllanes (Janus Collaboration)

Proc. Natl. Acad. Sci. **121** (2) e2312880120

`https://doi.org/10.1073/pnas.2312880120`

In many subjects (physics, chemistry, geology, biology, etc.), random objects apparently look the same when the observation scale is changed. We say that these systems present a scaling symmetry (see [Wil79, Par88, Bar12] for some examples) and are called fractals (or self-affine). This behavior is usually quantitatively characterized through a number, named the fractal dimension. However, there are systems where many different fractal behaviors coexist, and more than one fractal dimension is needed to characterize the scaling properties. We refer to these systems as multifractals (or multi-affine) [FP85, Har01]

Multifractal behavior was first observed in physics, in the context of turbulence [BPPV84], Anderson localization [CP86], and diffusion-limited aggregation [SM88]. Chaotic dynamics soon provided a unifying language for understanding multifractality [HJK$^+$86b, HJK$^+$86a]. The concept has gained popularity as the list of systems exhibiting multifractality has grown. Examples include surface growth [BS09], human heartbeat dynamics [IAG$^+$99], mating copepods [SS14, Klo14], rainfall [Dei00], and financial time series [ARAR08]. With the growing list of multifractal systems, different mathematical tools have been developed to characterize their scaling behavior.

Surprisingly, in the present chapter, we justify adding to the list the out-of-equilibrium dynamics of spin glass (SG) systems. Considering that these disordered magnetic alloys have long been studied for their paradigmatic value as a toy model for studying glassiness, optimization, biology, financial markets, and social dynamics (recall Sect 1.1), it is surprising that such a prominent feature as multifractality has gone unnoticed for such a well-studied model.

To understand this paradox, it is necessary to consider the typical way of studying and working with these systems. Typically, the SG that is initially at high temperature is cooled below its critical temperature T_c and allowed to relax for a time t_w —in most experimental studies, equilibrium conditions are not reached [VHO$^+$97]. As t_w increases, the glassy domains, characterized by the coherence length $\xi(t_\mathrm{w})$, become larger. It is worth noting how slow this dynamics is, so that after waiting for $t_\mathrm{w} \sim 1$ hour, only $\xi \sim 200$ lattice spacings is reached [ZPBJ$^+$20, PZBJ$^+$21]. In this situation, the response to an external magnetic field is typically measured to probe the SG dynamics experimentally. In this measure, an average over the entire system is carried out. Since the sample is effectively composed of many independent domains of linear size $\sim \xi(t_\mathrm{w})$, the central limit theorem ensures that the large fluctuations that could ultimately cause multifractal behavior are eliminated.

In the case of numerical simulations, the framework in this chapter, the emphasis has traditionally been on studying the spatial-averaged correlation function, thus following the experimental works. Furthermore, the computational difficulty of studying correlations without considering a spatial average is very high. However, recent works have considered working at scales of the coherence length to study phenomena such as chaos in temperature [BJCC+21], or memory and rejuvenation [BJCC+23], which were discussed in Chapter 1. The work presented in this chapter also focuses on studying the correlation function in the scale of the coherence length ξ through the analysis of simulations generated by the Janus II dedicated supercomputer [BJBnC+14c].

This chapter is divided into the following sections: Sect. 5.1 covers the standard framework used for studying the correlation functions in spin glasses, also, in Sect. 5.1 we compare the diluted Ising ferromagnet with the Ising spin glass to show the different behavior of the statistical fluctuations of the correlation function in both models. In Sect. 5.2, we focus our attention on the spatial fluctuations presented in the correlation function. After that, in Sect. 5.3 we quantify these fluctuations through the moments of the probability distribution function (pdf) of the correlation function. The main conclusion of this chapter is presented in Sect. 5.4 using the multifractal formalism. Finally, Sect. 5.5 gives a technical description of how we study the pdf of the correlation function from N_R independent trajectories (or replicas), as well as other relevant technical details that pertain solely to this chapter.

5.1 Correlation function in Ising spin models

The spatial correlation function provides us with information about the spatial correlations of the system. In order to study its fluctuations, in Sect. 5.1.1 we discuss the models that we are going to study, namely Edwards-Anderson model model and Ising link-diluted model. After that, in Sect. 5.1.2 we compare both models.

5.1.1 Model definition and observables

This chapter considers the Edwards-Anderson model (EA) introduced in Sect. 1.1. We work without a magnetic field in a cubic lattice with linear size $L = 160$ and periodic boundary conditions. Hence, Hamiltonian (1.4) takes the form

$$\mathcal{H} = -\sum_{\langle \vec{x},\vec{y}\rangle} J_{\vec{x},\vec{y}} s_{\vec{x}} s_{\vec{y}}\,. \tag{5.1}$$

Remember that the spins $s_{\vec{x}} = \pm 1$, placed at the lattice sites $\vec{x}$, interact with their nearest neighbors through the coupling constant $J_{\vec{x},\vec{y}}$. The coupling constants are independent random variables, $J_{\vec{x},\vec{y}} = \pm 1$ with equal probability, fixed once and define a sample (recall the quenched disorder introduced in Sect. 1.2).

As we mentioned in the introduction for this chapter, we also consider the Ising link-diluted model (DIL) as a null experiment. The only difference with the Hamiltonian in Eq. (5.1) is the choice of the couplings: $J_{\vec{x},\vec{y}} = 1$ (with 70% probability) or $J_{\vec{x},\vec{y}} = 0$ (with 30% probability). The reader will notice that this is a ferromagnetic system without frustration. Let us remark that both models, EA and DIL, display domain-growth out-of-equilibrium dynamics.

We have simulated both models using Metropolis dynamics on the Janus II supercomputer [BJBnC⁺14c]. Our time unit is a full-lattice sweep, roughly equivalent to a picosecond of physical time [Myd93]. The critical temperatures for these models are $T_\text{c} = 1.1019(29)$ for the EA [BJBnC⁺13] and $T_\text{c}^\text{DIL} = 3.0609(5)$ for DIL [BCBJ04] (this is twice the value reported by [BCBJ04] due to our use of an Ising, rather than Potts, formulation). With some abuse of language, from now on, we refer to the DIL temperatures as $\tilde{T}$ rather than their actual value $T^\text{DIL} = \tilde{T}(T_\text{c}^\text{DIL}/T_\text{c}^\text{EA})$. The list of temperatures and the corresponding maximum coherence lengths achieved in our simulations are summarized in Table 5.1.

T or $\tilde{T}$	t_w (EA)	ξ_max(EA)	t_w (DIL)	ξ_max (DIL)
0.7	46531866276	12	498	15
0.8	18734780191	15	919	21
0.9	15172184825	20	954	23

Table 5.1: Maximum t_w and coherence length ξ_max reached for each of our models and simulation temperatures.

For both models, we consider 16 samples. For each of these samples, we simulated N_R replicas. Recall the notation introduced in Sect. 1.3, we denote by $\langle \cdots \rangle$ the average over thermal noise for one sample (which is estimated by averaging over the replicas) and by $\overline{\langle \cdots \rangle}$ the subsequent average over the samples.

As stated above, we are interested in the four-body correlation function [recall Eq. (1.31)].

$$C_4(\vec{x},\vec{y};t_\text{w}) = \langle s_{\vec{x}}(t_\text{w}) s_{\vec{y}}(t_\text{w}) \rangle^2 \,. \tag{5.2}$$

The reader will see that for a given sample and given $(\vec{x},\vec{y},t_\text{w})$, $C_4(\vec{x},\vec{y};t_\text{w})$ is not a stochastic variable. However, if we consider the variation induced by the different samples, $\{J\}$, and sites $(\vec{x},\vec{y})$, the four-body correlation function is a stochastic variable. From now on, we shall refer to this stochastic variable as C_4, without arguments.

Although it is impossible to compute $C_4(\vec{x},\vec{y};t_\text{w})$ with a finite number of replicas, unbiased estimators of its moments can be calculated (see Sect. 5.5 for a detailed explanation). In particular, the average, including space average, of the (four-body) correlation function (see Fig. 5.1)

$$C_4^\text{av}(\vec{r},t_\text{w}) = \frac{1}{L^3} \sum_{\vec{x}} \overline{C_4(\vec{x},\vec{y}=\vec{x}+\vec{r};t_\text{w})} \tag{5.3}$$

is a well-known quantity and the basis of the computation of the coherence length $\xi(t_\text{w})$ (see Appendix G for a detailed explanation of the estimation of the coherence length).

5.1.2 Comparing the spin glass with the Ising link-diluted models

Cubic symmetry, present in average over the samples, allows us to average over the three equivalent displacements $\vec{r} = (r,0,0)$ and permutations. We shall use the shorthand $C_4^\text{av}(r;t_\text{w})$ to indicate this average over the three equivalent $\vec{r}$.

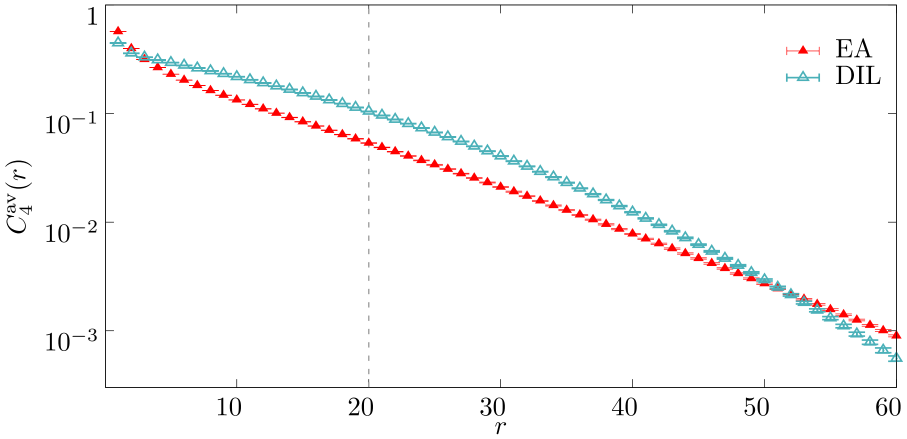

Figure 5.1: Average four-body correlation function, Eq. (5.3) versus distance r. Data computed for the 3-dimensional DIL and the EA. Both models have a coherence length $\xi(t_\mathrm{w}) = 20$ (dashed vertical line) at temperature T (or $\tilde{T}$ for DIL) equals 0.9 —recall that $T_\mathrm{c}^{\mathrm{EA}} \approx 1.1$ [BJBnC⁺13]. Error bars are smaller than the point size.

In Fig. 5.1, we compare this spatial-average four-body correlation function for the DIL and the EA with coherence length $\xi(t_\mathrm{w}) = 20$. It should be noted that both systems exhibit qualitatively similar behavior. This feature —as we mentioned above— is explained by the average over the sample destroying the large fluctuations presented in $C_4(\vec{x}, \vec{y} = \vec{x} + \vec{r}; t_\mathrm{w})$ since the sample is effectively composed of many independent domains of linear size $\sim \xi(t_\mathrm{w})$, the central limit theorem eliminates from the average response the large fluctuations.

The above consideration implies that multifractal behavior in SG should be investigated in large statistical deviations that occur at a length scale smaller than (or compatible with) $\xi(t_\mathrm{w})$. This is not the usual framework neither for experiments (see [ZPBJ⁺20, PZBJ⁺21, ZOS22], for instance) nor for simulations [BCC⁺08a, BJCC⁺17b, BJCC⁺18]. However, there is an important exception. Recently, [BJCC⁺23] achieved progress in the theoretical interpretation of the experimental rejuvenation and memory effects in spin glasses [JVH⁺98] (see Sect. 1.1.2). The study of the temperature chaos played a crucial role in this step forward (see Sect. 1.1.2) in the out-of-equilibrium dynamics at the $\xi(t_\mathrm{w})$ length scale [BJCC⁺21], through numerical simulations using the Janus II dedicated supercomputer [BJBnC⁺14c]. As we shall show in Sect. 5.2 and 5.3, when one considers the fluctuations at the $\xi(t_\mathrm{w})$ length scale the surprising multifractal behavior emerges.

The reader may object that it is difficult to find large statistical fluctuations in a mathematical object bounded between 0 and 1, such as the spin-glass correlation function $C_4(\vec{x}, \vec{y} = \vec{x} + \vec{r}; t_\mathrm{w})$. Indeed, large fluctuations are only possible when the average of the considered bounded object goes to zero. Fig. 5.2 shows this behavior for the four-body correlation function in EA (bottom panel) when the coherence length $\xi(t_\mathrm{w})$ grows. So, we realize that the SG correlation function at a given site can exhibit large fluctuations if we measure it in units of the average correlation. In particular, in the spin glass, the correlation function scales as

$$C_4^{\mathrm{av}}(r; t_\mathrm{w}) \sim \frac{G[r/\xi(t_\mathrm{w})]}{r^\theta} \tag{5.4}$$

for large r, where the cut-off $G(x)$ decays faster than exponentially as x grows (see e.g. Refs. [BCC⁺08b, FMMM⁺19]). Hence, for $r \sim \xi(t_\mathrm{w})$, one may consider a power-law

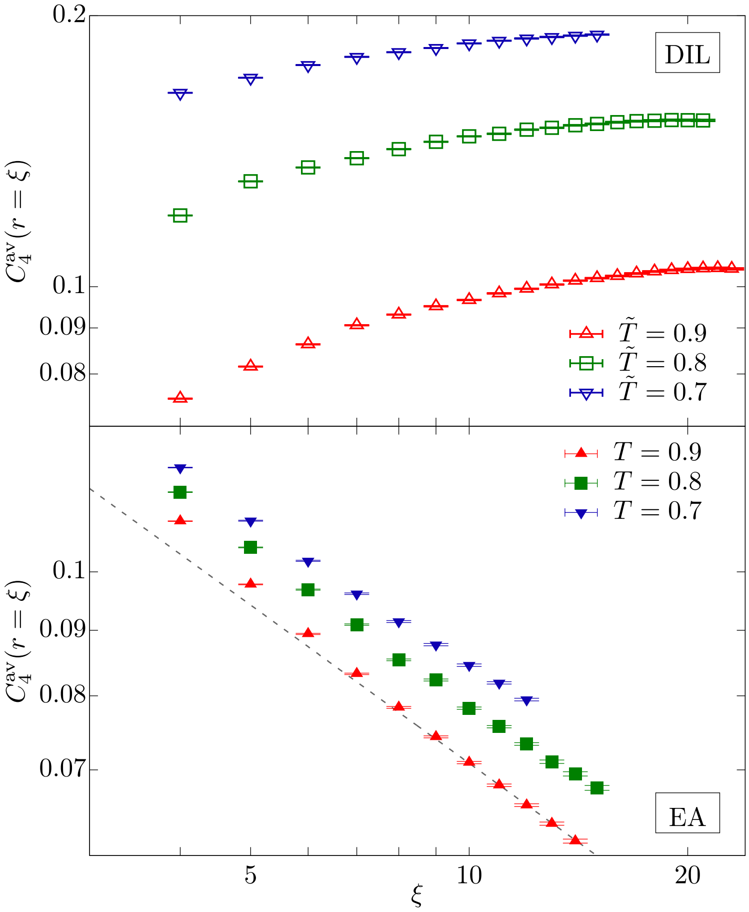

Figure 5.2: Average four-body correlation function $C_4^{\mathrm{av}}\left[r = \xi(t_{\mathrm{w}})\right]$, see Eq. (5.3) as a function of the coherence length $\xi(t_{\mathrm{w}})$. Data computed for the 3-dimensional DIL (**top**) and the EA (**bottom**) at temperatures T, $\tilde{T} = 0.9, 0.8$ and 0.7. The dashed line is our fit to Eq. (5.7), with $q = 1$, for the EA at $T = 0.9$ (we avoid scaling corrections fitting in the range $\xi(t_{\mathrm{w}}) \in [10, 20]$, see Table 5.2 for further information). Error bars are smaller than the point size.

scaling in ξ — as we did to fit the data for $T = 0.9$ in Fig. 5.2 bottom panel (the dashed line correspond to $\theta \approx 0.4$, see Table 5.2, which coincide with the result reported by [BJCC+18])— or in r as we will consider in Sect. 5.2.

However, in the DIL, (Fig 5.2 top panel), the correlation function goes to a constant value (the squared spontaneous magnetization) as $\xi(t_{\mathrm{w}})$ grows. Therefore, large deviations and multifractality are possible for the ferromagnet only at the critical point, where the spontaneous magnetization vanishes [DC00, MMMP+23].

5.2 Statistical fluctuations in the correlation function

In order to confirm the possibility of large deviations in the statistics of the spin-glass correlation function C_4, we compare the ratio of the second moment of C_4 at $r = \xi(t_{\mathrm{w}})$, $\overline{C_4^2}$, to the first moment squared, $\overline{C_4}^2$, as a function of the coherence length, see Fig. 5.3. Note that this ratio, computed for the DIL, tends to a finite limit for large coherence length. This is in contrast with the power-law followed by the EA data, which indicates that in the scaling limit [i.e. $\xi(t_{\mathrm{w}}) \to \infty$], the order of magnitude of $\overline{C_4^2}$ is larger than that

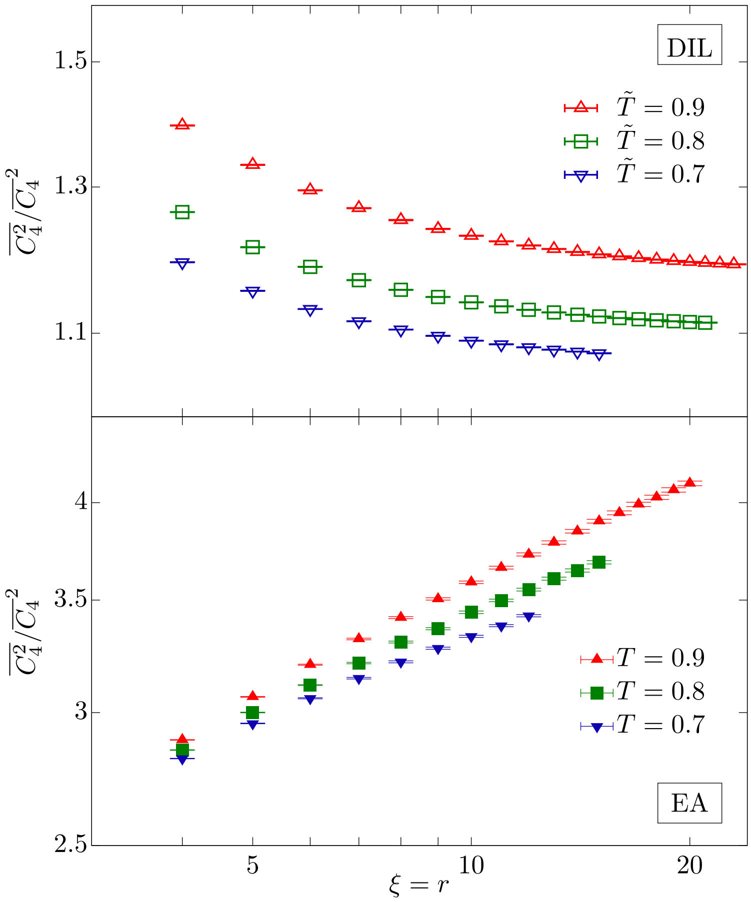

Figure 5.3: Ratio of the second moment of the four-body correlation function $\overline{C_4^2}$, computed at $r = \xi(t_\mathrm{w})$, to the square first moment $\overline{C_4}^2$, versus the coherence length $\xi(t_\mathrm{w})$. Data computed for DIL (**top**) and for EA (**bottom**) for different temperatures T, or $\tilde{T}$. Error bars are smaller than the point size.

of $\overline{C_4}^2$. This behavior is not reminiscent of a monofractal, which in the scaling limit is characterized by a single quantity (say, $\overline{C_4}$).

In Fig. 5.4, we represent the same ratio of the second moment to the first moment squared as in Fig. 5.3, but as a function of the first moment. Our data in Fig. 5.4 nicely follows a power law as a function of $\overline{C_4}$ (this type of analysis was pioneered by [BCT+93]). More interesting is the fact that our data for $T < T_\mathrm{c}$ follow the same scaling curve, which slightly differs from the results for the critical temperature. The independence on T justifies our choice of focusing our attention on data at $T = 0.9$, namely the temperature in the spin-glass phase where we can reach the largest $\xi(t_\mathrm{w})$ (see Table 5.1).

After the previously mentioned results in Figs. 5.3 and 5.4, we may expect a different behavior for the average and the local correlation functions when distances up to $r \sim \xi(t_\mathrm{w})$ are considered:

$$C_4^{\mathrm{av}}(r, t_\mathrm{w}) \sim \frac{1}{r^\theta}\,, \qquad C_4(\vec{x}, \vec{x}+\vec{r}; t_\mathrm{w}) \sim \frac{1}{r^{\theta M(\vec{x},\vec{x}+\vec{r},t_\mathrm{w})}}\,. \tag{5.5}$$

Indeed, in order to characterize the difference, we have introduced in Eq. 5.5 the order-of-magnitude modulating factor $M(\vec{x}, \vec{y}; t_\mathrm{w})$. The order-of-magnitude modulating factor will

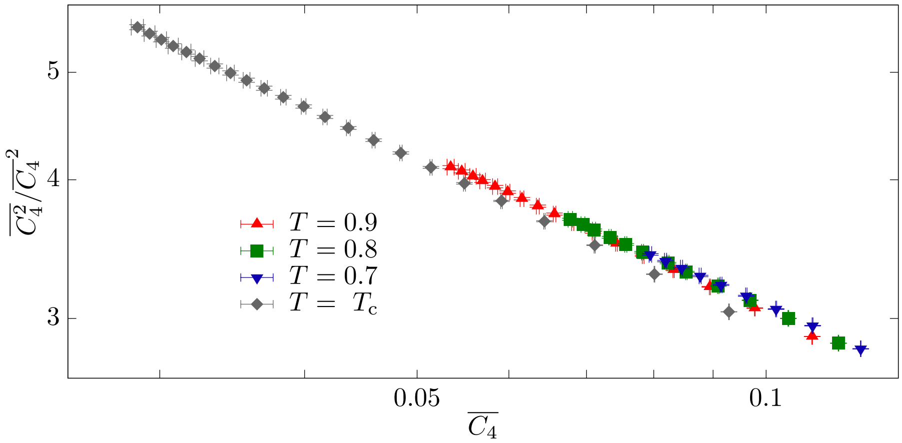

Figure 5.4: Ratio of the second moment of the four-body correlation function $\overline{C_4^2}$, computed at $r = \xi(t_w)$, to the square first moment $\overline{C_4}^2$, versus the first moment $\overline{C_4}$. Data computed for the EA and all the temperatures T considered. Error bars are smaller than the point size.

be computed as

$$M(\vec{x}, \vec{x} + \vec{r}, t_w) = \frac{\log |[C_4(\vec{x}, \vec{x} + \vec{r}; t_w)]_1|}{\log C_4^{\text{av}}(\sqrt{r_x^2 + r_y^2 + r_z^2})}, \tag{5.6}$$

where $[C_4(\vec{x}, \vec{x} + \vec{r}; t_w)]_1$ is the first moment estimator of $C_4(\vec{x}, \vec{x} + \vec{r}; t_w)$ computed with $N_R = 512$ independent replicas (see Sect. 5.5.1 for more details). $C_4^{\text{av}}(r)$ is interpolated to non-integer arguments using a fit obtained from data with integer r (see Sect. 5.5.5).

A picture of the physical situation is presented in Fig. 5.5. In particular, the results shown in Fig. 5.5 reveal that the order-of-magnitude factor $M(\vec{x}, \vec{y}; t_w)$ varies a lot (by a factor of 16 for the considered region), which indicates that there are sites pairs $(\vec{x}, \vec{x} + \vec{r})$ a lot more —or a lot less— correlated than the average. In fact, we can see in Fig. 5.6 that the median correlation function at distance $r = \xi(t_w)$ scales as $[C_4^{\text{av}}]^a$, with $a \approx 1.5$. This result implies that the *typical* correlation function is much smaller than the average value.

5.3 Quantifying the multifractal behavior

To quantify the fluctuations of the four-body correlation function, we consider the moments of the pdf of C_4 at distance $r = \xi(t_w)$. The q-th moment turns out to follow a scaling law

$$\overline{C_4^q} \sim \frac{A_q}{\xi^{\tau(q)}}. \tag{5.7}$$

Below are some details about our computation of $\tau(q)$. Fig. 5.2 [from which we obtain $\tau(1)$] and Fig. 5.3 confirm this behavior. Fig. 5.7 shows the $\tau(q)$ function, which clearly differs from the monofractal behavior $\tau^{\text{mono}}(q) = q\tau^{\text{mono}}(1)$. This departure from linear behavior justifies the use of the term *multifractal* to describe spin-glass dynamics (see, e.g. [HJK+86b]).

Notice that for large moments, the inset in Fig. 5.7 suggests that $\tau(q)$ grows as $\log q$. This logarithmic growth seems to originate in the behavior of the pdf $P(C_4)$ near $C_4 = 1$. In particular, our data is compatible with $P(C_4) \propto (1 - C_4)^{B(\xi)}$ for C_4 close to 1, with an

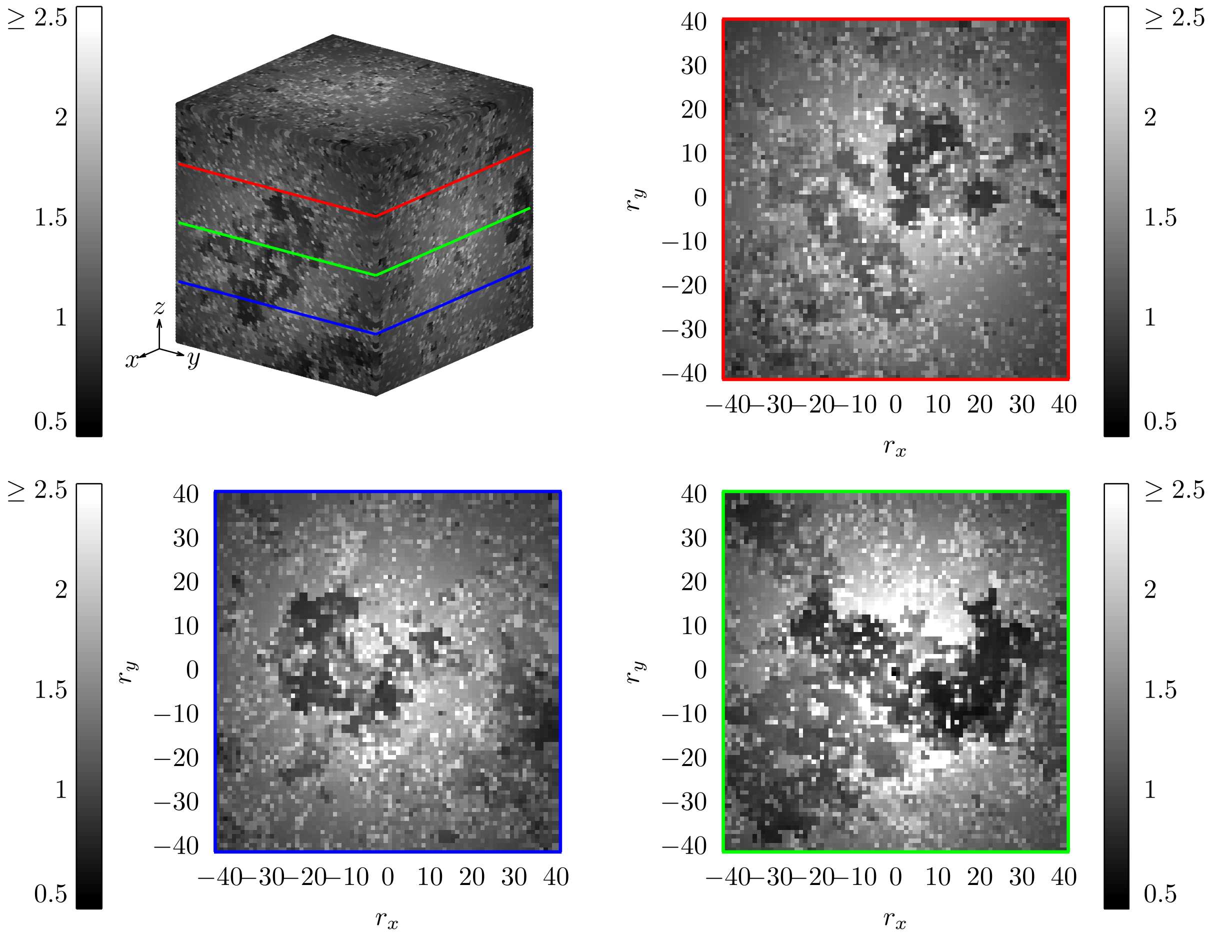

Figure 5.5: Grayscale representation of the order-of-magnitude modulating factor $M(\vec{x},\vec{y};t_\mathrm{w})$, see Eq. (5.6). Data computed for site $\vec{x}=(64,64,64)$ of a sample with coherence length $\xi(t_\mathrm{w})=20$, at $T=0.9$, with $N_\mathrm{R}=512$ estimators. We show results for displacement vector $\vec{r}=(r_x,r_y,r_z)$ in a cube $-40\le r_x,r_y,r_z\le 40$. The top-left panel depicts the three visible faces of the cube, while the other three panels show sections at $r_z=-20,0$ and 20, respectively. Our color code is darker the smaller $M(\vec{x},\vec{y};t_\mathrm{w})$ (hence, the more slowly correlation decay with distance). The color code is linear between the minimal value of $M(\vec{x},\vec{y};t_\mathrm{w})$ and 2.5. Displacements r with $M(\vec{x},\vec{y};t_\mathrm{w})>2.5$ are depicted as if $M(\vec{x},\vec{y};t_\mathrm{w})=2.5$. The maximum value of $M(\vec{x},\vec{y};t_\mathrm{w})$ for the considered data is ≈ 8.

exponement that grows as $B[\xi(t_\mathrm{w})]\sim\log\xi(t_\mathrm{w})$ (see Sect. 5.5.4 for more details). This result would explain the logarithmic growth of $\tau(q)$ shown in the inset of Fig. 5.7. However, to be on the safe side, we have tried two different functional forms to fit the data in Fig. 5.7:

$$\tau_1(q)=m1\frac{1+c_1q}{1+c_2q}\,,\qquad \tau_2(q)=mq\frac{1+d_1q\log q}{(1+d_2q)^2}\,. \tag{5.8}$$

Both expressions have the same derivative m at $q=0$. We take the value of m from the scaling of the *median* of the distribution function $P(C_4)$ with ξ (see Sect. 5.5 for details on the computation of m). The complete information of the goodness-of-fit shown in Table 5.2 illustrate the excellent job that both $\tau_1(q)$ and $\tau_2(q)$ make at fitting our data.

In Fig. 5.7 we also compare the functions $\tau(q)$ as obtained at $T=0.9$ and T_c temperatures. We see that the multiscaling behavior at T_c differs from its equivalent in the SG. This result is not surprising if we consider that the data for the critical temperature T_c in

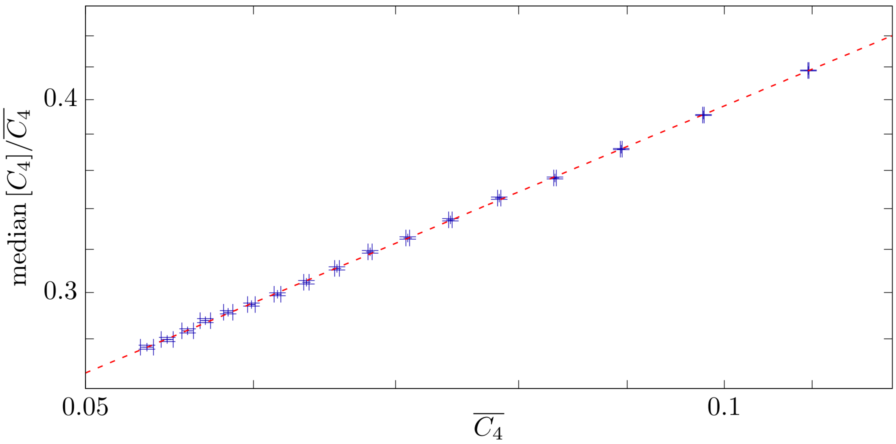

Figure 5.6: Median of the distribution function $P[C_4(r=\xi)]$ in units of the first moment, $\overline{C_4}(r=\xi)$, versus the first moment. Data computed for the EA at temperature $T=0.9$. We show data on a logarithmic scale. Therefore, the dashed line (a power-law fit with exponent ~ 0.5, see Table 5.2 for details) appears as a straight line. Error bars are smaller than the point size.

Fig. 5.4 do not collapse with the scaling curve followed by the data for $T<T_{\rm c}$.

Computation of $\tau(q)$

Comparing Figs. 5.3 and 5.4, the reader may notice that a fit of the form

$$\frac{\overline{C_4^q}}{\overline{C_4}^q}=\left[\frac{A_q}{\overline{C_4}}\right]^{\rho(q)} \tag{5.9}$$

can minimize corrections to scaling, see Fig. 5.4. From Eq. (5.7) one can obtain the relation

$$\tau(q)=\tau(1)[q-\rho(q)]\,. \tag{5.10}$$

Eq. (5.10) allows us to obtain good fits (see Table 5.2) discarding (at most) one data point corresponding to the smallest coherence length $\xi(t_{\rm w})$. Notice that we only need to consider the $\xi(t_{\rm w})$ dependence to obtain $\tau(1)$, as shown in Fig. 5.2.

We compute the errors by following the strategy of [Yll11], namely carrying out all fit separately for each jackknife block (when minimizing χ^2 to perform the fits, we only consider the diagonal elements of the covariance matrix). Errors in the fit parameter are obtained from the fluctuations of the jackknife blocks (see Appendix H for more details).

5.4 Conclusions: The large-deviation function

Following [HJK$^+$86b], we will now discuss our results in terms of a different stochastic variable, $\alpha=\log C_4[r=\xi(t_{\rm w})]/\log[1/\xi(t_{\rm w})]$, so that (we drop the argument in ξ for the sake of shortness)

$$C_4=\frac{1}{\xi^\alpha}\,,\quad P(C_4)\frac{{\rm d}C_4}{{\rm d}\alpha}\sim\xi^{f(\alpha)}\,. \tag{5.11}$$

Eq. (5.11) defines the large-deviation function $f(\alpha)$. Then, we can obtain the moments of C_4 in terms of α

$$\overline{C_4^q}=\int_0^1{\rm d}C_4P(C_4)C_4^q\sim\int{\rm d}\alpha e^{\log(\xi)[f(\alpha)-q\alpha]}\,. \tag{5.12}$$

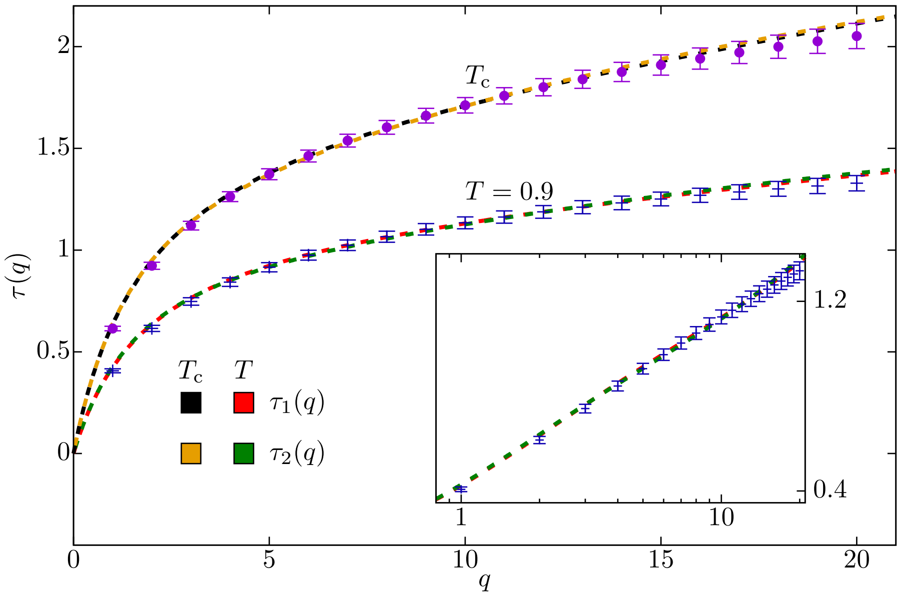

Figure 5.7: Scaling exponent $\tau(q)$ for the q-th moment $\overline{C_4(r = \xi(t_{\rm w})^q} \sim \xi^{-\tau(q)}$. Data computed for the EA at temperature $T = 0.9$ and $T_{\rm c}$. Dashed lines are fitted to the functional forms in Eq. (5.8) (the goodness-of-fit statistics are presented in Table 5.2). **Inset**: same data for $T = 0.9$ in semi-logarithmic scale.

Notice that for large coherence lengths ξ, the above integral is dominated by the maximum of $|f(\alpha) - q\alpha|$ at some value $\alpha = \alpha^*$:

$$\overline{C_4^q} \sim \frac{1}{\xi^{-[f(\alpha^*)-q\alpha^*]}} \,. \tag{5.13}$$

If we compare Eqs. (5.7) and (5.13), we realize that the large-deviation function $f(\alpha)$ is just (minus) the Legendre transformation of the singularity spectrum $\tau(q)$:

$$f(\alpha) = -\max_q \left[\tau(q) - q\alpha\right] \,. \tag{5.14}$$

The Legendre transformation $f(\alpha)$ is shown in Fig. 5.8 as computed from our fitting ansätze $\tau_1(q)$ and $\tau_2(q)$ in Eq. (5.9). In the range of Fig. 5.8 —recall that $\alpha(q) = \tau'(q)$— the results from our ansaätze are indistinguishable. However, the two differ in that, for $\tau_2(q)$, the range of α goes all the way down to $\alpha = 0$ (because $\alpha_2(q) = \mathrm{d}\tau_2/\mathrm{d}q \sim 1/q$). In fact, if $\tau(q)$ grows logarithmically for large q [as $\tau_2(q)$], then the large-deviation functions go logarithmically as well for $\alpha \to 0$, i.e. $f(\alpha \to 0) \sim \log \alpha$.

Let us summarize: the probability of finding a sites pair $(\vec{x}, \vec{x}+\vec{r})$ with $C_4(\vec{x}, \vec{x}+\vec{r})$ scaling as $1/r^\alpha$ for $r \sim \xi$ goes, in the scaling limit, as $\xi^{f(\alpha)}$, recall Eq. (5.11). This implies, see Fig. 5.5, that there are a lot more pair of sites displaying the median scaling exponent $\alpha \approx 0.65$ than there are for the average scaling $\alpha \approx 0.3$ [because $f(0.65) > f(0.3)$, recall Fig. 5.8]. This difference becomes more pronounced as $\xi(t_{\rm w})$ grows.

Thus, the expression ”silent majority” introduced by [BJBnC$^+$14b] perfectly describes the spin-glass dynamics: the central limit theorem ensures that it is the (somewhat exceptional) average value the one that can be measured on the length scales larger than $\xi(t_{\rm w})$ (hence, in experiments). However, the experimental-scale dynamic is not completely

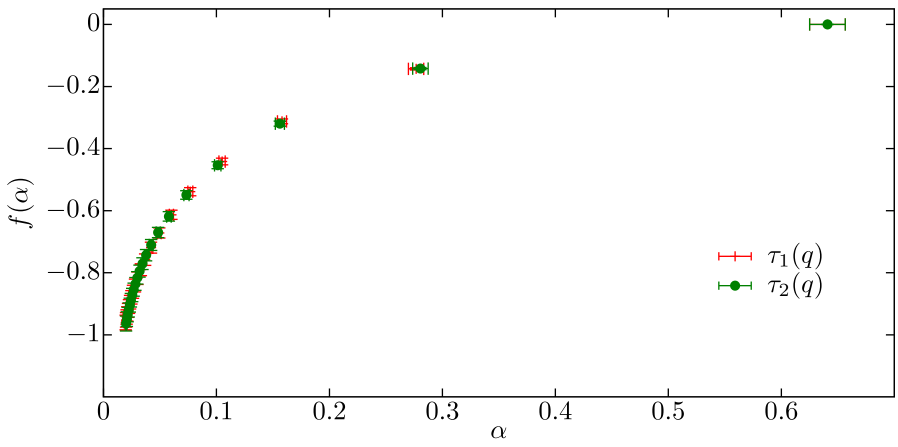

Figure 5.8: Legendre transformation $f(\alpha)$ of function $\tau(q)$, see Eq. (5.14), as a function of $\alpha = \mathrm{d}\tau/\mathrm{d}q$. Data computed from the fitting ansätze in Eq. (5.9) for EA at temperature $T = 0.9$. Errors in both axes have been obtained following the strategy of [Yll11].

blind to these short-scale fluctuations. In fact, the previously mentioned temperature chaos [BJCC+21]— and, hence, rejuvenation [BJCC+23], which is experimentally observable (see, e.g. [JVH+98])— is ruled by statistical fluctuations at the scale of r smaller than, or similar to, $\xi(t_{\mathrm{w}})$. A new set of experiments are planned at the University of Texas-Austin that could measure C_4 at $r < \xi(t_{\mathrm{w}}$.

5.5 On the study of $C_4(\vec{x},\vec{y},t_{\mathrm{w}})$ statistics

As discussed at the beginning of this chapter, this section provides technical details about the study of the pdf of $C_4(\vec{x},\vec{y},t_{\mathrm{w}})$. We have decided to include this information here (instead of as an appendix) because it is relevant only to this chapter.

Due to the complexity of the discussion of the correlation function, we have divided this section into the main problems we have found in conducting this study. Therefore, Sect. 5.5.1 discusses the problem of obtaining unbiased estimators of the powers of $C_4(\vec{x},\vec{y},t_{\mathrm{w}})$. Next, in Sect 5.5.2, we analyze the distribution function of $C_4(\vec{x},\vec{y},t_{\mathrm{w}})$, from which we will obtain the estimators of the distribution moments [cf. Eq. (5.7)]. Sect. 5.5.3 then discusses the estimation of the mean from the distribution function, while Sect. 5.5.4 focuses on the behavior of the distribution in the limit of $C_4 = 1$. Finally, Sect. 5.5.5 provides an explanation of how we have interpolated $C_4^{\mathrm{av}}(r;t_{\mathrm{w}})$ for real values of r, and Sect. 5.5.6 summarizes the results of all the fits.

5.5.1 Unbiased estimators of powers of $C_4(\vec{x},\vec{y},t_{\mathrm{w}})$

In order to compute the q-th moment of $C_4(\vec{x},\vec{y};t_{\mathrm{w}})$ we need an unbiased estimator of $C_4^q(\vec{x},\vec{y};t_{\mathrm{w}}) = \langle s_{\vec{x}}(t_{\mathrm{w}}) s_{\vec{y}}(t_{\mathrm{w}})\rangle^{2q}$, for a given sites pair $(\vec{x},\vec{y})$.

If we have (at least) $2q$ replicas at our disposal, we can obtain a poor estimator

$$[C_4(\vec{x},\vec{y};t_{\mathrm{w}})]_q^{\mathrm{poor}} = \prod_{a=1}^{2q} s_{\vec{x}}^{(a)}(t_{\mathrm{w}}) s_{\vec{y}}^{(a)}(t_{\mathrm{w}})\,. \tag{5.15}$$

Notice that $[C_4(\vec{x},\vec{y};t_\mathrm{w})]^\mathrm{poor}_q = (-1)^p$, where p is the number of replicas for which $c_a \equiv s^{(a)}_{\vec{x}}(t_\mathrm{w}) s^{(a)}_{\vec{y}}(t_\mathrm{w}) = -1$. The reader will notice that the statistical independence of the different replicas ensures the expectation value

$$\langle [C_4(\vec{x},\vec{y};t_\mathrm{w})]^\mathrm{poor}_q \rangle = \langle s_{\vec{x}}(t_\mathrm{w}) s_{\vec{y}}(t_\mathrm{w}) \rangle^{2q} \,.$$

Let us now use the $N_\mathrm{R} \gg 2q$ replicas at our disposal. Specifically, we can consider all the possible picks of $2q$ different replicas from the total N_R. In this situation, we use the probability $\tilde{P}(N_\mathrm{R}, M; S = 2q, p)$ of choosing p values $c_a = -1$, when one picks S replicas when there are M negative values in the set of N_R replicas (see next paragraph). Thus, we can compute an unbiased estimator of $\langle s_{\vec{x}}(t_\mathrm{w}) s_{\vec{y}}(t_\mathrm{w}) \rangle^{2q}$ as

$$[C_4(\vec{x},\vec{y};t_\mathrm{w})]_q \equiv G(N_\mathrm{R}, M, q) = \sum_{p=0}^{2q} (-1)^p \tilde{P}(N_\mathrm{R}, M; S = 2q, p) \,. \tag{5.16}$$

Now, the problem of estimating the powers of $C_4^q(\vec{x},\vec{y};t_\mathrm{w})$ translates to the problem of determining the probability $\tilde{P}(N_\mathrm{R}, M; S = 2q, p)$, which we will explain in the next section.

Computation of $\tilde{P}(N_\mathbf{R}, M; S, p)$

As it was just discussed at the beginning of Sect. 5.5.1, we need to consider the following problem: given a set of N_R different signs $c_a = \pm 1$, M of which negative, we need to obtain the probability $\tilde{P}(N_\mathrm{R}, M; S = 2q, p)$ of getting p negative signs when we pick S *distinct* signs. In order to organize the computation, we consider both the sign labels and the pick orderings as distinguishable. Hence, the number of possible picks is

$$N_\mathrm{picks} = \frac{N_\mathrm{R}!}{(N_\mathrm{R} - S)!} \,. \tag{5.17}$$

Let us denote by $K(N_\mathrm{R}, M; S, p)$ the number of picks of S distinct signs that contain exactly p negative signs. So that, we can compute the probability $\tilde{P}(N_\mathrm{R}, M; S, p)$ as

$$\tilde{P}(N_\mathrm{R}, M; S, p) = \frac{K(N_\mathrm{R}, M; S, p)}{N_\mathrm{picks}} \,. \tag{5.18}$$

$K(N_\mathrm{R}, M; S, p)$ can be obtained as a product of three factors

$$K(N_\mathrm{R}, M; S, p) = F_1 F_2 F_3 \,, \tag{5.19}$$

where the meaning of the different factors is as follows:

- F_1 is the number of ways that we can choose p tags of negative signs among M possibilities.
- F_2 is the number of ways in which a given set of p tags of negative signs can be extracted: the first tag can be obtained in the first selection, or the second, etc. So there are S possibilities for the first tag, which leaves us with $S-1$ options for the second tag, and so on.
- Finally, F_3 is concerned with the $S-p$ positive signs that we need to complete the pick of S signs. We have $N_\mathrm{R} - M$ choices for the first tag to be chosen, $N_\mathrm{R} - M - 1$ for the second tag, and so forth.

Therefore, by considering that whenever the factorial of a negative integer arises, it should interpreted as ∞ (hence the corresponding factor vanishes), we can calculate each factor as

$$F_1 = \frac{M!}{p!(M-p)!}\,, \quad F_2 = \frac{S!}{(S-p)!}\,, \quad F_3 = \frac{(N_\mathrm{R}-M)!}{(N_\mathrm{R}-M-S+p)!}\,. \tag{5.20}$$

However, to compute $\tilde{P}$, we have preferred to use a Pascal-Tartaglia-like relation. To obtain this relation, it is useful to consider a pick of S signs as two consecutive picks. We get $S-1$ signs from the first pick, and the last sign c_α is chosen only afterward:

$$K(N_\mathrm{R}, M; S, p) = \mathcal{A}\,K(N_\mathrm{R}, M; S-1, p-1) + \mathcal{B}\,K(N_\mathrm{R}, M; S-1, p), \tag{5.21}$$

where $\mathcal{A}$ is the number of negative signs available for the last pick (given that we obtained $p-1$ negative signs from the first pick), while $\mathcal{B}$ is the number of positive signs available for the last pick (given that we already obtained p negative signs from the first pick), specifically:

$$\mathcal{A} = \max\{0, M-p+1\}\,, \quad \mathcal{B} = \max\{\,0\,,\, N_\mathrm{R} - (S-1) \,-\, \max\{0, M-p\}\,\}\,. \tag{5.22}$$

The recursion relation for $K(N_\mathrm{R}, M; S, p)$ instantaneously translates to a recursion relation for the probability:

$$\tilde{P}(N_\mathrm{R}, M; S, p) = \frac{\mathcal{A}}{N_\mathrm{R}-S+1}\,\tilde{P}(N_\mathrm{R}, M; S-1, p-1) + \frac{\mathcal{B}}{N_\mathrm{R}-S+1}\,\tilde{P}(N_\mathrm{R}, M; S-1, p)\,. \tag{5.23}$$

Starting the recursion from

$$P(N_\mathrm{R}, M; S=1, p=0) = \frac{N_\mathrm{R}-M}{N_\mathrm{R}}\,, \quad P(N_\mathrm{R}, M; S=1, p=1) = \frac{M}{N_\mathrm{R}}\,, \tag{5.24}$$

we can accurately compute $P(N_\mathrm{R}, M; S, p)$ for whatever values of M, S, and p we need, respecting, of course, the obvious bounds:

$$N_\mathrm{R} \geq M, S, p\,, \quad M \geq p\,, \quad S \geq p\,. \tag{5.25}$$

5.5.2 The probability distribution function of the correlation function

As it was discussed in Sect. 5.3, we want to study the pdf for C_4 given $r = \xi(t_\mathrm{w}$. Let us call this pdf $\mathcal{P}[C_4]$. To study this pdf we have considered that there are three sources of stochastic $[C_4(\vec{x}, \vec{x}+\vec{r}; t_\mathrm{w})$ is not a stochastic variable]: (i) the sample, (ii) the site $\vec{x}$, and (iii) the displacement choice, $\vec{r} = (r, 0, 0)$, or $\vec{r} = (0, r, 0)$, or $\vec{r} = (0, 0, r)$

Given the pdf $\mathcal{P}[C_4]$, the q-th moment of C_4 is given by

$$\overline{C_4^q} = \int \mathrm{d}C_4 C_4^q \mathcal{P}[C_4]\,. \tag{5.26}$$

Unfortunately, we can only access the moments of $\mathcal{P}[C_4]$.

However, as we discussed in Sect. 5.5.1, $C_4^q(\vec{x}, \vec{x}+\vec{r}; t_\mathrm{w})$ is only exactly measurable in the limit $N_\mathrm{R} \to \infty$. Thus, we have to use the unbiased estimators of the q-th power of

$C_4(\vec{x},\vec{x}+\vec{y};t_{\mathrm{w}})$ from $N_{\mathrm{R}} \gg 2q$ replicas, recall Eq. (5.16), to estimate the q-th moment of $C_4(\vec{x},\vec{x}+\vec{r};t_{\mathrm{w}})$.

As the reader will remember, the value of the unbiased estimator $[C_4(\vec{x},\vec{y};t_{\mathrm{w}})]_q$ is a function $G(N_{\mathrm{R}},M,q)$ of the number M of negative signs in the set of N_{R} replicas. Thus, we can think that the Eq. (5.26) can be written (in terms of an accessible estimator from our simulation) as

$$\overline{C_4^q}(\xi) = \sum_{M=0}^{N_{\mathrm{R}}} \mathcal{P}(M;N_{\mathrm{R}},\xi) G(N_{\mathrm{R}},M,q)\,, \tag{5.27}$$

where $\mathcal{P}(M;N_{\mathrm{R}},\xi)$ is a pdf computed over the samples, starting point $\vec{x}$ and the choice of displacement $\vec{r}$, which represents the probability that exactly M of the N_{R} signs c_a turn out to be -1 in our simulation.

Therefore, most of the analyses considered in this chapter are based on the calculation of the pdf $\mathcal{P}(M;N_{\mathrm{R}},\xi)$ from the system configurations. To achieve this task, given the size of the system —160^3 sites $\vec{x}$—, and the large number of replicas, and samples, we have needed to use a multispin coding method (see Appendix D for a detailed explanation).

Symmetry of the probability distribution $\mathcal{P}(M;N_{\mathbf{R}},\xi)$

The reader will notice that the probability $\tilde{P}(N_{\mathrm{R}},M;S,p)$ is equivalent to the probability of choosing $S-p$ positive signs from the $N_{\mathrm{R}}-M$ that are available when picking S signs, but focusing on positive or negative signs is irrelevant, because of the bijection that transforms $\{c_a\}_{a=1}^{N_{\mathrm{R}}}$ into $\{-c_a\}_{a=1}^{N_{\mathrm{R}}}$. Then, the probability $\tilde{P}(N_{\mathrm{R}},M;S,p)$ satisfies the following relation

$$\tilde{P}(N_{\mathrm{R}},M;S,p) = \tilde{P}(N_{\mathrm{R}},N_{\mathrm{R}}-M;S,S-p)\,. \tag{5.28}$$

Both features, Eq. (5.28) and the bijection, implies that

$$G(N_{\mathrm{R}},M,q) = G(N_{\mathrm{R}},N_{\mathrm{R}}-M,q)\,. \tag{5.29}$$

For instance, for even N_{R}, we can conclude from Eq. (5.29) that the minimum value of $G(N_{\mathrm{R}},M,q=1)$ is reached at $M=N_{\mathrm{R}}/2$. Indeed,

$$G(N_{\mathrm{R}},M,q=1) = [(N_{\mathrm{R}}-2M)^2 - N_{\mathrm{R}}]/[N_{\mathrm{R}}(N_{\mathrm{R}}-1)]\,.$$

Therefore, it is preferable to use a symmetrized probability rather than $\tilde{P}(N_{\mathrm{R}},M;S,p)$ introduced in Sect. 5.5.2. Specifically,

$$\begin{aligned} \mathcal{P}_s\left(n=\frac{N_{\mathrm{R}}}{2};N_{\mathrm{R}},\xi\right) &= \mathcal{P}(n;N_{\mathrm{R}},\xi)\,, \\ \mathcal{P}_s\left(\frac{N_{\mathrm{R}}}{2} < n \le N_{\mathrm{R}};N_{\mathrm{R}},\xi\right) &= \mathcal{P}(n;N_{\mathrm{R}},\xi) + \mathcal{P}(N_{\mathrm{R}}-n;N_{\mathrm{R}},\xi)\,. \end{aligned} \tag{5.30}$$

Thus, the moments of C_4 can be computed as

$$\overline{C_4^q}(\xi) = \sum_{n=N_{\mathrm{R}}/2}^{N_{\mathrm{R}}} \mathcal{P}_s(n;N_{\mathrm{R}},\xi) G(N_{\mathrm{R}},n,q)\,. \tag{5.31}$$

In fact, as we explain in Sect. 5.5.3, this symmetrized probability has a special role in the computation of the median of $C_4(\vec{x},\vec{y},t_{\mathrm{w}})$.

5.5.3 Computation of the medians of $C_4(\vec{x},\vec{y},t_\mathbf{w})$

Lets start computing the cumulative distribution function of C_4 from the symmetric probability $\mathcal{P}_s(n;N_\mathrm{R},\xi)$

$$\mathcal{S}(n) = \sum_{\ell=N_\mathrm{R}/2}^{n} \mathcal{P}_s(\ell;N_\mathrm{R},\xi)\,. \tag{5.32}$$

In order to estimate the median, we need to determine the smallest integer $n^* \geq N_\mathrm{R}/2$ such that $\mathcal{S}(n^*) > 0.5$. After that, we linearly interpolate $\mathcal{S}(n)$ in n by assign positive weights ω_- and ω_+ to (n^*-1) and n^*, in such a way that

$$\omega_- + \omega_+ = 1 \quad \text{and} \quad \omega_-\mathcal{S}(n^*-1) \;+\; \omega_+\mathcal{S}(n^*) = 0.5\,. \tag{5.33}$$

This allows us to obtain a cumulative exactly equal to 0.5. However, the reader may notice that we need to convert the integer n^* into a real number, namely an estimator of the median of C_4. To do so, we need to consider the physical meaning of the fact that exactly M of the N_R signs $s_{\vec{x}}^{(a)}(t_\mathrm{w})s_{\vec{y}}^{(a)}(t_\mathrm{w})$ turn out to be -1 in our simulation of a specific sample:

$$\frac{1}{N_\mathrm{R}}\sum_{a=1}^{N_\mathrm{R}} s_{\vec{x}}^{(a)}(t_\mathrm{w})s_{\vec{y}}^{(a)}(t_\mathrm{w}) = \frac{N_\mathrm{R}-2M}{N_\mathrm{R}} = \langle s_{\vec{x}}(t_\mathrm{w})s_{\vec{y}}(t_\mathrm{w})\rangle + \eta\sqrt{\frac{1-C_4}{N_\mathrm{R}}}\,, \tag{5.34}$$

where $C_4 = \langle s_{\vec{x}}(t_\mathrm{w})s_{\vec{y}}(t_\mathrm{w})\rangle^2$ and η is a random variable that verifies

$$\langle\eta\rangle = 0\,,\quad \langle\eta^2\rangle = 1\,. \tag{5.35}$$

Notice that η is statistically uncorrelated with $\langle s_{\vec{x}}(t_\mathrm{w})s_{\vec{y}}(t_\mathrm{w})\rangle$. Furthermore, because of the central limit theorem, η tends to be a normally distributed stochastic variable in the limit of large N_R. Thus, we may consider the (very) biased estimator of C_4 [sgn(x) is the sign function]:

$$\begin{aligned}[s_{\vec{x}}(t_\mathrm{w})s_{\vec{y}}(t_\mathrm{w})]^2 &\equiv \left(\frac{N_\mathrm{R}-2M}{N_\mathrm{R}}\right)^2 \\ &= C_4 + 2\eta\,\mathrm{sgn}(\langle s_{\vec{x}}(t_\mathrm{w})s_{\vec{y}}(t_\mathrm{w})\rangle)\sqrt{\frac{C_4(1-C_4)}{N_\mathrm{R}}} + \eta^2\frac{(1-C4)}{N_\mathrm{R}}\,.\end{aligned} \tag{5.36}$$

We do not expect problems from the term linear in η. Indeed, as we said above, for N_R large enough, η approaches a normal variable (so, symmetrically distributed around zero); hence, it should not cause a significant bias on the estimation of the median. The real problem comes from the term proportional to η^2, which induces departure from the true value of C_4 of order $1/N_\mathrm{R}$. Hence, we may consider our first (very biased) estimator of the median

$$\mathrm{median}_\mathrm{vb}([s_{\vec{x}}(t_\mathrm{w})s_{\vec{y}}(t_\mathrm{w})]^2) = \omega_-\left(\frac{N_\mathrm{R}-2(n^*-1)}{N_\mathrm{R}}\right)^2 \;+\; \omega_+\left(\frac{N_\mathrm{R}-2n^*}{N_\mathrm{R}}\right)^2\,. \tag{5.37}$$

As explained above, we expect that this estimator of the median of C_4 will have a bias of order $1/N_\mathrm{R}$.

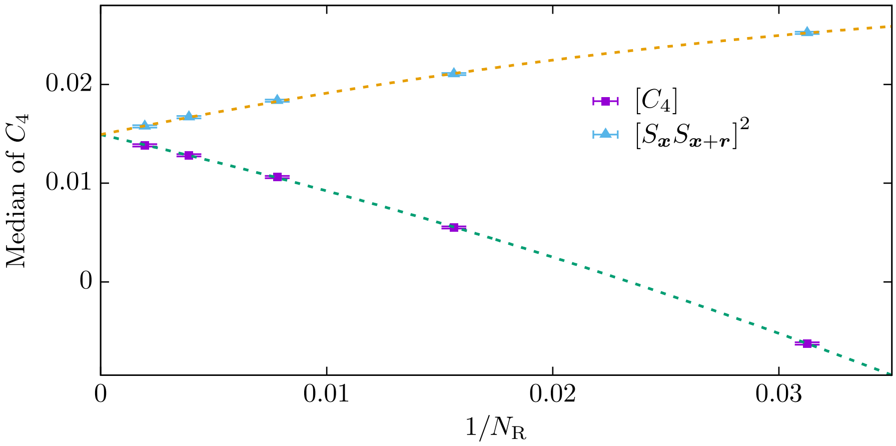

Figure 5.9: Biased estimators of the median, see (5.36) and (5.38), as functions of the inverse number of replicas, N_R, for $T = 0.9$ and $\xi(t_\mathrm{w}) = 20$. The dashed lines are fits quadratic functions to extrapolate to $N_\mathrm{R} \to \infty$ (complete fit statistics are available in Table 5.2).

Alternatively, we may consider an unbiased estimator of C_4:

$$\begin{aligned}[C_4] = G(N_\mathrm{R}, M, q = 1) &\equiv \frac{(N_\mathrm{R} - 2M)^2 - N_\mathrm{R}}{N_\mathrm{R}(N_\mathrm{R} - 1)} \\ &= C_4 + 2\eta\,\mathrm{sgn}(\langle s_{\vec{x}}(t_\mathrm{w}) s_{\vec{y}}(t_\mathrm{w})\rangle) \sqrt{\frac{N_\mathrm{R} C_4(1 - C_4)}{(N_\mathrm{R} - 1)^2}} + \frac{(\eta^2 - 1)}{N_\mathrm{R} - 1}\,.\end{aligned} \tag{5.38}$$

Notice that, although the expectation value of $\eta^2 - 1$ is zero, this term is not symmetrically distributed around zero (not even in the limit $N_\mathrm{R} \to \infty$, when η is normally distributed). Hence, the $\eta^2 - 1$ will also distort the computation of the median by a quantity of order $1/N_\mathrm{R}$. Accordingly, we expect corrections of order $1/N_\mathrm{R}$ for the corresponding estimator of the bias of the median of C_4

$$\mathrm{median}_\mathrm{B}([C_4]) = \omega_- G(N_\mathrm{R}, n^* - 1, q = 1) \; + \; \omega_+ G(N_\mathrm{R}, n^*, q = 1)\,. \tag{5.39}$$

The extrapolation to $N_\mathrm{R} \to \infty$ from both biased estimators is illustrated in Fig. 5.9. Notice that both extrapolations (very biased and biased) coincide in the $N_\mathrm{R} \to \infty$ limit.

In order to perform this extrapolation, we compute our biased estimators [recall Eqs. (5.37) and (5.39)] for a sequence $N'_\mathrm{R} = 32, 64, 128, 256$ and 512, see Fig. 5.9. The reader will notice that we need the $\mathcal{P}(M'; N'_\mathrm{R}, \xi)$ to perform these calculations. However, we can obtain these probabilities from their $N_\mathrm{R} = 512$ counterpart as [$\tilde{P}$ was defined in Eq. (5.18)]

$$\mathcal{P}(M'; N'_\mathrm{R}, \xi) = \sum_{M=0}^{N_\mathrm{R}} \mathcal{P}(M; N_\mathrm{R}, \xi)\, \tilde{P}(N_\mathrm{R}, M; S = N'_\mathrm{R}, p = M')\,. \tag{5.40}$$

To conclude this section, let us explain that, to estimate the slope m in Eq. (5.9) near $q = 0$, we perform a power law fit of our estimate of the median of C_4 as a function of the first moment of C_4, $\overline{C_4}$, see Fig. 5.10.

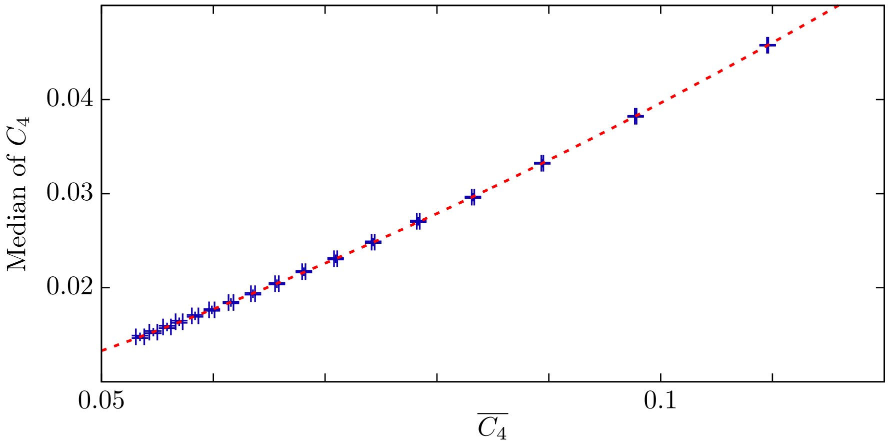

Figure 5.10: Median of the distribution $P[C_4(r=\xi)]$ versus the first moment, $\overline{C_4}(r=\xi)$, for $T=0.9$. The median is calculated through the extrapolation to $N_\mathrm{R}\to\infty$ shown in Fig. 5.9. The dashed line is fit to a power law to obtain the slope of $\tau(q)$ near $q=0$ (complete fit information available in Table 5.2).

5.5.4 Probability distribution near $C_4=1$

As we have shown in the inset of Fig. 5.7, the scaling exponent for the q-th moment $\tau(q)$, i.e., $\overline{C_4^q}\sim 1/[\xi(t_\mathrm{w})]^{\tau(q)}$, goes as $\tau(q)\sim\log q$ for large q. This is to be expected if the probability distribution function for C_4 near 1 behaves as

$$P(C_4\to 1)\propto(1-C_4)^{B(\xi)}\,, \tag{5.41}$$

with an exponent $B(\xi)$ that grows logarithmically with ξ. Indeed, a simple saddle-point estimation yields

$$\overline{C_4^q}=\int_0^1 \mathrm{d}C_4\,P(C_4)C_4^q\sim\int_0^1\mathrm{d}C_4\,\exp\left[B(\log(1-C_4)+q\log C_4\right]\approx\frac{1}{q^B}\,. \tag{5.42}$$

Thus, if $B(\xi)\sim A\log(\xi)$ (A is an amplitude)

$$\frac{1}{q^{A\log\xi}}=\frac{1}{\xi^{A\log q}}\,. \tag{5.43}$$

We have checked the behavior of the pdf $P(C_4\to 1)$ as computed from the $N_\mathrm{R}=512$ estimator in (5.38). We obtain a good fit to $(1-C_4)^{B(\xi)}$, but the determination of the exponent $B(\xi)$ is quite difficult, as it depends significantly on the fitting range. This is why we have turned to a different strategy. We have considered the following expectation value

$$\mathcal{I}(N_\mathrm{R})=\sum_{n=N_\mathrm{R}/2}^{N_\mathrm{R}}\mathcal{P}_s(n;N_\mathrm{R},\xi)\mathrm{e}^{-4(N_\mathrm{R}-n)}\,. \tag{5.44}$$

The above sum is clearly dominated by values of n near N_R where, recall (5.36), $C_4\approx 1-4(N_\mathrm{R}-n)/N_\mathrm{R}$. Hence, we can approximate

$$\mathcal{I}(N_\mathrm{R})\approx\int_0^1\mathrm{d}C_4\,P(C_4)\mathrm{e}^{-N_\mathrm{R}(1-C_4)}\sim\int_0^1\mathrm{d}C_4\,(1-C_4)^{B(\xi)}\mathrm{e}^{-N_\mathrm{R}(1-C_4)}\sim\frac{1}{N_\mathrm{R}^{1+B(\xi)}}\,. \tag{5.45}$$

Then, our chosen strategy has been to fit our data for $\mathcal{I}(N_\mathrm{R})$ as a power law in $1/N_\mathrm{R}$, see Fig. 5.11. Generally speaking, we obtain fair fits (although for $\xi < 10$, we had to discard the $N_\mathrm{R} = 32$ data from the fits). The resulting exponents $B(\xi)$ are shown in Fig. 5.12. As it can be checked, the hypothesis $B(\xi) \propto \log(\xi)$ is tenable, particularly for $\xi > 10$.

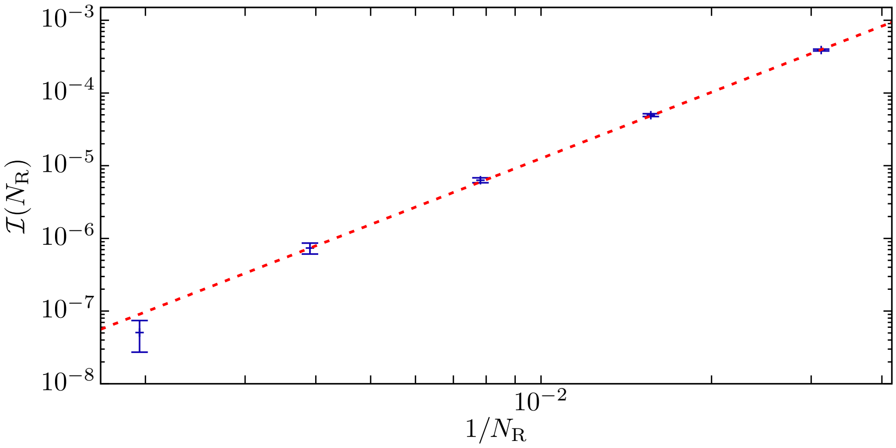

Figure 5.11: Expectation value $\mathcal{I}(N_\mathrm{R})$, see (5.44), versus the inverse of the number of replicas N_R, at $T = 0.9$ and $\xi(t_\mathrm{w}) = 20$. The dashed line is a fit to (5.45) with $N_\mathrm{R} \in [64, 512]$ (full details of the fit available in Table 5.2).

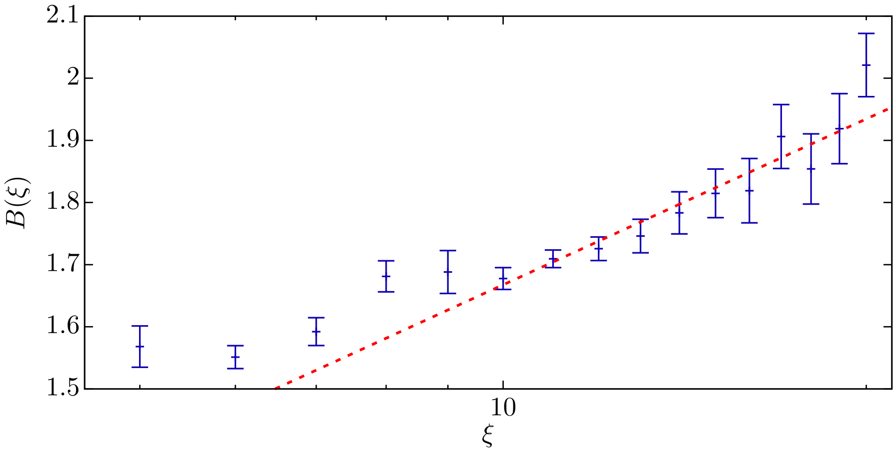

Figure 5.12: Exponent $B(\xi)$ for $T = 0.9$. The dashed line is a fit to $a + b\log(\xi)$ for $\xi \geq 10$ (see Table 5.2 for complete fit statistics). These results make more plausible a logarithmic behavior of $\tau(q)$ for large q.

5.5.5 Interpolation of $C_4^\mathrm{av}(r; t_\mathrm{w})$

Let us recall the interpolation of $C_4^\mathrm{av}(r; t_\mathrm{w})$ for non-integer values, needed to calculate the order-of-magnitude factor $M(\vec{x}, \vec{x} + \vec{r}; t_\mathrm{w})$ in Eq. (5.6). We consider *only* the interpolation for our data for the EA at $T = 0.9$ and t_w such that $\xi(t_\mathrm{w}) = 20$.

In order to interpolate our data obtained for integer r, we have performed a fit that should account for both the short- and long-distance behavior of the correlations:

$$C_4^\mathrm{av}(r, t_\mathrm{w}) = F_\mathrm{sd}(r) + F_\mathrm{ld}(r)\,, \quad F_\mathrm{sd}(r) = (b_0 + b_1 r + b_2 r^2)\mathrm{e}^{-(r/2.6)^4}\,, \quad F_\mathrm{ld}(r) = \frac{A}{r^\alpha}\mathrm{e}^{-(r/\xi_\mathrm{exp})^\beta}\,. \tag{5.46}$$

The functional form for $F_\mathrm{ld}(r)$ is well known and physically motivated [BCC+08b, BCF+09, BJCC+18]. However, $F_\mathrm{sd}(r)$ is a purely ad-hoc fitting function. The above functional form fits our integer-r data (within errors) for all $r \geq 1$. Of course, the fitting function can be evaluated whether the argument is integer or not. The fit's figure of merit is $\chi^2/\mathrm{dof} = 9.18/71$ (dof stands for 'degrees of freedom'), where we have considered only the diagonal part of the covariance matrix. This explains the small value of χ^2 that we obtained in the fit (the departure of the p-value from one is $\sim 10^{-18}$). To compute χ^2, we considered as well the first image at $L - r$ [FMMM+19], i.e., we compared the numerical data to $F_\mathrm{sd}(r) + F_\mathrm{sd}(L-r) + F_\mathrm{ld}(r) + F_\mathrm{ld}(L-r)$.

We conclude by giving the fit parameters (we report many digits for the sake of reproducibility). For the short-distance piece, we have:

$$b_0 = 0.0453360389027432\,, \quad b_1 = -0.0264096080489446\,, \quad b_2 = 0.00558776268187863\,. \tag{5.47}$$

The parameters of the long-term decay are:

$$\alpha = 0.45829\,, \quad \beta = 1.41217\,, \quad A = 0.551495\,, \quad \xi_\mathrm{exp} = 20.5207\,. \tag{5.48}$$

5.5.6 Summary information about fits in the chapter

As the reader will notice from the previous sections, the present chapter needed a large number of fits. This would be impossible without some automation, detailed in Appendix H. The complete statistical information on the fits of this chapter is summarized in Table 5.2.

As a check of the complete fitting process, Fig. 5.13 shows the evolution of the 10th and 20th moments of C_4 as a function of the coherence length with the corresponding fits to a power law (5.7). Both fits have performed with only the amplitude constant A_q as a fitting parameter. We take the respective value of $\tau(q)$ of our analysis. These fits, included in Table 5.2, confirm our analysis.

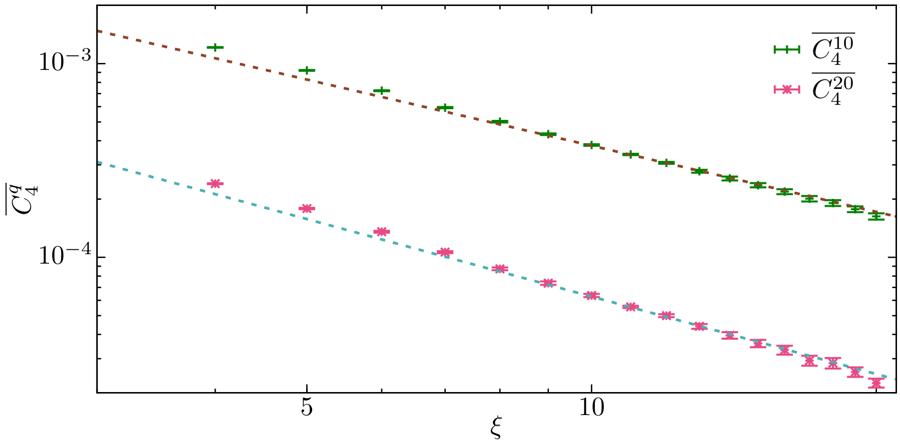

Figure 5.13: The 10th and 20th moments of c_4 as function of the coherence length ξ at $T = 0.9$ for EA. Dashed lines are fits to $a\xi^{-\tau(q)}$ where the only fitting parameter is the proportional constant a. The values of $\tau(10)$ and $\tau(20)$ are our final estimates presented in Fig. 5.7.

Identifier	Functional Form	Fitting Range	χ^2/dof	Parameters
$[C_4]$, Fig. 5.9	$f(x) = a + bx + cx^2$	$N_\mathrm{R} \in [32, 512]$	0.872768/2	$a = 0.01492(12),\ b = -0.52(2),\ c = -5.0(6)$
$[s_{\vec{x}}\vec{x} + \vec{r}]^2$, Fig. 5.9			0.946227/2	$a = 0.01492(12),\ b = 0.46(2),\ c = -4.3(6)$
$\mathcal{I}(N_\mathrm{R})$, Fig. 5.11	$f(x) = ax^{(b+1)}$		3.70448/3	$a = 14(2)$, $b = 2.02(4)$
$B(\xi)$, Fig. 5.12	$f(x) = a + b \log x$	$\xi \in [10, 20]$	5.95738/9	$a = 0.78(11)$, $b = 0.39(4)$
$\overline{C_4^{q=10}}$, Fig. 5.13	$f(x) = ax^{-\tau(q)}$		5.6406/10	$a = 0.00513(2)$
$\overline{C_4^{q=20}}$, Fig. 5.13			7.64613/10	$a = 0.001337(11)$
Median of C_4, Fig. 5.10	$f(x) = ax^b$	$\overline{C_4}(\xi \in [4, 20])$	1.86484/15	$a = 1.489(16)$, $b = 1.575(4)$
median$[C_4]/\overline{C_4}$, Fig. 5.6		$\overline{C_4}(\xi \in [4, 20])$	8.88094/15	$a = 1.488(7)$, $b = 0.575(2)$
$C_4^\mathrm{av}(r = \xi; T = 0.9)$, Fig. 5.2		$\xi \in [10, 20]$	1.99859/9	$a = 0.182(2)$, $b = -0.411(5)$
$\tau_1(q)$ for $T = 0.9$, Fig. 5.7	$f(x) = mx\frac{1+ax}{1+bx}$	$q \in [1, 20]$	5.01227/18	$a = 0.0129(18)$, $b = 0.547(12)$
$\tau_1(q)$ for $T = T_\mathrm{c}$, Fig. 5.7			5.37753/18	$a = 0.1718(17)$, $b = 0.574(10)$
$\tau_2(q)$ for $T = 0.9$, Fig. 5.7	$f(x) = mx\frac{1+ax}{(1+bx)^2}$		9.33556/18	$a = 0.039(2)$, $b = 0.232(5)$
$\tau_2(q)$ for $T = T_\mathrm{c}$, Fig. 5.7			8.23336/18	$a = 0.0446(2)$, $b = 0.242(4)$

Table 5.2: Summary of the statistical information of all the fits reported in this chapter. The fits have been done with Gnuplot. We have used this data to calibrate our analysis, which has been automated to estimate the errors following the strategy of [Yll11].

Part V

Quantum spin glasses

6

Quantum spin glasses in two dimensions

The Quantum Transition of the Two-Dimensional Ising Spin Glass: A Tale of Two Gaps

M. Bernaschi, I. González-Adalid Pemartín, V. Martín-Mayor, G. Parisi

Preprint: Arxiv

`https://doi.org/10.48550/arXiv.2310.07486`

Optimization problems, recall Sect. 1.1.3, appear in a variety of situations in everyday life. Consider, for example, choosing the best delivery route, designing the urban public transport layout, deciding assignments in a company budget, etc. In these problems, N agents (e.g., company departments) try to satisfy their goals, which are sometimes mutually contradictory. Under these circumstances, the different solutions for the problem cause some agents to be frustrated. The natural way to choose a solution is to consider a cost function that quantifies the *frustration* in the system. Our goal will be to minimize the cost function.

All the above features are well represented in spin glasses, which, as we have discussed in Sect. 1.1.3, fall in the NP-complete computational complexity class. Indeed, finding the minimal energy state —the ground state (GS)— of an Ising spin-glass Hamiltonian on a non-planar graph is the most familiar example of an NP-complete problem in physics [Bar82, Ist00]. NP-completeness explains the interest in these systems, evidenced by the up-surge of hardware specifically designed for minimizing a spin-glass Hamiltonian through a variety of algorithms and physical principles (see e.g [GTD19, MTM$^+$20, MF20, MMH$^+$16, BJBnC$^+$14c]).

In analogy to the use of out-of-equilibrium dynamics to accelerate the relaxation process presented in Part. II of this thesis, [KN98] presented a novel strategy that uses the quantum fluctuations to accelerate the exploration of the spin-glass configuration space. In this way, they hope to find the GS on an Ising spin glass. This strategy, the so-called Quantum Annealing, has been implemented in hardware [J$^+$11, MF20]. In particular, D-wave chips solve Ising spin glass in space dimension $D = 2$ (fortunately, problems with $D' > 2$ can be coded over D-wave's $D = 2$ graph [KRL$^+$23]; see [Bax08] for more on the definition of D).

These devices use a transverse field Γ to control the quantum fluctuations; see Eq. (6.1) below. Specifically, for $\Gamma = \infty$, the GS has all spins as much aligned with the transverse field as Quantum Mechanics allows them to be [paradoxically enough, from the point of view of the computational basis that diagonalizes the $\sigma^Z_{\vec{x}}$ matrices —c.f. Eq. (6.1), this GS seems a random statistical mixture]. Diminishing the transverse field at zero temperature adiabatically, the GS varies. Finally, at $\Gamma = 0$, the system, which has remained in the GS throughout the process, encodes the solution of the optimization problem (the GS of the considered sample). However, at some point along the annealing process, Γ goes through a critical point at Γ_c (see Fig. 6.1). This critical point separates the disordered GS from the spin-glass GS that does show a glassy order in the computational basis. As we explain below, the phase transition poses an obstacle to the annealing.

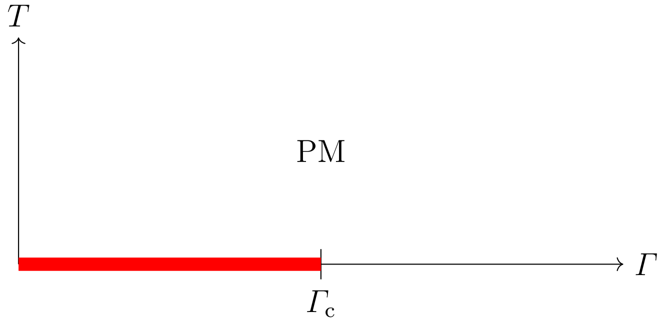

Figure 6.1: Phase diagram for a 2-dimensional Ising SG in terms of the temperature T and the transverse field Γ. For $T > 0$, the system is disordered when it is studied at large lengthscales, i.e., it is in the paramagnetic phase (PM). At $T = 0$, for $\Gamma > \Gamma_c$, the GS seems disordered (from the point of view of the computational basis). In contrast, for $\Gamma < \Gamma_c$ there is a spin-glass phase (SG) —different for every disorder realization [see Eq. (6.1)].

Although all of this may seem very far-fetched (due to hardware difficulties), recent experiments conducted on a D-Wave chip [KRL+23] have shown that 5,000 qubits (a qubit is the equivalent of our spins; we shall coin the term *qspin* to refer to quantum spins) exhibit coherent quantum dynamics for a few nanoseconds as Γ cross the critical point. This highlights the importance of having a solid theory of the phase transition at Γ_c.

The usual and most powerful framework to study analytically phase transitions is the Renormalization Group (RG). In particular, the RG helps to identify which properties of the critical point are universal, meaning that they are the same regardless of the specific microscopic details of the system. Only very broad features, such as symmetries, matter (making it possible to classify problems into universality classes). In fact, the study of disordered systems was among the first applications of the RG (see, e.g., Refs. [GL76, Par79a, PS79]), a strategy that is now well-established in $D = 2$ [Car96]. Nevertheless, it has taken a lot of work to show that the RG —and the accompanying universality— applies to disordered systems in $D > 2$ as well [BFMM+98, HPV08, FMM13, FMMPS16, FMMP+19] (even in $D = 2$ this was a challenging endeavor for spin glasses [FMMM+16]). Furthermore, as we discussed in Chapter 4, due to the complexity of the theory, there is still controversy over how to use the RG to make predictions for a system in dimension $D < 6$.

When we consider the scenario of the quantum transition in SG, the situation is even more complicated. In fact, only the case of $D = 1$ is well understood [MW68, MW69, McC69, Fis92]. In the case of SG in two dimensions, the problem becomes more complex. Contrarily, predictions are obtained using different approaches. In addition, these results affect the physical quantity that ultimately determines whether the computational complexity of the quantum problem is greater or less than its classical counterpart. Specifically, we are referring to the energy gap Δ that separates the GS from the first excited state of the system.

The relevance of this energy gap for the quantum annealing comes from its relation with the annealing time (the time required to remove the external field). In particular, this time is proportional to $1/\Delta^2$ [AL18]. In a spin glass with $N \propto L^2$ qspins at $\Gamma = \Gamma_c$ (L is the linear size of the system), $\Delta \propto L^{-z}$ (z is the so called dynamic critical exponent, see e.g. [Car12]).

Unfortunately, the determination of the dynamical exponent z is controversial. On the one hand, Monte Carlo (MC) simulations [RY94, GBH94, RY96] and a series-expansion study [SY17] found finite values of z (e.g., $z \approx 1.5$ for $D = 2$ spin glasses [RY94]). This result coincides with the predicted one for the droplet model for the quantum spin-glass transition [TH95]. On the other hand, a real-space RG analysis concludes $z = \infty$ in space dimension $D = 2$ and 3 [MN13]. Recent Monte Carlo simulation claims as well $z = \infty$ in $D = 2$ [MFR16]. Notice that $z = \infty$ would probably imply that the annealing time to enter adiabatically the SG phase will scale superpolinomically with the system size L. Let us remark that an annealer should not only go through $\mathit{\Gamma}_\mathrm{c}$, but it also should reach $\mathit{\Gamma} = 0$.

Here, we intend to clarify the situation through large-scale simulations on GPUs using highly tuned custom codes (see Appendix D for details). It is essential that, as it will be seen in Sect. 6.4, we have made no assumptions about the value of z. Another crucial piece of our analysis is the spin-flip symmetry of the system, implemented by the parity operator P (see Sect. 6.1).

We have decided to organize this chapter as follows: in Sect. 6.1, we introduce the theoretical aspects necessary to formulate the quantum spin-glass transition problem correctly. Sect. 6.2 summarize the main information of our numerical approaches: exact diagonalization and Markov Chain Monte Carlo simulations. Next, we will define the observables used to analyze and characterize the system in Sect. 6.3. Focusing on the results obtained in Sect. 6.4 we analyze the ground state and study the critical point. In order to settle the discussion on the dynamical exponent z, in Sect. 6.5 we study the excited states of the energy spectrum. Finally, in Sect. 6.6 we summarize the main results obtained in this chapter.

6.1 Our framework

As it was anticipated in Chapter 1, SG are the paradigmatic statistical model to study quenched disorder [Par94]. Moreover, there is a subtle but important difference between the previously discussed classical Hamiltonian and the quantum problem considered here: instead of considering an external magnetic field oriented in the same direction as the spins [recall Eq. (1.4)], the quantum version of the SG considers a transverse external field $\mathit{\Gamma}$. Indeed, the Hamiltonian in Eq. (1.1) for $s = 1/2$ spins (or qspins) now takes the form

$$\hat{\mathcal{H}} = -\frac{1}{2}\sum_{\vec{x},\vec{y}} \left[J_{\vec{x},\vec{y}} \hat{\sigma}^Z_{\vec{x}} \hat{\sigma}^Z_{\vec{y}} \right] - \mathit{\Gamma} \sum_{\vec{x}} \hat{\sigma}^X_{\vec{x}} \,. \tag{6.1}$$

As it was considered in Chapters 4 and 5, $J_{\vec{x},\vec{y}}$ are the random couplings that define the problem instance under consideration. A problem instance is named a sample in experimental science (more details are given in Sect. 6.2). In particular, we consider only nearest-neighbor interactions on the square lattice. Let us recall the use of the Pauli matrices $\hat{\sigma}^Z_{\vec{x}}$ and $\hat{\sigma}^X_{\vec{x}}$, instead of our previously used notation ($s_{\vec{x}}$), to emphasize the quantum fluctuations introduced by the second term in Eq. (6.1). In addition, we use the notation $\hat{\cdot}$ as a reminder of the quantum nature of the Hamiltonian operator.

The remainder part of this section is divided as follows: Sect. 6.1.1 briefly examines the gauge and parity symmetries of the system. In Sect. 6.1.2 we give the main ideas of the Trotter-Suzuki approximation [Tro59, Suz76], which allows us to implement a classical equivalent to Eq. (6.1) [see Eq. (6.6); Appendix A]. Finally, Sect. 6.1.3 discusses the study of the physical observables in terms of the transfer matrix.

6.1.1 Parity and Gauge symmetries

The most relevant symmetries in the quantum spin glass are the gauge and parity symmetries. In particular, parity symmetry has an important role in studying the energy excitation spectrum study in Sect. 6.5.

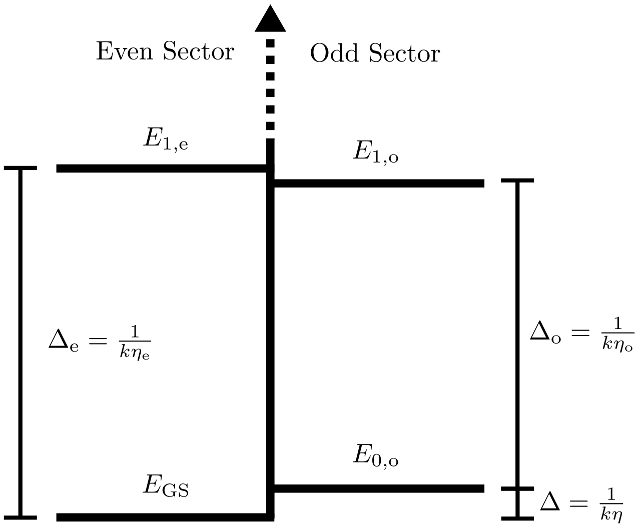

Figure 6.2: Schematic representation of the energy spectrum. The parity symmetry splits the spectra into even and odd sectors according to the parity of states. We shall name the even eigenvectors of the transfer matrix (6.10) as $|0_\mathrm{e}\rangle$, $|1_\mathrm{e}\rangle$, ..., with corresponding eigenvalues $\mathrm{e}^{-kE_\mathrm{GS}}$, and $\mathrm{e}^{-k(E_\mathrm{GS}+\Delta_{n,\mathrm{e}})}$ for $n = 1, 2, 3, \ldots$ [we use the shorthand $\Delta_\mathrm{e} = \Delta_{1,\mathrm{e}}$]. For the odd sector, we have $|0_\mathrm{o}\rangle$, $|1_\mathrm{o}\rangle$, ... with eigenvalues $\mathrm{e}^{-k(E_\mathrm{GS}+\Delta)}$, and $\mathrm{e}^{-k(E_\mathrm{GS}+\Delta+\Delta_{n,\mathrm{o}})}$ for $n = 1, 2, 3, \ldots$ [we use the shorthands $\Delta = E_{0,\mathrm{o}} - E_\mathrm{GS}$, and $\Delta_\mathrm{o} = \Delta_{1,\mathrm{o}}$]. Notice that expectation values at zero temperature, $T=0$, are determined solely by $|0_\mathrm{e}\rangle$. This energy level diagram is based on the numerical results in Fig. 6.4.

The parity operator

$$\hat{P} \equiv \prod_{\vec{x}} \hat{\sigma}^X_{\vec{x}}\,, \tag{6.2}$$

which implements a global spin-flip in the system

$$\hat{P}\hat{\sigma}^Z_{\vec{x}}\hat{P} = -\hat{\sigma}^Z_{\vec{x}} \quad \forall\vec{x}\,, \tag{6.3}$$

is a self-adjoint, unitary operator that commutes with the Hamiltonian (6.1). This symmetry splits the space of states V, with $\dim(V) = 2^{L^D}$, into two orthogonal subspaces, according to the parity eigenvalue, either $+1$ (even states) or -1 (odd states). Fig 6.2 represents an oversimplified but enlightening cartoon of the energy spectra. Let us consider a number n to identify the n-th lower energy level, i.e., greater n greater energy n. With this notation, the ground state is represented by $|0\rangle$, and the original space would be write as $V = \mathrm{lin}\{|n\rangle\}_{n=0}^{2^{L^D}-1}$. However, parity allows to write V as a direct sum of two orthogonal subspaces, i.e.

$$V_\mathrm{sp} = \mathrm{lin}\{|n_\mathrm{e}\rangle\}_{n_\mathrm{e}=0}^{R-1} \oplus \mathrm{lin}\{|n_\mathrm{o}\rangle\}_{n_\mathrm{o}=0}^{R-1}\,, \tag{6.4}$$

with $R = 2^{L^D-1}$, and where the sub-index refers to the parity of the state (we can use the same notation for the energy of the states, see Fig. 6.2). In the splitted representation, V_sp, the GS (which is an even state) is represented by $|0_\mathrm{e}\rangle$.

Moreover, we can classify the operators as either *even* (i.e. $\hat{P}\hat{\mathcal{A}}\hat{P} = \hat{\mathcal{A}}$) or *odd* ($\hat{P}\hat{\mathcal{A}}\hat{P} = -\hat{\mathcal{A}}$). As the reader will notice, the matrix elements of even operators can be non-vanishing only if the two states have the same parity. The situation is the opposite for the odd operators, i.e., the parity of the two states differ for non-vanishing matrix elements.

The parity symmetry is just a particular case of gauge transformation. Let us arbitrarily choose $n_{\vec{x}} = 0$ or 1 for each site. The corresponding gauge operator

$$G_{\{n_{\vec{x}}\}} \equiv \prod_{\vec{x}} (\sigma^X_{\vec{x}})^{n_{\vec{x}}} \tag{6.5}$$

is self-adjoint and unitary. When we apply this transform to the Hamiltonian in Eq. (6.1), we obtain a Hamiltonian of the same type, but with modified couplings [Tou77]:

$$J_{\vec{x},\vec{y}} \longrightarrow J_{\vec{x},\vec{y}}(-1)^{n_{\vec{x}}+n_{\vec{y}}}\,.$$

The reader could complain about the fact that this is not a symmetry in the usual sense. However, the gauge symmetry naturally emerges when we consider the average over the disorder (the quenched average, recall 1.4). Indeed, the gauge-transformed coupling matrix has the same probability as the original one. Therefore, meaningful observables should be invariant under an arbitrary gauge transformation.

To obtain the parity operator from the gauge one, we must set $n_{\vec{x}} = 1$ for all sites, which does not modify the couplings $J_{\vec{x},\vec{y}}$ (hence, parity is a symmetry for a given sample —or problem instance— not just a symmetry induced by the disorder average).

6.1.2 The Trotter-Suzuki approximation

Following Refs. [Tro59, Suz76], it is possible to replace the original qspins on a $L \times L$ lattice by *classical* spins on a $L \times L \times L_\tau$ lattice $s_{\vec{x},\tau} = \pm 1$ (see Appendix A for a complete derivation). The Trotter-Suzuki approximation introduces L_τ copies of the system —along the so-called *Euclidean time* τ— which interact in a ferromagnetic way. Specifically, the resulting classical Hamiltonian takes the form

$$\mathcal{H}(\boldsymbol{S}) = -\sum_{\tau=0}^{L_\tau - 1} \left[\frac{1}{2} \sum_{\vec{x},\vec{y}} J_{\vec{x},\vec{y}} s_{\vec{x},\tau} s_{\vec{y},\tau} + \sum_{\vec{x}} s_{\vec{x},\tau} s_{\vec{x},\tau+1} \right], \tag{6.6}$$

where $\boldsymbol{S}$ as a shorthand for the configuration of the $L^D L_\tau$ spins in the system (here, $D = 2$). We will refer as $\boldsymbol{S}_\tau$ to the configuration of the L^D spins at Euclidean time τ. For the new classical system, the probability of a spin configuration $\boldsymbol{S}$ turns out to be

$$p(\boldsymbol{S}) = \frac{\mathrm{e}^{-k\mathcal{H}(\boldsymbol{S})}}{Z}, \tag{6.7}$$

in terms of the partition function of the system

$$Z = \sum_{\{\boldsymbol{S}\}} \mathrm{e}^{-k\mathcal{H}(\boldsymbol{S})}. \tag{6.8}$$

As the reader will notice, the external field that drives the transition in the quantum system is replaced by the new parameter k. The exact relation between both parameters (the derivation can be found in Appendix A) has the form

$$\Gamma = \frac{-1}{2k} \log \tanh k, \tag{6.9}$$

which implies that k grows as Γ decreases. Even though the Trotter-Suzuki approximation assumed periodic boundary conditions (PBC) along the Euclidean time, in Sects. 6.4 and 6.5 we shall find it useful to consider as well anti-periodic boundary conditions (APBC) *only* along the τ direction.

Recall that, in this classical formulation, the energy gap Δ translates into a correlation length $\eta = 1/(k\Delta)$ along the Euclidean time. In addition, as it is explained in Appendix A, the limit $T \to 0$ (of interest for studying the GS — see Sect. 6.4) transforms into the limit $L_\tau \to \infty$.

6.1.3 The transfer matrix

As in Chapter 2, the transfer matrix method provides a powerful tool for studying the behavior of the physical observables. In addition, it makes the connection between the original quantum problem defined in Eq. (6.1) and the classical one in Eq. (6.6) [Kog79, Par88]. Appendix A discusses this connection in more detail.

For the sake of clarity, let us define

$$\hat{\mathcal{H}}_0 = -\frac{1}{2}\sum_{\vec{x},\vec{y}} J_{\vec{x},\vec{y}}\hat{\sigma}^Z_{\vec{x}}\hat{\sigma}^Z_{\vec{y}} \quad \text{and} \quad \hat{\mathcal{H}}_1 = -\mathit{\Gamma}\sum_{\vec{x}} \hat{\sigma}^X_{\vec{x}}\,.$$

The original transfer matrix takes the form

$$\tilde{\mathcal{T}} = \mathrm{e}^{-k(\hat{\mathcal{H}}_0+\hat{\mathcal{H}}_1)}\,. \tag{6.10}$$

Hence, the quantum thermal expectation value of an operator $\hat{\mathcal{A}}$ at temperature $T = 1/(kL_\tau)$ (see Apendix A for a discussion on the relation between the quantum-system temperature T and the Euclidean length L_τ in the classical system) is

$$\langle\langle\hat{\mathcal{A}}\rangle\rangle = \frac{\mathrm{Tr}\,\hat{\mathcal{A}}\,\tilde{\mathcal{T}}^{L_\tau}}{\mathrm{Tr}\,\tilde{\mathcal{T}}^{L_\tau}}\,. \tag{6.11}$$

Now, for an operator $\hat{\mathcal{A}}$ such that $\hat{\mathcal{A}} = A_{\mathrm{cl}}(\{\hat{\sigma}^Z_{\vec{x}}\})$, i.e. $\hat{\mathcal{A}}$ is an arbitrary function A_{cl} of the operators $\hat{\sigma}^Z_{\vec{x}}$, the Trotter-Suzuki approximation is equivalent to replacing the true transfer matrix in Eq. (6.11) by its proxy,

$$\mathcal{T} \equiv \mathrm{e}^{-\frac{k}{2}\hat{\mathcal{H}}_0}\mathrm{e}^{-k\hat{\mathcal{H}}_1}\mathrm{e}^{-\frac{k}{2}\,\hat{\mathcal{H}}_0} = \tilde{\mathcal{T}} + \mathcal{O}(k^3)\,, \tag{6.12}$$

with expected value

$$\langle\hat{\mathcal{A}}\rangle_{\mathrm{Q}} = \frac{\mathrm{Tr}_{\mathrm{Q}}\,\hat{\mathcal{A}}\,\mathcal{T}^{L_\tau}}{\mathrm{Tr}_{\mathrm{Q}}\,\mathcal{T}^{L_\tau}} \tag{6.13}$$

[the subscript Q, is an abuse of language that has been introduced to highlight the fact that the expected value and the trace in (6.13) are taken over the Hilbert space of 2^{L^D} states]. The most interesting feature in Eq. (6.13) is that averaging $A_{\mathrm{cl}}(\boldsymbol{S}_\tau)$ over configurations distributed according to (6.7) we can compute $\langle\hat{\mathcal{A}}\rangle$ as well. In addition, because the τ does not play any role in the expression, we may gain statistics by averaging over τ. In summary, the expected value in Eq. (6.13) can be obtained as

$$\langle\hat{\mathcal{A}}\rangle_{\mathrm{Q}} = \frac{1}{L_\tau}\sum_\tau \langle A_{\mathrm{cl}}(\boldsymbol{S}_\tau)\rangle\,, \tag{6.14}$$

where $\langle\cdots\rangle$ denotes the classical thermal average discussed in Sect. 1.4.

Coming back to Eq. (6.13), and using the spectral decomposition of the transfer matrix one obtains (for the sake of brevity we use the unsplit representation of the spectrum; for clarity sake, we only consider PBC)

$$\langle\hat{\mathcal{A}}\rangle_{\mathrm{Q}} = \frac{\langle 0|\hat{\mathcal{A}}|0\rangle + \sum_{n>0}\langle n|\hat{\mathcal{A}}|n\rangle \mathrm{e}^{-L_\tau/\eta_{n,0}}}{1 + \sum_{n>0}\mathrm{e}^{-L_\tau/\eta_{n,0}}} \tag{6.15}$$

Let us finalize this section by emphasizing that both $\mathcal{T}$ and $\tilde{\mathcal{T}}$ are self-adjoint, positive-define transfer matrices that commute with the parity operator (specifically, the two transfer matrices share the symmetries discussed in Sect. 6.1.1).

6.2 Our simulations

We studied a spin system on a square lattice of side L with PBC (as will be seen in Sect. 6.3.2, we also consider APBC along the Euclidean time). The coupling matrix $J_{\vec{x},\vec{y}}$ in Eq. 6.1 is nonzero only for nearest neighbors on the lattice, taking values J_0 and $-J_0$ with 50% probability. Our units of energy are such that $J_0 = 1$. Let us recall that the matrix $J_{\vec{x},\vec{y}}$ defines a problem instance (or sample).

To address the problem, we considered two approaches: exact diagonalization of the Trotter-Suzuki transfer matrix [recall Eq. (6.12)], whose results are detailed in Sect. 6.4.1, and Markov Chain MC simulations, which account for the majority of our results. In both cases, we use highly tuned custom codes for GPU. Appendices C, D and F contain detailed information on the algorithms and methods used for diagonalization and Monte Carlo simulations, respectively.

Let us remark that these customizations have allowed us to achieve sub-picosecond times per spin update, competitive with dedicated hardware [BJBnC$^+$14c]. Nevertheless, due to the sizes of the systems studied (see table) and the large number of samples analyzed (see below), this work would not have been possible without the two EuroHPC computing grants: specifically, we had access to the Meluxina-GPU cluster through grant EHPC-REG-2022R03-182 (158306.5 GPU computing hours) and to the Leonardo facility (CINECA) through a LEAP (*Leonardo Early Access Program*) grant.

6.2.1 Exact diagonalization

Despite the efficiency of our algorithms, due to the large size of the transfer matrix, $2^{L^D} \times 2^{L^D}$, we have limited the analysis by exact diagonalization to small systems. In particular, we have considered $L = 6$, obtaining the four lowest energy states $|0_\mathrm{e}\rangle$, $|0_\mathrm{o}\rangle$, $|1_\mathrm{e}\rangle$, and $|1_\mathrm{o}\rangle$, as well as their four eigenvalues $\mathrm{e}^{kE_{0,\mathrm{e}}}$, $\mathrm{e}^{kE_{1,\mathrm{e}}}$, $\mathrm{e}^{kE_{0,\mathrm{o}}}$, and $\mathrm{e}^{kE_{1,\mathrm{o}}}$, for 1280 samples at $k = 0.31$ and 0.305. In addition, for $k = 0.3$ and 0.295, we also analyzed a subset of 320 samples. The results obtained are presented in Sect. 6.4.1.

6.2.2 Monte Carlo

With regard to our MC simulations, we used a Parallel Tempering algorithm [HN96], implemented over a range of k values, to ensure equilibrium (see Appendix D and F for more details about the implemented algorithm). We analyzed a total of 1280 samples for each system size (see Table 6.1). As a rule, as applied to the disordered average, we have estimated errors using the bootstrap method [ET94]. Finally, we have simulated six real replicas of every sample (i.e., six statistically independent simulations of the system). This allows us to implement the equilibration tests based on the tempering dynamics [BFM$^+$18] and to calculate unbiased estimators of products of thermal averages [cf. Eq. (6.17)] and also the statistical errors for the time correlation functions [cf. Eq. (6.25)], as computed in a single sample (see Appendix H).

L	L_τ	k_{min}	k_{max}	N° of k	MC steps
8	2^9	0.265	0.305	16	4.5×10^7
12	2^9	0.265	0.305	24	10.5×10^7
16	2^{11}	0.265	0.295986	48	50.1×10^7
20	2^{11}	0.265	0.295986	56	67.8×10^7
24	2^{11}	0.265	0.292	60	78×10^7

Table 6.1: Simulation parameters for the different system sizes. The k ranges have been chosen to ensure the critical point k_{c} belonged to the range (see Sect. 6.4.3). The N° values of k, $k_{\mathrm{min}} \le k \le k_{\mathrm{max}}$, are uniformly distributed. We also provide the number of Metropolis sweeps performed (an elementary step consisting of 30 full-lattice Metropolis sweeps, followed by a Parallel Tempering attempt of exchanging the k value. Appendix D and F provided more details about the MC algorithm

6.3 Observables

In this chapter, we study two distinct problems. One is the behavior of the GS as k [hence Γ, recall (6.9)] crosses the critical point. The second problem regards the energy spectrum at the critical point. Therefore, we must consider two distinct strategies to carry out each of the analyses presented in Sects. 6.4 and 6.5, respectively. These strategies can be summarized by considering two types of physical observables: On the one hand, the study of the GS demands studying observables that are independent of Euclidean time and averaged over disorder. On the other hand, the energy spectrum is accessible by considering correlation functions along Euclidean time of several observables. Let us emphasize that, unlike the one-time observables used to study the GS, these correlation functions must be analyzed sample by sample.

6.3.1 Time-independent observables

Ref. [RY94] showed that the spin-glass susceptibility, named $\chi^{(n=2)}$ as we explain below, is barely divergent at the critical point. Therefore, we have had to consider other observables, namely the generalized susceptibilities and their corresponding correlation length, in order to find divergences that can help us study the critical point.

The basic building block for obtaining the different time-independent observables is the spin correlation, $\hat\sigma^Z_{\vec{x}}\hat\sigma^Z_{\vec{y}}$. In this way, we can construct the $L^D \times L^D$ correlation matrices M and $\tilde{M}$ [Yan62, SCM00] —$\vec{p}=(2\pi/L,0)$ or $(0,2\pi/L)$:

$$M_{\vec{x},\vec{y}} = \langle \hat\sigma^Z_{\vec{x}}\hat\sigma^Z_{\vec{y}}\rangle_{\mathrm{Q}}\,, \quad [\tilde{M}]_{\vec{x},\vec{y}} = M_{\vec{x},\vec{y}}\mathrm{e}^{\mathrm{i}\vec{p}\cdot(\vec{x}-\vec{y})}\,. \tag{6.16}$$

From these matrices, we can define the $2n$-body spin-glass susceptibilities at both zero and minimal momentum:

$$\chi^{(n)} = \frac{\overline{\mathrm{Tr}\big[M^n\big]}}{L^D}\,,\ F^{(n)} = \frac{1}{L^D}\overline{\mathrm{Tr}\big[\tilde{M}M^{n-1}\big]}\,. \tag{6.17}$$

Using $\chi^{(n)}$ and $F^{(n)}$, we can calculate the second-moment correlation length (see, e.g., Ref. [AMM05])

$$\xi^{(n)} = \frac{1}{2\sin(\pi/L)}\sqrt{\frac{\chi^{(n)}}{F^{(n)}} - 1}\,. \tag{6.18}$$

Notice that our $\chi^{(n=2)}$ and $\xi^{(n=2)}$ are just the standard quantities considered in the spin-glass literature [PC99, BCF+00].

Indeed, $\chi^{(n)}$ and $\xi^{(n)}$ are sensitive to the existence of the phase transition at Γ_c. In particular, as L grows, $\chi^{(n)}$ and $\xi^{(n)}$ remain of order 1 in the paramagnetic phase. Close enough to the critical point, in the critical region, they diverge as $\chi^{(n)} \sim L^{\gamma^{(n)}/\nu}$ and $\xi^{(n)} \sim L$. On the other hand, in the spin-glass phase, the susceptibility diverges as$\chi^{(n)} \sim L^{D(n-1)}$ and the correlation length as $\xi^{(n)} \sim L^{\alpha}$ (with some unknown exponent $\alpha > 1$).

Let us consider the critical scaling in more details. In the simplest approximation — see Ref. [CMMM02] for a more paused exposition— in the critical point and for large separations r between $\vec{x}$ and $\vec{y}$, $M_{\vec{x},\vec{y}} \sim v_{\vec{x}} v_{\vec{y}}/r^a$ with $v_{\vec{x}}, v_{\vec{y}} \sim 1$. Using this idea, we can obtain the scaling behavior for $\chi^{(n)}$

$$\begin{aligned}\chi^{(n)} &\approx \frac{1}{L^D}\int_0^L \mathrm{d}^D\vec{x}_1 \cdots \mathrm{d}^D\vec{x}_n \frac{1}{|\vec{x}_1 - \vec{x}_2|^a} \cdots \frac{1}{|\vec{x}_1 - \vec{x}_2|^a} \\ &= \frac{L^{nD}}{L^{D-na}}\int_0^1 \mathrm{d}^D\vec{u}_1 \cdots \mathrm{d}^D\vec{u}_n \frac{1}{|\vec{u}_1 - \vec{u}_2|^a} \cdots \frac{1}{|\vec{u}_1 - \vec{u}_2|^a}\,,\end{aligned} \tag{6.19}$$

where we introduce the n dimensionless variables $\vec{u}_i = \vec{x}_i/L$ for $i = 1, 2, \cdots, n$. Therefore, $\gamma^{(n)}/\nu = (n-1)D - na$ in this approximation. So, if $D > a$, $\gamma^{(n)}$ grows with n. Since $\chi^{(n=2)}$ barely diverges [RY94], we decided to focus our attention on $n = 3$, which presents a good compromise between statistical errors that grow with n, and a strong enough critical divergence.

Besides, we have computed the Binder cumulant

$$B = \frac{Q_4}{Q_2^2}\,,\; Q_4 = \sum_{\vec{x},\vec{y},\vec{z},\vec{u}} \overline{\langle \sigma^Z_{\vec{x}} \sigma^Z_{\vec{y}} \sigma^Z_{\vec{z}} \sigma^Z_{\vec{u}} \rangle^2_\mathrm{Q}}\,, \tag{6.20}$$

where $Q_2 = L^D \chi^{(n=2)}$. Notice that in the paramagnetic phase, because of the Gaussian nature of the fluctuations, B approaches three as L grows for fixed $k < k_\mathrm{c}$. On the other side of the transition, in the spin-glass phase, B reaches a different large-L limit for fixed $k \geq k_\mathrm{c}$ (for $k > k_\mathrm{c}$ various behaviors may arise depending on the degree of Replica Symmetry Breaking [MPV87]).

6.3.2 Euclidean time-correlation functions

As mentioned at the beginning of Sect. 6.3, in order to study the energy excitation spectra, we must consider observables that are Euclidean-time dependent, the so-called Euclidean time correlation functions. Let us consider (for simplicity) an operator $\hat{\mathcal{A}}$, which is a product of $\hat{\sigma}^Z$ operators at some spatial sites. The Euclidean correlation function for this observable $\hat{\mathcal{A}}$ can be computed as

$$C_{\hat{\mathcal{A}}}(\tau) = \frac{\mathrm{Tr}_\mathrm{Q}\, \hat{\mathcal{A}}\, \mathcal{T}^{\tau}\, \hat{\mathcal{A}}\, \mathcal{T}^{L_\tau - \tau}}{\mathrm{Tr}_\mathrm{Q}\, \mathcal{T}^{L_\tau}}\,. \tag{6.21}$$

As in the computation of expected values [recall Eq. (6.14)], $C_{\hat{\mathcal{A}}}(\tau)$ can be computed from our spin configurations distributed according to the classical weight (6.7) by averaging

$$C_{\hat{\mathcal{A}}}(\tau) = \frac{1}{L_\tau} \sum_{\tau_1=0}^{L_\tau-1} A_{\mathrm{cl}}(\boldsymbol{S}_{\tau_1}) A_{\mathrm{cl}}(\boldsymbol{S}_{\tau_1+\tau})\,. \tag{6.22}$$

In particular, in the present chapter we focus our attention on the Euclidean time correlation function of two operators, $\hat{\sigma}^Z_{\vec{x}}$ and the spin-spin interaction $\hat{\sigma}^Z_{\vec{x}}\hat{\sigma}^Z_{\vec{y}}$, which we average over the system:

$$C(\tau) = \frac{\sum_{\vec{x}} C_{\hat{\sigma}^Z_{\vec{x}}}(\tau)}{L_\tau^D}\,, \quad Q_2(\tau) = \frac{\sum_{\vec{x},\vec{y}} C_{\hat{\sigma}^Z_{\vec{x}}\hat{\sigma}^Z_{\vec{y}}}(\tau)}{L_\tau^{2D}}\,. \tag{6.23}$$

τ-dependence of the correlation functions

Let us go a step back and use the spectral decomposition of the transfer matrix (see [Kog79, Par88]; and also Appendix B for details) in Eq. (6.21) to obtain some general results about $C_{\mathcal{A}}(\tau)$ (for the sake of clarity, let us first disregard the parity symmetry and consider PBC).

Now, consider the base of energy states $\{|n\rangle\}$, which also are eigenvectors of $\mathcal{T}$ with eigenvalues e^{-kE_n} (recall that, in the unsplit representation V, E_n is the energy of the state $|n\rangle$, n is the ordinal that identifies the growing energy states, and we use $n=0$ for the GS; see Sect. 6.1.1 for details). The trace in the numerator of (6.21) is

$$\begin{aligned} Tr_{\mathrm{Q}}[\hat{\mathcal{A}}\mathcal{T}^{\tau}\hat{\mathcal{A}}\mathcal{T}^{L_\tau-\tau}] &= \sum_{n,m} \langle n|\hat{\mathcal{A}}\mathcal{T}^{\tau}|m\rangle\langle m|\hat{\mathcal{A}}\mathcal{T}^{L_\tau-\tau}|n\rangle \\ &= \sum_{n,m} |\langle n|\hat{\mathcal{A}}\,|m\rangle|^2 \mathrm{e}^{-kE_m\tau}\mathrm{e}^{-kE_n(L_\tau-\tau)} \\ &= \sum_{n} |A_{n,n}|^2 \mathrm{e}^{-kE_nL_\tau} \\ &+ \sum_{n<m} |A_{n,m}|^2 \mathrm{e}^{-kE_nL_\tau}\left[\mathrm{e}^{-k\Delta_{m,n}\tau} + \mathrm{e}^{-k\Delta_{m,n}(L_\tau-\tau)}\right]\,, \end{aligned} \tag{6.24}$$

where $A_{n,m} \equiv \langle n|\hat{\mathcal{A}}\,|m\rangle$, and $\Delta_{m,n} = E_m - E_n$. Let us define the Euclidean time correlation length $\eta_{m,n} = 1/(k\Delta_{m,n})$. By proceeding similarly for the denominator in Eq. (6.21) and taking out the common factor of the term associated with the ground state, one arrives at

$$\begin{aligned} C_{\hat{\mathcal{A}}}(\tau) =& \frac{|\langle 0|\hat{\mathcal{A}}|0\rangle|^2 + \sum\limits_{n>0} |A_{n,n}|^2 \mathrm{e}^{-L_\tau/\eta_{n,0}}}{1 + \sum\limits_{n>0} \mathrm{e}^{-L_\tau/\eta_{n,0}}} \\ &+ \frac{\sum\limits_{n<m} |A_{n,m}|^2 \mathrm{e}^{-L_\tau/\eta_{n,0}}\left[\mathrm{e}^{-\tau/\eta_{m,n}} + \mathrm{e}^{-(L_\tau-\tau)/\eta_{m,n}}\right]}{1 + \sum\limits_{n>0} \mathrm{e}^{-L_\tau/\eta_{n,0}}}\,. \end{aligned} \tag{6.25}$$

The presence of the parity symmetry allows to simplify (6.25). Specifically, for an even operator $\hat{\mathcal{A}}$ we find that $\langle n|\hat{\mathcal{A}}|m\rangle$ is zero if the parity of the states $|n\rangle$ and $|m\rangle$ differ (for odd operators $\langle n|\hat{\mathcal{A}}|m\rangle = 0$ if both states have the same parity). Therefore, for large L_τ, the largest correlation length to which $Q_2(\tau)$ is sensitive is the largest of η_{e} and η_{o} (see Fig. 6.2), while in the case of $C(\tau)$ the relevant correlation length is η (recall Fig. 6.2 for an explanation of the notation).

Moreover, for an even operator, every state $|n\rangle$ provides an additive contribution, given by the term $|A_{n,n}|^2 \mathrm{e}^{-L_\tau/\eta_{n,0}}$, to the τ-independent term in Eq.(6.25) (namely the plateau in Fig. 6.3). Because for odd operators $\langle n|\hat{\mathcal{A}}|n\rangle = 0$, $C_{\hat{\mathcal{A}}}(\tau)$ for odd operators lack a plateau.

Let us briefly explain how to take care of the APBC in the Euclidean time axis for even operators. In the case of considering a system with APBC, we would only need to add a parity operator P to the end of each of the traces in the Eq. (6.25) [also in Eq. (6.15)]. Taking into account that parity is a symmetry of the system, we need to add a factor p_n, which accounts for the parity of state $|n\rangle$ ($p_n = +1$ for even states, and $p_n = -1$ for odd states), to each term in the summations. In this way, for example, the denominator in Eq. (6.25) [also in Eq. (6.15)] would become

$$\mathrm{Tr}_{\mathrm{Q}}\, \mathcal{T}^{L_\tau} \hat{P} = \mathrm{e}^{-kL_\tau E_0} \left[1 + \sum_{n>0} p_n \mathrm{e}^{-L_\tau/\eta_{n,0}} \right] . \tag{6.26}$$

The zero temperature limit

As it was mentioned in Sect. 6.1.2 (Appendix A), the zero temperature limit in the Trotter-Suzuki approximation is equivalent to the $L_\tau \to \infty$ limit. Therefore, let us assume that L_τ is large enough to have $\mathrm{e}^{-L_\tau/\eta_\mathrm{e}}, \mathrm{e}^{-L_\tau/\eta_\mathrm{o}} \ll 1$ (see Fig. 6.2 for the notation). However, although we can neglect terms of the form $\mathrm{e}^{-L_\tau/\eta_{n,0}}$ for $n > 1$, we cannot assume that $\epsilon \equiv \mathrm{e}^{-L_\tau/\eta}$ is small (in fact, for some samples one could even have $\epsilon \approx 1$).

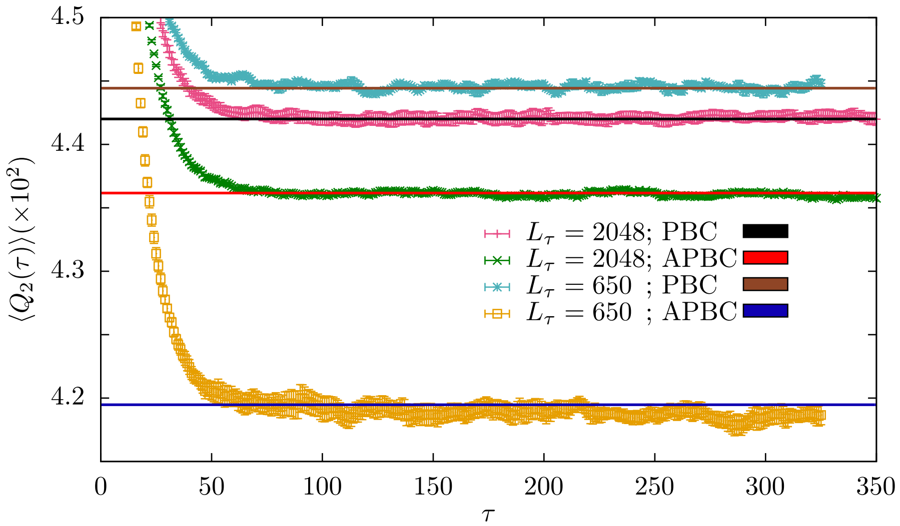

Figure 6.3: Even correlation functions $Q_2(\tau)$ defined in Eq. (6.23), as computed for a single sample of $L = 20$ at $k = 0.29 \approx k_\mathrm{c}$ (see Sect. 6.4.3). The corresponding Q_2 value calculated from $\mathrm{Tr}M^2/L^{2D}$ is represented by a complementary colored horizontal line.

Now, for and even operator $\hat{\mathcal{A}}$, and using the splited notation for the spectrum V_sp [see Eq. (6.4) and Fig. 6.2], we can define $\mathcal{A}_\mathrm{e} = \langle 0_\mathrm{e}|\hat{\mathcal{A}}|0_\mathrm{e}\rangle$ and $\mathcal{A}_\mathrm{o} = \langle 0_\mathrm{o}|\hat{\mathcal{A}}|0_\mathrm{o}\rangle$. Let us remark that $\mathcal{A}_\mathrm{e}$ is the expectation value at exactly $T = 0$ [taking the $L_\tau \to \infty$ in Eq. (6.15), it is straightforward to check this result]. With this notation, the plateau at $\tau \gg \eta_\mathrm{e}, \eta_\mathrm{o}$, see Fig. 6.3, is given by

$$C_{\hat{\mathcal{A}}}(\tau \gg \eta_\mathrm{e}, \eta_\mathrm{o}) = \mathcal{A}_\mathrm{e}^2 \; + \; [\mathcal{A}_\mathrm{o}^2 - \mathcal{A}_\mathrm{e}^2] \frac{\zeta\epsilon}{1 + \zeta\epsilon} , \tag{6.27}$$

where $\zeta = 1$ for PBC and $\zeta = -1$ for APBC.

Notice that the difference between the plateau $C_{\hat{\mathcal{A}}}(\tau \gg \eta_{\mathrm{e}}, \eta_{\mathrm{o}})$ and the value of $\langle \hat{\mathcal{A}} \rangle_{\mathrm{Q}}^2$ in this situation is

$$C_{\hat{\mathcal{A}}}(\tau \gg \eta_{\mathrm{e}}, \eta_{\mathrm{o}}) - \langle \hat{\mathcal{A}} \rangle_{\mathrm{Q}}^2 = \frac{\zeta\epsilon(\mathcal{A}_{\mathrm{e}} - \mathcal{A}_{\mathrm{o}})^2}{(1+\zeta\epsilon)^2}\,,$$

i.e. quadratic in $(\mathcal{A}_{\mathrm{e}} - \mathcal{A}_{\mathrm{o}})$ rather than linear as in Eq. (6.27). Indeed, in Fig. 6.3, for the largest systems with $L_\tau = 2048$, the plateau of the correlation function and the corresponding expected value are essentially indistinguishable (taking into account the measurement error).

Let us focus on the plateau of $Q_2(\tau)$ [recall Fig. 6.3 and Eq. (6.23)]

$$Q_2(\tau \gg \eta_{\mathrm{e}}, \eta_{\mathrm{o}}) = Q_{2,\mathrm{e}} + [Q_{2,\mathrm{o}} - Q_{2,\mathrm{e}}]\frac{\zeta\epsilon}{1+\zeta\epsilon}\,, \tag{6.28}$$

where $Q_{2,\mathrm{e}}$ and $Q_{2,\mathrm{o}}$ are, respectively, the average over all pairs $(\vec{x}, \vec{y})$ of $\mathcal{A}_{\mathrm{e}}^2$ and $\mathcal{A}_{\mathrm{o}}^2$. Two consequences can be drawn from Eqs (6.27) and (6.28):

1. The limit $T \to 0$ (or $L_\tau \to \infty$) is approached monotonically. Furthermore, the PBC results approach the limit from above, while the APBC from below. To confirm this, we have explicitly checked all our simulated samples, finding no cases where the APBC plateau is higher than the PBC plateau (it is intuitive to expect that the PBC system will be more ordered than the APBC system).

2. Since $Q_2(\tau)$ and $Q_{2,\mathrm{e}}$ are bounded between 0 and 1 also for the APBC, it is straightforward to conclude that $|Q_{2,\mathrm{o}} - Q_{2,\mathrm{e}}| < (1-\epsilon)/\epsilon$. Hence, the most difficult samples $\epsilon \approx 1$ present a tiny finite-temperature bias in the PBC estimator [indeed, compare the L_τ dependence of the PBC and the APBC plateaux in Fig. 6.3].

6.4 The phase transition in the ground state

In this section, we focus our attention on the study of the phase transition. To avoid polemics about the value of the dynamical exponent z, we have left aside the effects of the excitation spectrum, focusing on the GS. To do this, it has been necessary to ensure that the considered observables reach their zero-temperature limit (or, in the Trotter-Suzuki formulation, $L_\tau \to \infty$).

Even though our main results stem from Monte Carlo simulations, we have also performed a numerical diagonalization of the transfer matrix for small systems (see Appendix C for a detailed explanation of the algorithm). This diagonalization has been very useful, not only to tune our analysis but also for the information it affords about how the limit $T \to 0$ is approached (recall Sect. 6.3.2).

Therefore, in this section, we discuss the main results of the exact diagonalization in Sect. 6.4.1. With this information, in Sect. 6.4.2, we confirm that we achieve the $T \to 0$ limit in our MC simulation. Finally, the Sect. 6.4.3 provides our main results concerning the critical point.

6.4.1 Exact diagonalization

For small systems, $L \leq 6$, by exact diagonalization of the transfer matrix, we obtain the energy states of the Trotter deformed Hamiltonian (see Appendix B). This spectrum is divided into even energy levels ($E_{0,\mathrm{e}} < E_{1,\mathrm{e}} < \ldots$) and odd levels ($E_{0,\mathrm{o}} < E_{1,\mathrm{o}} < \ldots$) due to the parity symmetry (recall Sect.6.1.1).The GS is even and its energy is $E_{\mathrm{GS}} = E_{0,\mathrm{e}}$. Furthermore, the first excited state is odd with energy $E_{0,\mathrm{o}}$. In this way, the minimum gap Δ is given by $\Delta = E_{0,\mathrm{o}} - E_{0,\mathrm{e}}$. Our results, shown in Fig. 6.4-**Left**, display dramatic fluctuations among samples, up to the point that the statistical analysis should be conducted in terms of $\log \Delta$. Moreover, as we will discuss from our MC data in Sect. 6.5, the sample-to-sample distribution function of $\eta = 1/(k\Delta)$ is a Levi flight [i.e. for large η, the empirical distribution function decays as $F(\eta) = 1 - \frac{B}{\eta^b}$ with $b < 2$].

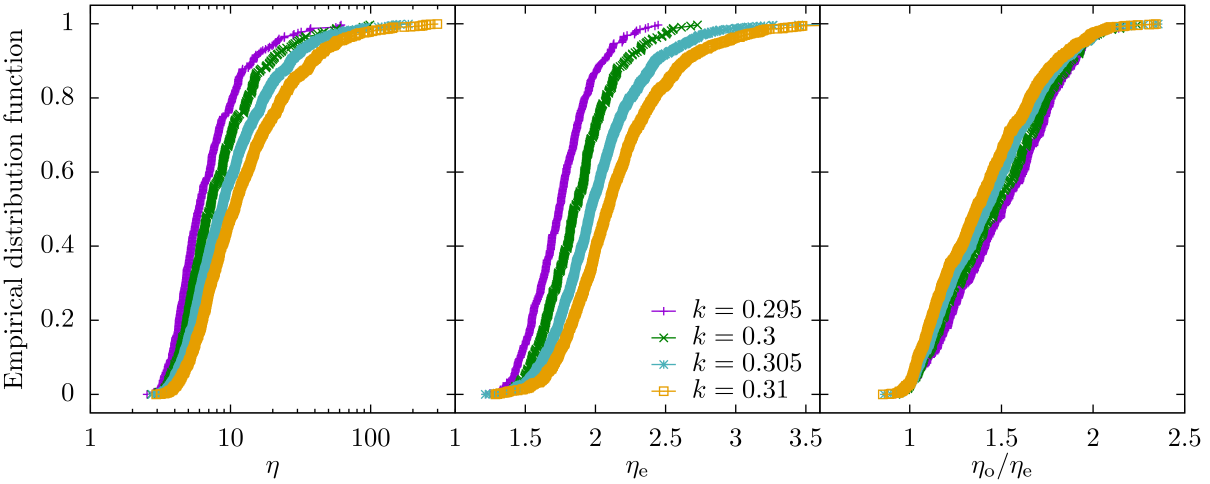

Figure 6.4: Empirical distribution function of the different Euclidean correlation lengths presented in the system, for different values of k. Data from the exact diagonalization of a $L = 6$ system. Data from $k = 0.295$, and $k = 0.3$ are calculated over 320 samples, instead of 1280.

Additionally, as it can be seen in Fig. 6.4, the value of η depends significantly on the value of k [and therefore on the external field (6.9)]. This implies that the exponent b also changes with k. Let us consider a sample at k_1 and k_2 ($k_1 < k_2$) to understand what happens. From the results of Fig. 6.5 we can conclude that (approximately) $\eta(k_2) = \alpha[\eta(k_1)]^{1+\beta}$, where α, β are constants (for fixed k_1 and k_2) and $\beta > 0$. This monotonic relation implies that *the same* sample occupies percentile F in the distribution for k_1 and k_2. Thus, the exponent b that characterize the Levy flight satisfy the relation $b(k_2) = b(k_1)/(1 + \beta)$. So, because $b(k_2) < b(k_1)$, the tail at large η becomes heavier as k increases (see Sect. 6.5 for an extended discussion).

The other main result in this section is related to the next excited states, $E_{1,\mathrm{e}}$ and $E_{1,\mathrm{o}}$. In particular, the study of the sample-to-sample fluctuations of the same parity gaps $\Delta_{\mathrm{e}} \equiv E_{1,\mathrm{e}} - E_{0,\mathrm{e}}$ and $\Delta_{\mathrm{o}} \equiv E_{1,\mathrm{o}} - E_{0,\mathrm{o}}$ show a behavior different from our findings for Δ. Specifically, the fluctuations for both Δ_{e} and Δ_{o} are moderate (see Fig. 6.4-**Center**). Furthermore, for all our samples, we found that η_{e} and η_{o} are of similar magnitude (see Fig. 6.4-**Rigth**) and $\Delta_{\mathrm{e}}, \Delta_{\mathrm{o}} \gg \Delta$, unless Δ turns out to be inordinately large.

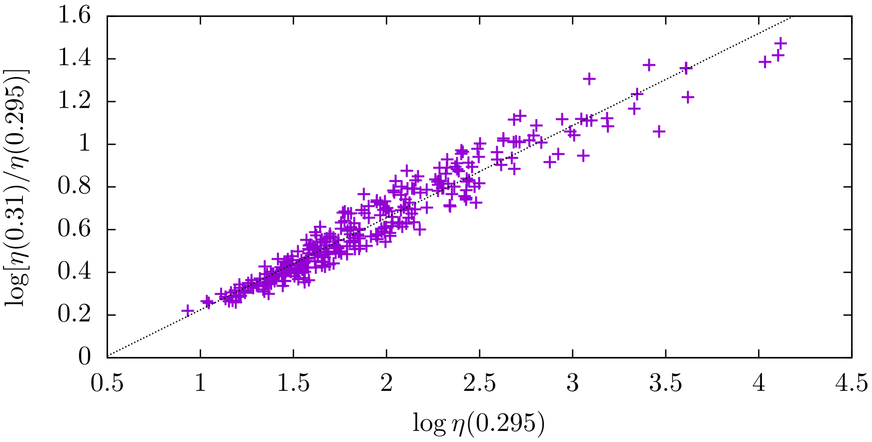

Figure 6.5: Dependence on k of the odd correlation length η. Logarithm of the ratio of $\eta(k=0.31)$ and $\eta(k=0.295)$ (as computed for the same $L=6$ samples through exact diagonalization). The results show an approximately linear relation with a positive slope. Data for the 320 samples we studied at $k=0.295$ and $k=0.31$.

6.4.2 Achieving zero temperature

As was mentioned in Sect. 6.1.2 and 6.3.2, the limit $T\to 0$ in the Trotter-Suzuki approximation is equivalent to the limit $L_\tau\to\infty$. Hence, the simplest way to approach the zero temperature limit would be to study a fixed set of samples for a sequence of growing Euclidean lengths L_τ (which is equivalent to the naive way to study the thermodynamic limit in other systems). When the results become L_τ independent, we achieve the $L_\tau\to\infty$ limit. Indeed, the $T>0$ effects are suppressed as $\mathrm{e}^{-L_\tau/\eta}$ [c.f Eq. (6.27)].

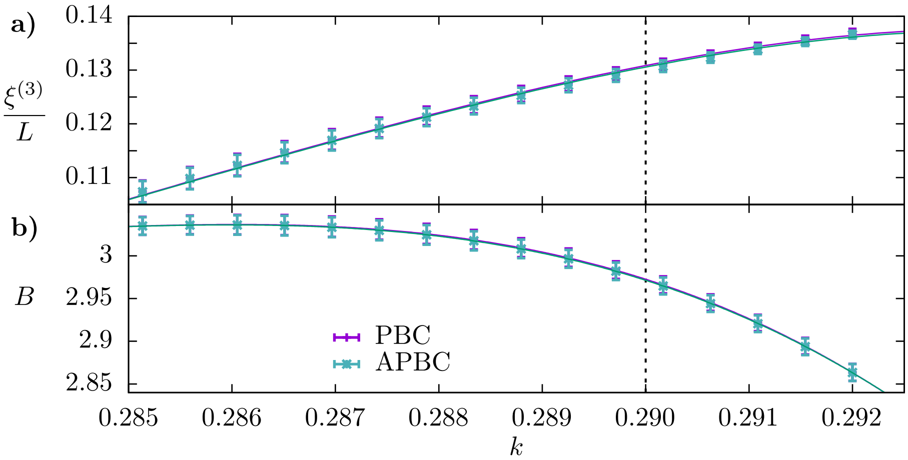

Figure 6.6: Ensuring that the zero temperature limit has been reached through the comparison of periodic and antiperiodic boundary conditions (PBC and APBC) along the Euclidean time. (a): correlation length $\xi^{(3)}$ [cf. Eq. (6.18)] vs. k, as computed for our largest systems $L=24$, $L_\tau=2048$ with both PBC and APBC for the *same* set of 1280 samples. The PBC/APBC statistical agreement indicates that the $T\to 0$ limit has been effectively reached for this quantity. **(b)**: as in panel **(a)** for the Binder cumulant [cf. Eq. (6.20)]. The dashed line represents our critical point estimation, $k_c\approx 0.29$ (see Sect. 6.4.3). Errors in both panels are one standard deviation.

Nevertheless, as it was shown in Fig. 6.4 (see Fig. 6.11 for larger-L data from MC simulations), some samples have an inordinately small gap, and hence a huge Euclidean correlation length η. So, there are instances with $\mathrm{e}^{-L_\tau/\eta}\approx 1$ for all the values of L_τ that we can simulate (recall that we want to have $\mathrm{e}^{-L_\tau/\eta} \ll 1$). This consideration makes the naive approach sketched above risky.

Fortunately, recall Sect. 6.3.2, using PBC and APBC along the Euclidean time, we can determine whether we have reached the zero-temperature limit. In particular, the PBC results monotonically approach their $L_\tau \to \infty$ limit from above, while the APBC converges to the same limit from below (see Fig. 6.3). In this way, the statistical compatibility of the results from both boundary conditions guarantees that we have reached the zero-temperature limit. For instance, Fig. 6.6 shows the specific case of the correlation length and the Binder ratio for our largest system $L = 24$ and $L_\tau = 2048$. The statistical results ensure we have achieved the zero-temperature limit in a wide range of k, allowing us to study the phase transition at $T = 0$.

6.4.3 The critical point

[RY94] showed that the spin-glass susceptibility $\chi^{(2)}$ is barely divergent at the critical point. In particular, in Sect. 6.3.1 we discussed that, in the GS, the standard spin-glass correlation function is affected by a very large anomalous dimension $\chi^{(2)} \propto L^{2-\eta}$ with large η. Nevertheless, the susceptibility $\chi^{(3)}$ [see Eq. (6.17)] presents a divergent behavior, as we discussed with the help of Eq. (6.18). Therefore, the corresponding correlation length $\xi^{(3)}$ is suitable for a standard Finite-Size scaling study of the phase transition [FF67, FB72, Bar83, Car12], which is illustrated in Fig 6.7. Under these conditions, we can apply the quotients method [Nig76, BFMMMS96, AMM05] to compute the critical exponents and the critical point.

In the scaling region, any magnitude behaves as

$$A(k \approx k_\mathrm{c}) \approx \xi^{x_A/\nu} F[\xi^{1/\nu}(k - k_\mathrm{c})]\,.$$

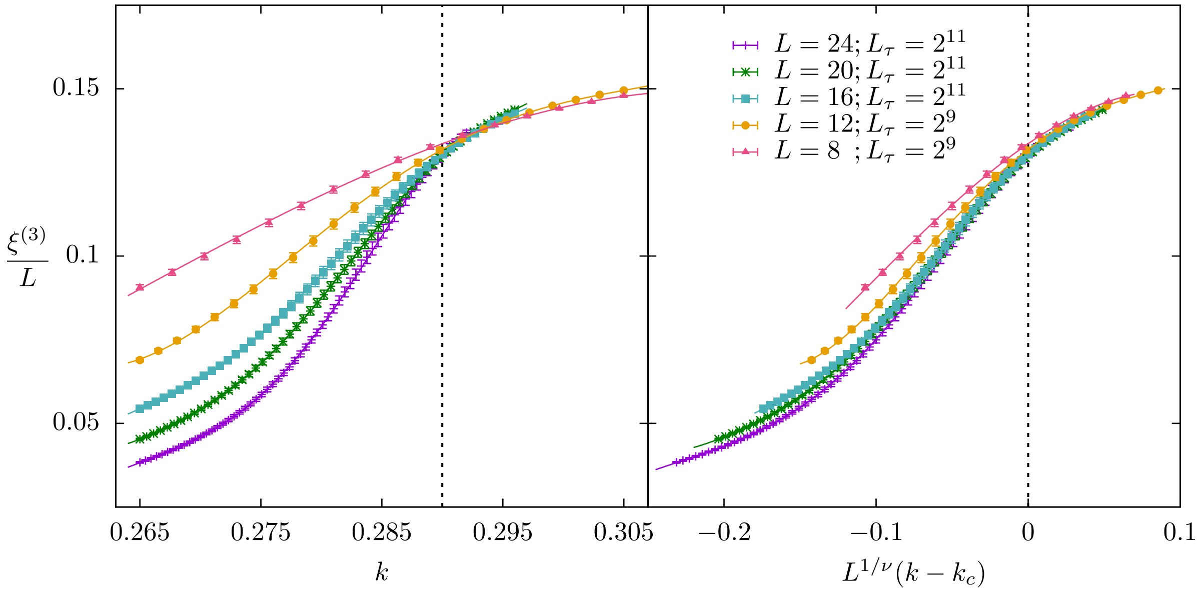

Figure 6.7: Illustrate our Finite-Size Scaling analysis (see, e.g., [AMM05, Nig76]) of the critical point at $T = 0$ and $\Gamma = \Gamma_\mathrm{c}$, in terms of the parameter k that represents Γ in the Trotter-Suzuki formulation [cf. Eq. (6.9)]. **Left:** correlation length $\xi^{(3)}$ in units of the lattice size L versus k. The curves for the different L's intersect at the critical point $k_\mathrm{c} \approx 0.29$ (see Sect. 6.4.3). **Right**: Data in **Left**, when represented as a function of the scaling variable $L^{1/\nu}(k - k_\mathrm{c})$, with $1/\nu = 0.7$, converge to a limiting curve as L grows. Errors in both panels are one standard deviation.

The quotients method considers a dimensionless quantity at two sizes $L_a < L_b$ as a function of k. In our case, we focus on $\xi^{(3)}/L$. In the scaling region, both curves for L_a and L_b must cross at some point $k^*(L_a, L_b)$ (see Fig. 6.7). Now, for dimensionful quantities A (such as $\chi^{(2)}$ or $\chi^{(3)}$), we consider the quotient

$$Q_A = \left.\frac{A_{L_b}}{A_{L_a}}\right|_{k=k^*(L_a,L_b)} . \tag{6.29}$$

Therefore, because the quantities A scales as $\xi^{x_A/\nu}$ in the thermodynamic limit (recall that for finite size systems, ξ is traded with L) and barring scaling corrections, we can approximate Q_A as

$$Q_A = \left(\frac{L_b}{L_a}\right)^{x_A/\nu} . \tag{6.30}$$

As the reader will notice, we can obtain an effective estimate of x_A/ν from this relation. Table 6.2 summarizes our estimation of the effective exponents. However, we must extrapolate the results in Table 6.2 to the thermodynamic limit. Let us consider only the leading correction to the scaling exponent, ω so that we can extrapolate the thermodynamic limit through

L_a	L_b	k^*	$\gamma^{(2)}/\nu$	$\gamma^{(3)}/\nu$	$1/\nu$
8	12	0.2910(15)	0.47(4)	1.73(7)	1.07(7)
8	16	0.2914(8)	0.45(3)	1.68(5)	1.04(6)
8	20	0.2911(6)	0.45(2)	1.68(4)	0.98(3)
8	24	0.2906(5)	0.42(2)	1.62(4)	0.98(6)
12	16	0.2917(18)	0.43(6)	1.62(11)	0.99(13)
12	20	0.2912(10)	0.43(4)	1.65(7)	0.90(6)
12	24	0.2905(8)	0.38(3)	1.55(6)	0.92(9)
16	20	0.290(3)	0.42(12)	1.7(2)	0.8(2)
16	24	0.2897(14)	0.35(6)	1.50(12)	0.85(16)
20	24	0.289(2)	0.27(10)	1.3(2)	0.9(3)

Table 6.2: Crossing points $k^*(L_a, L_b)$ obtained for $\xi^{(3)}/L$ and the size-dependent, effective critical exponents [see Eq. (6.31)] as estimated from $\partial_k\xi^{(3)}/L$ ($1/\nu$), $\chi^{(2)}$ ($\gamma^{(2)}/\nu$) and $\chi^{(3)}$ ($\gamma^{(3)}/\nu$). Errors are obtained using a bootstrap method. Data are represented in Fig. 6.8

$$\left.\frac{x_A}{\nu}\right|_{L_a,L_b} = \frac{x_A}{\nu} + \frac{1}{\log(\frac{L_b}{L_a})} \log\frac{1 + D_A L_b^{-\omega}}{1 + D_A L_a^{-\omega}} , \tag{6.31}$$

where D_A is an amplitude.

Unfortunately, we have not been able to obtain a reasonable estimate for the exponent ω. This is mainly due to two difficulties: firstly, the range of L values at our disposal was not sufficiently large, and secondly, the non-divergent analytic background for the $n = 2$ observables (and the Binder parameter) competes with the $L^{-\omega}$ corrections.

However, we have circumvented this difficulty using an alternative strategy. Specifically, we have fitted our effective exponents in Table 6.2 to Eq. (6.31) with fixed ω, i.e. the fit parameters were the extrapolated x_A/ν and the amplitude D_A. To account for our ignorance about ω, we made it vary in a wide range $0.5 \leq \omega \leq 2$. We estimate the statistical error by a bootstrap method [Yll11] with $\omega = 1$. We considered only the diagonal part of the covariance matrix in the fits, performing a new fit for every bootstrap realization (see Appendix H for more details in the automatic fitting process). Errors were computed from the fluctuations of the fit parameters. In addition to the statistical error, we obtain a second error that accounts for the ω-dependence of the extrapolated x_A/ν. We estimate this error as the semi-difference of x_A/ν estimated with $\omega = 0.5$ and $\omega = 2$. Thus, we obtain for the correlation-length exponent ν and exponents $\gamma^{(n)}$ $[\chi^{(n)}(k_c) \sim L^{\frac{\gamma^{(n)}}{\nu}}]$:

$$\frac{1}{\nu} = 0.71(24)(9)\,, \qquad \frac{\gamma^{(2)}}{\nu} = 0.27(8)(8)\,, \qquad \frac{\gamma^{(3)}}{\nu} = 1.39(23)(11)\,. \tag{6.32}$$

The first error estimate is statistical, whereas the second error accounts for systematic effects. Fortunately, as the reader will notice, systematic errors were comparable (for $1/\nu$, even smaller) with the statistical ones. Notice also that the bound $\nu \geq 2/D$ [CCFS86] is verified, and that $\chi^{(2)} \sim L^{\frac{\gamma^{(2)}}{\nu} \approx 0.3}$ is, indeed, barely divergent [RY94].

Finally, to determine the critical point, k_c, we must proceed similarly to the case of the critical exponents and extrapolate k^* to the thermodynamic limit. In this case, taking into account the scaling corrections, one finds [Bin81]

$$k^*(L_a, L_b) = k_c + D_k F(L_a, L, b)\,, \tag{6.33}$$

where D_k is an amplitude, and the function $F(L_a, L, b)$ takes the form

$$F(L_a, L_b) = L_a^{-(\omega + \frac{1}{\nu})} \frac{1 - s^{-\omega}}{s^{1/\nu} - 1}\,, \quad s = \frac{L_b}{L_a}\,. \tag{6.34}$$

Unfortunately, this extrapolation is not possible without knowing the value of ω.

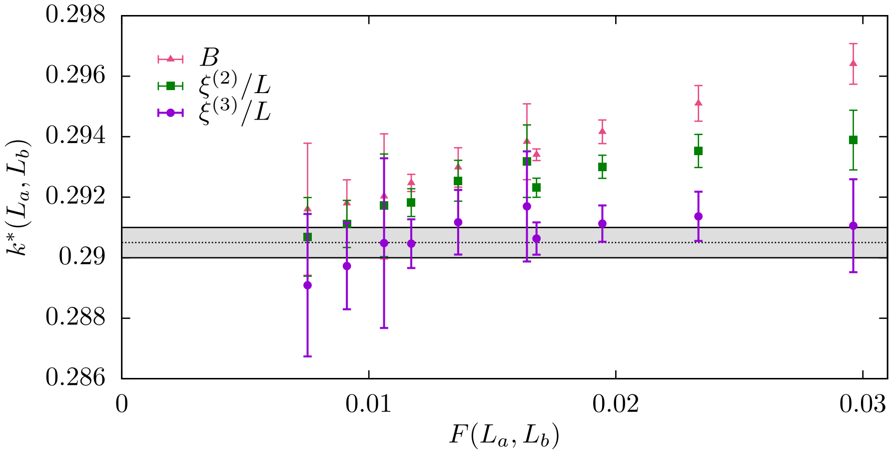

Figure 6.8: Crossing point $k*(L_a, L_b)$ for dimensionless quantities for two system sizes $L_a < L_b$, see Fig. 6.7. Data computed for B, $\xi^{(2)}/L$ and $\xi^{(3)}/L$ versus $F(L_a, L_b)$ (6.34). We set $1/\nu = 0.7$ and $\omega = 1$ to compute $F(L_a, L_b)$. The curves should extrapolate linearly to k_c as $F(L_a, L_b)$ tends to zero. The shaded area represents our uncertainty in estimating k_c.

However, as shown in Fig. 6.8, our results for k^* obtained from $\xi^{(3)}/L$ do not show significant finite-size effects. In fact, our estimate for the critical point k_c is a band that is consistent with all our results (see Fig. 6.8):

$$k_\mathrm{c} = 0.2905(5)\,. \tag{6.35}$$

Furthermore, the crossing points for B and $\xi^{(2)}/L$, see Fig. 6.8, seem also reasonably well represented by Eq. (6.35). Thus, we have considered $k_\mathrm{c} \approx 0.29$ for the study of the energy spectrum discussed in Sect. 6.5.

6.5 Spectra of excitations at the critical point

In Sect. 6.3.2, we discussed the τ dependence of the Euclidean-time correlation functions. A remarkable feature we extract from Eq. (6.25) is that for *even* operators the τ dependence is only sensible to same-parity gaps (such as $\varDelta_\mathrm{e}$ and $\varDelta_\mathrm{o}$ —see Fig. 6.2), while for *odd* operators only the different-parity energy gap $\varDelta$ have a role in the decay.

Moreover, for both symmetry sectors, the correlation functions computed in a sample decay exponentially (to zero for odd operators or to a plateau for even operators —recall the discussion in Sect. 6.3.2— as it is shown in Fig. 6.3), and the relevant energy gap drives this exponential decay. Therefore, what determines the behavior of the average over samples of an Euclidean-time correlation function, $\overline{C_{\hat{\mathcal{A}}}}(\tau)$, is the probability distribution function (pdf), as computed over the different samples, of the relevant correlation length: η for odd operators, and η_e or η_o for even operators.

6.5.1 Even operators

Despite the main dynamical exponent z of the quantum spin-glass phase transition is only related to the $\varDelta$ energy gap (or η), the even excited states remain relevant. Specifically, an (ideal) quantum annealer for the Hamiltonian (6.1) is blind to the odd excited states, so only the even ones may cause the system to leave its GS. Our approach is not entirely satisfying in this respect because, for a given sample, our analysis obtains the smallest of the two same-parity gaps $\varDelta_\mathrm{e}$ and $\varDelta_\mathrm{o}$, while $\varDelta_\mathrm{e}$ is the only relevant one for the quantum annealing process. Fortunately, our exact diagonalization analysis showed that both same-parity gaps are of similar magnitude (recall Fig. 6.4-**Right**) —so, from now on, we will refer to this correlation length as η_e.

As the reader will have anticipated from the discussion in Sect. 6.3.2, the correlation function that we will consider to study excitations of the same parity is $Q_2(\tau)$. Since this correlation function decays to a constant [as do all even observables, cf, Eq. (6.25)], we have subtracted this plateau to construct what we call $Q_{2,\mathrm{s}}(\tau)$ (the sub-index s stands for subtracted). Fig. 6.9-**Left** shows our result for the average over samples of $Q_{2,\mathrm{s}}(\tau)$ in log-scale, where we can confirm that $Q_{2,\mathrm{s}}(\tau)$ indeed decays to zero.

By the fitting process described in Appendix. H, we estimate the correlation lengths η_e for all our working samples. With this data, we estimate the empirical distribution function over samples for η_e (see Fig. 6.9). The distribution function indicates mild sample-to-sample fluctuations as we obtained from the exact diagonalization (recall Fig. 6.4).

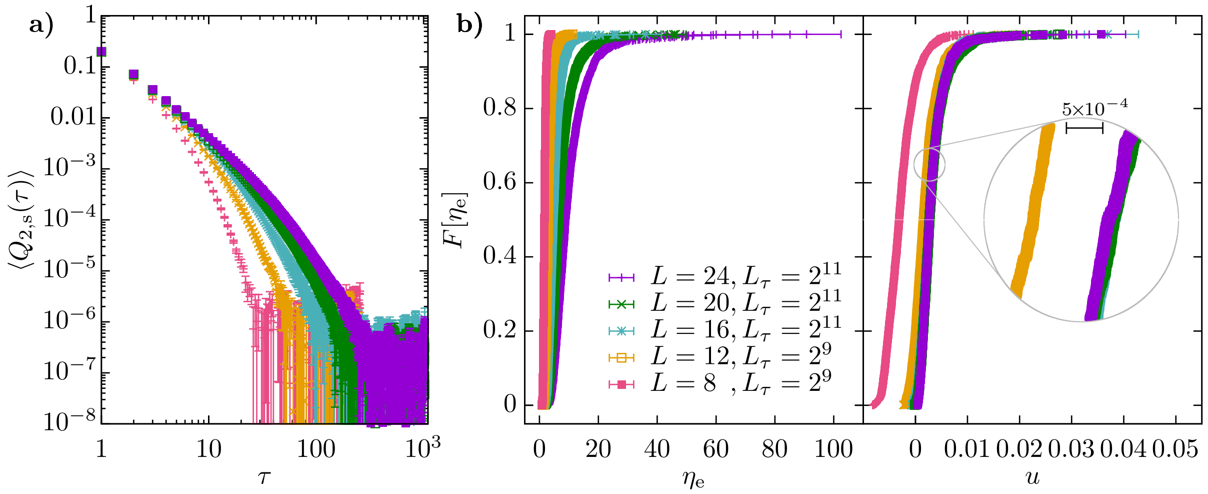

Figure 6.9: Studying the spectra of even excitations at the critical point. **(a)**: The sample-averaged substracted correlation function $Q_{2,s}(\tau)$ (see **Methods**) gets compatible with zero for moderate values of τ for all our system sizes. **(b)-Left:** After computing the Euclidean correlation length $\eta_e^{(s)}$ for each sample, we compute for each L the empirical distribution function $F(\eta_e)$, namely the probability F of finding a sample with $\eta_e^{(s)} < \eta_e$ (mind the horizontal error bars). **(b)-Right:** the data in panel **(b)-Left**, when plotted as a function of the scaling variable u, see Eq. (6.36), do not show any L residual L dependence but for our smallest sizes $L = 8, 12$. Errors in **(a)** and **(b)** are one standard deviation.

In addition, we can see a weak dependence on the system size L. In fact, as shown in Fig. 6.9, for all $L > 12$, the pdf turns out to depend on the scaling variable

$$u = \frac{\eta_e - \eta_e^0}{L^{z_e}}\,,\ \eta_e^0 = 2.2(3)\,,\ z_e = 2.46(17)\,. \tag{6.36}$$

Remark that setting $\eta_e^0 = 0$, the scaling process fails and the resulting estimate for the exponent is $z_e \approx 1.7$, closer to the result $z \approx 1.5$ reported in [RY94] (recall that in their work,[RY94] did not distinguish the parity sectors). The reader will notice that exponent z_e plays the same role as the dynamical exponent z, but only for the same-parity sector. Thus, we conclude that the even symmetry sector, the relevant sector for an (ideal) quantum annealer, shows algebraic scaling for its gap.

6.5.2 Odd operators

In order to conclude our study of the excitation spectrum, we must focus on the gap Δ. To do this, we will consider the correlation function $C(\tau)$ [cf. Eq. (6.23)].

The exact results in $D = 1$ [MW68, McC69, Fis92] and the approximate Renormalization Group for $D = 2$ [MN13] make us to expect that $\overline{C(\tau)}$ will display, for large L, a power law decay $\overline{C(\tau)} \propto 1/\tau^{\tilde{b}}$. In Fig. 6.10-**Left** we can see the behavior of $\overline{C(\tau)}$. However, the periodicity induced by the PBC in Fig. 6.10-**Left** makes it difficult to study the τ-dependence at large τ. Thus, to reduce the effect (see 6.10-**Center** and **Right**), we consider the modified Euclidean-time variable

$$\tilde{\tau} = \frac{L_\tau}{\pi}\sin(\pi\tau/L_\tau) = \tau[1 + \mathcal{O}(\tau^2/L_\tau^2)]\,; \tag{6.37}$$

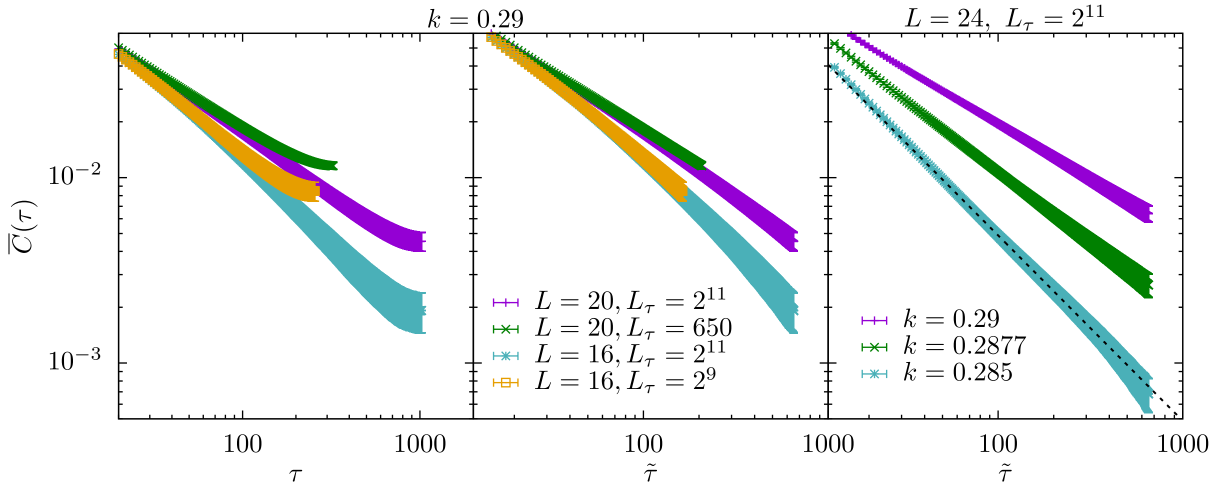

Figure 6.10: **Sample-averaged Euclidean correlation function** as a function of the Euclidean distance τ (**left** panel), $\tilde{\tau}$ [cd. Eq. (6.37)] to avoid distortions due to the periodic boundary conditions (**center** and **right** panels). **Left** and **center** panels show the system size dependence for $k = 0.29$, despite the **right** panel shows the k-dependence for the bigger system, $L = 24$ and $L_\tau = 2^{11}$. The dashed line in the **right** panel is a guide to the eye to show the critical exponent $\tilde{b} = 1$ encountered for $k = 0.285$ (see Sect 6.5.2).

that largely absorbs the finite L_τ-dependence. Thus armed, we can study the long-time decay of $C(\tau) \propto 1/\tilde{\tau}^{\tilde{b}}$ as a function of k. Looking at the results in Fig. 6.10-**Right**, the reader will notice that exponent $\tilde{b}$ decreases as k increases. Moreover, our results for $k = 0.285$ in Fig. 6.10 are compatible with $\tilde{b} = 1$. As we explain next, this has some relevant implications.

Divergence of the magnetic susceptibility

Due to the relationship between the linear magnetic susceptibility $\chi^{(h)}_{\text{lin}}$ —the linear response to a magnetic field along the Z axis— and the correlation function $\overline{C(\tau)}$, namely

$$\chi^{(h)}_{\text{lin}} = 1 + 2\sum_{\tau=1}^{\infty} \overline{C(\tau)}\,, \tag{6.38}$$

the observation of a slow decay [i.e. $\tilde{b} < 1$ for large τ in $\overline{C(\tau)}$] implies a divergence in $\chi^{(h)}_{\text{lin}}$. Thus, from the decreasing exponent $\tilde{b}$ when k increases and the fact that $\tilde{b} = 1$ for $k \approx 0.285$ (see Fig. 6.10), we conclude that the susceptibility is divergent in the paramagnetic phase as well. Notice that this is also the behavior reported for $D = 1$ [MW68, McC69, Fis92]. In the critical point, see Fig. 6.11, we obtain a decay with $\tilde{b} = 0.6$, producing a divergent susceptibility as well.

Probability distribution function of η

In order to understand the divergent behavior of the linear susceptibility, we need to consider the pdf of the Euclidean correlation length η [recall that, for a single sample, $C(\tau) \sim Be^{-\tau/\eta}$]. The pdf for η is studied in Fig. 6.11. In particular, as it was anticipated in Sect. 6.4.1, the results shown in Fig. 6.11-Right suggest that we are in presence of a Levy flight (a distribution with an extremely fat tail). Notice that the heavy tail of

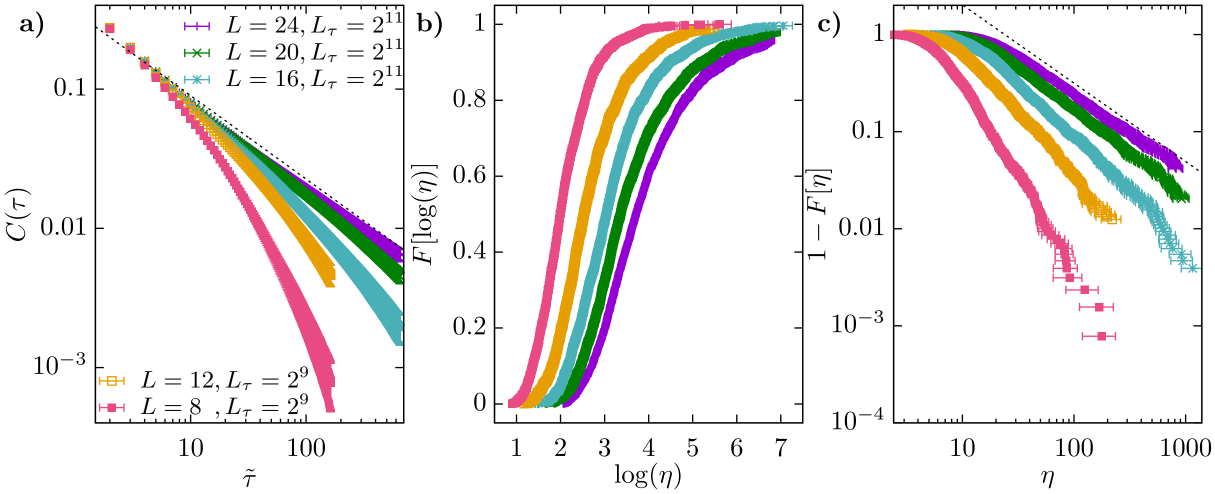

Figure 6.11: Studying the spectra of odd operators at the critical point. (a): The decay of the sample-averaged correlation function $C(\tau)$ approaches a power-law as L increases (dashed line as a guide to the eyes). Indeed, we have needed to represent $C(\tau)$ in terms of $\tilde{\tau} = \frac{L_\tau}{\pi}\sin(\pi\tau/L_\tau)$ to avoid distortions due to the periodic boundary conditions ($\tilde{\tau}$ and τ are almost identical for small τ/L_τ). **(b):** Empirical distribution function $F(\eta)$ as a function of $\log\eta$ for all our system sizes. Mind that we can compute only up to some L-dependent F because our largest L_τ is not large enough to safely determine η in some samples. **(c):** For large η, the assymptotic behavior $F(\eta) = 1 - \frac{B}{\eta^b}$ is evinced by the linear behavior —in logaritmic scale— of $1-F$ as a function of η (we find $b \approx 0.8$ —dashed line as a guide to the eyes). Errors in **(a)**, **(b)** and **(c)** are one standard deviate.

the empirical distribution function $F(\eta)$ becomes heavier as k increases, which implies a decreasing exponent $\tilde{b}$ in the power-law decay $\overline{C}(\tau) \sim 1/\tilde{\tau}^{\tilde{b}}$.

In addition, the Levy-flight perspective provides a simple explanation for the results obtained by [GBH94, TH95]: Let us consider the different susceptibilities to a magnetic field (linear, third-order, etc.) for a *single* sample. These susceptibilities are proportional to increasing powers of η. Hence, the average over samples of any (generalized) susceptibility is related to the corresponding moment of the pdf of η. In this situation, if $F(\eta)$ decays for large η as a power law, some (initially a higher-order one) disorder-averaged susceptibility will diverge. Because the power-law exponent decreases as k increases, the lower-order susceptibilities diverge at larger values of k. In fact, the linear susceptibility turns out to diverge in the paramagnetic phase. Thus, using the divergent behavior of some-order susceptibilities is not advisable to determine the critical point.

6.6 Conclusions

In the present chapter, we have studied the quantum phase transition of the Hamiltonian (6.1). Our study has used an unprecedented extreme-scale simulation on GPUs and the consideration of the main symmetries of the system to solve a decades-long debate about the nature of the transition.

We have found that both parties in the polemics regarding the dynamic critical exponent z (recall $\Delta \propto L^{-z}$) grasped parts of the truth. Recall that, Refs [RY94, GBH94, TH95, RY96, SY17] supported a finite value for z, while Refs. [MN13, MFR16] claimed a $z=\infty$. Our results imply that, while closing the gap Δ at the critical point is indeed super-algebraic (i.e., $z = \infty$), it remains algebraic if one restricts the possible energy excitations to the same parity sector.

Since this symmetry restriction is experimentally achievable (at least nominally), we conclude that there is no fundamental principle that prevents a quantum annealer from remaining in the ground state while entering into the spin-glass phase, recall Fig. 6.2. In order to adiabatically enter the spin-glass phase, the annealing time would need to grow as a power-law with the number of qspins, recall Eq. (6.36), provided that parity-changing excitations are avoided. Moreover, universality suggests that this optimistic result extends to all problems that share the space dimension and the fundamental symmetries with our spin glass on the square lattice.

However, getting into the SG phase is only part of the process of solving an optimization problem through quantum annealing. One still needs to reach a zero transverse field in an adiabatic way. Despite this seems difficult for problems with space dimension $D \to \infty$ [Kny16], recent investigations argued that an algebraic speed-up, as compared to classical algorithms, is possible [KRL+23].

Our results also pose several questions to be addressed in future work. Let us conclude this chapter by briefly discussing some of these questions.

We know that spin glasses in $D = 2$ can be both difficult and easy to solve on classical computers. Problems on the square lattice with nearest-neighbor interactions can be solved quite efficiently (e.g., [KW18]). However, introducing second-neighbor interactions changes the computational complexity of the problem, making it an NP-complete problem. Whether or not this new problem belongs to the same (quantum) computational complexity class as the case studied in this chapter is still unclear. In this sense, because the second-neighbor interaction does not modify the critical behavior, any difference between both models should arise from $\mathit{\Gamma} < \mathit{\Gamma}_{\mathrm{c}}$.

In the same way, considering a three-dimensional Ising spin glass could also have an impact on the characterization of the system. In this sense, recent experiments conducted on D-Wave devices suggest that $z \approx 1.3$ [KRL+23].

Finally, in our work, we have not privileged any instance. However, one could focus on studying those problems that are difficult to solve on a classical computer [FMMPS13, MMMH16, BFM+18]. Although we know that these classical problems remain difficult to solve with D-Wave systems [MMH15], knowing if the scaling given by Eq. (6.36) does not change in these circumstances could help to determine if this is the reason underlying the poor performance of quantum hardware or if other effects are at play (see,e.g., [AMMH17, AMMH19]).

Part VI

Conclusions

7

Conclusions

> **"Perché dovremmo studiare questo problema se non ci divertiamo?"**
>
> *N. Cabibbo*
>
> Quoted by G. Parisi in:
> *Giorgio Parisi, la pace vince con la scienza*
> Corriere della senza
>
> Corriere della sera (28 November 2022)

Although it has been almost 100 years since Ernst Ising first introduced the Ising-Lenz model and 50 years since the modifications introduced by Edward and Anderson to explain the behavior of glassy systems, these models continue to surprise us. Furthermore, the list of subjects in which these models are used, or the techniques developed for their study, grows daily. This thesis tries to add to this effort to bring us closer to understanding the physics of complex systems.

In this thesis, we have focused on studying the Ising-Lenz and Edward-Anderson models from a numerical point of view. We have had to resort to specially dedicated computers, such as Janus I and Janus II, to design highly optimized programs that run on CPUs and GPUs or to automate analysis processes. Readers who are more interested in these technical aspects can review the information contained in the appendices of this thesis.

In the first part of this dissertation, specifically Chapters 2 and 3, we have focused our attention on the out-of-equilibrium dynamics of systems that do not exhibit proper glassy behavior (in the sense of not showing slow dynamics). At this point, the reader has undoubtedly wondered what connection, beyond the one that the model description can establish, can justify the relevance of the study of this type of model to understand glassy dynamics. In this sense, it should be remembered that one of the main difficulties presented by the glassy systems is to have a dynamic that approaches equilibrium very slowly. Thus, understanding and controlling the keys that govern other out-of-equilibrium dynamics could give us clues to designing new protocols, algorithms, or other techniques to accelerate glassy dynamics. Moreover, the ability to control and accelerate out-of-equilibrium dynamics already has experimental applications and could also help manage industrial processes.

Chapters 4, 5 and 6 have focused on spin glasses. Although we have studied different phenomena in each chapter, correlations are the common thread. Thus, in chapter 4, we saw that properties of the significant correlations present in spin glasses for dimension 4 coincide with the theoretical predictions found by field theory in dimension 6. In chapter 5, we observed that by studying correlations locally and on a microscopic scale, a new paradigm, such as multifractality, emerges to describe the dynamics in spin glasses. Finally, Chapter 6makes contact with the search for routes that take advantage of the properties of the systems to accelerate their dynamics, as we did in the first part of this thesis. To this end, in chapter 6, we have related a fundamental physics problem, such as studying the phase transition present in quantum spin glasses, with the efficiency of the quantum annealers. With our study of the phase transition, we have resolved (numerically) the debate about the nature of the transition in quantum spin glasses: Although the problem is dominated by an infinite randomness fixed-point, parity invariant excitations behave as in a conventional critical point. This result explains the divergence between previous works and leaves the door open to computational acceleration through quantum annealers.

In the following sections, we will present the main ideas and results of this thesis. The interested reader can read the conclusions of each chapter, where more details about them are given.

7.1 Unifying paradoxical dynamic effects

Many systems exhibit counterintuitive behavior when out of equilibrium. A clear example is the Mpemba effect: Two identical systems, albeit at different temperatures, are brought into contact with a thermal bath at a lower temperature. The initially at higher temperature system takes less time to reach equilibrium at the temperature of the thermal bath.

The Mpemba effect, and others of similar nature, can be explained by studying the out-of-equilibrium dynamics employing the spectral decomposition of the dynamics generator, provided that we have a separation of time scales. In the case of Markov dynamics, the spectral decomposition can be approached from two points of view: one focused on the time evolution of the probability distributions governing the evolution of the system or in terms of the evolution of observable quantities.

We tested the observable perspective for an Ising spin chain with antiferromagnetic interaction. Thanks to the simplicity of the model, we have been able to verify that the observable point of view not only allows for the explanation of these phenomena but, given the experimental accessibility of the relevant quantities, allows for making predictions and even controlling the dynamics of the system. In both cases, the existence of a parameter of order $\mathcal{M}$, such that the expected value of $\mathcal{M}^2$ is a non-monotonic function of the temperature, turns out to be a sufficient condition to find counter-intuitive dynamics such as that of the Mpemba effect. Moreover, we have verified that under these circumstances, it is possible to use protocols based on a previous preparation at a temperature different from the final one, such as preheating the system, to obtain exponential accelerations in the thermalization process.

7.2 Accelerating out-of-equilibrium dynamics

Chapter 3 of the thesis faces a problem similar to the one addressed in Chapter 2, but it does so under unfavorable conditions. Indeed, unlike systems with time-scale separation, where spectral decomposition can help us understand and exploit the dynamical properties of the system to our advantage, near a second-order phase transition, we have no time-scale separation. Knowing the processes governing the dynamics in this unfavorable situation can allow us to control it. Thus, we have decided to study the two-dimensional Ising model through Monte Carlo simulations. We have found that the growth of the magnetic domains not only governs the phenomena taking place in the ferromagnetic phase, as it was already well known but also affects the dynamics of the paramagnetic phase. Thus, controlling the size of the magnetic domains would allow faster relaxation processes to be obtained.

For this purpose, we have proposed and tested a thermalization protocol that takes advantage of an excursion to the low-temperature phase to rapidly grow the magnetic domains up to a specific size before bringing the system to the temperature at which it is desired to thermalize (in the paramagnetic phase). We have obtained this result for two different local dynamics, which makes us think that this property can be extrapolated to other systems belonging to the same universality class.

7.3 Large correlations in spin glasses in a field

Although the spin glass model was proposed almost 50 years ago (as measured at the time of writing this thesis) to explain the behavior of magnetic alloys at low temperatures, today, there are still unanswered questions.

One of these open problems is concerned with the large correlations in spin glasses with external magnetic field at low temperatures. Although mean-field theory predicts a phase transition, in the finite-dimensional case, below the upper critical dimension $D_\mathrm{u} = 6$ (it has recently been proposed that, actually, $D_\mathrm{u} = 8$ [ALP+22], which highlights how little certainty we have about this problem), there is still no clear theory that explains the behavior of these systems at low temperatures. This is due to the inherent complexity of the theory, which leaves open the possibility of at least three possible scenarios to explain the behavior of spin glasses in the field: (i) either a *crossover* occurs because the corrections to mean-field theory destroy the phase transition or shift it to zero temperature, (ii) or the transition is of first order, with no critical behavior, i.e., with large but finite correlations, (iii) or the phase transition is of second order. The difficulty is due, in part, to the rich and complex structure of the divergences proposed by (finite-dimensional) mean-field theory.

We have focused on studying the properties of correlations in the region of large susceptibilities. For this purpose, we have reanalyzed equilibrium configurations for a large number of samples in a tetradimensional lattice ($L = 16$) generated by the dedicated Janus I computer. In this way, we have tested the theoretical predictions obtained for $D > 6$ in dimension 4.

Our results indicate that the mean-field predictions are fulfilled for systems below the upper critical dimension. Furthermore, our study does not seem to suggest that a first-order phase transition exists in this problem.

7.4 Multifractal behavior of spin-glass correlations

Multifractality is the property of specific systems to exhibit not one but several self-similarity relations simultaneously. Although the term was first used to describe physical systems, such as turbulence in fluids or the growth of aggregates, there are many fields where the concept of multifractality has been observed. Some examples range from studying the human heartbeat, time series in economics, or the mating process of tiny crustaceans.

Adding spin glasses, one of the most studied systems in recent years, to the list of systems with multifractal behavior has surprised us. This achievement has required a paradigm shift in the study of spin glasses. This change has been driven, among other factors, by the growing technological development that has allowed the development of algorithms and specially dedicated computers, such as Janus I and Janus II, which have allowed access to microscopic information for systems comparable to the experimental ones.

Indeed, recent work has made it possible to explain phenomena such as chaos in temperature, memory, or the aging of spin glasses, thanks to effects occurring at mesoscopic scales. Specifically, to understand these phenomena it is necessary to study the system at distances comparable to the size of the domains of the system. At this scale, we have found that the correlations between spins at distances comparable to the size of the domains have a heavy-tailed distribution. Thanks to the characterization of the distribution function of the correlations through the distribution moments, we have identified the multifractal behavior inherent to spin glasses. These results, among others, have spotlighted the need to study correlations in spin glasses at the local level. A new generation of experiments to test these ideas is in the planning stage.

7.5 Quantum spin glasses in two dimensions

The phase transition associated with quantum fluctuations of spin glasses with a transverse field has been a source of discussion for a long time, thus posing a fundamental physics problem that is still unsolved. Specifically, the problem was associated with determining the very nature of the phase transition, represented by its dynamical exponent z.

Our work has focused on solving this problem by systematically studying the phase transition in two-dimensional quantum spin glasses by determining the critical point and the critical exponents of the system. We must consider the spin-flip symmetry of the system implemented by the parity operator $\hat{P}$. This symmetry separates the states of the system according to the effect of the parity operator $\hat{P}$ on them. In this way, we have even and odd states. This has allowed us to verify that there are, in fact, two relevant dynamical exponents: the one dominating the phase transition z, associated with the lower energy states of both parity sectors, and the one related to the states of the same parity z_{e}. The results obtained coincide with a finite value for the exponent of the even sector, $z_{\mathrm{e}} \approx 2.5$. At the same time, the actual nature of the phase transition of the system is characterized by a divergence in the exponent, i.e., $z = \infty$, as the predictions of the real-space renormalization group indicated.

It has been necessary to push the computational capabilities to their limits in order to achieve these results. In particular, we have developed highly optimized programs that run on graphics processors (GPUs) to obtain the highest possible performance. This has made the execution speeds of our codes comparable to those obtained by computers specifically designed to solve spin glass problems, such as Janus I and II.

Interestingly enough, this theoretical problem has direct application thanks to the quantum annealers. These devices solve optimization problems by determining the lowest energy state in a spin glass. The quantum annealers take advantage of the quantum fluctuations introduced by an external field $\varGamma$, which varies the fundamental state of the system. As the external field decreases adiabatically, the system remains in its lowest energy state so that, upon reaching the null field, we solve the problem under study. However, the system goes through the studied phase transition throughout this process. The annealing time required to maintain an adiabatic evolution at the critical point scales with the size of the system as $\tau_{\mathrm{an}} \propto L^{2z}$. Thus, if $z = \infty$, we would need an annealing time that scales superpolynomially with the number of qubits in the system.

Although we have obtained results consistent with a divergence in the dynamical exponent z, parity symmetry ensures that the quantum annealing process is governed only by the even-state sector so that it is the exponent z_{e} that determines how the runtime scales with system size. In other words, there is no first-principles theoretical objection to the quantum annealing paradigm. Not, at least, as far as going through the phase transition adiabatically is concerned.

It is interesting to speculate that our main conclusions, i.e., z_{e} finite and $z = \infty$, extend to three dimensions. Testing this hypothesis will be the task of future work.

8

Conclusiones

“¿Por qué debemos estudiar este problema si no nos divierte?”

N. Cabibbo

Citado por G. Parisi en:
Giorgio Parisi, la pace vince con la scienza
Corriere della senza

Corriere della sera (28 November 2022)

A pesar de que ya hace casi más de 100 años desde que Ernst Ising introdujera por primera vez el modelo de Ising-Lenz, y 50 años de las modificaciones introducidas por Edward y Anderson para explicar los comportamientos en sistemas vítreos, estos modelos aún nos siguen sorprendiendo. En este sentido, cabe reseñar que la lista de materias en las que se utilizan estos modelos, o las técnicas desarrolladas para su estudio, crece día a día. Esta tesis trata de sumarse a este esfuerzo, con el objetivo de acercarnos a comprender la física de los sistemas complejos.

En esta tesis nos hemos centrado en estudiar los modelos de Ising-Lenz y Edward-Anderson desde el punto de vista específicamente numérico. Para ello, hemos tenido que recurrir a ordenadores especialmente dedicados como Janus I y Janus II, diseñar programas altamente optimizados tanto para ejecutarse sobre CPUs, como GPUs, o automatizar procesos de análisis. El lector más interesado en estos aspectos técnicos puede revisar la información contenida en los Apéndices de esta tesis.

En la primera parte de esta disertación, específicamente los capítulos 2 y 3, hemos centrado nuestra atención en la dinámica fuera del equilibrio de sistemas que no presentan un verdadero comportamiento vítreo (en el sentido de no presentar dinámicas extremadamente lentas). En este punto el lector seguramente se haya preguntado que conexión, más allá de la que se puede establecer mediante la descripción del modelo, puede justificar la relevancia del estudio de este tipo de modelos para entender la dinámica vítrea. En este sentido, hay que recordar que uno de las principales dificultades que presentan los sistemas vítreos es la de tener una dinámica que se acerca muy lentamente al equilibrio. Así pues, entender las clave que rigen otras dinámicas fuera del equilibrio, y controlarlas, podría darnos claves para diseñar nuevos protocolos, algoritmos, u otras técnicas para acelerar las dinámicas vítreas. Además, la capacidad de controlar, y por tanto acelerar, las dinámicas fuera del equilibrio no sólo tienen ya aplicación experimental, sino que también podría tener utilidad para controlar procesos industriales.

Los capitulos 4, 5 y 6 han centrado su atención en los vidrios de espines. Aunque en cada capítulo hemos estudiado fenómenos distintos, el hilo conductor que enlaza todos ellos son las correlaciones. Así pues, en el capítulo 4 vimos que propiedades de las grandes correlaciones presentes en vidrios de espines para dimension 4 coinciden con las predicciones teóricas encontradas por la teoría de campos en dimension 6. En el capítulo 5 observamos que al estudiar las correlaciones de forma local y a escala microscópica, surge un nuevo paradigma, como es la multifractalidad, para describir la dinámica en los vidrios de espines. Por último, el capítulo 6 enlaza con la idea de buscar rutas que aprovechen las propiedades de los sistemas para acelerar su dinámica, como hicimos en la primera parte de esta tesis. Para ello, en el capítulo 6 hemos puesto en relación un problema de fisica fundamental, como es el estudio de la transición de fase presente en vidrios de espines cuánticos, con la eficiencia de los *quantum annealers*. Con nuestro estudio de la transición de fase, hemos resuelto (numericamente) el debate sobre la naturaleza de la transición en vidrios de espines cuánticos: Aunque el problema esta dominado por un *infinite randomness fixed-point*, las excitaciones invariantes por paridad se comportan como un punto crítico convencional. Este resultado permiten explicar la divergencia entre trabajos anteriores, además de dejar la puerta abierta a la aceleración computacional mediante *quantum annealers*.

En las subsiguientes secciones vamos a recoger las ideas y resultados principales de esta tesis. El lector interesado puede leer las conclusiones propias de cada capitulo, donde se dan más detalles acerca de las mismas.

8.1 Unificando efectos dinámicos paradójicos

Muchos sistemas exhiben comportamientos poco intuitivos cuando se encuentran fuera del equilibrio. Un claro ejemplo de esto es el efecto Mpemba: Dos sistemas idénticos, aunque a temperaturas distintas, se ponen en contacto con un baño térmico a una temperatura más baja. El sistema inicialmente a mayor temperatura tarda menos tiempo en llegar al equilibrio a la temperatura del baño térmico.

El efecto Mpemba, así como otros de la misma índole, pueden explicarse estudiando la dinámica fuera del equilibrio mediante la descomposición espectral del generador de la dinámica, siempre que tengamos separación de escalas de tiempo. En el caso de las dinámicas de Markov, la descomposición espectral puede abordarse desde dos puntos de vista: uno centrado en la evolución temporal de las distribuciones de probabilidad que rigen la evolución del sistema, o bien en términos de la evolución de magnitudes observables.

Hemos puesto a prueba la explicación basada en observables para una cadena de espines de Ising con interacción anti-ferromagnética. Gracias a la sencillez del modelo, hemos podido comprobar que la visión basada en los observables no sólo permite explicar estos fenómenos, sino que, dada la accesibilidad experimental de dichos observables, permite hacer predicciones e incluso controlar la dinámica del sistema. En ambos casos la existencia de un parámetro de orden $\mathcal{M}$, tal que el valor esperado de $\mathcal{M}^2$ sea una función no-monótona de la temperatura, resulta ser una condición suficiente para encontrar dinámicas antintuitivas como la del efecto Mpemba. Además, hemos comprobado que bajo estas circunstancias es posible utilizar protocolos basados en una preparación previa a una temperatura distinta de la final, como precalentar el sistema, para obtener aceleraciones exponenciales en el proceso de termalización.

8.2 Acelerando la dinámica fuera del equilibrio

El capítulo 3 de la tesis afronta un problema parecido al abordado en el capítulo 2, pero lo hace en condiciones desfavorables. En efecto, a diferencia de los sistemas con separación de escalas temporales, donde la descomposición espectral nos puede ayudar a entender y aprovechar las propiedades dinámicas del sistema para nuestro benefício, cerca de una transición de fase de segundo orden no tenemos una separación de escalas temporales. En esta situación desfavorables, conocer los procesos que rigen la dinámica puede permitirnos controlarla. De esta manera, hemos decidido estudiar el modelo de Ising bidimensional mediante simulaciones de Monte Carlo. Hemos comprobado que el crecimiento de los dominios magnéticos no sólo gobierna los fenómenos que tienen lugar en la fase ferromagnética, como ya era bien conocido, sino que también tienen efecto en la dinámica de la fase paramagnética. De esta forma, controlar el tamaño de los dominiós magnéticos permitiría obtener procesos de relajación más rápidos.

Para ello, hemos planteado y puesto a prueba un protocolo de termalización que aprovecha una excursión a la fase de baja temperatura, para hacer crecer rápidamente los dominios magnéticos hasta un cierto tamaño, antes de llevar el sistema a la temperatura a la que se desea termalizar el sistema en la fase paramagnética. Este resultado lo hemos obtenido para dos dinámicas de Metrópolis distintas, lo que nos hace pensar que esta propiedad puede ser extrapolable a otros sistemas pertenecientes a la misma clase de universalidad.

8.3 Grandes correlaciones en vidrios de espines en campo magnético

A pesar de que el modelo de los vidrios de espines haya sido propuesto hace casi 50 años (en el momento de publicar esta tesis) para explicar el comportamiento de las aleaciones magnéticas a baja temperatura, aún hoy en día sigue habiendo preguntas sin responder.

Una de estas incógnitas se refiere a las grandes correlaciones que surgen en los vidrios de espines con campo magnético externo, a bajas temperaturas. Aunque la teoría de campo medio predice una transición de fase, en el caso de dimensión finita, por debajo de la dimension crítica superior $D_\mathrm{u} = 6$ (recientemente se ha propuesto que $D_\mathrm{u} = 8$ [ALP+22], lo que pone de manifiesto las pocas seguridades que tenemos sobre este problema), aún no existe una teoría clara que explique el comportamiento de estos sistemas a bajas temperaturas. Esto se debe a la complejidad inherente a la teoría, que deja abierta la posibilidad de, al menos, tres escenarios posibles para explicar el comportamiento de los vidrios de espines en campo: (i) se produce un *crossover* debido a que las correcciones a la teoría de campo medio destruyen la transición de fase o la desplazan a temperatura nula, (ii) o la transición es de primer orden, sin comportamiento crítico, es decir, con correlaciones grandes pero finitas, (iii) o bien, la transición de fase es de segundo orden. La dificultad estriba, en parte, en la rica y compleja estructura de las divergencias propuesta por la teoría de campo medio en dimension finita.

Nos hemos enfocado en estudiar las propiedades de las correlaciones en la región de grandes susceptibilidades. Para ello hemos analizado configuraciones en equilibrio para un gran numero de muestras de un retículo tetradimensional ($L = 16$) generadas por el ordenador dedicado Janus I. De esta manera, hemos podido poner a prueba las predicciones teóricas, obtenidas para $D > 6$, en dimension 4.

Nuestros resultados parecen indicar que las predicciones de campo medio se cumplen para sistemas por debajo de la dimensión crítica superior. Además, nuestro estudio no parece indicar que exista una transición de fase de primer orden en este problema.

8.4 Comportamiento multifractal de las correlaciones en vidrios de espines

La multifractalidad es la propiedad de ciertos sistemas de presentar, no una, sino varias relaciones de autosemejanza simultáneamente. Aunque el termino se utilizó por primera vez para describir sistemas físicos, como es la turbulencia en fluidos o el crecimiento de agregados, son muchos los campos donde el concepto de multifractalidad se ha observado. Algunos de estos ejemplos van desde el estudio del latido cardíaco humano, hasta el estudio de series temporales en economía, pasando por la el proceso de emparejamiento de pequeños crustáceos.

Añadir a la lista de sistemas con un comportamiento multifractal los vidrios de espines, siendo estos uno de los sistemas más estudiados en los últimos años, ha sido una sorpresa para nosotros. Para ello ha sido necesario un cambio de paradigma en el estudio de estos sistemas. Dicho cambio ha sido impulsado, entre otros factores, por el creciente desarrollo tecnológico que ha permitido desarrollar algoritmos y ordenadores especialmente dedicados, como Janus I y Janus II, que han permitido acceder a información microscópica para sistemas equiparables a los experimentales.

En efecto, trabajos recientes han permitido explicar fenómenos como el caos en temperatura, la memoria o el envejecimiento de los vidrios de espin, gracias a los efectos que ocurren a escalas mesoscópicas. Específicamente, para entender estos fenómenos es necesario estudiar el sistema a distancias equiparables a las del tamaño de los dominios del sistema. En esta escala, y centrándonos en las propiedades locales del sistema, hemos comprobado que las correlaciones entre espines del sistema a distancias comparables con el tamaño de los dominios tienen una distribución con una cola pesada. Gracias a la caracterización de la función de distribución de las correlaciones mediante los momentos de la distribución, hemos sido capaces de identificar el comportamiento multifractal inherente a los vidrios de espines. Estos resultados, entre otros, han puesto el foco sobre la necesidad de estudiar las correlaciones a nivel local en vidrios de espines. Una nueva generación de experimentos que puedan contrastar estas ideas está en fase de planificación.

8.5 Vidrios de espines cuánticos en dos dimensiones

La transición de fase asociada a las fluctuaciones cuánticas de los vidrios de espines con campo transversal ha sido origen de discusión durante mucho tiempo, planteando así un problema de física fundamental aún sin resolver. Especificamente, el problema estaba asociado con la determinación de la naturaleza misma de la transición de fase, representada por su exponente dinámico z.

Nuestro trabajo se ha centrado en resolver este problema mediante el estudio sistemático de la transición de fase en vidrios de espines cuánticos bidimensionales, mediante la determinación del punto crítico y los exponentes críticos del sistema. Para ello hemos necesitado considerar la simetría de *spin-flip* del sistema que implementa el operador paridad $\hat{P}$. Esta simetría separa los estados del sistema atendiendo al efecto del operador de paridad sobre los mismos. De esta manera, tenemos estados pares e impares. Esto nos ha permitido comprobar que, en realidad, existen dos exponentes dinámicos relevantes: el que domina la transición de fase z, asociado a la interacción de los estados de menor energía de ambos sectores de paridad, y el asociado a la interacción de estados de la misma paridad z_e. Los resultados obtenidos coinciden con un valor finito para el exponente del sector par, $z_\mathrm{e} \approx 2.5$, mientras que la naturaleza real de la transición de fase del sistema está caracterizada por una divergencia en el exponente z, tal y como las predicciones del grupo de renormalización en el espacio real indicaban.

Para llegar a estos resultados ha sido necesario llevar al límite las capacidades computacionales actuales. En particular, hemos desarrollo programas altamente optimizados que se ejecutan en procesadores gráficos (GPU) para obtener el máximo rendimiento posible. Esto ha hecho que las velocidades de ejecución de nuestros códigos sean comparables a las obtenidas por ordenadores especificamente diseñados para resolver problemas de vidrios de espines, como son Janus I y II.

Por otro lado, este problema de carácter teórico tiene aplicación directa gracias a los *quantum annealers*. Estos dispositivos son empleados para resolver problemas de optimización mediante la determinación del estado de menor energía en un vídrio de espines. Los *quantum annealres* aprovechan las fluctuaciones cuánticas introducidas por un campo externo $\mathit{\Gamma}$, que hace variar el estado fundamental del sistema. Al ir disminuyendo adiabáticamente el campo externo, el sistema permanece en su estado de menor energía, por lo que, al alcanzar el campo nulo, llegamos a la solución del problema estudiado. Sin embargo, a lo largo de este proceso, el sistema atraviesa la transición de fase estudiada en el Capítulo 6. El tiempo de *annealing* necesario para mantener una evolución adiabática en el punto crítico escala con el tamaño del sistema como $\tau_\mathrm{an} \propto L^{2z}$. Así pues, si $z = \infty$, necesitaríamos un tiempo de *annealing* que escala superpolinómicamente con el número de qubits del sistema.

Pese a que hemos obtenido unos resultados que concuerdan con una divergencia en el exponente dinámico z de la transición de fases, la simetría de paridad garantiza que el proceso del *quantum annealing* esta gobernado únicamente por el sector de estados pares, con lo que es el exponente z_e el que determina cómo escala el tiempo de ejecutión con el tamaño del sistema. Esto implica que no existe una restricción teórica para la ejecución del *quantum annealing*. No, al menos, en lo que a atravesar la transición de fase de manera adiabática se refiere.

Es interesante especular que nuestras principales conclusiones, es decir, z_e finito y $z = \infty$, se extienden a tres dimensiones. Comprobar esta hipótesis será tarea de futuros trabajos.

Part VII

APPENDIX

A

Trotter-Suzuki approximation

This appendix details the derivation of the equivalent Trotter-Suzuki Hamiltonian in Eq. (6.6) from the original quantum Hamiltonian (6.1). For the sake of simplicity, instead of the original Hamiltonian (6.1) let us consider the following notation:

$$\hat{\mathcal{H}} = -\sum_{\langle i,j\rangle} J_{i,j}\hat{\sigma}_i^Z\hat{\sigma}_j^Z - \Gamma\sum_i \hat{\sigma}_i^X \,, \tag{A.1}$$

where Γ is the transverse field, the qspins are in the i-node of a D dimensional square lattice, and the couplin matrix $J_{i,j}$ is non-vanishing only for nearest-neigbors.

The partition function of this system can be expressed using the Transfer matrix formalism (see Appendix B for more details) as

$$Z = \mathrm{Tr}\left(\mathrm{e}^{-\beta\hat{\mathcal{H}}}\right) = \mathrm{Tr}\left[\mathrm{e}^{\beta\left(\sum_{\langle i,j\rangle} J_{i,j}\hat{\sigma}_i^Z\hat{\sigma}_j^Z + \Gamma\sum_i \hat{\sigma}_i^X\right)}\right] . \tag{A.2}$$

where β is the inverse temperature, i.e. $\beta = 1/(k_\mathrm{B}T)$ (K_B is the Boltzmann constant).

The Trotter-Suzuki decomposition [Tro59, Suz76], given by the following expression

$$\mathrm{e}^{A_1+A_2+\cdots+A_p} = \lim_{L_\tau\to\infty}\left(\mathrm{e}^{A_1/L_\tau}\mathrm{e}^{A_2/L_\tau}\cdots\mathrm{e}^{A_p/L_\tau}\right)^{L_\tau} \,, \tag{A.3}$$

can be applied to the partition function in Eq. (A.2). The resulting expression is

$$Z = \lim_{L_\tau\to\infty}\mathrm{Tr}\left[\left(\mathrm{e}^{\frac{\beta}{L_\tau}\sum_{\langle i,j\rangle} J_{i,j}\hat{\sigma}_i^Z\hat{\sigma}_j^Z}\,\mathrm{e}^{\frac{\beta\Gamma}{L_\tau}\sum_i\hat{\sigma}_i^X}\right)^{L_\tau}\right] , \tag{A.4}$$

where we have L_τ copies of the system.

Let us take the computational basis, i.e., the base of states that diagonalize the operators $\hat{\sigma}_i^Z$, $\{|\vec{S}\rangle\}$, and insert L_τ unity decompositions over this base in Eq. (A.4). Then, the partition function can be expressed as

$$\begin{aligned} Z = \lim_{L_\tau\to\infty}\sum_{\{S^{(1)},\cdots,S^{(L_\tau)}\}} & \mathrm{e}^{\frac{\beta}{L_\tau}\sum_{\langle i,j\rangle} J_{i,j}S_i^{(1)}S_j^{(1)}}\langle\vec{S}^{(1)}|\mathrm{e}^{\frac{\beta\Gamma}{L_\tau}\sum_i\hat{\sigma}_i^X}|\vec{S}^{(2)}\rangle\cdots \\ & \mathrm{e}^{\frac{\beta}{L_\tau}\sum_{\langle i,j\rangle} J_{i,j}S_i^{(L_\tau)}S_j^{(L_\tau)}}\langle\vec{S}^{(L_\tau)}|\mathrm{e}^{\frac{\beta\Gamma}{L_\tau}\sum_i\hat{\sigma}_i^X}|\vec{S}^{(1)}\rangle \,. \end{aligned} \tag{A.5}$$

Now, we can define $k = \frac{\beta}{L_\tau}$. Focusing on the matrix element

$$\begin{aligned} \langle\vec{S}^{(\tau)}|\mathrm{e}^{k\Gamma\sum_i\hat{\sigma}_i^X}|\vec{S}^{(\tau+1)}\rangle = & \\ & = \langle S_1^{(\tau)},\cdots,S_N^{(\tau)}|\mathrm{e}^{k\Gamma\hat{\sigma}_1^X}\cdots\mathrm{e}^{k\Gamma\hat{\sigma}_N^X}|S_1^{(\tau+1)},\cdots,S_N^{(\tau+1)}\rangle \\ & = \langle S_1^{(\tau)}|\mathrm{e}^{k\Gamma\hat{\sigma}_1^X}|S_1^{(\tau+1)}\rangle\cdots\langle S_N^{(\tau)}|\mathrm{e}^{k\Gamma\hat{\sigma}_N^X}|S_N^{(\tau+1)}\rangle \,, \end{aligned} \tag{A.6}$$

where we have used the fact that $\left[\hat{\sigma}_i^X, \hat{\sigma}_j^X\right] = 0$ because they are applied to different spins, and the base is a tensor product of the individual spin bases. We can study only one and omit the particle sub-index because we have N copies of the same term.

$$\langle S^{(\tau)}|\mathrm{e}^{k\Gamma\hat{\sigma}^X}|S^{(\tau+1)}\rangle = \langle S^{(\tau)}|\sum_{n=0}^{\infty}\frac{\left(k\Gamma\hat{\sigma}^X\right)^n}{n!}|S^{(\tau+1)}\rangle\,. \tag{A.7}$$

Using the fact that $\hat{\sigma}^{2m} = \mathcal{I}$, and $\hat{\sigma}^{2m+1} = \hat{\sigma}$; and $\hat{\sigma}^X|S^Z = \pm\rangle = |S^Z = \mp\rangle$, is easy to check that

$$\langle S^{(\tau)}|\mathrm{e}^{k\Gamma\hat{\sigma}^X}|S^{(\tau+1)}\rangle = \begin{cases} \cosh(k\Gamma) & \text{if} \quad S^{(\tau)} = S^{(\tau+1)} \\ \sinh(k\Gamma) & \text{if} \quad S^{(\tau)} = -S^{(\tau+1)} \end{cases}, \tag{A.8}$$

then we can be written as

$$\langle S^{(\tau)}|\mathrm{e}^{k\Gamma\hat{\sigma}^X}|S^{(\tau+1)}\rangle = \sqrt{\frac{1}{2}\sinh\left(2k\Gamma\right)}\mathrm{e}^{-\frac{1}{2}S^{(\tau)}S^{(\tau+1)}\log[\tanh(k\Gamma)]}\,. \tag{A.9}$$

Coming back to the complete expression we have:

$$\langle\vec{S}^{(\tau)}|\mathrm{e}^{k\Gamma\sum_i\hat{\sigma}_i^X}|\vec{S}^{(\tau+1)}\rangle = \left[\frac{1}{2}\sinh\left(2k\Gamma\right)\right]^{\frac{N}{2}}\mathrm{e}^{-\frac{1}{2}\log[\tanh(k\Gamma)]\sum_{\tau=0}^{m}\sum_i S_i^{(\tau)}S_i^{(\tau+1)}}\,. \tag{A.10}$$

Finally, we can write the partition function as

$$Z = \lim_{L_\tau\to\infty}\mathcal{C}\sum_{\{\{\vec{S}^{(1)}\},\cdots,\{\vec{S}^{(L_\tau)}\}\}}\mathrm{e}^{k\left[\sum_\tau\sum_{\langle i,j\rangle}J_{i,j}S_i^{(\tau)}S_j^{(\tau)}+\frac{k_\tau}{k}\sum_\tau\sum_i S_i^{(\tau)}S_i^{(\tau+1)}\right]}\,, \tag{A.11}$$

with $\mathcal{C} = \left[\frac{1}{2}\sinh\left(2k\Gamma\right)\right]^{\frac{NL_\tau}{2}}$, $k = \beta/L_\tau$ and

$$k_\tau = -\frac{\log\left[\tanh\left(k\Gamma\right)\right]}{2} \Leftrightarrow k\Gamma = -\frac{\log\left[\tanh(k_\tau)\right]}{2}\,, \text{ so } \Gamma = -\frac{\log\left[\tanh(k_\tau)\right]}{2k}\,. \tag{A.12}$$

If we consider a classical system with: D spacial dimensions with a coupling $J_{i,j}$ between neighborhoods, and an extra Euclidean time (i.e. a system with $D+1$ dimensions) dimension with a ferromagnetic coupling; in a lattice of size $L^D \times L_\tau$ with the action

$$S = -k\mathcal{H} = k\left[\sum_\tau\sum_{\langle i,j\rangle}J_{i,j}S_i^{(\tau)}S_j^{(\tau)} + \frac{k_\tau}{k}\sum_\tau\sum_i S_i^{(\tau)}S_i^{(\tau+1)}\right]\,, \tag{A.13}$$

the partition function is given by equation (A.11). We use the approximation $k_\tau/k = 1$.

B

Transfer Matrix

As it is well known in statistical physics, all the information about the system is contained in the partition function [Hua87]. However, calculating the partition function is often a difficult task. Therefore, different strategies have been designed to calculate the partition function (or to obtain an estimate of the associated Boltzmann weights, such as Monte Carlo methods).

One such method is the so-called transfer matrix method [KW41a, KW41b]. The main idea is evaluating the partition function from the eigenvalues of some power of the transfer matrix $\mathcal{T}$. Specifically, we express the partition function as

$$Z \equiv \mathrm{Tr} e^{-\beta \mathcal{H}} = \mathrm{Tr} \mathcal{T}^n \,, \tag{B.1}$$

where β is the inverse temperature in units such that the Boltzmann constant $k_\mathrm{B} = 1$, and the trace operator refers to the sum over all the possible states (or configurations) of the system.

In the following sections, we present a discussion of the results obtained using the transfer-matrix method for the anti-ferromagnetic Ising chain (cf. Chapter 2), and the quantum spin glass (SG) in 2 dimensions (cf. Chapter 6).

B.1 One dimensional antiferromagnetic Ising model

Let us consider the anti-ferromagnetic chain Ising model of length N with periodic boundary conditions at finite temperature T, which Hamiltonian [cf. Eq (2.52)] has the form

$$\mathcal{H} = -J \sum_{i=0}^{N-1} s_i s_{i+1} + h \sum_{i=0}^{N-1} s_i \,, \tag{B.2}$$

where $J < 0$ is the coupling constant, and H the external magnetic field. This system presents a *crossover* near the line $2J + h = 0$ that separates a region with magnetization close to one (above the line) from another region with vanishing magnetization (below the line). This crossover is faster when the system is close to the critical point at temperature $T = 0$. For the sake of simplicity, from now on, we use the dimensionless parameter $K \equiv J/(k_\mathrm{B} T)$ and $H \equiv h/(k_\mathrm{B} T)$.

The partition function for this system is(see, e.g. , Ref. [Par88])

$$Z(H, K) = \sum_{\{s_i\}} \mathrm{e}^{K \sum\limits_i s_i s_{i+1} + H \sum\limits_i s_i} = Tr(T^N) \,, \tag{B.3}$$

where we define the transfer matrix as

$$T = \begin{pmatrix} \mathrm{e}^{K+H} & \mathrm{e}^{-K} \\ \mathrm{e}^{-K} & \mathrm{e}^{K-H} \end{pmatrix} . \tag{B.4}$$

The characteristic polynomial for the transfer matrix in Eq. (B.4) is

$$P(\lambda) = \lambda^2 - 2\lambda \mathrm{e}^K \cosh(H) + 2\sinh(2K) . \tag{B.5}$$

Thus, the eigenvalues of the transfer matrix are

$$\lambda_\pm = \mathrm{e}^K \cosh(H) \pm \sqrt{\mathrm{e}^{-2K} + \mathrm{e}^{2K} \sinh^2(H)} . \tag{B.6}$$

Therefore, the partition function is

$$Z(H,K) = \lambda_+^N + \lambda_-^N , \tag{B.7}$$

and we can define the corresponding free energy F_N as usual

$$F_N = \log \lambda_+ + \frac{1}{N} \log \left[1 + \left(\frac{\lambda_-}{\lambda_+} \right)^N \right] = \log \lambda_+ + \frac{1}{N} \log \left[1 + \psi(K,H)^N \right] , \tag{B.8}$$

where we have define the ratio $\psi(K,H) = \lambda_- / \lambda_+$. Let us define the auxiliary functions

$$\begin{aligned} y(K,H) &= \mathrm{e}^{2K} \sinh(H) = \frac{\mathrm{e}^{2K+H}}{2} \left(1 - \mathrm{e}^{-2H} \right) , && \text{(B.9)} \\ z(K,H) &= \mathrm{e}^{2K} \cosh(H) = \frac{\mathrm{e}^{2K+H}}{2} \left(1 + \mathrm{e}^{-2H} \right) . && \text{(B.10)} \\ & && \text{(B.11)} \end{aligned}$$

Thus, the eigenvalues can be written in terms of $y(K,H)$ and $z(K,H)$ as (for the sake of simplicity, we omit the functional dependence of K and H)

$$\lambda_\pm = \mathrm{e}^{-K} \left(z \pm \sqrt{1 + y^2} \right) , \tag{B.12}$$

and their ratio has the form

$$\psi = \frac{z - \sqrt{1+y^2}}{z + \sqrt{1+y^2}} . \tag{B.13}$$

Magnetization

In order to obtain uniform magnetization, we have to derive the free energy with respect to the external field H:

$$\mathcal{M}_\mathrm{u} = \partial_H F_N = \partial_H \log \lambda_+ + \frac{\psi^N}{1+\psi^N} \partial_H \log \psi = \frac{\mathcal{M}_{\mathrm{u},\infty}}{1+\psi^N} + \frac{\psi^N}{1+\psi^N} \partial_H \log \lambda_- , \tag{B.14}$$

where we defined $\mathcal{M}_{\mathrm{u},\infty} = \partial_H \log \lambda_+$. Let us calculate the partial derivative

$$\begin{aligned}
\partial_H \log \lambda_\pm &= \frac{e^K \sinh(H) \pm \frac{e^{2K}\sinh(H)\cosh(H)}{\sqrt{e^{-2K}+e^{2K}\sinh^2(H)}}}{e^K\cosh(H) \pm \sqrt{e^{-2K}+e^{2K}\sinh^2(H)}} \\
&= \frac{e^K\sinh(H)}{e^K\cosh(H)\pm\sqrt{e^{-2K}+e^{2K}\sinh^2(H)}} \times \frac{\sqrt{e^{-2K}+e^{2K}\sinh^2(H)} \pm e^K\cosh(H)}{\sqrt{e^{-2K}+e^{2K}\sinh^2(H)}} \\
&= \pm\frac{e^K\sinh(H)}{\sqrt{e^{-2K}+e^{2K}\sinh^2(H)}} = \pm\frac{e^{2K}\sinh(H)}{\sqrt{1+e^{4K}\sinh^2(H)}} = \pm\frac{y}{\sqrt{1+y^2}} \, .
\end{aligned}$$

Then, $\partial_H \log\lambda_- = -\partial_H\lambda_+ = -\mathcal{M}_{\mathrm{u},\infty}$. Therefore, substituting the result in Eq. (B.14) we obtain

$$\mathcal{M}_{\mathrm{u}} = \mathcal{M}_{\mathrm{u},\infty}\left(\frac{1-\psi^N}{1+\psi^N}\right) , \tag{B.15}$$

The reader will notice that substituting Eq. (B.9) in Eq. (B.15) we recover the expression in Eq. (2.53).

Spin-spin interaction

The process of obtaining the spin-spin interaction of the system is equivalent to the one for magnetization, with the only difference being that we have to derive respect to the coupling K. Then

$$\mathcal{C}_1 = \partial_K F_N = \partial_K \log\lambda_+ + \frac{\psi^N}{1+\psi^N}\partial_K\log\psi = \frac{\mathcal{C}_{1,\infty}}{1+\psi^N} + \frac{\psi^N}{1+\psi^N}\partial_K\log\lambda_- \, , \tag{B.16}$$

where we defined $\mathcal{C}_{1,\infty} = \partial_k \log\lambda_+$. The partial derivative of the eigenvalues is

$$\begin{aligned}
\partial_K \log\lambda_\pm &= \frac{e^K\cosh(H) \pm \frac{-e^{-2K}+e^{2K}\sinh^2(H)}{\sqrt{e^{-2K}+e^{2K}\sinh^2(H)}}}{e^K\cosh(H)\pm\sqrt{e^{-2K}+e^{2K}\sinh^2(H)}} \\
&= \frac{e^K\cosh(H)\sqrt{e^{-2K}+e^{2K}\sinh^2(H)} \pm \left[-e^{-2K}+e^{2K}\sinh^2(H)\right]}{e^K\cosh(H)\sqrt{e^{-2K}+e^{2K}\sinh^2(H)} \pm \left[e^{-2K}+e^{2K}\sinh^2(H)\right]} \\
&= \frac{\cosh(H)\sqrt{1+y^2} \pm \left[-e^{-2K}+e^{2K}\sinh^2(H)\right]}{\cosh(H)\sqrt{1+y^2}\pm\left[e^{-2K}+e^{2K}\sinh^2(H)\right]} = \frac{z\sqrt{1+y^2}\pm(y^2-1)}{z\sqrt{1+y^2}\pm(y^2+1)} \, .
\end{aligned}$$

By substituting the result for the derivative and Eqs. (B.9) (B.10) in Eq. B.16, after some simplifications, we recover the expression in Eq. (2.56).

Staggered susceptibility

In order to compute the staggered susceptibility, we must include a new term in the Hamiltonian (B.2), namely a staggered field h_{st}, then (for N even)

$$\begin{aligned} \mathcal{H}_{\text{st}} &= -J \sum_{i=0}^{N-1} s_i s_{i+1} + h \sum_{i=0}^{N-1} s_i + h_{\text{st}} \sum_{i=0}^{N-1} (-1)^i s_i \\ &= -J \sum_{i=0}^{N-1} s_i s_{i+1} + h_{\text{e}} \sum_{i=0}^{N/2-1} s_{2i} + h_{\text{o}} \sum_{i=0}^{N/2-1} s_{2i+1} \,, \end{aligned} \tag{B.17}$$

where we defined $h_{\text{e}} = h + h_{\text{st}}$ and $h_{\text{o}} = h + h_{\text{st}}$ (the sub-index stands for *even* and *odd* sites). Then, we can split the sum into even sites and odd sites and write the partition function as

$$Z\left(K, H, H_{\text{st}}\right) = \operatorname{Tr}\left(T_{\text{e}\to\text{o}} T_{\text{o}\to\text{e}}\right)^{N/2} \,, \tag{B.18}$$

where $H_{\text{st}} = h_{\text{st}}/T$, and the transfer matrices are

$$T_{\text{e}\to\text{o}}(K, H, H_{\text{st}}) = \begin{pmatrix} \mathrm{e}^{K+H} & \mathrm{e}^{-K+H_{\text{st}}} \\ \mathrm{e}^{-K-H_{\text{st}}} & \mathrm{e}^{K-H} \end{pmatrix} \tag{B.19}$$

for the even sites and

$$T_{\text{o}\to\text{e}}(K, H, H_{\text{st}}) = \begin{pmatrix} \mathrm{e}^{K+H} & \mathrm{e}^{-K-H_{\text{st}}} \\ \mathrm{e}^{-K+H_{\text{st}}} & \mathrm{e}^{K-H} \end{pmatrix} \tag{B.20}$$

for the odd sites. As the reader will notice, $T_{\text{e}\to\text{o}}(K, H, H_{\text{st}}) = T_{\text{o}\to\text{e}}(K, H, -H_{\text{st}})$, then using the cyclical property of the trace, we can straightforwardly demonstrate that

$$Z(K, H, H_{\text{st}}) = Z(K, H, -H_{\text{st}}) \,. \tag{B.21}$$

As for the original Hamiltonian (B.2), we can diagonalize the matrix product $T_{\text{e}\to\text{o}} T_{\text{o}\to\text{e}}$ and obtain the partition function,

$$Z(K, H, H_{\text{st}}) = \lambda_+^{N/2} + \lambda_-^{N/2} \,, \tag{B.22}$$

and, from it, the free energy $F_L(K, H, H_{\text{st}}) = \frac{1}{N} \log Z(K, H, H_{\text{st}})$. The new free energy is also symmetric under the transformation $H_{\text{st}} \to H_{\text{st}}$, then we can Taylor-expand the free energy close to the null field, i.e.

$$F_L(K, H, H_{\text{st}}) = F_L(K, H) + \frac{1}{2} \chi_{\text{st}} H_{\text{st}}^2 + \mathcal{O}(H_{\text{st}}^4) \,. \tag{B.23}$$

Then, to compute the staggered susceptibility, we must compute the second derivative of the free energy with respect to the staggered field and evaluate it in $H_{\text{st}} = 0$, i.e.

$$\chi_{\text{st}} = \partial_{H_{\text{st}}}^2 F_L(K, H, H_{\text{st}})|_{H_{\text{st}}=0} \,. \tag{B.24}$$

B.2 Two dimensional quantum spin glass

In Appendix A, we recalled that the partition function for a quantum spin glass given by Hamiltonian (6.1) can be expressed as

$$Z = \operatorname{Tr}\mathcal{T} = \operatorname{Tr}\left[\left(\mathrm{e}^{-k(\hat{\mathcal{H}}_0+\hat{\mathcal{H}}_1)}\right)^{L_\tau}\right] = \lim_{L_\tau\to\infty}\operatorname{Tr}\left[\left(\mathrm{e}^{-k\hat{\mathcal{H}}_0}\mathrm{e}^{-k\hat{\mathcal{H}}_1}\right)^{L_\tau}\right] = \lim_{L_\tau\to\infty}\operatorname{Tr}\left[\tilde{\tilde{\mathcal{T}}}^{L_\tau}\right]\,, \tag{B.25}$$

where we have defined

$$\hat{\mathcal{H}}_0 = -\frac{1}{2}\sum_{\langle i,j\rangle} J_{i,j}\hat{\sigma}_i^Z\hat{\sigma}_j^Z \quad , \quad \hat{\mathcal{H}}_1 = -\sum_i \hat{\sigma}_i^X\,, \tag{B.26}$$

and $\mathcal{T}$ is the original transfer matrix while $\tilde{\tilde{\mathcal{T}}}$ is the transfer matrix in the Trotter-Suzuki approximation. For the sake of simplicity, let us define

$$\hat{W} \equiv \mathrm{e}^{-k\hat{\mathcal{H}}_0} \quad , \quad \hat{U} \equiv \mathrm{e}^{-k\hat{\mathcal{H}}_1}\,, \tag{B.27}$$

so $\tilde{\tilde{\mathcal{T}}} = \hat{W}\hat{U}$. Using this notation, the expected value of some observable $\mathcal{A}$ which is diagonal in the computational basic, i.e., which is some function $A_{\mathrm{cl}}[\hat{\sigma}_i^Z]$, is [recall Eq. (6.15)]

$$\langle\mathcal{A}\rangle_{\mathrm{Q}} = \frac{1}{Z}\sum_{\{\mathbf{S}_\tau\}} A_{\mathrm{cl}}(\mathbf{S}_\tau)\mathrm{e}^{-k\mathcal{H}(\mathbf{S}_\tau)} = \frac{\operatorname{Tr}[A_{\mathrm{cl}}[\hat{\sigma}_i^Z]\left(\hat{W}\hat{U}\right)^{L_\tau}]}{Z}\,. \tag{B.28}$$

Let us consider the similarity transformation given by $\hat{D} = \mathrm{e}^{-\frac{k}{2}\hat{\mathcal{H}}_0}$. Recall that the trace is not affected by a similarity transformation, i.e., $\operatorname{Tr}[\hat{D}^{-1}\hat{M}\hat{D}] = \operatorname{Tr}\hat{M}$, and the fact that we can apply the transformation to the whole product or each element, i.e., $\hat{D}^{-1}\hat{M}_1\hat{M}_2\cdots\hat{M}_n\hat{D} = \hat{D}^{-1}\hat{M}_1\hat{D}\hat{D}^{-1}\hat{M}_2\hat{D}\cdots\hat{D}^{-1}\hat{M}_n\hat{D}$. Then,

$$\langle\mathcal{A}\rangle_{\mathrm{Q}} = \frac{\operatorname{Tr}[\hat{D}^{-1}A_{\mathrm{cl}}(\hat{\sigma}_i^Z)\hat{D}\left(\hat{D}^{-1}\hat{W}\hat{U}\hat{D}\right)^{L_\tau}]}{Z}\,. \tag{B.29}$$

As the reader will notice, $\hat{D}$ and $A_{\mathrm{cl}}(\hat{\sigma}_i^Z)$ commute because both are diagonal in the computational basis. Then, we can write

$$\langle\mathcal{A}\rangle_{\mathrm{Q}} = \frac{\operatorname{Tr}[A_{\mathrm{cl}}(\hat{\sigma}_i^Z)\tilde{\mathcal{T}}^{L_\tau}]}{Z}\,, \tag{B.30}$$

where $\tilde{\mathcal{T}} = \mathrm{e}^{-\frac{k}{2}\hat{\mathcal{H}}_0}\mathrm{e}^{-k\hat{\mathcal{H}}_1}\mathrm{e}^{-\frac{k}{2}\hat{\mathcal{H}}_0}$ [cf. Eq. (6.12)]. It is clear that $\tilde{\mathcal{T}}$ (at variance with $\tilde{\tilde{\mathcal{T}}}$) is a real symmetric matrix.

In order to compute the error introduce by considering $\tilde{\mathcal{T}}$ instead of $\mathcal{T}$, we can consider the Taylor expansion of both operators:

$$\mathcal{T} = \mathbb{I} - k(\hat{\mathcal{H}}_0+\hat{\mathcal{H}}_1) + \frac{k^2}{2}(\hat{\mathcal{H}}_0^2+\hat{\mathcal{H}}_1^2+\hat{\mathcal{H}}_0\hat{\mathcal{H}}_1+\hat{\mathcal{H}}_1\hat{\mathcal{H}}_0) + \mathcal{O}(k^3)\,, \tag{B.31}$$

$$\begin{aligned}\tilde{\mathcal{T}} = &\left(\mathbb{I} - \frac{k}{2}\hat{\mathcal{H}}_0 + \frac{k^2}{8}\hat{\mathcal{H}}_0 + \mathcal{O}(k^3)\right)\times\\ &\left(\mathbb{I} - k\hat{\mathcal{H}}_1 + \frac{k^2}{2}\hat{\mathcal{H}}_1 + \mathcal{O}(k^3)\right)\times\\ &\left(\mathbb{I} - \frac{k}{2}\hat{\mathcal{H}}_0 + \frac{k^2}{8}\hat{\mathcal{H}}_0 + \mathcal{O}(k^3)\right)\,.\end{aligned} \tag{B.32}$$

By computing the product in Eq. (B.32) it is direct to check that $\tilde{\mathcal{T}} = \mathcal{T} + \mathcal{O}(k^3)$.

The reader will notice that $\tilde{\mathcal{T}}$ is a defined positive operator. Then, we can proceed as usual and define an effective Hamiltonian $\tilde{\mathcal{H}}$ such that $\tilde{\mathcal{T}} = \mathrm{e}^{-k\tilde{\mathcal{H}}}$. We expect that, because the error introduce by $\tilde{\mathcal{T}}$ is cubic in k, the error respect the real Hamiltonian (6.1) is quadratic, i.e. $\tilde{\mathcal{H}} = \mathcal{H} + \mathcal{O}(k^2)$. However, we do not regard this as a major problem. Indeed, $\mathcal{H}$ and $\tilde{\mathcal{H}}$ share their basic properties (recall Sect. 6.1). Hence, the two Hamiltonians belong to the same universality class.

B.2.1 The parity-aware basis

Finally, let us see explicitly that the parity operator divides the state spectrum of the transfer matrix into the even and odd subspaces. To do so, let us introduce some notations that will help us study the transfer matrix [cf. Eq. (6.12)]

$$\tilde{\mathcal{T}} = \mathrm{e}^{-\frac{k}{2}\hat{\mathcal{H}}_0} \frac{\mathrm{e}^{-k\hat{\mathcal{H}}_1}}{\mathcal{N}^{L^2}} \mathrm{e}^{-\frac{k}{2}\hat{\mathcal{H}}_0} , \tag{B.33}$$

where $\mathcal{N} = 2\,\mathrm{e}^{-k}\cosh k\, \cosh k\Gamma$ is an irrelevant, but useful normalization.

From now on, instead of considering the two-dimensional Cartesian coordinates $\vec{x} = (x, y)$, we may use a one-dimensional lexicographic index

$$j = x + L * y\,, \quad j = 0, 1, \ldots L^2 - 1 \text{ (because } x, y = 0, 1, ...L - 1)\,. \tag{B.34}$$

It's important to note that the transformation $j \leftrightarrow (x, y)$ is a one-to-one correspondence. Therefore, we will use the site labeling (either lexicographic or Cartesian) that results in the most straightforward expressions.

We shall code an element of the computational basis (i.e., the basis that diagonalizes the L^2 matrices $\hat{\sigma}_j^Z$) through a L^2-bits integer $\mathtt{n}$. If the j-th bit in $\mathtt{n}$ is one, then the corresponding eigenvalue for σ_j^Z will be $s_j^{\mathtt{n}} = +1$ (or, switching to the Cartesian site-labelling, $s_{\vec{x}}^{\mathtt{n}} = +1$). Instead, the eigenvalue is $s_j^{\mathtt{n}} = -1$ if the j-th bit vanishes.

In the computational basis, $\mathrm{e}^{-\frac{k}{2}\hat{\mathcal{H}}_0}$ is diagonal:

$$\mathrm{e}^{-\frac{k}{2}\hat{\mathcal{H}}_0}|\mathtt{n}\rangle = \mathrm{e}^{\frac{k}{2}\sum\limits_{\langle\vec{x},\vec{y}\rangle} J_{\vec{x},\vec{y}} s_{\vec{x}}^{\mathtt{n}} s_{\vec{y}}^{\mathtt{n}}} |\mathtt{n}\rangle\,. \tag{B.35}$$

The central factor in Eq. (B.33) takes the form:

$$\frac{\mathrm{e}^{-k\hat{\mathcal{H}}_1}}{\mathcal{N}^{L^2}} = \prod_{j=0}^{L^2-1} \left[\frac{\mathrm{e}^{k}}{\mathrm{e}^{k} + \mathrm{e}^{-k}} \mathbb{I}_j \;+\; \frac{\mathrm{e}^{-k}}{\mathrm{e}^{k} + \mathrm{e}^{-k}} \hat{\sigma}_j^X\right] , \tag{B.36}$$

where $\mathbb{I}_j$ is the 2×2 identity matrix acting on site j [mind that all the matrices in Eq. (B.36) are mutually commuting]. Implementing the action of the matrix σ_j^X on the computational basis becomes simpler in the C programming language, as it corresponds to flipping the j-th bit:

$$\hat{\sigma}_j^X|\mathtt{n}\rangle = |\mathtt{n\^{}(1<<}j\mathtt{)}\rangle\,, \tag{B.37}$$

where `<<` stands for a *right shift* (i.e. multiply by 2^j), and `^` is the XOR bitwise operator. In the computational basis, the parity operator

$$\hat{P} = \prod_{j=0}^{L^2-1} \hat{\sigma}_j^X \,, \tag{B.38}$$

is not diagonal. However, parity stands out as a crucial symmetry in our problem. Hence, we must select a good-suited basis for $\hat{P}$. In order to introduce the new basis, let us consider a (L^2-1)-bits integer $\mathtt{m}$ (in the computational basis, we can regard this state as $|0,\mathtt{m}\rangle$, i.e. an element of the computational basis with the L^2-1 spin fixed to $s^{\mathtt{m}}_{j=L^2-1} = -1$). The effect of a global spin-flip on this state is given by

$$\hat{P}|0,\mathtt{m}\rangle = |1,\bar{\mathtt{m}}\rangle \,, \text{ where } \bar{\mathtt{m}} = 2^{L^2-1} - 1 - \mathtt{m}\,. \tag{B.39}$$

Notice that $\bar{\mathtt{m}}$ is the (L^2-1)-bit word obtained by changing all the bits in $\mathtt{m}$.

Then, the new basis for the even subspace is

$$|\mathtt{m}\rangle_{\mathrm{e}} = \frac{|0,\mathtt{m}\rangle \;+\; |1,\bar{\mathtt{m}}\rangle}{\sqrt{2}} \,,\; \mathtt{m} = 0,1,\ldots,2^{L^2-1}-1\,, \quad \hat{P}|\mathtt{m}\rangle_{\mathrm{e}} = +|\mathtt{m}\rangle_{\mathrm{e}}\,, \tag{B.40}$$

whereas for the odd subspace, we have

$$|\mathtt{m}\rangle_{\mathrm{o}} = \frac{|0,\mathtt{m}\rangle \;-\; |1,\bar{\mathtt{m}}\rangle}{\sqrt{2}} \,,\; \mathtt{m} = 0,1,\ldots,2^{L^2-1}-1\,, \quad \hat{P}|\mathtt{m}\rangle_{\mathrm{o}} = -|\mathtt{m}\rangle_{\mathrm{o}}\,. \tag{B.41}$$

A nice feature of the new basis is that almost all the crucial operators behave exactly as they did on the computational basis (for $\mathrm{e}^{-kH_0/2}$, think of $\mathtt{m}$ as a L^2-bit integer with the most significant bit set to be zero):

$$\mathrm{e}^{-\frac{k}{2}\hat{\mathcal{H}}_0}|\mathtt{m}\rangle_{\mathrm{e,o}} = \mathrm{e}^{\frac{k}{2}\sum\limits_{\langle\vec{x},\vec{y}\rangle} J_{\vec{x},\vec{y}} S^{\mathtt{m}}_{\vec{x}} S^{\mathtt{m}}_{\vec{y}}}|\mathtt{m}\rangle_{\mathrm{e,o}}\,, \tag{B.42}$$

$$\hat{\sigma}_j^X|\mathtt{m}\rangle_{\mathrm{e,o}} = |\mathtt{m}\texttt{\^{}}(1\texttt{<<}j)\rangle_{\mathrm{e,o}} \quad \text{if } j < L^2-1\,. \tag{B.43}$$

The only exception is $\hat{\sigma}^X_{j=L^2-1}$:

$$\hat{\sigma}^X_{j=L^2-1}|\mathtt{m}\rangle_{\mathrm{e}} = |\bar{\mathtt{m}}\rangle_{\mathrm{e}}\,, \quad \sigma^X_{j=L^2-1}|\mathtt{m}\rangle_{\mathrm{o}} = -|\bar{\mathtt{m}}\rangle_{\mathrm{o}}\,. \tag{B.44}$$

As the reader will notice, in the new bases, the action of the transfer matrix $\mathcal{T}$ over the even (equiv. odd) subspace remains in the even (odd) subspace.

C

Diagonalization problems in this thesis

In this thesis, we have dealt with two different diagonalization problems. On the one hand, in Chapter 2 the matrix that generates the Markov dynamics, see Eq. (2.18) for an antiferromagnetic Ising spin chain in the presence of a magnetic field. On the other hand, in Chapter 6, we diagonalized the transfer matrix in the Trotter approximation [see Eq. (6.12)] for a two-dimensional quantum spin glass. We have used different methods to address each of the problems. In this appendix, we describe the methods used for each of them.

C.1 Antiferromagnetic Ising spin chain

Let us consider a Ising chain of length N with a Hamiltonian [recall Eq. (2.11)]

$$\mathcal{H}(\boldsymbol{x}) = -J\sum_{i=1}^{N} s_i\, s_{i+1} - h\sum_{i=1}^{N} s_i\,. \tag{C.1}$$

Notice that the $2^N \times 2^N$ matrix R^{HB}, which define the probability that the system goes from state $\boldsymbol{x}$ to state $\boldsymbol{y}$, does not depend on ϵ_r [recall Eqs. (2.30) and (2.41)]. Then, in continuous-time Heat Bath dynamics, R^{HB} is given by [recall Eq. (2.18)]

$$R^{\mathrm{HB}}_{\boldsymbol{x},\boldsymbol{y}} = \frac{\exp\{-[\mathcal{H}(\boldsymbol{y})-\mathcal{H}(\boldsymbol{x})]/(k_{\mathrm{B}}T_{\mathrm{b}})\}}{1+\exp\{-[\mathcal{H}(\boldsymbol{y})-\mathcal{H}(\boldsymbol{x})]/(k_{\mathrm{B}}T_{\mathrm{b}})\}}\,, \tag{C.2}$$

if $\boldsymbol{x}$ and $\boldsymbol{y}$ differs in only one spin, and zero otherwise. The completeness relation fixes the diagonal elements [recall Eq. (2.31)]

$$R^{(\mathrm{b})}_{\boldsymbol{x},\boldsymbol{x}} = -\sum_{\boldsymbol{y}\in\Omega\{\boldsymbol{x}\}} R^{(\mathrm{b})}_{\boldsymbol{x},\boldsymbol{y}}\,. \tag{C.3}$$

As the reader will notice, this matrix is very sparse because only $N+1$ elements of each row are nonvanishing.

In order to compute the eigenvalues and the right-eigenvectors of matrix R (from now on, we omit the superindex for R^{HB}), we have used MATHEMATICA by following the next steps:

1. We have calculated R and the probability density [recall Eq. (2.4)]

$$\pi^{(\mathrm{b})}_{\boldsymbol{x}} = \frac{\exp\{-\mathcal{H}(\boldsymbol{x})/(k_{\mathrm{B}}T_{\mathrm{b}})\}}{Z_N(T_{\mathrm{b}})} \tag{C.4}$$

symbolically as a functions of the coupling and field (J,h) and the temperature T_{b} of the thermal bath.

2. To make sure that we have calculated both of them correctly, we check *symbolically* their basic properties: detailed balance, $R\mathbf{1} = \mathbf{0}$ and $\boldsymbol{\pi}^{(\mathrm{b})}R = \mathbf{0}$, where $\mathbf{0}$ and $\mathbf{1}$ are the constant functions with values zero and one respectively, i.e., $\mathbf{0}(\boldsymbol{x}) = 0$ and $\mathbf{1}(\boldsymbol{x}) = 1$ for all $\boldsymbol{x} \in \Omega$.
3. We have evaluated the expressions for R and $\pi^{(\mathrm{b})}_{\boldsymbol{x}}$.
4. We have computed the eigenvalues $(0, \lambda_2, \lambda_3, \ldots)$ and right-eigenvectors $(\mathbf{1}, \mathcal{O}^{\mathrm{b}}_2, \mathcal{O}^{\mathrm{b}}_3, \ldots)$ of R.

Step four has been carried out following the proof of Lemma 12.2 of Ref. [LP17]: if D is the diagonal matrix whose diagonal elements are $D_{\boldsymbol{x},\boldsymbol{x}} = (\pi^{T_{\mathrm{b}}}_{\boldsymbol{x}})^{1/2}$, then the matrix R is similar to the symmetric (and real) matrix $A = D\,R\,D^{-1}$. The spectral theorem for this kind of matrices ensures the existence of an *orthonormal* basis of right-eigenvectors $\{\mathcal{P}_k\}_{k=1}^{|\Omega|}$ w.r.t. the inner product

$$\langle\, \mathcal{A} \mid \mathcal{B} \,\rangle_0 \;=\; \sum_{\boldsymbol{x}\in\Omega} \mathcal{A}(\boldsymbol{x})\, \mathcal{B}(\boldsymbol{x})\,, \tag{C.5}$$

and such that the eigenvector $\mathcal{P}_k$ corresponds to the eigenvalue λ_k.

As the reader will notices, if we define $\mathcal{O}^{\mathrm{b}}_k = D^{-1}\,\mathcal{P}_k$, then $\mathcal{O}^{\mathrm{b}}_k$ is a right-eigenvector of R with eigenvalue λ_k. In this way we obtained the sets $\{\mathcal{O}^{\mathrm{b}}_k\}_{k=1}^{|\Omega|}$ and $\{\lambda_k\}_{k=1}^{|\Omega|}$.

Moreover, we verified to high accuracy that these eigenfunctions form an orthonormal basis w.r.t. the inner product (2.6), and they satisfied that $R\,\mathcal{O}^{\mathrm{b}}_k = \lambda_k\,\mathcal{O}^{\mathrm{b}}_k$ for all k.

Finally, by computing the probability density $\boldsymbol{P}^{(t=0)}$ as the Boltzmann weight at temperature T_0 (which is the preparation temperature of the system), we can obtain the evolution of the expected value of an observable $\mathcal{A}$ through the expression:

$$\mathbb{E}_t[\mathcal{A}] \;=\; \mathbb{E}^{(\mathrm{b})}[\mathcal{A}] + \sum_{k\geq 2} \alpha_k^{(t=0)} \beta_k^{\mathcal{A}}\, e^{-|\lambda_k| t/\tau_0}\,, \tag{C.6}$$

$$\beta_k^{\mathcal{A}} \;=\; \langle\, \mathcal{O}^{\mathrm{b}}_k \,|\, \mathcal{A} \,\rangle\,, \tag{C.7}$$

$$\alpha_k^{(t=0)} \;=\; \sum_{\boldsymbol{x}\in\Omega} P^{(t=0)}_{\boldsymbol{x}}\, \mathcal{O}^{\mathrm{b}}_k(\boldsymbol{x})\,. \tag{C.8}$$

With this method, we have analyzed systems up to $N = 12$, which implies that R is a 4096×4096 matrix. The next system length $N = 14$ supposes a matrix of size 16384×16384, which is beyond our computing capabilities through the method discussed in this section.

C.2 Quantum spin glass

As already mentioned in Chapter 6 (and discussed in Appendix B), in order to study the quantum phase transition in the bidimensional spin glass model, we have focused our attention on the transfer matrix in the Trotter-Suzuki approximation [Tro59, Suz76] [cf. Eq. (6.12)]. Then, for a system of linear size L, we need to diagonalize the matrix

$$\mathcal{T} \equiv \mathrm{e}^{-\frac{k}{2}\hat{\mathcal{H}}_0} \frac{\mathrm{e}^{-k\hat{\mathcal{H}}_1}}{\mathcal{N}^{L^2}} \mathrm{e}^{-\frac{k}{2}\,\hat{\mathcal{H}}_0}\,, \tag{C.9}$$

where

$$\hat{\mathcal{H}}_0 = -\frac{1}{2}\sum_{\vec{x},\vec{y}} J_{\vec{x},\vec{y}}\hat{\sigma}^Z_{\vec{x}}\hat{\sigma}^Z_{\vec{y}} \quad \text{and} \quad \hat{\mathcal{H}}_1 = -\Gamma\sum_{\vec{x}} \hat{\sigma}^X_{\vec{x}}\,, \tag{C.10}$$

and $\mathcal{N} = 2\,\mathrm{e}^{-k}\cosh k\, \cosh k\Gamma$ is an irrelevant, but convenient, normalization.

As discussed in Chapter 6, we are interested only in the lowest energy states, which correspond to the eigenvectors of $\mathcal{T}$ with the largest eigenvalues. Therefore, we have used the classic Lanczos method, an iterative algorithm for computing the extremal eigenvalues and corresponding eigenvectors of a large, symmetric matrix [Lan50].

As it was mentioned in Sect. C.1, what makes the problem demanding is the size of the matrix, which grows with the linear size of the problem as $2^{L^2} \times 2^{L^2}$ (notice that in Sect. C.1, it was $2^L \times 2^L$, due to the dimensionality of the problem). When considering $L = 5$, the transfer matrix takes the form of a $2^{25} \times 2^{25}$ matrix, and the Lanczos algorithm is manageable even on a high-end laptop. However, transitioning from $L = 5$ to $L = 6$ brings about a significant shift in the scenario. This is due to the matrix size expanding to $2^{36} \times 2^{36}$ (approximately 69 billion rows), posing a considerable computational challenge.

Exploiting the parity symmetry of the transfer matrix (see Appendix B) allows us to express it as the direct sum of two matrices, each with a size half that of the original. These matrices, termed "even" and "odd," are diagonalized separately. Specifically, our code calculates the two primary eigenvalues within each sector. Additionally, we retrieve the eigenvector corresponding to the leading eigenvalue in both the "even" and the "odd" sectors.

Although we split the matrix into two submatrices, the challenge persists as GPUs have limited memory (as compared to CPUs with Terabytes of RAM). However, a matrix-free approach alleviates this issue. In Lanczos's algorithm, instead of storing all the matrix coefficients, we can explicitly represent the matrix by evaluating the matrix-vector product.

Our code is built upon a fusion of two extensively employed open-source software packages: Petsc and Slepc. Our original contribution lies in a highly tuned multi-GPU-CPU solution designed to efficiently compute the matrix-vector product for transfer matrices. The product is carried out in three phases:

1. *Initialization:* It corresponds with the rightmost matrix multiplication in Eq. (C.9). The Slepc library (running on CPU) provides an input vector `in[]`, that is copied to the GPU, Then, on GPU, we execute

   ```
   for(i=0; i<Nloc; i++) {
           psi[i]=in[i]*w[i];
   }
   ```

   where

   - `Nloc`$=\frac{2^{(L\times L)-1}}{P}$; `P` is the number of GPUs;
   - `w[]` is the vector that contains the (pre-computed) Boltzmann factors $e^{-k\times H_0/2}$, see Eq. (C.10), for all possible configurations of spins;
   - `psi[]` is a temporary vector

2. *Computation:* the central product in Eq. (C.9) is carried out in `L2=`$(L \times L) - 1$ *rounds*

```
for(j=0;j<L2;j++){
    for(i=0;i<Nloc;i++){
        scra[i]=jP*psi[i]+jM*psi[$i \oplus 2^j$];
    }
    swap(scra,psi)
}
```

where

- `scra[]` is a temporary vector;
- `Jp` is equal to $\frac{e^k}{e^k+e^{-k}}$ and `Jm` is equal to $\frac{e^{-k}}{e^k+e^{-k}}$, see Eq. (B.36).
- $\oplus$ is the *bitwise exclusive OR* (between `i` and 2^j).

The connection defined by the $i \oplus 2^j$ stride is shown for the first 4 values of i and the first 4 *rounds* below

round 0

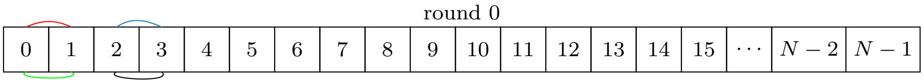

round 1

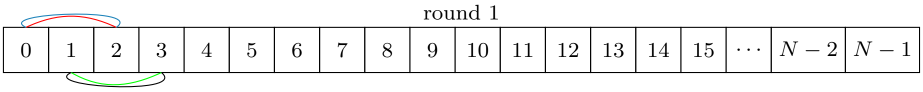

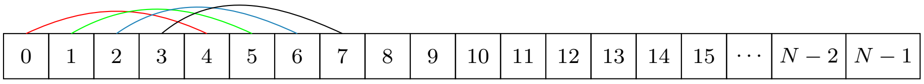

round 2

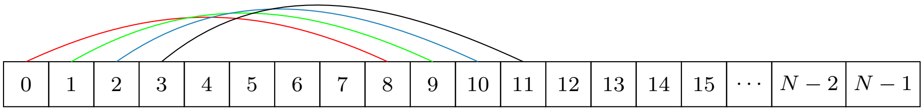

round 3

Actually, the last *round* is slightly different from the previous rounds in the indexing (and with an additional difference between the *even* and *odd* half of the transfer matrix) as shown in equation B.44. The interested reader may check directly the code for the details.

For small spin systems (up to $L = 5$), if the GPU has enough memory, all rounds may be executed on a single GPU (*i.e.*, `P=1`). However, for $L = 6$, the matrix size is such that multiple GPU are required (`P`> 1). In this case, the first $K = L2 - \log_2 P$ rounds may run in parallel on each GPU. Then, the temporary vector `psi[]` is copied to the CPU because it must be exchanged among the different tasks using MPI (the stride $i \oplus 2^j$ exceeds `Nloc`). It looks like we could copy them back to the GPUs after the exchange, but since *each* round after the K^{th} requires an exchange with a different task, the overhead of copying back and forth the data from the GPU to the CPU overrides the advantage of running on GPU, so the last rounds, after the K^{th}, run in parallel on CPU (using OpenMP). The value of K (that determines how many rounds are executed on GPU) depends on the memory available on each GPU. For $L = 6$ the computation requires 5 double precision arrays of 2^{35} elements: ~ 1.5

TB of GPU memory. Even using high-end GPUs, like the Nvidia A100, at least 20 GPU are required. Obviously, the more GPUs are used, the faster the computation, but, at the same time, the number of computation rounds that are local to the GPU decreases. Hence, it is necessary to find the best trade-off between GPU/CPU efficiency and scalability that also depends on the network speed (although the MPI scalability is close to ideal). With our platform (Infiniband based), we found that the best tradeoff was reached by using (for $L = 6$) 256 GPUs, each one having (at least) 32 Gbytes.

3. *Finalization:* the final leftmost matrix product in Eq. (C.9) is computed in parallel on CPUs and returned to the invoking SLEPC function in the output vector `out[]`

```
for(int i=0; i<Nloc; i++) {
    out[i]=psi[i]*w[i];
}
```

D

Multispin coding

Parallelization is probably the first way to improve the efficiency of many processes (in computation science and beyond). The main idea is to split all the work into independent tasks that different workers complete simultaneously.

Different degrees of parallelization are accessible (or bring some benefits) to the considered problem. For example, in our case —a numerical study of spin glass— we can use different computers to simulate different samples, replicas, temperatures, or system sizes and obtain an improvement in the efficiency (i.e., simulate more samples in less time). However, efficient parallelization crucially depends on the properties of the system under study and of the hardware that will carry out the simulation.

In our case, the Ising model, spins, and couplings may be coded a single bit. Moreover, it is possible to implement the dynamical algorithms using Boolean operations, giving us the opportunity to take advantage of one of the most internal parallelization that is possible in a computer: the computer units (cores in the CPU or threads in the GPU) work by cycles. In each of these cycles, they can perform basic Boolean operations (AND, XOR, etc.; actually, they can do more than boolean algebra in a cycle, but let us stop here for the sake of clarity) with *words* of m-bits. Nowadays, the standard for the CPU is $m = 128$ or $m = 256$, but $m = 512$ is available. For GPU $m = 32$ is a typical value

In simple terms, we can perform some calculations over m spins in parallel. However, we can use (at least) two approaches to take advantage of this parallelization. These are the multispin MUlti-SAmple (MUSA) and the multispin MUlti-SIte (MUSI) multispin coding [JR81, BFPP12]. Each solves different problems related to the study of SG. This appendix brings the main ideas of both techniques.

Finally, let us mention that the problem of implementing an efficient multispin coding algorithm to study SG poses two main difficulties. The first one is the implementation itself, i.e., how to drive the algorithm using only Boolean operations, place the spins in our m-bits words, etcetera. The second problem is generating the random numbers needed for the Monte Carlo process. Appendix F focuses on this second problem.

D.1 MUlti-SAmple (MUSA) multispin coding

The MUSA approach consists of using the m-bits words to carry out in parallel the simulation of m different samples (or replicas of the same sample). To achieve this, we store all the spins s_i at site i from the m samples in the same m-bits words. Then, if the system under study has N spins, using N of these m-bits words, we can store the whole

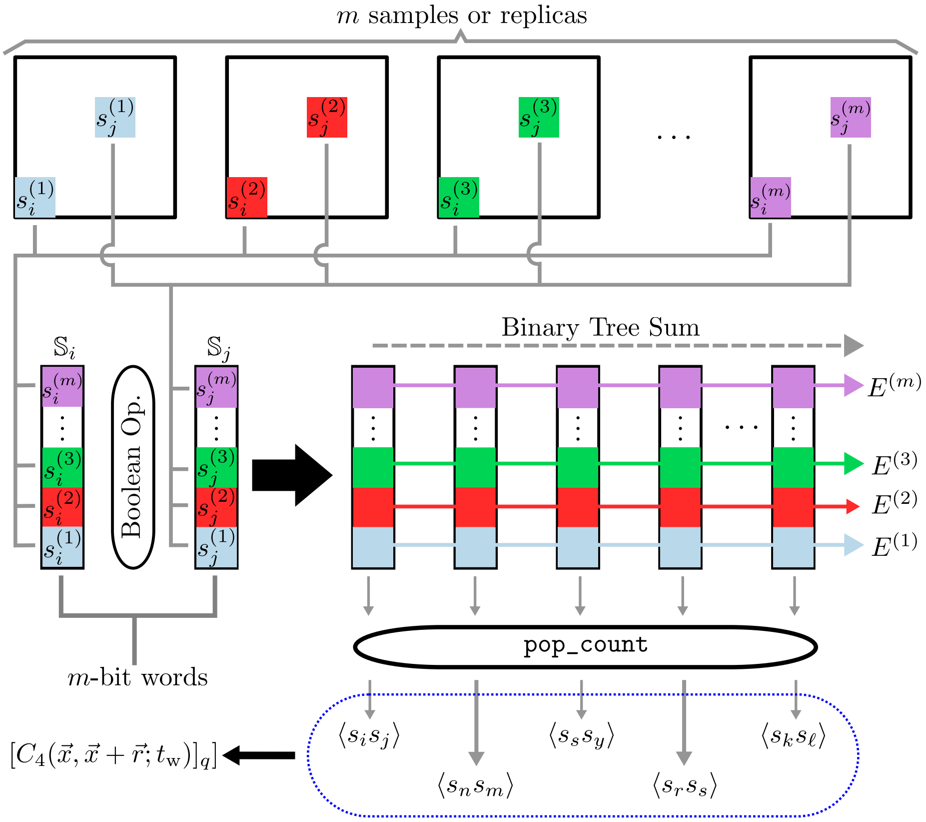

Figure D.1: Schematic representation of the MUlti-SAmple multispin coding. The spin s_i, located in the same position i from m different samples or replicas are stored in the same m-bits word. Using Boolean operation, it is possible to take measurements over all the m samples in parallel (for example, the energy of the system). We use a binary tree to sum (in parallel) the contribution of each spin-spin interaction. Another possibility, see text, allows us to perform the thermal average (we store the same spin from different replicas) using a *population count* to compute the sum over different pairs of replicas.

m samples. In addition, similarly, we can store the couplings $J_{i,j}$.

Then, by using basic Boolean operations, we can compute different observables or drive the Monte Carlo algorithm. As an example, consider the computation of the energy in an EA model without a field, i.e.,

$$\mathcal{H} = -\sum_{\langle i,j \rangle} J_{i,j} s_i s_j \,. \tag{D.1}$$

As a convention, we codify the spin states and the couplings as follows:

$$\begin{aligned} s_i = 1 \rightarrow \mathtt{b}(s_i) = 1 \quad &, \quad s_i = -1 \rightarrow \mathtt{b}(s_i) = 0 \\ J_{i,j} = 1 \rightarrow \mathtt{b}(J_{i,j}) = 0 \quad &, \quad J_{i,j} = -1 \rightarrow \mathtt{b}(J_{i,j}) = 1 \,. \end{aligned} \tag{D.2}$$

For the sake of simplicity, let us consider from now on that s_i and $J_{i,j}$ refer to their corresponding binary representation. Notice that inHamiltonian (D.1), the contribution of each of the links will be 1 (satisfied links) or -1 (frustrated links), which in our bit convention will be represented by 0 (satisfied) and 1 (frustrated), respectively.

Then, the energy contribution of each link can be computed as $J_{i,j}$ XOR s_i XOR s_j, so we can compute the contribution of each of the links in parallel to the m samples. Now, we can compute the energy of the system as

$$\begin{aligned} E &= -(\text{Number of satisfied links} - \text{ Number of frustrated links}) \\ &= -[\text{Total links} - 2 \times (\text{Number of frustrated links})] \,. \end{aligned} \tag{D.3}$$

As the reader will notice, because we represent the frustrated links as 1 (and by 0 the satisfied), a sum of the bits given by $J_{i,j}\,\mathrm{XOR}\,s_i\,\mathrm{XOR}\,s_j$ allows us to compute the number of frustrated links. We compute this sum using a binary tree strategy, which maintains separated the result for the m samples.

In order to perform the Monte Carlo algorithm, we use the algorithm presented in Ref. [IK90]. In this case, we must include m-bit words that codify, for a given site i, in which of the m samples we shall perform a spin-flip (performed by a simple NOT operation over the spin).

We also use the MUSA multispin coding to estimate the thermal average (or other quantities that involve the interaction of different replicas). For example, in Chapter 5, we have stored different replicas in the same m-bit word. Hence, estimate the number p of replicas such that $s_i^{(a)} s_j^{(a)} = -1$ is

$$p = \text{pop\_count}\,(\text{WORD}_i \text{ XOR } \text{WORD}_j) \ , \tag{D.4}$$

where pop_count is the *population count* and WORD_i is the m-bit word which keeps spin $s_i^{(a)}$ from the different m replicas. We have speed-up the computation of $[C_4(\vec{x},\vec{y};t_\mathrm{w})]_q$, recall Eq. (5.16), in this way.

D.2 MUlti-SImple (MUSI) multispin coding

In the MUSI approach, instead of packing different samples in the same m-bits word, we store spins from the same lattice of linear size L, forming a *superspin* [FMM15]. There are many different ways to make this codification, and according to the geometry of the system, interactions, etc., some of them are more efficient than others. In general, our packing tries to solve two problems:

(i) In systems with nearest-neighbor interaction in a bipartite lattice, we can assign colors according to the sublattice to which a spin belongs [for instance, in a cubic lattice, the color is set according to the parity of the site, e.g., in a 3-dimensional system the parity is $(x + y + z) \bmod 2 = (x\,\mathrm{XOR}\,y\,\mathrm{XOR}\,z)\,\mathrm{AND}\,1$; red (blue) will correspond to even (odd) parity], in such a way that red sites interact only with blue sites, and vice versa. We want to preserve this property because it allows us to update all the red sites in parallel and all the blue ones afterward.

(ii) If a set of m spins, $s_{i_1}, s_{i_2}, \ldots s_{i_m}$ is packed on the same m-bit word S, then their m neighbors along the (say) positive X lattice direction should also all be packed into a single m-bit word S_{X+} (i.e. the set of m lattice neighbors cannot be scattered among several m-bit words).

In this thesis, we have worked with two MUSI packings, one for the bidimensional Ising model studied in Chapter 3, and another for the quantum spin glass in two dimensions, see Chapter 6. In the following subsection, we detail both packings.

D.2.1 Our MUSI packing for the two-dimensional Ising model

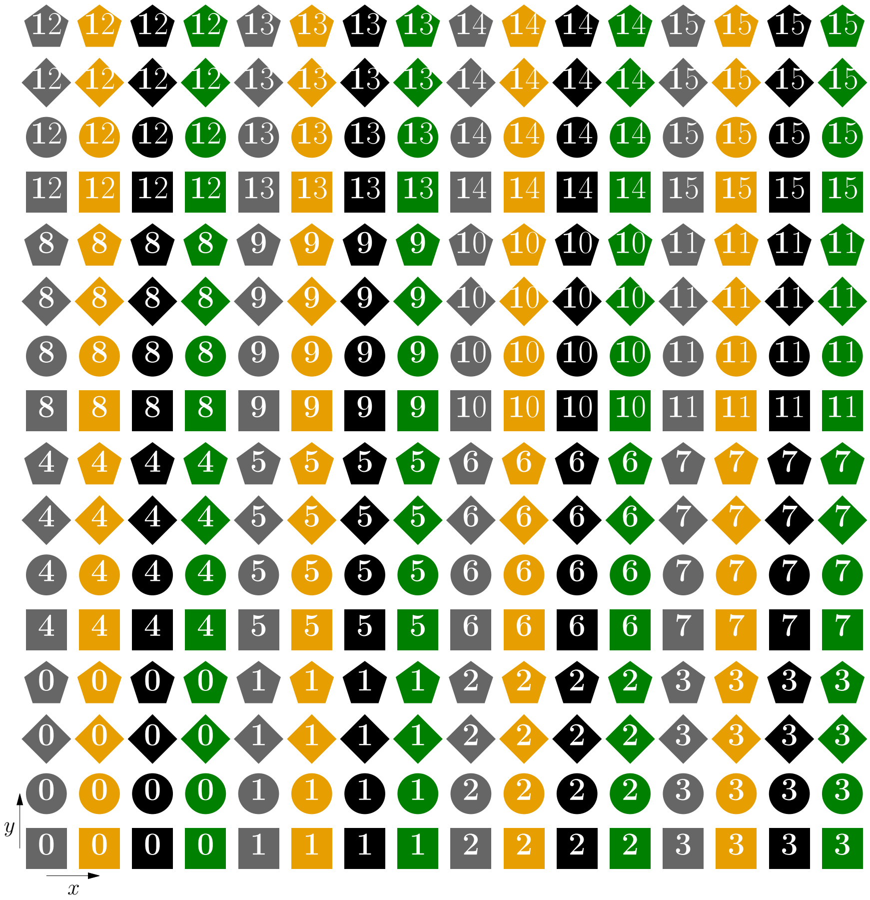

Figure D.2: Graphical representation of the packing process for a square lattice of size 16×16 using 16-bit computer word. $M = 4$ in this example. The superspin lattice has a linear size of 16/4. Colors and symbols represent the i_x and i_y coordinates, respectively. Therefore, spins with the same color and symbol are stored in the same superspin. The numbers inside the symbols are the bit index $i_b = Mb_x + x_y$.

Let us consider a square lattice of size $L \times L$, which we want to package in M^2-bit words. Then, the new superspin lattice has size $(L/M) \times (L/M)$. The original coordinates $\vec{x} = (x, y)$ and the packing superspin coordinates (i_x, i_y) are related by

$$\begin{aligned} x &= b_x \frac{L}{M} + i_x\,, \quad \text{where} \\ b_x &= 0, 1, \cdots, M-1 \quad \text{and} \\ i_x &= 0, 1, \cdots, \frac{L}{M} - 1\,, \end{aligned} \tag{D.5}$$

$$\begin{aligned} y &= b_y \frac{L}{M} + i_y\,, \quad \text{where} \\ b_y &= 0, 1, \cdots, M-1 \quad \text{and} \\ i_y &= 0, 1, \cdots, \frac{L}{M} - 1\,. \end{aligned} \tag{D.6}$$

As the reader will notice, M^2 physical coordinates (x, y) have the same superspin coordinates (i_x, i_y). The bit index $i_b = Mb_y + b_x$ is the position inside the superspin (so

$0 \leq i_b < M^2$). Fig. D.2 shows a graphical example of the packing process of a $L = 16$ square lattice using $M = 4$.

Recall that this packing process satisfies our constraints:

- The parity of the original lattice, given by $(x + y) \bmod 2$, coincides with the parity of the corresponding superspin site $(i_x + i_y) \bmod 2$. So, the superspin lattice is bipartite as well.
- For a superspin (i_x, i_y), the M^2 nearest-neighbors spins along the (say) forward x-direction in the physical lattice are all packed within the same superspin, which is the nearest-neighbor superspin in the forward i_x-direction (see Fig. D.2). As the reader will notice, the only difficult part arises from the borders of the superspin lattice. Let us consider the site (x, y) and its nearest neighbor in the forward x-direction, with coordinate x $(x + 1) \bmod L$. This neighbor is packed in the super spin of coordinate $(i_x + 1) \bmod (L/M)$, but we must consider two possibilities:
    - If $i_x < L/M - 1$, the coordinates i_y, b_x and b_y remain unchanged,
    - but if $i_x = L/M - 1$, then b_x changes as $b_x \to (b_x + 1) \bmod M$ (int the forward y-direction we have an analogous situation, but with i_y and b_y).

Then, we can use the color update scheme, i.e., update all the even sites and after all the odd ones. This scheme allows the superspins to be stored in separate memory regions (see below for an explicit example).

A working example

In order to exemplify the problem of determining the spin changes within the same word in the MUSI scheme, we will discuss our solution for the two-dimensional Ising model. For the sake of clarity, we shall constantly be referring to a single bit, $\mathtt{s}_{\boldsymbol{x}}(t)$, in the superspin (remember that all the boolean operations are performed simultaneously on the m bits $\mathtt{s}_{\boldsymbol{x}}(t)$ contained in the superspin).

We want to obtain a change bit $\mathtt{B}_{\boldsymbol{x}}(t)$, which is one if (and only if) the spin at site $\boldsymbol{x}$ is to be flipped at Monte Carlo time t (for the sake of clarity, let us use C language notation):

$$\mathtt{s}_{\boldsymbol{x}}(t+1) = \mathtt{s}_{\boldsymbol{x}}(t) \,\hat{}\, \mathtt{B}_{\boldsymbol{x}}(t)\,, \tag{D.7}$$

where ˆ refers to the XOR Boolean operation.

The computation of $\mathtt{B}_{\boldsymbol{x}}(t)$ is naturally decomposed in two steps (the first is a deterministic step, while the second step involves randomness):

1. In the first step, we compute the energy change ΔE that flipping spin $s_{\boldsymbol{x}}(t)$ would cause. In the two-dimensional Ising model, ΔE can take five values, $\{-8, -4, 0, 4, 8\}$. Hence, using standard Boolean operations, one computes five bits —$\{\mathtt{cm8}_{\boldsymbol{x}}, \mathtt{cm4}_{\boldsymbol{x}}, \mathtt{c0}_{\boldsymbol{x}}, \mathtt{c4}_{\boldsymbol{x}}, \mathtt{c8}_{\boldsymbol{x}}\}$ respectively— in such a way, only the bit associated with ΔE is one. The remaining four bits are, of course, zero.
2. The second step depends on the dynamics and determines whether or not the spin-flip is allowed. This is represented by other five bits $\{\mathtt{bm8}_{\boldsymbol{x}}, \mathtt{bm4}_{\boldsymbol{x}}, \mathtt{b0}_{\boldsymbol{x}}, \mathtt{b4}_{\boldsymbol{x}}, \mathtt{b8}_{\boldsymbol{x}}\}$, which are set to one with probability $p(\Delta E)$ (see below).

Then, we obtain $\mathtt{B}_{\boldsymbol{x}}(t)$ from these bits as (for shortness, we will omit their dependence on $\boldsymbol{x}$ and t):

$$\texttt{B = [c8 \& b8] | [c4 \& b4] | [c0 \& b0] | [cm4 \& bm4] | [cm8 \& bm8]}\,, \tag{D.8}$$

where `&` and `|` stand for the Booleand *bitwise* AND and OR, respectively.

As the reader will notice, Eq. (D.8) tells us that we will use only one of the five bits `b` (although we cannot know in advance which one). Indeed, the AND conditions make irrelevant those bits `b` which are not related to the current ΔE. Hence, the five `b` bits do not need to be mutually independent (instead, the `b` bits corresponding to different $\vec{x}$ or t must be statistically independent). We can use this observation to reduce the number of `b` bits we need to compute. For this purpose, we must consider that the probability of setting to one of the random bits `b` depends on the dynamics we simulate. For example, in Chapter 3 we have considered:

a) Metropolis:

$$p_{\mathrm{MET}}(\Delta E) = \min\{1, e^{-\Delta E/T}\}\,, \tag{D.9}$$

b) Heat-Bath:

$$p_{\mathrm{HB}}(\Delta E) = \frac{e^{-\Delta E/T}}{1 + e^{-\Delta E/T}}\,. \tag{D.10}$$

Therefore, we can make use of these observations to reduce the number of `b` bits that we need to compute according to the dynamics:

a) In the Metropolis dynamics, we only need two bits because $p_{\mathrm{MET}}(\Delta E) = 1$ for $\Delta E \leq 0$. Therefore, we set `bm8 = bm4 = b0 = 1`.

b) In the Heat-Bath dynamics, because $p_{\mathrm{HB}}(\Delta E) = 1 - p_{\mathrm{HB}}(-\Delta E)$, we set `bm8 = ~b8` and `bm4 = ~b4`, where `~` is the Boolean NOT.

Thus, generating two statistically independent bits `b4` and `b8` for each spin contained in our superspin is enough to carry out our Monte Carlo. The Appendix F describes how to generate these bits.

D.2.2 Our MUSI packing for the two-dimensional quantum spin glass

In our study of the two-dimensional quantum SG, we have considered a packing that only refers to the Euclidean-time axis (remember the Trotter approximation — see Appendix A). We decided to use this scheme because, while along the Euclidean time, the system has only ferromagnetic interactions, in the XY-plane, we have random interactions given by the coupling matrix $J_{\vec{x},\vec{y}}$. Furthermore, we have considered systems with $L_\tau \gg L$. Then, in our chosen scheme, the geometry of the XY-plane is not modified.

Let us start by packing the complete physical lattice site (x, y, τ) in the superspin (with 32 bits each of them) lattice of sites $(\tilde{x}, \tilde{y}, \tilde{\tau})$ by the relations

$$\begin{aligned} x &= \tilde{x}\,, \\ y &= \tilde{y}\,, \\ \tau &= b\frac{L_\tau}{32} + \tilde{\tau}\,, \end{aligned} \tag{D.11}$$

where $i_\tau = 0, 1, \cdots, L_\tau/32 - 1$, and $b = 0, 1, \cdots, 31$. As the reader will notice, this scheme also preserves the original parity $p = (x \,\mathrm{XOR}\, y \,\mathrm{XOR}\, \tau) \,\mathrm{AND}\, 1 = (\tilde{x} \,\mathrm{XOR}\, \tilde{y} \,\mathrm{XOR}\, \tilde{\tau}) \,\mathrm{AND}\, 1$, provided that L_τ is a multiple of 64 (our program requires it to be a multiple of 2048). Then, we can store the superspin $(\tilde{x}, \tilde{y}, \tilde{\tau})$ lattice in two separated lattices according to their parity (or color in the checkerboard sense). Then, the superspin coordinates $(\tilde{x}, \tilde{y}, \tilde{\tau})$ are related with the split lattice coordinates (i_x, i_y, i_τ) as

$$\begin{aligned} \tilde{x} &= i_x \,, \\ \tilde{y} &= i_y \,, \\ \tilde{\tau} &= 2i_\tau + \mathrm{color}_\tau \,, \end{aligned} \tag{D.12}$$

where color_τ is the corresponding color in the checkerboard scheme of the superspin lattice, which can be computed as $\mathrm{color}_\tau = p \,\mathrm{XOR}\, [(i_x \,\mathrm{XOR}\, i_y), \mathrm{AND}\, 1]$.

D.2.3 The daemon bits

As we did for the case of the two-dimensional Ising model, in order to carry out our Monte Carlo simulation of the quantum spin glass in two dimensions, we have to find a way to update all the spins contained in one of our superspins synchronously. To achieve this through the algorithm of Ref. [IK90], we need to obtain 32 independent and identically distributed integers d_j that identify what spins can be flipped in the superspin (according to their ΔE). These 32 integers are coded in the two 32-bit daemon words `id1` and `id2`: $d_j = \mathtt{id1}_j + 2 * \mathtt{id2}_j$, where $\mathtt{id1}_j$ and $\mathtt{id2}_j$ are, respectively, the j-th bits of `id1` and `id2`. The distribution of interest for d_j is

$$\begin{aligned} &\text{Probability for } d_j = 0 \ (\mathtt{id1}_j = 0\,, \mathtt{id2}_j = 0): && 1 - \mathrm{e}^{-4k}\,, \\ &\text{Probability for } d_j = 1 \ (\mathtt{id1}_j = 1\,, \mathtt{id2}_j = 0): && \mathrm{e}^{-4k} - \mathrm{e}^{-8k}\,, \\ &\text{Probability for } d_j = 2 \ (\mathtt{id1}_j = 0\,, \mathtt{id2}_j = 1): && \mathrm{e}^{-8k} - \mathrm{e}^{-12k}\,, \\ &\text{Probability for } d_j = 3 \ (\mathtt{id1}_j = 1\,, \mathtt{id2}_j = 1): && \mathrm{e}^{-12k}\,. \end{aligned}$$

To obtain the `id1` and `id2` daemons, let us consider 3 statistically independent 32-bit word `b4`, `b8` and `b12` such that:

1. Each bit in the word is statistically independent.
2. A given bit is set to one with probability e^{-4k}.

In Appendix F, we discuss how to generate such a `b4`, `b8` and `b12`.

Then, if we successfully derive $\mathtt{id1}_j$ and $\mathtt{id2}_j$ from the corresponding bits $\mathtt{b4}_j$, $\mathtt{b8}_j$ and $\mathtt{b12}_j$ (by applying boolean operators to the words `b4`, `b8`, `b12`) the statistical independence of the 32 d_j will be assured.

Our first step consists of applying the boolean AND operator in the following way (for the sake of shortness, let us use C language notation):

```
b8=b4&b8;
b12=b8&b12;
```

As the reader will notice, the new value of the bit $\mathtt{b8}_j$ will be equal to 1 only if the two original bits $\mathtt{b4}_j$ and $\mathtt{b8}_j$ were equal to one, which happens with probability e^{-8k} (as the initial two bits were statistically independent, their probabilities of being set to one are multiplied through the AND operation). Similarly, the new $\texttt{b12}_j$ will be one only if the three original bits $\texttt{b4}_j$, $\texttt{b8}_j$ and $\texttt{b12}_j$ were also one, which happens with probability e^{-12k}. Hence, the probabilities for the three bits *after* the AND operations are

$$\begin{aligned}
&\text{Probability for } \texttt{b4}_j = 0\,,\ \texttt{b8}_j = 0\,,\ \texttt{b12}_j = 0\ : && 1 - \mathrm{e}^{-4k}\,,\\
&\text{Probability for } \texttt{b4}_j = 1\,,\ \texttt{b8}_j = 0\,,\ \texttt{b12}_j = 0\ : && \mathrm{e}^{-4k} - \mathrm{e}^{-8k}\,,\\
&\text{Probability for } \texttt{b4}_j = 1\,,\ \texttt{b8}_j = 1\,,\ \texttt{b12}_j = 0\ : && \mathrm{e}^{-8k} - \mathrm{e}^{-12k}\,,\\
&\text{Probability for } \texttt{b4}_j = 1\,,\ \texttt{b8}_j = 1\,,\ \texttt{b12}_j = 1\ : && \mathrm{e}^{-12k}\,.
\end{aligned}$$

These probabilities are exactly what we want for d_j. Therefore, we will have achieved our goal if we can define a Boolean operation function $f(\texttt{b4}_j, \texttt{b8}_j, \texttt{b12}_j) \to (\texttt{id1}_j, \texttt{id2}_j)$ which satisfies the following relationships

$$\begin{aligned}
\texttt{b4}_j = 0\,,\ \texttt{b8}_j = 0\,,\ \texttt{b12}_j = 0\ &\Rightarrow \texttt{d1}_j = 0\,,\ \texttt{d2}_j = 0\,,\\
\texttt{b4}_j = 1\,,\ \texttt{b8}_j = 0\,,\ \texttt{b12}_j = 0\ &\Rightarrow \texttt{d1}_j = 1\,,\ \texttt{d2}_j = 0\,,\\
\texttt{b4}_j = 1\,,\ \texttt{b8}_j = 1\,,\ \texttt{b12}_j = 0\ &\Rightarrow \texttt{d1}_j = 0\,,\ \texttt{d2}_j = 1\,,\\
\texttt{b4}_j = 1\,,\ \texttt{b8}_j = 1\,,\ \texttt{b12}_j = 1\ &\Rightarrow \texttt{d1}_j = 1\,,\ \texttt{d2}_j = 1\,.
\end{aligned}$$

By building the truth table, it is straightforward to show that the desired function $f(\texttt{b4}_j, \texttt{b8}_j, \texttt{b12}_j) \to (\texttt{id1}_j, \texttt{id2}_j) \to (\texttt{id1}_j, \texttt{id2}_j)$ is given by the following C code:

```
id2=b8;
id1=(b4^b8)|b12,
```

where `^` is the *bitwise* XOR and `|` is the *bitwise* OR operator.

E

Continuous-time Monte Carlo

In Chapter 2, we have considered a continuous-time Monte Carlo (MC) method. In this appendix, we discuss our implementation. We refer the reader to Chapter 2 for an explanation of our notation convention. Let us start by saying that, in a continuous time MC algorithm, we first need to determine the interval time Δt between changes in the configuration. To compute this interval time, we need to consider the probability of not changing the configuration $\boldsymbol{x}$ in the time interval $(t, t+\Delta t)$. From the discussion in Sect. 2.1.2 we can straightforwardly show that this probability is

$$\lim_{r\to\infty} [W_{\epsilon_r}]^{n_r}_{\boldsymbol{x},\boldsymbol{x}} = \mathrm{e}^{-|R_{\boldsymbol{x},\boldsymbol{x}}|\Delta t/\tau_0}\,, \tag{E.1}$$

where τ_0 defines our time units. As the reader will notice, a Poisson process gives the probability for the interval time between changes in the configuration. This situation is canonical for a n-fold way simulation [BKL75, Gil77]. Let us briefly review the process of conducting such a simulation.

Consider that we want to update our system for times $t \in [t_1, t_2]$ starting from configuration $\boldsymbol{x}_{\text{ini}}$ at time t_1. So, we set our clock to $t = t_1$ and execute the following steps (for the sake of clarity, we name $\boldsymbol{x}$ to the current spin configuration):

1. Generate the time increment Δt until the next spin-flip as

   $$\Delta t = -\frac{\tau_0}{|R_{\boldsymbol{x},\boldsymbol{x}}|}\log(u)\,, \tag{E.2}$$

   where u is a uniformly distributed random number in the unit interval $(0, 1]$.

2. Now, there are two possibilities according to the value of $t + \Delta t$:

   a If $t + \Delta t > t_2$, stop the simulation. For observables that must be computed for a time $t' \in (t_1, t_2)$, compute them in the final spin configuration.

   b If $t + \Delta t < t_2$ continue to (3).

3. Update the clock $t \to t + \Delta t$. Because the spin configuration is constant for all the times $t' \in (t, t + \Delta t)$, any observable that must be computed at t' should be computed *before* changing the configuration in step (4).

4. Choose the spin to be flipped with probability $R_{\boldsymbol{x},\boldsymbol{y}}/R_{\boldsymbol{x},\boldsymbol{x}}$. Remember that $R_{\boldsymbol{x},\boldsymbol{y}} \neq 0$ if the new state $\boldsymbol{y}$ differ from the old state $\boldsymbol{x}$ in the value of more than one spin. Note that this step should be skipped if $t + \Delta t > t_2$.

5. Return to (1).

For an Ising model, there is a simple technical trick to speed up the simulation considerably. For simplicity, we will consider the Ising chain studied in Chapter 2. Let us recall that

$$R^{\mathrm{HB}}_{\boldsymbol{x},\boldsymbol{y}} = \frac{\exp\{-[\mathcal{H}(\boldsymbol{y}) - \mathcal{H}(\boldsymbol{x})]/(k_{\mathrm{B}}T_{\mathrm{b}})\}}{1 + \exp\{-[\mathcal{H}(\boldsymbol{y}) - \mathcal{H}(\boldsymbol{x})]/(k_{\mathrm{B}}T_{\mathrm{b}})\}}\,, \tag{E.3}$$

where $\mathcal{H}(\boldsymbol{x})$ is the energy of the state configuration $\boldsymbol{x}$ given by the Hamiltonian

$$\mathcal{H}(\boldsymbol{x}) = -J\sum_{i=1}^{N} s_i\, s_{i+1} - h\sum_{i=1}^{N} s_i\,. \tag{E.4}$$

Therefore, $R_{\boldsymbol{x},\boldsymbol{y}}$ depends only on the energy change when flipping one of the spins in the initial configuration $\boldsymbol{x}$. Let us consider that we modify the spin s_k, so the energy change depends solely on $s_{k-1} + s_{k+1}$ (which has three possible values: $-2, 0, 2$), and on the value of $s_k = \pm 1$ itself. Then, there are only 3×2 possible kinds of spins. We can use this classification to create six lists of spins (one of every type of spin) and use them to efficiently compute Δt and decide which spin to update. Notice that after making a spin-flip, we need to perform some bookkeeping to keep our list up to date. To associate each spin s_k with its list, we can use the binary representation of spins $s_i = -1 \to b_i = 0$ and $s_i = 1 \to b_i = 1$ so that the binary number $b_{k-1}b_k b_{k+1}$ unequivocally identifies the kind of spin.

Our random bits for MUSI simulations

To obtain the results of Chapters 3 and 6 we have used multispin MUlti-SIte (MUSI) multispin coding (see Appendix D). This has forced us to generate words of m independent random bits with prescribed probabilities. In the following sections of this appendix, we describe our employed methods.

F.1 Our random bits for the two-dimensional Ising model

In Appendix D, we mentioned that to carry out our MUSI simulations of the two-dimensional Ising model, we need to generate a set of m independent random bits that take the value 1 with an arbitrary probability p. The textbook solution [NB99] fails the independence requirement unless p can be precisely represented with a limited number of bits. Conversely, the Gillespie method [FMM15] proves inefficient for our particular problem due to the elevated critical temperature, resulting in an excessively large p. To address this challenge, we devise a solution that combines elements of the textbook and Gillespie methods through strategic interpolation.

Everything we are going to discuss below is valid for generating any one of the 5 bits $\{\texttt{bm8}_x,\ \texttt{bm4}_x,\ \texttt{b0}_x,\ \texttt{b4}_x,\ \texttt{b8}_x\}$ discussed in Appendix D. Therefore, we will consider only one, e.g., `b4`. We obtain `b` as `b4 = d1 | d2`, where `d1` and `d1` are two independent random bits which are set to one with probabilities p_1 and p_2, respectively, and `|` is the Boolean *bitwise* operator. It is straightforward to show that the probability $p(4)$ for having $\texttt{b4} = 1$ is $p(4) = p_1 + p_2(1 - p_1)$. Hence, if we choose p_1 in some convenient way (see below), we need to set p_2 as

$$p_2 = \frac{p(4) - p_1}{1 - p_1}\,. \tag{F.1}$$

The overall idea is the following: if we can generate `d1` efficiently with a probability p_1 that is very close to, but smaller than, $p(4)$, we will then have a sufficiently small p_2 to enable an efficient application of the Gillespie method to obtain `d2`.

Specifically, we require that p_1 be exactly representable with n bits

$$\begin{aligned} p_1 = \frac{k^*+1}{2^n},\ \text{with } k^* \in \mathbb{N},\ 0\ \le\ k^* < 2^n,\ \text{ and} \\ \frac{k^*+1}{2^n}\ \le\ p(4)\ <\ \frac{k^*+2}{2^n}\,. \end{aligned} \tag{F.2}$$

We obtain `d1` by generating an integer-valued random number k, $0 \leq k < 2^n$, with uniform probability. We set $\texttt{d1} = 1$ if $k \leq k^*$.

Note that the value of n determines the efficiency of the algorithm. On the one hand, to get a smaller value of p_2 that allows a higher efficiency of the Gillespie method, we want a value of n large so that p_1 is very close to $p(4)$. On the other hand, to generate the number k, we need n independent random bits set to one with 50% probability. A tradeoff must be found, minimizing the number of calls to our random number generator.

A significant simplification is that we can use the same random integer k for all the possible changes in the energy, ΔE, only the threshold $k^*(\Delta E)$ varies. In this way, we obtain all the bits `d1` for every `b8` and `b4` (recall that we only need to generate `b8` and `b4`; see Appendix D).

At this point, it is worth noting that although the discussion on generating d_1 has been done for a single bit, in the case of having m bit words, we must generate m independent numbers k. In particular, in our work, we have used $m = 265$. To achieve this, we have used the xoshiro256++ generator [BV21], ensuring the same randomness level on each of its 64 bits. In fact, we employed a 256-bit streaming extension to implement a parallel version of xoshiro256++, composed of four independent xoshiro256++ random sequences, which produces 256 independent random bits, which are 1 with 50% probability. Therefore, n calls to our xoshiro256++ implementation produce 256 independent k random numbers.

Finally, in the general case where we only need to generate one bit with probability p, we would have to obtain the bit`d2` with probability p_2. For this, we could use a Gillespie method. However, in our case, instead of using two Gillespie methods to generate `b4` and `b8`, one for each of the bits `d2` needed, we can use a faster way.

We have two different probabilities p_2, one for `b8` $[p_2(8)]$, and other for `b4` $[p_2(4)]$. Let us define $p_{\max} = \max\{p_2(4), p_2(8)\}$ and $p_{\min} = \min\{p_2(4), p_2(8)\}$. Then, we can implement the Gillespie method for $p_{\max}$, which gives the bits $\texttt{d2}^{\max}$ for the ΔE with bigger p_2 probability. Finally, the bit $\texttt{d2}^{\min}$ corresponding to $p_{\min}$ is set to one if two conditions are met:

1. The bit $\texttt{d2}^{\max}$ corresponding to $p_{\max}$ is set to one,
2. An independent random number r, extracted with uniform probability in $[0, 1)$, turns out to be smaller than $p_{\min}/p_{\max}$.

F.2 Our random bits for the two-dimensional quantum spin glasses

As described in Appendix D, to use our implementation of the daemon algorithm [IK90] in our MUSI program (see Appendix D), we must be able to generate 32-bit words (that are named `b4`, `b8` and `b12` in Appendix D) that should meet the following two criteria:

(i) all bits should be statistically independent;

(ii) (each bit) is set to one with probability equal to e^{-4k} [recall k in Eq. (6.9)].

The process to obtain one of these words, for example `b4`, uses four "50/50" 64-bit random words (i.e., each bit has the same probability 1/2 of being one or 0). To generate one of these 64-bit random words, we use our own CUDA implementation of the D.E. Shaws's counter-based philox_4x32_10 parallel generator [SMDS11]. We combine a subset of the philox_4x32_10 bits with another subset produced by a single iteration of the xoroshiro128++ transformation [BV21]. From each of these 64-bit random words, we obtain an 8-bit random integer (so a total of 32 bits), which satisfies our constraints (i) and (ii). To generate these 8 bits integers, we proceed as follows:

1. Let us consider an integer $n = 0, 1, \ldots, 255$ (notice it is an 8-bit integer) with a probability
$$P[n] = \mathrm{e}^{-4k*\texttt{pop\_count}(n)} * (1 - \mathrm{e}^{-4k})^{[8-\texttt{pop\_count}(n)]}\,, \tag{F.3}$$
where pop_count(n) is the *population count* function that returns the number of bits equal to 1 in n.[†]

2. For each n, we build a "normalized cumulative"
$$\begin{aligned} \texttt{cum\_float}(0) &= P[0]\,, \\ &\vdots \\ \texttt{cum\_float}(n) &= \texttt{cum\_float}(n-1) + P(n)\,, \\ \texttt{cum\_float}(n) &= 2^{64} * \texttt{cum\_float}(n)\,, \text{ for } n = 0, 1, 2, \cdots, 255\,, \end{aligned}$$
and a $\texttt{cumulative}(n)$ that is the 64-bit truncation of $\texttt{cum\_float}(n)$
$$\texttt{cumulative}(-1) = -1, \ldots, \texttt{cumulative}(255) = \tilde{}0\,, \tag{F.4}$$
where ~ stands for computational negation.

3. Then, given one of the 64 bit "50/50" random words, we find $0 \leq n^* \leq 255$ such that
$$\texttt{cumulative}(n^*-1) \leq 64 \text{ bit "50/50" random word} < \texttt{cumulative}(n^*)\,. \tag{F.5}$$
We set as well $n^* = 255$ if the "50/50" 64-bit random word equals `~0`.

To speed up the search for n^*, we resort to a binary search combined with a look-up table. Repeating this procedure four times, we compute our 32-bit word, which satisfies (i) and (ii).

[†] Hence, every one of the 8 bits in n is statistically independent, and set to 1 with probability e^{-4k}. Even for the largest k value in our simulations [BPMMP23], $k = 0.32$, one has $\mathrm{e}^{-4*k*8} = \mathrm{e}^{-10.24} \approx 2^{-14.773}$ which is perfectly representable with 64-bit arithmetics.

G

Space integrals of correlation function

Estimating the coherence length $\xi(t)$ in out-of-equilibrium systems has been a problem in numerical analysis. Part of the problem arises from the fact that, despite our ability to compute the correlation function $C(r;t)$ [or $C_4(r;t)$; see Sect. 1.4.2] and our knowledge that it decays as

$$C(r \to \infty; t) \sim \frac{1}{r^a} f\left[\frac{r}{\xi(t)}\right] \tag{G.1}$$

for long distances, the explicit form of function $f(x)$ and exponent a are known only at equilibrium. However, as we discussed in Sect. 1.4.2, it is possible to compute the coherence length from the integral estimators

$$I_k(t) = \int_0^\infty r^k C(T,r,t) \mathrm{d}r \,. \tag{G.2}$$

Specifically, we can define the estimator

$$\xi_{k,k+1}(t) \equiv \frac{I_{k+1}(t)}{I_k(t)} \,, \tag{G.3}$$

which is proportional to $\xi(t)$. Following Refs. [BJCC+18, FMMM+18, FMMM+19] (and references therein), we have been chosen as our estimator of the coherence length $\xi(t)$ the ratio $\xi_{1,2}(t)$.

Then, we are interested in estimating the integrals Eq. (G.2) for $k = 1$ and 2. The difficulty arises from the significant relative errors $\Delta C(r;t)/C(r;t)$ in the large-r tail of the correlation function. The same problem arises in the analysis of noise time series (see, e.g., Ref. [Sok97]). In fact, our solution is inspired by the methods of Refs. [BJCC+18, FMMM+18, FMMM+19], our strategy combines two ideas: (1) we reduce the relative error by considering a sufficiently large number of replicas, and (2) estimate the integrals $I_k(t)$ carefully.

Specifically, we estimate the integral $I_k(t)$ as the sum of two contributions: the numerical integration of our measured $C(r;t)$ up to a noise-dependent cut-off, and a tail contribution from a smooth extrapolation function, namely

$$F(r) = \frac{A\mathrm{e}^{-(r/\xi_F)^\alpha}}{r^b} \,, \tag{G.4}$$

where the amplitude A, the length scale ξ_F and the exponent α are the fitting parameters. The exponent b, is $b = 1/2$ in the Ising model (see Chapter 3), while it is also a fitting parameter in the Edwards-Anderson model (see Chapter 5).

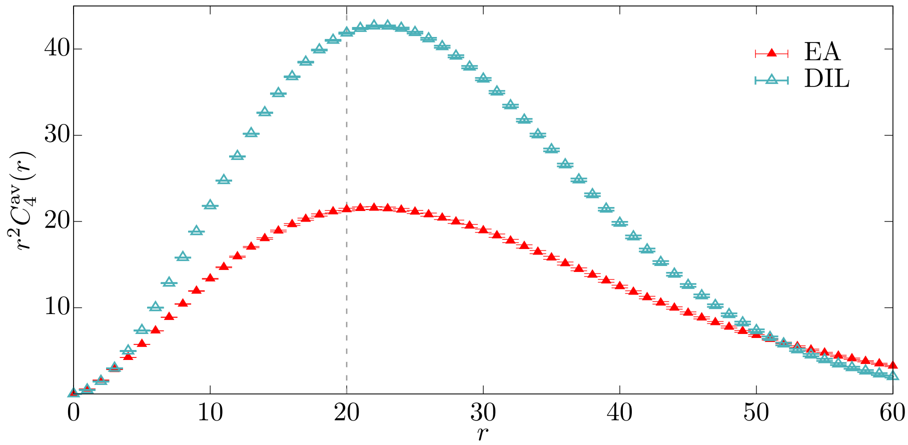

Figure G.1: Integrator for $I_2(t)$, i.e $r^2C_4^{\mathbf{av}}(r,t_{\mathbf{w}})$, as computed for the three-dimensional Ising link-diluted model (DIL) and for the Edwards-Anderson model (EA), versus the distance r. Data obtained in system of linear size $L = 160$ with coherence length $\xi(t_{\text{w}}) = 20$ (dashed vertical line) at temperature $T = 0.9$. Study of the coherence length performed in the analysis of the four-body correlation function in Chapter 5.

The reader will complain about the value of $b = 1/2$ chosen for studying the ferromagnetic phase in the Ising model —Chapter 3. It is true that, strictly speaking, $b = 1/2$ is only valid in the paramagnetic phase. However, in other situations, the exponential term decays very fast, making the value of b irrelevant.

The complete procedure to compute I_k in Chapter 3 (in Chapter 5 is very similar, with the exception that b is also a fit parameter) is:

1. The statisitcal errors determine a spatial cut-off r_{cut}. The cut-off is the shortest distance such that $C(r_{\text{cut}}+1;t)$ is smaller than three times its error, i.e. $C(r_{\text{cut}}+1;t) < \Delta C(r_{\text{cut}}+1;t)$. Recall that r_{cut} is time-dependent.
2. Define a region $[r_{\text{min}}, r_{\text{max}}]$ where we perform the fit to $F(r)$. To calculate this interval, we follow the next steps:
   (a) Locate the position r^* where $r^2C(r;t)$ is maximum. Let us call $\rho = r^{*2}C(r^*;t)$ to such maximum value.
   (b) Locate the values r_{min} and r_{max}, which must verify the inequalities
   $$r^* < r_{\text{min}} < r_{\text{max}} < r_{\text{cut}}\,.$$
   The values of r_{min} (resp. r_{max}) is the smaller r such that $r^2C(r;t) < 0.9\rho$ [resp. $r^2C(r;t) < \rho/3$].
   (c) if $r_{\text{max}} \geq r_{\text{cut}}$, we consider that we need more replicas.
3. Finally, we calculate the integrals. There are two possibilities (in both cases, we estimate errors with the jackknife method; see Appendix H for more details):
   - If $r_{\text{max}} - r_{\text{min}} > 8$, we fit the correlation function in the interval $[r_{\text{min}}, r_{\text{max}}]$ to $F(r)$, which fitting parametes the amplitude A, the length scale ξ_F and the exponent β. Then, the integral is the sum of the integral of our data of $C(r;t)$ from $r = 0$ to r_{max} and the integral of the fit $F(r)$ from r_{max} to $r = 20\xi_F$.

- If $[r_{\mathrm{min}}, r_{\mathrm{max}}]$ is small (i.e. $r_{\mathrm{max}} - r_{\mathrm{min}} \leq 8$, we integrate only numerically our data of $C(r;t)$ up to the cut-off r_{cut}.

To compute the integral, we consider a second-order Gaussian quadrature. In addition, if an interpolation of $C(r;t)$ is needed, we use a cubic spline interpolation. In Fig. G.1, we show the integrand for $k = 2$ in the case of the Ising link-diluted model (DIL) and Edwards-Anderson model (EA) models corresponding to the study carried out in the Chapter 5. To clarify the process, we include in Fig. G.1 the definitions of the different parameters considered when calculating the integral $I_k(t)$.

H

Error estimation and automatic fitting process

This appendix lists the main statistical techniques used throughout this thesis. As the reader will have noticed, due to the nonlinearity of the quantities studied and the large amount of data at our disposal (sometimes correlated), we have decided to employ two resampling methods to compute the statistical errors: jackknife and bootstrap. Both techniques are widely known, and extensive literature exists (e.g., [You12]). Therefore, we will limit ourselves to briefly describing our implementation of both methods.

Another difficulty we have faced in obtaining the results of chapters 5 and 6 is related to the large number of fits we have made. Indeed, because specific quantities (think, for instance, of the Euclidean correlation lengths discussed in Chapter 6) are only accessible by fitting, and because of the large number of samples we have analyzed, we have been forced to develop automatic procedures to perform these fits. In Sect. H.3 of this appendix, we will describe how such automation was performed for the study presented in Chapter 6.

H.1 Jackknife method

Let us consider a set $\mathcal{A}$ of N measures of some observable $\mathcal{O}_i$. The jackknife method (JK) considers groups of n of the N samples, called jackknife blocks. In our case, we have used the most widespread method, which consists of making blocks of length $n = N - 1$. Then, we label each block by the non-considered measure, i.e., $\mathcal{O}_i^{\mathrm{JK}} = \mathcal{A}/\mathcal{O}_i$.

For each of the jackknife blocks, we can compute its estimator

$$\mathbb{E}(\mathcal{O}_i^{\mathrm{JK}}) = \frac{1}{n-1} \sum_{j \neq i} \mathcal{O}_i \,. \tag{H.1}$$

Then, for any function $f(x)$ (the relevance of the method is achieved for non-linear functions), we can define its JK blocks as $f_i^{\mathrm{JK}} = f[\mathbb{E}(\mathcal{O}_i^{\mathrm{JK}})]$. The JK error estimator for $f(\mathcal{O})$ is (see, e.g., [You12])

$$\sigma_f = \sqrt{\frac{N-1}{N} \sum_i \left[f_i^{\mathrm{JK}} - \mathbb{E}_{\mathrm{JK}}(f^{\mathrm{JK}})\right]^2} \,, \tag{H.2}$$

where $\mathbb{E}_{\mathrm{JK}}(f^{\mathrm{JK}})$ is the expected value of f^{JK}, defined as

$$\mathbb{E}_{\mathrm{JK}}(f^{\mathrm{JK}}) = \frac{1}{N} \sum_i f_i^{\mathrm{JK}} \,. \tag{H.3}$$

H.2 Bootstrap method

As in the discussion of the Jackknife method, we have a set $\mathcal{A}$ of N measures of some observable $\mathcal{O}_i$. However, unlike the previous case, $N_\mathrm{B} \neq N$ blocks of N samples are generated in the bootstrap method. To generate every one of these blocks, N samples are randomly chosen with uniform probability from the set $\mathcal{A}$, allowing the same sample to be chosen several times. Then, we have created N_B “new” sets $\mathcal{A}_k$ with N samples.

The expected values for set sets $\mathcal{A}_k$ $(k = 1, 2, \cdots, N_\mathrm{B})$ are

$$\mathbb{E}(\mathcal{O}^\mathrm{B}) \equiv \frac{1}{N} \sum_i^N n_{i,k} \mathcal{O}_i \,, \tag{H.4}$$

where $n_{i,k}$ is the number of times that sample i appears in the $\mathcal{A}_k$ set.

In close analogy with the jackknife method method, for a function $f(x)$ we can define its corresponding bootstrap blocks as $f_k^\mathrm{B} = f[\mathbb{E}(\mathcal{O}_k^\mathrm{B})]$. Then, the mean value of f over the bootstrap block is

$$\mathbb{E}_\mathrm{B}(f^\mathrm{B}) = \frac{1}{N_\mathrm{B}} \sum_k^{N_\mathrm{B}} f_k^\mathrm{B} \,. \tag{H.5}$$

Thus, the estimator of the standard deviation of $f(\mathcal{O})$ calculated by the bootstrap method is given by the following expression [You12]:

$$\sigma_f = \sqrt{\frac{N}{(N-1)(N_\mathrm{B}-1)} \sum_k^{N_\mathrm{B}} \left[f_k^\mathrm{B} - \mathbb{E}_\mathrm{B}(f^\mathrm{B})\right]^2} \,. \tag{H.6}$$

H.3 Automatic fitting process

As the reader will notice, in chapters 5 and 6, we have performed many different fits. To mention a few examples, to make the extrapolations of the median of C_4 for each of the 16 samples to the various $\xi(t_\mathrm{w})$ in chapter 5, or to obtain the Euclidean correlation lengths in chapter 6. Carrying out these processes manually would have been nearly impossible.

As a solution, we have implemented in a C-code a nonlinear least-square method using the Levenberg-Marquardt solver [Lev44] routine available at the GNU Scientific Library along this process. We performed a series of manual adjustments with GNUplot to calibrate the automatic adjustment procedure. In all of our fits, we consider the χ^2/dof computed with the diagonal part of the covariance matrix as a figure of merit.

In the remainder of this section, we describe the more complex example of the above procedure in this thesis: the process followed to obtain the distribution function of the Euclidean correlation lengths discussed in chapter 6. In addition, we include our computation of the distribution function of the Euclidean correlation lengths.

H.3.1 Automatic fits for the Euclidean correlation lengths

For a fixed value of k [recall Eq. (6.9)] we have obtained the functions $C(t)$ and $Q_2(t)$ [recall Eq. (6.23)], and their error, for each of our samples from the 6 replicas at our disposal.

As in Appendix G, we need a fitting window [Sok97, BCC+08b] to analyze the noisy correlation functions. We have chosen the upper limit of the fitting window as

$$\tau_{\mathrm{w},f} \equiv \min_\tau\{\tau | f(\tau) \leq 3.5\, \sigma_{f(\tau)}\}\,, \tag{H.7}$$

with $f(\tau)$ either $C(\tau)$ or $Q_{2,\mathrm{s}}(\tau) = Q_2(\tau) - Q_{2,\mathrm{pl}}$ (we refer as $Q_{2,\mathrm{pl}}$ the plateau, see Fig. 6.3), and $\sigma_{f(\tau)}$ the corresponding standard error. At this point, we need to face two different problems, one related with $C(\tau)$, the other with $Q_{2,\mathrm{s}}(\tau)$.

Fitting $C(\tau)$

In our investigation of the odd correlation function, we have found that for some samples, $\tau_{\mathrm{w},C} > L_\tau/2$. This means that the ratio between the Euclidean correlation length η and L_τ, namely η/L_τ, is not small enough to allow for a safe determination of η (see Fig. 6.11). This will affect our estimation of the distribution function of η and its errors, but let us focus now on the samples for which we are able to estimate η, i.e., samples with $\tau_{\mathrm{w},C} < L_\tau/2$.

We have fitted our data from samples with $\tau_{\mathrm{w},C} < L_\tau/2$ to

$$C(\tau) = B\left[\mathrm{e}^{-\tau/\eta} + \mathrm{e}^{(\tau - L_\tau)/\eta}\right]\,, \tag{H.8}$$

where the amplitude B and the correlation length η are the fitting parameters.

To perform this fit we have considered the fitting window $[\tau_{\mathrm{min},C}, \tau_{\mathrm{w},C}]$. We made a series of fits varying $\tau_{\mathrm{min},C}$ to obtain the best window. Specifically, we have been increasing $\tau_{\mathrm{min},C}$ in steps of 1, starting from $\tau_{\mathrm{min},C} = \tau_{\mathrm{w},C}/10$ to $\tau_{\mathrm{w},C}/2$. We stop when the corresponding χ^2/dof goes below 1.

Fitting $Q_{2,\mathrm{s}}(\tau)$

Despite $Q_{2,\mathrm{s}}(\tau)$ is not affected by the impossibility of determining its corresponding Euclidean correlation lengths, η_e and η_o (see Fig. 6.9), we need to estimate the plateau $Q_{2,\mathrm{pl}}$.

To do so, we fit $Q_{2,\mathrm{s}}(\tau)$ for $\tau \in [L_\tau/4, L_\tau/2]$ to a constant $Q_{2,\mathrm{pl}}$. In those rare cases in which this fit was not acceptable (as determined by its χ^2/dof), we consider $\tau_{\mathrm{w},C} = L_\tau/2$ and we take $Q_{2,\mathrm{pl}}$ as a fitting parameter.

Therefore, to obtain the Euclidean correlation lengths, we fit our data to

$$Q_2(\tau) = Q_{2,\mathrm{pl}} + B_\mathrm{e}\mathrm{e}^{-\tau/\eta_\mathrm{e}} + B_\mathrm{o}\mathrm{e}^{-\tau/\eta_\mathrm{o}}\,, \tag{H.9}$$

where only the amplitudes B_i and the correlation lengths η_e and η_o are fitting parameters (and also $Q_{2,\mathrm{pl}}$ for the above alluded to exceptional samples).

We first perform a fit to only one exponential. As in the previous case, we modify the fitting window $[\tau_{\mathrm{min},Q_2}, \tau_{\mathrm{w},Q_2}]$, by increasing τ_{min,Q_2} from 1 to $\tau_{\mathrm{w},Q_2}/2$ until $\chi^2/\mathrm{dof} < 0.5$. After that, we consider a fit with the two exponential terms and keep the best fit. In cases where we employ two exponential terms, because we cannot determine which of the two correlation lengths corresponds to η_e, we take the larger of the two.

H.3.2 Interpolating the distribution function of Euclidean correlation lengths

Once the Euclidean correlation lengths have been determined, we have calculated their empirical distribution functions $F(\log\eta)$ and $F(\eta_{\mathrm{e}})$. For the sake of simplicity, let us consider X be either $\log\eta$ or η_{e}. Then, we can compute the inverse function $X[F]$ by sorting in increasing order the N_{S} values of X and setting $X[F = i/N_{\mathrm{S}}]$ as the i-th item in the ordered list.

To calculate the value of $X[F]$ at k, we have performed a linear interpolation from the results of $X[F]$ at the two nearest k values of the Parallel Tempering grid.

To estimate errors in $X[F]$, we employ a bootstrap method with $N_{\mathrm{B}} = 10000$. In order to create the bootstrap blocks, we extract each value X from a normal distribution centered in the X_i, and with standard deviation, the fitting error of X_i (i identifies the chosen sample).

To conclude, we should mention that for the case $X = \log\eta$, we had to face the problem of only being able to calculate X for N_{OK} of the N_{S} samples. For this we have decided to determine $X[F]$ only up to (see Fig. 6.11)

$$F_{\mathrm{safe}} \equiv \frac{1}{N_{\mathrm{S}}}\left[N_{\mathrm{OK}} - 4\sqrt{\frac{N_{\mathrm{OK}}(N_{\mathrm{S}} - N_{\mathrm{OK}})}{N_{\mathrm{S}}}}\right] , \tag{H.10}$$

i.e., the maximum possible F minus four standard deviates. Then, we only consider bootstrap blocks for which X could be obtained in at least $F_{\mathrm{safe}}N_{\mathrm{S}}$ samples.

I

RSB couplings in 4D: combinatorial problem

In Sect. 4.1.4, we discussed the calculation of the coupling constants ω_1 and ω_2 for the Edwards-Anderson model model in finite dimension [cf. Eqs. (4.10) and (4.11)], which can be computed from the connected-correlations at zero external momentum [PR13] as:

$$\omega_1 \equiv \frac{1}{N}\sum_{ijk}\overline{\langle s_i s_j\rangle_{\mathrm{c}}\langle s_j s_k\rangle_{\mathrm{c}}\langle s_k s_j\rangle_{\mathrm{c}}}\,, \tag{I.1}$$

$$\omega_2 \equiv \frac{1}{2N}\sum_{ijk}\overline{\langle s_i s_j s_k\rangle_{\mathrm{c}}^2}\,. \tag{I.2}$$

By defining the overlap fluctuation δQ_{ab} between replicas

$$\delta Q_{ab} \equiv \frac{1}{N}\sum_i s_i^{(a)} s_i^{(b)} - \frac{1}{N}\sum_i \overline{\langle s_i\rangle^2} = Q_{ab} - q\,, \tag{I.3}$$

it is possible to express both couplings ω_1 and ω_2 in terms of the following eight cubic overlaps [cf. Eqs. (4.20) and (4.21)] [PR13].

$$\begin{array}{lclclcl}
\mathcal{W}_1 & \equiv & N^2\overline{\langle \delta Q_{12}\delta Q_{23}\delta Q_{31}\rangle}\,, & \qquad & \mathcal{W}_5 & \equiv & N^2\overline{\langle \delta Q_{12}\delta Q_{13}\delta Q_{21}\rangle}\,,\\
\mathcal{W}_2 & \equiv & N^2\overline{\langle \delta Q_{12}^3\rangle}\,, & & \mathcal{W}_6 & \equiv & N^2\overline{\langle \delta Q_{12}\delta Q_{13}\delta Q_{14}\rangle}\,,\\
\mathcal{W}_3 & \equiv & N^2\overline{\langle \delta Q_{12}^2\delta Q_{13}\rangle}\,, & & \mathcal{W}_7 & \equiv & N^2\overline{\langle \delta Q_{12}\delta Q_{13}\delta Q_{45}\rangle}\,,\\
\mathcal{W}_4 & \equiv & N^2\overline{\langle \delta Q_{12}^2\delta Q_{34}\rangle}\,, & & \mathcal{W}_8 & \equiv & N^2\overline{\langle \delta Q_{12}\delta Q_{34}\delta Q_{56}\rangle}\,.
\end{array}$$

Thus, substituting Eq. (I.3) in the definitions of the eight cubic overlaps, we can obtain the expressions that allow us to perform the calculations of the couplings constants ω_1 and ω_2 from the results of numerical simulations. For example, for $\mathcal{W}_1$ we have that

$$\begin{aligned}
\mathcal{W}_1 &= N^2\overline{\langle \delta Q_{ab}\delta Q_{bc}\delta Q_{ca}\rangle} = N^2\overline{\langle (Q_{ab}-q)(Q_{bc}-q)(Q_{ca}-q)\rangle}\\
&= N^2\overline{\langle Q_{ab}Q_{bc}Q_{ca} - q(Q_{ab}Q_{bc}+Q_{bc}Q_{ca}+Q_{ba}Q_{ac}) + q^2(Q_{ab}+Q_{bc}+Q_{ca}) - q^3\rangle}\\
&= N^2[\overline{\langle Q_{ab}Q_{bc}Q_{ca}\rangle} - 3q\overline{\langle Q_{ab}Q_{bc}\rangle} + 2q^3]
\end{aligned} \tag{I.4}$$

where we have use the fact that Q_{ab} is a symmetric matrix, i.e. $Q_{ab} = Q_{ba}$, an that $\overline{\langle Q_{ab}\rangle} = q$.

Following the same method, it is straightforward to obtain that

$$
\begin{aligned}
\mathcal{W}_1 &= N^2[\overline{\langle Q_{ab}Q_{bc}Q_{ca}\rangle} - 3q\overline{\langle Q_{ab}Q_{bc}\rangle} + 2q^3]\,,\\
\mathcal{W}_2 &= N^2[\overline{\langle Q_{ab}^3\rangle} - 3q\overline{\langle Q_{ab}^2\rangle} + 2q^3]\,,\\
\mathcal{W}_3 &= N^2[\overline{\langle Q_{ab}^2 Q_{bc}\rangle} - q(\overline{\langle Q_{ab}^2\rangle} - 2\overline{\langle Q_{ab}Q_{bc}\rangle}) + 2q^3]\,,\\
\mathcal{W}_4 &= N^2[\overline{\langle Q_{ab}^2 Q_{cd}\rangle} - q(\overline{\langle Q_{ab}^2\rangle} - 2\overline{\langle Q_{ab}Q_{cd}\rangle}) + 2q^3]\,,\\
\mathcal{W}_5 &= N^2[\overline{\langle Q_{ab}Q_{ac}Q_{bd}\rangle} - q(2\overline{\langle Q_{ab}Q_{bc}\rangle} + \overline{\langle Q_{ab}Q_{cd}\rangle}) + 2q^3]\,,\\
\mathcal{W}_6 &= N^2[\overline{\langle Q_{ab}Q_{ac}Q_{ad}\rangle} - 3q\overline{\langle Q_{ab}Q_{bc}\rangle} + 2q^3]\,,\\
\mathcal{W}_7 &= N^2[\overline{\langle Q_{ab}Q_{bc}Q_{de}\rangle} - q(\overline{\langle Q_{ab}Q_{bc}\rangle} + 2\overline{\langle Q_{ab}Q_{de}\rangle}) + 2q^3]\,,\\
\mathcal{W}_8 &= N^2[\overline{\langle Q_{ab}Q_{cd}Q_{ef}\rangle} - 3q\overline{\langle Q_{ab}Q_{cd}\rangle} + 2q^3]\,.
\end{aligned}
$$

The number of different subindexes in each expression determines the number of independent replicas needed to evaluate the expression. Then, because we have four replicas we have not compute directly $\mathcal{W}_7$ and $\mathcal{W}_8$ (see discussion on Sect. 4.1.4).

Let us mention that, to compute each of the different expected values for the product of different overlaps, we have averaged over all possible combinations of sub-indices at our disposal. For example, with four replicas

$$
\overline{\langle Q_{ab}Q_{bc}Q_{ca}\rangle} = \frac{1}{4}\overline{\langle Q_{12}Q_{23}Q_{31} + Q_{23}Q_{34}Q_{42} + Q_{34}Q_{41}Q_{13} + Q_{41}Q_{12}Q_{24}\rangle}\,. \tag{I.5}
$$

In order to determine the number of possible ways to choose the replicas and the order of replicas, it is useful to use a pictorial representation. In particular, we represent the replicas as the vertex of a square (because we have four replicas), and the connections between vertices are the terms Q_{ab}. Then, for example, we can represent $\overline{\langle Q_{ab}Q_{bc}Q_{ca}\rangle}$ as

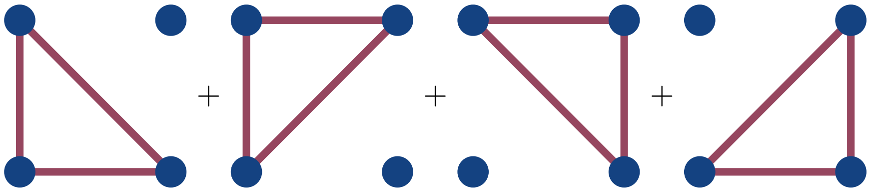

Bibliography

[ABCS07] Jeferson J. Arenzon, Alan J. Bray, Leticia F. Cugliandolo, and Alberto Sicilia. Exact results for curvature-driven coarsening in two dimensions. *Phys. Rev. Lett.*, 98:145701, Apr 2007. 45

[ABL+21] Samuel Albert, Giulio Biroli, Fran çois Ladieu, Roland Tourbot, and Pierfrancesco Urbani. Searching for the gardner transition in glassy glycerol. *Phys. Rev. Lett.*, 126:028001, Jan 2021. 59

[ABM+16] S. Albert, Th. Bauer, M. Michl, G. Biroli, J.-P. Bouchaud, A. Loidl, P. Lunkenheimer, R. Tourbot, C. Wiertel-Gasquet, and F. Ladieu. Fifth-order susceptibility unveils growth of thermodynamic amorphous order in glass-formers. *Science*, 352(6291):1308–1311, 2016. 59

[AL18] Tameem Albash and Daniel A. Lidar. Adiabatic quantum computation. *Rev. Mod. Phys.*, 90:015002, Jan 2018. 96

[ALP+22] Maria Chiara Angelini, Carlo Lucibello, Giorgio Parisi, Gianmarco Perrupato, Federico Ricci-Tersenghi, and Tommaso Rizzo. Unexpected upper critical dimension for spin glass models in a field predicted by the loop expansion around the bethe solution at zero temperature. *Phys. Rev. Lett.*, 128(7):075702, 2022. 59, 66, 121, 127

[AMM05] D. J. Amit and V. Martín-Mayor. *Field Theory, the Renormalization Group and Critical Phenomena.* World Scientific, Singapore, third edition, 2005. 23, 62, 63, 103, 109

[AMMH17] Tameem Albash, Victor Martin-Mayor, and Itay Hen. Temperature scaling law for quantum annealing optimizers. *Phys. Rev. Lett.*, 119:110502, Sep 2017. 116

[AMMH19] Tameem Albash, Victor Martin-Mayor, and Itay Hen. Analog errors in ising machines. *Quantum Science and Technology*, 4(2):02LT03, apr 2019. 116

[And70] P.W. Anderson. Localisation theory and cumn problems - spin glasses. *Materials Research Bulletin*, 5:549, 1970. 4, 12

[AOH86] M. Alba, M. Ocio, and J. Hammann. Ageing process and response function in spin glasses: An analysis of the thermoremanent magnetization decay in ag:mn (2.6%). *Europhysics Letters*, 2(1):45, jul 1986. 9

[ARAR08] Jose Alvarez-Ramirez, Jesus Alvarez, and Eduardo Rodriguez. Short-term predictability of crude oil markets: a detrended fluctuation analysis approach. *Energy Economics*, 30(5):2645–2656, 2008. 73

[Arr65] Anthony Arrott. Neutron Diffraction Studies of Pd, Ni, FeMn, and Cu(Mn) Single Crystals. *Journal of Applied Physics*, 36(3):1093–1093, 07 1965. 4

[Bar82] F Barahona. On the computational complexity of ising spin glass models. *Journal of Physics A: Mathematical and General*, 15(10):3241, 1982. 11, 95

[Bar83] M. N. Barber. Finite-size scaling. volume 8 of *Phase Transitions and Critical Phenomena*. Academic Press, 1983. 109

[Bar12] Michael F. Barnsley. *Fractals Everywhere*. Dover Publications, Inc., USA, 2012. 73

[Bax08] Rodney Baxter. *Exactly Solved Models in Statistical Mechanics*. Dover Publications, 2008. 95

[BB02] Ludovic Berthier and Jean-Philippe Bouchaud. Geometrical aspects of aging and rejuvenation in the ising spin glass: A numerical study. *Phys. Rev. B*, 66:054404, Aug 2002. 45, 54

[BBB$^+$05] L. Berthier, G. Biroli, J.-P. Bouchaud, L. Cipelletti, D. El Masri, D. L'Hôte, F. Ladieu, and M. Pierno. Direct experimental evidence of a growing length scale accompanying the glass transition. *Science*, 310:1797, 2005. 59

[BCBJ04] P.-E. Berche, C. Chatelain, B. Berche, and W. Janke. Bond dilution in the 3d ising model: a monte carlo study. *The European Physical Journal B - Condensed Matter and Complex Systems*, 38:463–474, 2004. 75

[BCC$^+$08a] F. Belletti, M. Cotallo, A. Cruz, L. A. Fernandez, A. Gordillo, A. Maiorano, F. Mantovani, E. Marinari, V. Martín-Mayor, A. Muñoz Sudupe, D. Navarro, S. Perez-Gaviro, J. J. Ruiz-Lorenzo, S. F. Schifano, D. Sciretti, A. Tarancon, R. Tripiccione, and J. L. Velasco. Simulating spin systems on IANUS, an FPGA-based computer. *Comp. Phys. Comm.*, 178:208–216, 2008. 45, 66, 76

[BCC$^+$08b] F. Belletti, M Cotallo, A. Cruz, L. A. Fernandez, A. Gordillo-Guerrero, M. Guidetti, A. Maiorano, F. Mantovani, E. Marinari, V. Martín-Mayor, A. M. Sudupe, D. Navarro, G. Parisi, S. Perez-Gaviro, J. J. Ruiz-Lorenzo, S. F. Schifano, D. Sciretti, A. Tarancon, R. Tripiccione, J. L. Velasco, and D. Yllanes. Nonequilibrium spin-glass dynamics from picoseconds to one tenth of a second. *Phys. Rev. Lett.*, 101:157201, 2008. 46, 76, 91, 169

[BCF$^+$00] H. G. Ballesteros, A. Cruz, L. A. Fernandez, V. Martín-Mayor, J. Pech, J. J. Ruiz-Lorenzo, A. Tarancon, P. Tellez, C. L. Ullod, and C. Ungil.

Critical behavior of the three-dimensional Ising spin glass. *Phys. Rev. B*, 62:14237–14245, 2000. 23, 103

[BCF$^+$09] F. Belletti, A. Cruz, L. A. Fernandez, A. Gordillo-Guerrero, M. Guidetti, A. Maiorano, F. Mantovani, E. Marinari, V. Martín-Mayor, J. Monforte, A. Muñoz Sudupe, D. Navarro, G. Parisi, S. Perez-Gaviro, J. J. Ruiz-Lorenzo, S. F. Schifano, D. Sciretti, A. Tarancon, R. Tripiccione, and D. Yllanes. An in-depth look at the microscopic dynamics of Ising spin glasses at fixed temperature. *J. Stat. Phys.*, 135:1121, 2009. 24, 91

[BCT$^+$93] R. Benzi, S. Ciliberto, R. Tripiccione, C. Baudet, F. Massaioli, and S. Succi. Extended self-similarity in turbulent flows. *Phys. Rev. E*, 48:R29–R32, Jul 1993. 78

[BDHV01] Jean-Philippe Bouchaud, Vincent Dupuis, Jacques Hammann, and Eric Vincent. Separation of time and length scales in spin glasses: Temperature as a microscope. *Phys. Rev. B*, 65:024439, Dec 2001. 4

[Bec71] P.A. Beck. Some recent results on magnetism in alloys. *Metallurgical Transactions*, 2:2015, 1971. 3, 4

[BFM$^+$18] A Billoire, L A Fernandez, A Maiorano, E Marinari, V Martin-Mayor, J Moreno-Gordo, G Parisi, F Ricci-Tersenghi, and J J Ruiz-Lorenzo. Dynamic variational study of chaos: spin glasses in three dimensions. *Journal of Statistical Mechanics: Theory and Experiment*, 2018(3):033302, 2018. 21, 101, 116

[BFMM$^+$98] H. G. Ballesteros, L. A. Fernández, V. Martín-Mayor, A. Muñoz Sudupe, G. Parisi, and J. J. Ruiz-Lorenzo. Critical exponents of the three-dimensional diluted ising model. *Phys. Rev. B*, 58:2740–2747, Aug 1998. 96

[BFMMMS96] H. G. Ballesteros, L. A. Fernandez, V. Martín-Mayor, and A. Muñoz Sudupe. New universality class in three dimensions?: the antiferromagnetic RP^2 model. *Phys. Lett. B*, 378:207, 1996. 109

[BFPP12] M. Bernaschi, M. Fatica, G. Parisi, and L. Parisi. Multi-gpu codes for spin systems simulations. *Computer Physics Communications*, 183(7):1416–1421, 2012. 149

[BGM$^+$09] F. Belletti, M. Guidetti, A. Maiorano, F. Mantovani, S. F. Schifano, R. Tripiccione, M. Cotallo, S. Perez-Gaviro, D. Sciretti, J. L. Velasco, A. Cruz, D. Navarro, A. Tarancon, L. A. Fernandez, V. Martín-Mayor, A. Muñoz-Sudupe, D. Yllanes, A. Gordillo-Guerrero, J. J. Ruiz-Lorenzo, E. Marinari, G. Parisi, M. Rossi, and G. Zanier. Janus: An FPGA-based system for high-performance scientific computing. *Computing in Science and Engineering*, 11:48, 2009. 23

[Bin81] K. Binder. Finite size scaling analysis of ising model block distribution functions. *Z. Phys. B – Condensed Matter*, 43:119–140, 1981. 63, 111

[Bin87] K Binder. Theory of first-order phase transitions. *Reports on Progress in Physics*, 50(7):783, jul 1987. 45

[BJBnC$^+$13] M. Baity-Jesi, R. A. Baños, Andres Cruz, Luis Antonio Fernandez, Jose Miguel Gil-Narvion, Antonio Gordillo-Guerrero, David Iniguez, Andrea Maiorano, F. Mantovani, Enzo Marinari, Victor Martín-Mayor, Jorge Monforte-Garcia, Antonio Muñoz Sudupe, Denis Navarro, Giorgio Parisi, Sergio Perez-Gaviro, M. Pivanti, F. Ricci-Tersenghi, Juan Jesus Ruiz-Lorenzo, Sebastiano Fabio Schifano, Beatriz Seoane, Alfonso Tarancon, Raffaele Tripiccione, and David Yllanes. Critical parameters of the three-dimensional Ising spin glass. *Phys. Rev. B*, 88:224416, 2013. 75, 76

[BJBnC$^+$14a] M. Baity-Jesi, R. A. Baños, Andres Cruz, Luis Antonio Fernandez, Jose Miguel Gil-Narvion, Antonio Gordillo-Guerrero, David Iniguez, Andrea Maiorano, Mantovani F., Enzo Marinari, Victor Martín-Mayor, Jorge Monforte-Garcia, Antonio Muñoz Sudupe, Denis Navarro, Giorgio Parisi, Sergio Perez-Gaviro, M. Pivanti, F. Ricci-Tersenghi, Juan Jesus Ruiz-Lorenzo, Sebastiano Fabio Schifano, Beatriz Seoane, Alfonso Tarancon, Raffaele Tripiccione, and David Yllanes. Dynamical Transition in the D =3 Edwards-Anderson spin glass in an external magnetic field. *Phys. Rev. E*, 89:032140, 2014. 59

[BJBnC$^+$14b] M. Baity-Jesi, R. A. Baños, Andres Cruz, Luis Antonio Fernandez, Jose Miguel Gil-Narvion, Antonio Gordillo-Guerrero, David Iniguez, Andrea Maiorano, Mantovani F., Enzo Marinari, Victor Martín-Mayor, Jorge Monforte-Garcia, Antonio Muñoz Sudupe, Denis Navarro, Giorgio Parisi, Sergio Perez-Gaviro, M. Pivanti, F. Ricci-Tersenghi, Juan Jesus Ruiz-Lorenzo, Sebastiano Fabio Schifano, Beatriz Seoane, Alfonso Tarancon, Raffaele Tripiccione, and David Yllanes. The three dimensional Ising spin glass in an external magnetic field: the role of the silent majority. *J. Stat. Mech.*, 2014:P05014, 2014. 59, 67, 82

[BJBnC$^+$14c] M. Baity-Jesi, R. A. Baños, Andres Cruz, Luis Antonio Fernandez, Jose Miguel Gil-Narvion, Antonio Gordillo-Guerrero, David Iniguez, Andrea Maiorano, F. Mantovani, Enzo Marinari, Victor Martín-Mayor, Jorge Monforte-Garcia, Antonio Muñoz Sudupe, Denis Navarro, Giorgio Parisi, Sergio Perez-Gaviro, M. Pivanti, F. Ricci-Tersenghi, Juan Jesus Ruiz-Lorenzo, Sebastiano Fabio Schifano, Beatriz Seoane, Alfonso Tarancon, Raffaele Tripiccione, and David Yllanes. Janus II: a new generation application-driven computer for spin-system simulations. *Comp. Phys. Comm*, 185:550–559, 2014. 5, 11, 17, 74, 75, 76, 95, 101

[BJCC$^+$17a] M. Baity-Jesi, E. Calore, A. Cruz, L. A. Fernandez, J. M. Gil-Narvion, A. Gordillo-Guerrero, D. Iñiguez, A. Maiorano, E. Marinari, V. Martin-Mayor, J. Monforte-Garcia, A. Muñoz Sudupe, D. Navarro, G. Parisi, S. Perez-Gaviro, F. Ricci-Tersenghi, J. J. Ruiz-Lorenzo, S. F. Schifano, B. Seoane, A. Tarancon, R. Tripiccione, and D. Yllanes. Matching microscopic and macroscopic responses in glasses. *Phys. Rev. Lett.*, 118:157202, Apr 2017. 45

[BJCC$^+$17b] Marco Baity-Jesi, Enrico Calore, Andres Cruz, Luis Antonio Fernandez, José Miguel Gil-Narvión, Antonio Gordillo-Guerrero, David Iñiguez, Andrea Maiorano, Enzo Marinari, Victor Martin-Mayor, Jorge Monforte-Garcia, Antonio Muñoz Sudupe, Denis Navarro, Giorgio Parisi, Sergio Perez-Gaviro, Federico Ricci-Tersenghi, Juan Jesus Ruiz-Lorenzo, Sebastiano Fabio Schifano, Beatriz Seoane, Alfonso Tarancón, Raffaele Tripiccione, and David Yllanes. A statics-dynamics equivalence through the fluctuation–dissipation ratio provides a window into the spin-glass phase from nonequilibrium measurements. *Proceedings of the National Academy of Sciences*, 114(8):1838–1843, 2017. 45, 76

[BJCC+18] M. Baity-Jesi, E. Calore, A. Cruz, L. A. Fernandez, J. M. Gil-Narvion, A. Gordillo-Guerrero, D. Iñiguez, A. Maiorano, E. Marinari, V. Martin-Mayor, J. Moreno-Gordo, A. Muñoz Sudupe, D. Navarro, G. Parisi, S. Perez-Gaviro, F. Ricci-Tersenghi, J. J. Ruiz-Lorenzo, S. F. Schifano, B. Seoane, A. Tarancon, R. Tripiccione, and D. Yllanes. Aging rate of spin glasses from simulations matches experiments. *Phys. Rev. Lett.*, 120:267203, Jun 2018. 45, 76, 77, 91, 163

[BJCC+19] Marco Baity-Jesi, Enrico Calore, Andres Cruz, Luis Antonio Fernandez, José Miguel Gil-Narvión, Antonio Gordillo-Guerrero, David Iñiguez, Antonio Lasanta, Andrea Maiorano, Enzo Marinari, Victor Martin-Mayor, Javier Moreno-Gordo, Antonio Muñoz Sudupe, Denis Navarro, Giorgio Parisi, Sergio Perez-Gaviro, Federico Ricci-Tersenghi, Juan Jesus Ruiz-Lorenzo, Sebastiano Fabio Schifano, Beatriz Seoane, Alfonso Tarancón, Raffaele Tripiccione, and David Yllanes. The mpemba effect in spin glasses is a persistent memory effect. *Proceedings of the National Academy of Sciences*, 116(31):15350–15355, 2019. 27, 45, 46

[BJCC+21] M. Baity-Jesi, E. Calore, A. Cruz, L. A. Fernandez, J. M. Gil-Narvion, I. Gonzalez-Adalid Pemartin, A. Gordillo-Guerrero, D. Iñiguez, A. Maiorano, E. Marinari, V. Martin-Mayor, J. Moreno-Gordo, A. Muñoz Sudupe, D. Navarro, I. Paga, G. Parisi, S. Perez-Gaviro, F. Ricci-Tersenghi, J. J. Ruiz-Lorenzo, S. F. Schifano, B. Seoane, A. Tarancon, R. Tripiccione, and D. Yllanes. Temperature chaos is present in off-equilibrium spin-glass dynamics. *Communications physics*, 4(1):74, 2021. 74, 76, 83

[BJCC+23] M. Baity-Jesi, E. Calore, A. Cruz, L. A. Fernandez, J. M. Gil-Narvion, I. Gonzalez-Adalid Pemartin, A. Gordillo-Guerrero, D. Iñiguez, A. Maiorano, E. Marinari, V. Martin-Mayor, J. Moreno-Gordo, A. Muñoz Sudupe, D. Navarro, I. Paga, G. Parisi, S. Perez-Gaviro, F. Ricci-Tersenghi, J. J. Ruiz-Lorenzo, S. F. Schifano, B. Seoane, A. Tarancon, and D. Yllanes. Memory and rejuvenation effects in spin glasses are governed by more than one length scale. *Nat. Phys.*, 2023. 5, 11, 45, 74, 76, 83

[BK11] K. Binder and W. Kob. *Glassy Materials and Disordered Solids. An Introduction to Their Statistical Mechanics.* World Scientific, Singapore, 2011. 3

[BKC21] John Bechhoefer, Avinash Kumar, and Raphaël Chétrite. A fresh understanding of the mpemba effect. *Nat. Rev. Phys.*, 3:534, 2021. 27

[BKL75] A. B. Bortz, M. H. Kalos, and J. L. Lebowitz. A new algorithm for Monte Carlo simulation of Ising spin systems. *J. Comp. Phys.*, 17:10–18, 1975. 157

[BM87a] A. J. Bray and M. A. Moore. Chaotic nature of the spin-glass phase. *Phys. Rev. Lett.*, 58:57–60, Jan 1987. 16, 59, 66

[BM87b] A. J. Bray and M. A. Moore. Scaling theory of the ordered phase of spin glasses. In J. L. van Hemmen and I. Morgenstern, editors, *Heidelberg Colloquium on Glassy Dynamics*, number 275 in Lecture Notes in Physics. Springer, Berlin, 1987. 16, 59, 66

[BMdPSFdsdE86] H. Bouchiat, P. Monod, and Université de Paris-Sud. Faculté des sciences d'Orsay (Essonne). *Transition verre de spin: comportement critique et bruit magnétique.* Lille thèses. éditeur inconnu, 1986. 4, 8, 59

[BMP$^+$06] F. Belletti, F. Mantovani, G. Poli, S. F. Schifano, R. Tripiccione, I. Campos, A. Cruz, D. Navarro, S. Perez-Gaviro, D. Sciretti, A. Tarancon, J. L. Velasco, P. Tellez, L. A. Fernandez, V. Martín-Mayor, A. Muñoz Sudupe, S. Jimenez, A. Maiorano, E. Marinari, and J. J. Ruiz-Lorenzo. Ianus: And adaptive fpga computer. *Computing in Science and Engineering*, 8:41, 2006. 5, 17, 60

[BMRU82] F. Barahona, T. Maynard, R. Rammal, and J. P. Uhry. Morphology of ground states of two-dimensional frustration model. *J. Phys. A*, 15(02):673, 1982. 21

[BnCF$^+$12] R. A. Baños, Andres Cruz, Luis Antonio Fernandez, Jose Miguel Gil-Narvion, Antonio Gordillo-Guerrero, Marco Guidetti, David Iniguez, Andrea Maiorano, Enzo Marinari, Victor Martín-Mayor, Jorge Monforte-Garcia, Antonio Muñoz Sudupe, Denis Navarro, Giorgio Parisi, Sergio Perez-Gaviro, Juan Jesus Ruiz-Lorenzo, Sebastiano Fabio Schifano, Beatriz Seoane, Alfonso Tarancon, Pedro Tellez, Raffaele Tripiccione, and David Yllanes. Thermodynamic glass transition in a spin glass without time-reversal symmetry. *Proc. Natl. Acad. Sci. USA*, 109:6452, 2012. 59, 60, 66, 67, 68, 69, 70

[BNJ08] Elmar Bittner, Andreas Nußbaumer, and Wolfhard Janke. Make life simple: Unleash the full power of the parallel tempering algorithm. *Phys. Rev. Lett.*, 101:130603, Sep 2008. 20

[BPMMP23] Massimo Bernaschi, Isidoro González-Adalid Pemartín, Víctor Martín-Mayor, and Giorgio Parisi. The quantum transition of the two-dimensional ising spin glass: A tale of two gaps, 2023. 17, 161

[BPPV84] R Benzi, G Paladin, G Parisi, and A Vulpiani. On the multifractal nature of fully developed turbulence and chaotic systems. *Journal of Physics A: Mathematical and General*, 17(18):3521, dec 1984. 73

[BR80] A. J. Bray and S. A. Roberts. Renormalisation-group approach to the spin glass transition in finite magnetic fields. *J. Phys. C: Solid St. Phys.*, 13:5405, 1980. 59, 61, 66, 70

[Bra94] A. J. Bray. Theory of phase-ordering kinetics. *Adv. Phys.*, 43:357, 1994. 45, 48

[Bro59] R. Brout. Statistical mechanical theory of a random ferromagnetic system. *Phys. Rev.*, 115:824–835, Aug 1959. 12

[BRP23] Apurba Biwas, R Rajesh, and Arnab Pal. Mpemba effect in a langevin system: population statistics, metastability and other exact results. *arXiv:2304.06420*, 2023. 27

[BS09] A.-L. Barabási and H. E. Stanley. *Fractal Concepts in Surface Growth.* Cambridge University Press, New York, 2009. 73

[BSVI07] Paul Brenner, Christopher R. Sweet, Dustin VonHandorf, and Jesús A. Izaguirre. Accelerating the replica exchange method through an efficient all-pairs exchange. *The Journal of Chemical Physics*, 126(7):074103, 2007. 20

[BV21] David Blackman and Sebastiano Vigna. Scrambled linear pseudorandom number generators. *ACM Trans. Math. Softw.*, 47(4), sep 2021. 160, 161

[BY86] K. Binder and A. P. Young. Spin glasses: Experimental facts, theoretical concepts, and open questions. *Rev. Mod. Phys.*, 58:801–976, Oct 1986. 3

[Cal05] F. Calvo. All-exchanges parallel tempering. *The Journal of Chemical Physics*, 123(12):124106, 2005. 20

[Car96] J. Cardy. *Scaling and Renormalization in Statistical Field Theory*, volume 5 of *Lecture notes in physics.* P. Goddard and J. Yeomans, Cambridge University Press, Cambridge, 1996. 96

[Car12] John Cardy. *Finite-size scaling.* Elsevier, 2012. 96, 109

[Cav09] Andrea Cavagna. Supercooled liquids for pedestrians. *Physics Reports*, 476(4):51–124, 2009. 59, 61

[CCAMM$^+$06] I. Campos, M. Cotallo-Aban, V. Martín-Mayor, S. Perez-Gaviro, and A. Tarancon. *Phys. Rev. Lett.*, 97:217204, 2006. 3

[CCFS86] J. T. Chayes, L. Chayes, Daniel S. Fisher, and T. Spencer. Finite-size scaling and correlation lengths for disordered systems. *Phys. Rev. Lett.*, 57:2999–3002, Dec 1986. 111

[CFJ$^+$03] A. Cruz, L. A. Fernández, S. Jiménez, J. J. Ruiz-Lorenzo, and A. Tarancón. Off-equilibrium fluctuation-dissipation relations in the $3d$ ising spin glass in a magnetic field. *Phys. Rev. B*, 67:214425, Jun 2003. 59

[CFL+12] F. Caltagirone, U. Ferrari, L. Leuzzi, G. Parisi, F. Ricci-Tersenghi, and T. Rizzo. On the critical slowing down exponents of mode coupling theory. *Phys. Rev. Lett.*, 108:085702, 2012. 61

[Cha84] Ralph V. Chamberlin. Time decay of the thermoremanent magnetization in spin-glasses as a function of the time spent in the field-cooled state. *Phys. Rev. B*, 30:5393–5395, Nov 1984. 9

[CL23] Supraja S Chittari and Zhiyue Lu. Geometric approach to nonequilibrium hasty shortcuts. *arXiv:2304.06822*, 2023. 27, 28

[Cla04] J. Clarke. *The SQUID handbook Vol 1 Fundamentals and technology of SQUIDs and SQUID systems.* Wiley VCH, Germany, 2004. CONDENSED MATTER PHYSICS, SUPERCONDUCTIVITY AND SUPERFLUIDITY. 4

[CLL21] Federico Carollo, Antonio Lasanta, and Igor Lesanovsky. Exponentially accelerated approach to stationarity in markovian open quantum systems through the mpemba effect. *Phys. Rev. Lett.*, 127(6):060401, 2021. 27, 45

[CM72] V. Cannella and J. A. Mydosh. Magnetic ordering in gold-iron alloys. *Phys. Rev. B*, 6:4220–4237, Dec 1972. 4

[CMB71] V. Cannella, J. A. Mydosh, and J. I. Budnick. Magnetic Susceptibility of Au–Fe Alloys. *Journal of Applied Physics*, 42(4):1689–1690, 1971. 4, 8

[CMM+23] Patrick Charbonneau, Enzo Marinari, Marc Mézard, Giorgio Parisi, Federico Ricci-Tersenghi, Gabriele Sicuro, and Francesco Zamponi, editors. *Spin Glass Theory and Far Beyond.* World Sientific, 2023. 3, 15, 16

[CMMM02] L. Correale, E. Marinari, and V. Martín-Mayor. Eigenvalue analysis of the density matrix of four-dimensional spin glasses supports replica symmetry breaking. *Phys. Rev. B*, 66:174406, Nov 2002. 103

[CP86] C Castellani and L Peliti. Multifractal wavefunction at the localisation threshold. *Journal of physics A: mathematical and general*, 19(8):L429, 1986. 73

[CPR13] Francesco Caltagirone, Giorgio Parisi, and Tommaso Rizzo. Critical off-equilibrium dynamics in glassy systems. *Phys. Rev. E*, 87:032134, Mar 2013. 61

[Cro07] Gavin E. Crooks. Measuring thermodynamic length. *Phys. Rev. Lett.*, 99:100602, Sep 2007. 27

[CS92] A. Crisanti and H.-J. Sommers. The spherical p-spin interaction spin glass model: the statics. *Zeitschrift für Physik B Condensed Matter*, 87(3):341–354, Oct 1992. 3

[CY17] Patrick Charbonneau and Sho Yaida. Nontrivial critical fixed point for replica-symmetry-breaking transitions. *Phys. Rev. Lett.*, 118:215701, May 2017. 59, 66

[dAT78] J. R. L. de Almeida and D. J. Thouless. Stability of the Sherrington-Kirkpatrick solution of a spin glass model. *J. Phys. A: Math. Gen.*, 11:983, 1978. 4, 15, 59

[DC00] Tom Davis and John Cardy. Correlated correlation functions in random-bond ferromagnets. *Nuclear Physics B*, 570(3):713–725, 2000. 77

[DD91] David A. Huse and Daniel S. Fisher. On the behavior of ising spin glasses in a uniform magnetic field. *J. Phys. I France*, 1(5):621–625, 1991. 59

[dDG06] C. de Dominicis and I. Giardina. *Random Fields and Spin Glasses: a field theory approach*. Cambridge University Press, Cambridge, England, 2006. 3, 16

[Dei00] Roberto Deidda. Rainfall downscaling in a space-time multifractal framework. *Water Resources Research*, 36(7):1779–1794, 2000. 73

[DLP$^+$20] Maddalena Dilucca, Luca Leuzzi, Giorgio Parisi, Federico Ricci-Tersenghi, and Juan J. Ruiz-Lorenzo. Spin glasses in a field show a phase transition varying the distance among real replicas (and how to exploit it to find the critical line in a field). *Entropy*, 22(2), 2020. 59

[dNC59] J. de Nobel and F.J. Chatenier. Specific heats of dilute alloys of manganese in silver and copper at low temperatures and in magnetic fields. *Physica*, 25:969–979, January 1959. 3, 5

[Dot01] V. Dotsenko. *Introduction to the Replica Theory of Disordered Statistical Systems*. Cambridge University Press, Cambridge, England, 2001. 3, 16

[EA75] S. F. Edwards and P. W. Anderson. Theory of spin glasses. *Journal of Physics F: Metal Physics*, 5:965, 1975. 4, 5, 13, 14, 59

[ED05] David J. Earl and Michael W. Deem. Parallel tempering: Theory, applications, and new perspectives. *Phys. Chem. Chem. Phys.*, 7:3910–3916, 2005. 20

[ESW08a] Denis J. Evans, Debra J. Searles, and Stephen R. Williams. Erratum: On the fluctuation theorem for the dissipation function and its connection with response theory. *J. Chem. Phys.*, 128:249901, 2008. 27

[ESW08b] Denis J. Evans, Debra J. Searles, and Stephen R. Williams. On the fluctuation theorem for the dissipation function and its connection with response theory. *J. Chem. Phys.*, 128:014504, 2008. 27

[ET94] B. Efron and R. J. Tibshirani. *An Introduction to Bootstrap*. Chapman & Hall/CRC, London, 1994. 101

[FB72] Michael E. Fisher and Michael N. Barber. Scaling theory for finite-size effects in the critical region. *Phys. Rev. Lett.*, 28:1516–1519, Jun 1972. 109

[FF67] Michael E. Fisher and Arthur E. Ferdinand. Interfacial, boundary, and size effects at critical points. *Phys. Rev. Lett.*, 19:169–172, Jul 1967. 109

[FG88] H Freund and P Grassberger. Multispin coding for spin glasses. *Journal of Physics A: Mathematical and General*, 21(16):L801, 1988. 5

[FH86] D. S. Fisher and D. A. Huse. Ordered phase of short-range ising spin-glasses. *Phys. Rev. Lett.*, 56:1601, Apr 1986. 16, 59, 66

[FH88a] D. S. Fisher and D. A. Huse. *Phys. Rev. B*, 38:386, 1988. 16, 59, 66

[FH88b] Daniel S. Fisher and David A. Huse. Nonequilibrium dynamics of spin glasses. *Phys. Rev. B*, 38:373–385, Jul 1988. 4, 16, 59, 66

[FH91] K.H. Fisher and J.A. Hertz. *Spin Glasses.* Cambridge University Press, Cambridge England, 1991. 3

[FH93] K. H. Fischer and J. A. Hertz. *Spin Glasses.* Cambridge University Press, 1993. 59, 66

[Fis92] Daniel S. Fisher. Random transverse field ising spin chains. *Phys. Rev. Lett.*, 69:534–537, Jul 1992. 96, 113, 114

[FMM13] Nikolaos G. Fytas and Víctor Martín-Mayor. Universality in the three-dimensional random-field ising model. *Phys. Rev. Lett.*, 110:227201, May 2013. 96

[FMM15] Luis Antonio Fernández and Víctor Martín-Mayor. Testing statics-dynamics equivalence at the spin-glass transition in three dimensions. *Phys. Rev. B*, 91:174202, May 2015. 46, 151, 159

[FMMM$^+$16] L. A. Fernandez, E. Marinari, V. Martin-Mayor, G. Parisi, and J. J. Ruiz-Lorenzo. Universal critical behavior of the two-dimensional ising spin glass. *Phys. Rev. B*, 94:024402, Jul 2016. 96

[FMMM$^+$18] L. A. Fernández, E. Marinari, V. Martín-Mayor, G. Parisi, and J.J. Ruiz-Lorenzo. Out-of-equilibrium 2d ising spin glass: almost, but not quite, a free-f ield theory. *Journal of Statistical Mechanics: Theory and Experiment*, 2018(10):103301, 2018. 163

[FMMM$^+$19] L. A. Fernández, E. Marinari, V. Martín-Mayor, G. Parisi, and J.J. Ruiz-Lorenzo. An experiment-oriented analysis of 2d spin-glass dynamics: a twelve time-decades scaling study. *Journal of Physics A: Mathematical and Theoretical*, 52:224002, 2019. 46, 48, 76, 91, 163

[FMMP$^+$19] Nikolaos G. Fytas, Víctor Martín-Mayor, Giorgio Parisi, Marco Picco, and Nicolas Sourlas. Evidence for supersymmetry in the random-field ising model at $d = 5$. *Phys. Rev. Lett.*, 122:240603, Jun 2019. 96

[FMMPG$^+$09] L. A. Fernandez, V. Martín-Mayor, S. Perez-Gaviro, A. Tarancon, and A. P. Young. Phase transition in the three dimensional Heisenberg spin glass: Finite-size scaling analysis. *Phys. Rev. B*, 80:024422, 2009. 3

[FMMPS13] L. A. Fernandez, V. Martín-Mayor, G. Parisi, and B. Seoane. Temperature chaos in 3d ising spin glasses is driven by rare events. *EPL*, 103(6):67003, 2013. 116

[FMMPS16] Nikolaos G. Fytas, Víctor Martín-Mayor, Marco Picco, and Nicolas Sourlas. Phase transitions in disordered systems: The example of the random-field ising model in four dimensions. *Phys. Rev. Lett.*, 116:227201, Jun 2016. 96

[FP85] U Frisch and G. Parisi. On the singularity structure of fully developed turbulence. In M. Ghil, R. Benzi, and G. Parisi, editors, *Turbulence and predictability in geophysical fluid dynamics and climate dynamics (1983 International School of Physics "Enrico Fermi", Varenna)*. North-Holland, Amsterdam, 1985. 73

[FS85] D. S. Fisher and H. Sompolinsky. Scaling in spin-glasses. *Phys. Rev. Lett.*, 54:1063, 1985. 59, 66

[GAPML$^+$21] Isidoro González-Adalid Pemartín, Emanuel Mompó, Antonio Lasanta, Víctor Martín-Mayor, and Jesús Salas. Slow growth of magnetic domains helps fast evolution routes for out-of-equilibrium dynamics. *Phys. Rev. E*, 104:044114, Oct 2021. 51, 53, 54, 55

[Gar85] E. Gardner. Spin glasses with p-spin interactions. *Nuclear Physics B*, 257:747–765, 1985. 3, 59

[GBH94] Muyu Guo, R. N. Bhatt, and David A. Huse. Quantum critical behavior of a three-dimensional ising spin glass in a transverse magnetic field. *Phys. Rev. Lett.*, 72:4137–4140, Jun 1994. 96, 115

[Gil77] D. T. Gillespie. Exact stochastic simulation of coupled chemical reactions. *J. Phys. Chem.*, 81:2340–2361, 1977. 157

[GKS85] D. J. Gross, I. Kanter, and H. Sompolinsky. Mean-field theory of the potts glass. *Phys. Rev. Lett.*, 55:304–307, Jul 1985. 61

[GL76] G. Grinstein and A. Luther. Application of the renormalization group to phase transitions in disordered systems. *Phys. Rev. B*, 13:1329–1343, Feb 1976. 96

[GLH19] A. Gijón, A. Lasanta, and E. R. Hernández. Paths towards equilibrium in molecular systems: The case of water. *Phys. Rev. E*, 100(3):032103, 2019. 27, 45

[GLL18] K. Geirhos, P. Lunkenheimer, and A. Loidl. Johari-goldstein relaxation far below T_g: Experimental evidence for the gardner transition in structural glasses? *Phys. Rev. Lett.*, 120:085705, Feb 2018. 59

[GOJP$^+$22] David Guéry-Odelin, Chris Jarzynski, Carlos A Plata, Antonio Prados, and Emmanuel Trizac. Driving rapidly while remaining in control:

classical shortcuts from hamiltonian to stochastic dynamics. *Rep. Prog. Phys.*, 86:035902, 2022. 27

[GR20] A. Gal and O. Raz. Precooling strategy allows exponentially faster heating. *Phys. Rev. Lett.*, 124:060602, Feb 2020. 27, 37, 43, 45

[GSN$^+$91] K. Gunnarsson, P. Svedlindh, P. Nordblad, L. Lundgren, H. Aruga, and A. Ito. Static scaling in a short-range Ising spin glass. *Phys. Rev. B*, 43:8199–8203, 1991. 4, 8, 59

[GTD19] Hayato Goto, Kosuke Tatsumura, and Alexander R. Dixon. Combinatorial optimization by simulating adiabatic bifurcations in nonlinear hamiltonian systems. *Science Advances*, 5(4):eaav2372, 2019. 95

[Har01] D. Harte. *Multifractals. Theory and applications.* Chapman and Hall/CRC, New York, 1st edition, 2001. 73

[HC20] Andrew P. Hammond and Eric I. Corwin. Experimental observation of the marginal glass phase in a colloidal glass. *Proceedings of the National Academy of Sciences*, 117(11):5714–5718, 2020. 59

[HH77] P. Hohenberg and B. Halperin. Theory of dynamic critical phenomena. *Rev. Mod. Phys.*, 49:435–479, Jul 1977. 46, 53, 55

[HJK$^+$86a] Thomas C. Halsey, Mogens H. Jensen, Leo P. Kadanoff, Itamar Procaccia, and Boris I. Shraiman. Erratum: Fractal measures and their singularities: The characterization of strange sets [phys. rev. a 33, 1141 (1986)]. *Phys. Rev. A*, 34:1601–1601, Aug 1986. 73

[HJK$^+$86b] Thomas C. Halsey, Mogens H. Jensen, Leo P. Kadanoff, Itamar Procaccia, and Boris I. Shraiman. Fractal measures and their singularities: The characterization of strange sets. *Phys. Rev. A*, 33:1141–1151, Feb 1986. 73, 79, 81

[HK05] Koji Hukushima and Hikaru Kawamura. Monte carlo simulations of the phase transition of the three-dimensional isotropic heisenberg spin glass. *Phys. Rev. B*, 72:144416, Oct 2005. 3

[HKL90] U.T. Höchli, K. Knorr, and A. Loidl. Orientational glasses. *Advances in Physics*, 39(5):405–615, 1990. 3

[HM99] J. Houdayer and O. C. Martin. Ising spin glasses in a magnetic field. *Phys. Rev. Lett.*, 82:4934–4937, Jun 1999. 59

[HM00] J. Houdayer and O. C. Martin. Houdayer and martin reply:. *Phys. Rev. Lett.*, 84:1057–1057, Jan 2000. 59

[HN96] K. Hukushima and K. Nemoto. Exchange Monte Carlo method and application to spin glass simulations. *J. Phys. Soc. Japan*, 65:1604, 1996. 20, 101

[Hop82] J J Hopfield. Neural networks and physical systems with emergent collective computational abilities. *Proceedings of the National Academy of Sciences*, 79(8):2554–2558, 1982. 11

[HPV08] Martin Hasenbusch, Andrea Pelissetto, and Ettore Vicari. Critical behavior of three-dimensional ising spin glass models. *Phys. Rev. B*, 78:214205, Dec 2008. 96

[HR20] J. Höller and N. Read. One-step replica-symmetry-breaking phase below the de almeida–thouless line in low-dimensional spin glasses. *Phys. Rev. E*, 101:042114, Apr 2020. 59, 61, 66, 68, 70

[Hua87] K. Huang. *Statistical Mechanics.* John Wiley and Sons, Hoboken, NJ, second edition, 1987. 135

[IAG+99] Plamen Ch. Ivanov, Luís A. Nunes Amaral, Ary L. Havlin Goldberger, Michael G. Shlomo Rosenblum, Zbigniew R. Struzik, and H. Eugene Stanley. Multifractality in human heartbeat dynamics. *Nature*, 399:461 – 465, 1999. 73

[ID20] Sosuke Ito and Andreas Dechant. Stochastic time evolution, information geometry, and the cramér-rao bound. *Phys. Rev. X*, 10:021056, Jun 2020. 27

[IDL+23] Miguel Ibáñez, Cai Dieball, Antonio Lasanta, Aljaž Godec, and Raúl A Rica. Heating and cooling are fundamentally asymmetric and evolve along distinct pathways. *accepted in Nat. Phys.*, 2023. 27, 37, 43

[IK90] Nobuyasu Ito and Yasumasa Kanada. Monte Carlo simulation of the Ising model and random number generation on the vector processor. In *Proceedings SUPERCOMPUTING '90*, pages 753 – 763, 1990. 151, 155, 160

[Ist00] S. Istrail. Statistical mechanics, three-dimensionality and np-completeness: I. universality of intracatability for the partition function of the ising model across non-planar surfaces (extended abstract). In *Proceedings of the thirty-second annual ACM symposium on Theory of computing*, pages 87–96, 2000. 11, 21, 95

[J+11] M. W Johnson et al. Quantum annealing with manufactured spins. *Nature*, 473:194–198, 2011. 21, 95

[Jen06] Monwhea Jeng. The mpemba effect: When can hot water freeze faster than cold? *American Journal of Physics*, 74(6):514–522, 2006. 27

[JGFJ93] J.C. Ciria, G. Parisi, F. Ritort, and J.J. Ruiz-Lorenzo. The de almeida-thouless line in the four dimensional ising spin glass. *J. Phys. I France*, 3(11):2207–2227, 1993. 59

[JR81] L. Jacobs and C. Rebbi. Multi-spin coding: A very efficient technique for monte carlo simulations of spin systems. *J.Comput.Phys.*, 41:203, 1981. 149

[JVH+98] K. Jonason, E. Vincent, J. Hammann, J. P. Bouchaud, and P. Nordblad. Memory and chaos effects in spin glasses. *Phys. Rev. Lett.*, 81:3243–3246, Oct 1998. 10, 76, 83

[KAHR79] A. J. Kovacs, J. J. Aklonis, J. M. Hutchinson, and A. R. Ramos. Isobaric volume and enthalpy recovery of glasses. ii. a transparent multiparameter theory. *Journal of Polymer Science: Polymer Physics Edition*, 17(7):1097–1162, 1979. 54

[Kas56] Tadao Kasuya. A Theory of Metallic Ferro- and Antiferromagnetism on Zener's Model. *Progress of Theoretical Physics*, 16(1):45–57, 07 1956. 3, 12

[Kaw98] H. Kawamura. Dynamical simulation of spin-glass and chiral-glass orderings in three-dimensional heisenberg spin glasses. *Phys. Rev. Lett.*, 80:5421–5424, Jun 1998. 3

[KB63] Michael W. Klein and Robert Brout. Statistical mechanics of dilute copper manganese. *Phys. Rev.*, 132:2412–2426, Dec 1963. 3

[KB20] Avinash Kumar and John Bechhoefer. Exponentially faster cooling in a colloidal system. *Nature*, 584(7819):64, 2020. 27, 43

[KCB22] Avinash Kumar, Raphaël Chétrite, and John Bechhoefer. Anomalous heating in a colloidal system. *Proc. Natl. Acad. Sci. U.S.A.*, 119:e2118484119, 2022. 27

[KGV83] S. Kirkpatrick, C. D. Gelatt, and M. P. Vecchi. Optimization by simulated annealing. *Science*, 220(4598):671–680, 1983. 5, 20

[KH88] Koper, G.J.M. and Hilhorst, H.J. A domain theory for linear and nonlinear aging effects in spin glasses. *J. Phys. France*, 49(3):429–443, 1988. 4

[KL51] S Kullback and R A Leibler. On information and sufficiency. *Ann. Math. Statist.*, 22(22):79, 1951. 43

[Klo14] Abigail Klopper. Multifractal mating. *Nature Physics*, 10(3):183–183, Mar 2014. 73

[KN98] Tadashi Kadowaki and Hidetoshi Nishimori. Quantum annealing in the transverse ising model. *Phys. Rev. E*, 58:5355–5363, Nov 1998. 21, 95

[Kny16] Sergey Knysh. Zero-temperature quantum annealing bottlenecks in the spin-glass phase. *Nature communications*, 7(1):12370, 2016. 116

[Kog79] John B. Kogut. An introduction to lattice gauge theory and spin systems. *Rev. Mod. Phys.*, 51:659–713, Oct 1979. 100, 104

[Kou60] J. S. Kouvel. Exchange Anisotropy in Cu-Mn and Ag-Mn Alloys. *Journal of Applied Physics*, 31(5):S142–S147, 1960. 3

[Kou61] J.S. Kouvel. The ferromagnetic-antiferromagnetic properties of copper-manganese and silver-manganese alloys. *Journal of Physics and Chemistry of Solids*, 21(1):57–70, 1961. 3

[KRHV19] Israel Klich, Oren Raz, Ori Hirschberg, and Marija Vucelja. Mpemba index and anomalous relaxation. *Phys. Rev. X*, 9:021060, Jun 2019. 27, 45

[KRL$^+$23] Andrew D King, Jack Raymond, Trevor Lanting, Richard Harris, Alex Zucca, Fabio Altomare, Andrew J Berkley, Kelly Boothby, Sara Ejtemaee, Colin Enderud, et al. Quantum critical dynamics in a 5,000-qubit programmable spin glass. *Nature*, pages 1–6, 2023. 21, 95, 96, 116

[KTHT06] Helmut G Katzgraber, Simon Trebst, David A Huse, and Matthias Troyer. Feedback-optimized parallel tempering monte carlo. *Journal of Statistical Mechanics: Theory and Experiment*, 2006(03):P03018, 2006. 20

[Kub66] R Kubo. The fluctuation-dissipation theorem. *Rep. Prog. Phys.*, 29(255):035902, 1966. 27

[KW41a] H. A. Kramers and G. H. Wannier. Statistics of the two-dimensional ferromagnet. part i. *Phys. Rev.*, 60:252–262, Aug 1941. 135

[KW41b] H. A. Kramers and G. H. Wannier. Statistics of the two-dimensional ferromagnet. part ii. *Phys. Rev.*, 60:263–276, Aug 1941. 135

[KW18] Hamid Khoshbakht and Martin Weigel. Domain-wall excitations in the two-dimensional ising spin glass. *Phys. Rev. B*, 97:064410, Feb 2018. 116

[Lan50] Cornelius Lanczos. An iteration method for the solution of the eigenvalue problem of linear differential and integral operators. *J. Res. Natl. Bur. Stand. B*, 45:255–282, 1950. 145

[LB05] D. P. Landau and K. Binder. *A Guide to Monte Carlo Simulations in Statistical Physics*. Cambridge University Press, Cambridge, second edition, 2005. 46

[Lev44] Kenneth Levenberg. A method for the solution of certain non – linear problems in least squares. *Quarterly of Applied Mathematics*, 2:164–168, 1944. 168

[LG20] Alessio Lapolla and Alja ž Godec. Faster uphill relaxation in thermodynamically equidistant temperature quenches. *Phys. Rev. Lett.*, 125:110602, Sep 2020. 27, 37

[LKMY13] Derek Larson, H. G. Katzgraber, M. A. Moore, and A. P. Young. Spin glasses in a field: Three and four dimensions as seen from one space dimension. *Phys. Rev. B*, 87:024414, 2013. 59

[LP17] David A Levin and Yuval Peres. *Markov chains and mixing times*, volume 107. American Mathematical Soc., 2017. 28, 29, 30, 40, 144

[LPRTRL08] L. Leuzzi, G. Parisi, F. Ricci-Tersenghi, and J. J. Ruiz-Lorenzo. Dilute one-dimensional spin glasses with power law decaying interactions. *Phys. Rev. Lett.*, 101:107203, Sep 2008. 59

[LPRTRL09] L. Leuzzi, G. Parisi, F. Ricci-Tersenghi, and J. J. Ruiz-Lorenzo. Ising spin-glass transition in a magnetic field outside the limit of validity of mean-field theory. *Phys. Rev. Lett.*, 103:267201, 2009. 59

[LPRTRL11] L. Leuzzi, G. Parisi, F. Ricci-Tersenghi, and J.J. Ruiz-Lorenzo. Bond diluted levy spin-glass model and a new finite-size scaling method to determine a phase transition. *Philosophical Magazine*, 91(13-15):1917–1925, 2011. 59

[LR17] Zhiyue Lu and Oren Raz. Nonequilibrium thermodynamics of the markovian mpemba effect and its inverse. *Proceedings of the National Academy of Sciences*, 114(20):5083–5088, 2017. 27, 36, 37, 45

[LSB83] L. Lundgren, P. Svedlindh, and O. Beckman. Anomalous time dependence of the susceptibility in a Cu(Mn) spin glass. *J. Magn. Magn. Mater.*, 31–34:1349, 1983. 9

[LVRPS17] Antonio Lasanta, Francisco Vega Reyes, Antonio Prados, and Andrés Santos. When the hotter cools more quickly: Mpemba effect in granular fluids. *Phys. Rev. Lett.*, 119:148001, Oct 2017. 27, 45

[Mar60] W. Marshall. Specific heat of dilute alloys. *Phys. Rev.*, 118:1519–1523, Jun 1960. 3, 12

[Mar98] E. Marinari. Optimized Monte Carlo methods. In J. Kerstész and I. Kondor, editors, *Advances in Computer Simulation*. Springer-Verlag, 1998. 20

[McC69] Barry M. McCoy. Theory of a two-dimensional ising model with random impurities. iii. boundary effects. *Phys. Rev.*, 188:1014–1031, Dec 1969. 96, 113, 114

[McM84] W. L. McMillan. *J. Phys. C: Solid State Phys.*, 17:3179, 1984. 16

[MF20] C. McGeoch and P. Farré. The d-wave advantage system: an overview. *D-Wave Technical Report Series*, 2020. 21, 95

[MFR16] D. A. Matoz-Fernandez and F. Romá. Unconventional critical activated scaling of two-dimensional quantum spin glasses. *Phys. Rev. B*, 94:024201, Jul 2016. 97, 115

[MG21] Javier Moreno-Gordo. *Deepening the knowledge of Spin Glasses: Metastate, Off-equilibrium phenomena and Temperature Chaos.* PhD thesis, 2021. 5, 9, 10, 20

[MLCL+21] E. Mompó, M. A. López-Castaño, A. Lasanta, F. Vega Reyes, and A. Torrente. Memory effects in a gas of viscoelastic particles. *Phys. Fluids*, 33(6):062005, 2021. 27

[MM83] A.F.J. Morgownik and J.A. Mydosh. Analysis of the high-temperature spin-glass susceptibility: Determination of the local magnetic exchange. *Solid State Communications*, 47(5):321–324, 1983. 12

[MMH15] V. Martín-Mayor and I. Hen. Unraveling quantum annealers using classical hardness. *Scientific Reports*, 5:15324, October 2015. 116

[MMH+16] Peter L. McMahon, Alireza Marandi, Yoshitaka Haribara, Ryan Hamerly, Carsteñ Langrock, Shuhei Tamate, Takahiro Inagaki, Hiroki

Takesue, Shoko Utsunomiya, Robert L. Aihara, Kazuyuki an d Byer, M. M. Fejer, Hideo Mabuchi, and Yoshihisa Yamamoto. A fully programmable 100-spin coherent ising machine with all-to-all connections. *Science*, 354(6312):614–617, 2016. 95

[MMMH16] Jeffrey Marshall, Victor Martin-Mayor, and Itay Hen. Practical engineering of hard spin-glass instances. *Phys. Rev. A*, 94:012320, Jul 2016. 116

[MMMP$^+$23] E. Marinari, V. Martin-Mayor, G. Parisi, F. Ricci-Tersenghi, and J. J. Ruiz-Lorenzo. Multiscaling in the 3d critical site-diluted ising ferromagnet, 2023. 77

[MN13] Ryoji Miyazaki and Hidetoshi Nishimori. Real-space renormalization-group approach to the random transverse-field ising model in finite dimensions. *Phys. Rev. E*, 87:032154, Mar 2013. 97, 113, 115

[MNZ$^+$98] E. Marinari, C. Naitza, F. Zuliani, G. Parisi, M. Picco, and F. Ritort. General method to determine replica symmetry breaking transitions. *Phys. Rev. Lett.*, 81:1698–1701, Aug 1998. 59

[MO69] E. B. Mpemba and D. G. Osborne. Cool? *Physics Education*, 4(3):172–175, 1969. 27, 45

[MP01] M. Mézard and G. Parisi. *Eur. Phys. J. B*, 20:217, 2001. 65

[MP13] A. Malakis and T. Papakonstantinou. Comparative study of selected parallel tempering methods. *Phys. Rev. E*, 88:013312, Jul 2013. 20

[MPRL98] E. Marinari, G. Parisi, and J. J. Ruiz-Lorenzo. Numerical Simulations of Spin Glass Systems. In A. P. Young, editor, *Spin glasses and random fields*. World Scientific, Singapore, 1998. 59

[MPRLR96] E. Marinari, G. Parisi, J. Ruiz-Lorenzo, and F. Ritort. Numerical evidence for spontaneously broken replica symmetry in 3d spin glasses. *Phys. Rev. Lett.*, 76:843–846, Jan 1996. 45

[MPRV08] Umberto Marini Bettolo Marconi, Andrea Puglisi, Lamberto Rondoni, and Angelo Vulpiani. Fluctuation?dissipation: Response theory in statistical physics. *Phys. Rep.*, 461(4-6):111, 2008. 27

[MPS$^+$84a] M. Mézard, G. Parisi, N. Sourlas, G. Toulouse, and M.A. Virasoro. Nature of the spin-glass phase. *Phys. Rev. Lett.*, 52:1156, 1984. 4

[MPS$^+$84b] M. Mézard, G. Parisi, N. Sourlas, G. Toulouse, and M.A. Virasoro. Replica symmetry breaking and the nature of the spin glass phase. *J. Phys. France*, 45:843–854, 1984. 7

[MPV87] M. Mézard, G. Parisi, and M. Virasoro. *Spin-Glass Theory and Beyond*. World Scientific, Singapore, 1987. 3, 59, 103

[MPZ98] E. Marinari, G. Parisi, and F. Zuliani. Four-dimensional spin glasses in a magnetic field have a mean-field-like phase. *J. Phys. A: Math. and Gen.*, 31:1181, 1998. 59

[MPZ00] E. Marinari, G. Parisi, and F. Zuliani. Comment on “ising spin glasses in a magnetic field”. *Phys. Rev. Lett.*, 84:1056–1056, Jan 2000. 59

[MR18] M. A. Moore and N. Read. Multicritical point on the de almeida–thouless line in spin glasses in $d > 6$ dimensions. *Phys. Rev. Lett.*, 120:130602, Mar 2018. 61

[MTM$^+$20] Satoshi Matsubara, Motomu Takatsu, Toshiyuki Miyazawa, Takayuki Shibasaki, Kazuya Watanabe, Yasuhiro a nd Takemoto, and Hirotaka Tamura. Digital annealer for high-speed solving of combinatorial optimization problems and its applications. In *2020 25th Asia and South Pacific Design Automation Conference (ASP-DAC)*, pages 667–672, 2020. 95

[MvDM81] C. A. M. Mulder, A. J. van Duyneveldt, and J. A. Mydosh. Susceptibility of the CuMn spin-glass: Frequency and field dependences. *Phys. Rev. B*, 23:1384–1396, Feb 1981. 4

[MvDM82] C. A. M. Mulder, A. J. van Duyneveldt, and J. A. Mydosh. Frequency and field dependence of the ac susceptibility of the AuMn spin-glass. *Phys. Rev. B*, 25:515–518, Jan 1982. 4

[MW68] Barry M. McCoy and Tai Tsun Wu. Theory of a two-dimensional ising model with random impurities. i. thermodynamics. *Phys. Rev.*, 176:631–643, Dec 1968. 96, 113, 114

[MW69] Barry M. McCoy and Tai Tsun Wu. Theory of a two-dimensional ising model with random impurities. ii. spin correlation functions. *Phys. Rev.*, 188:982–1013, Dec 1969. 96

[MW73] B. M. McCoy and T. T. Wu. *The Two Dimensional Ising Model.* Harvard University Press, Cambridge, 1973. 46, 50

[Myd93] J. A. Mydosh. *Spin Glasses: an Experimental Introduction.* Taylor and Francis, London, 1993. 3, 59, 75

[Nat98] T. Nattermann. Theory of the Random Field Ising Model. In A. P. Young, editor, *Spin glasses and random fields.* World Scientific, Singapore, 1998. 6

[NB99] M. E. J. Newman and G. T. Barkema. *Monte Carlo Methods in Statistical Physics.* Clarendon Press, Oxford, 1999. 159

[NF19] Andrea Nava and Michele Fabrizio. Lindblad dissipative dynamics in the presence of phase coexistence. *Phys. Rev. B*, 100:125102, Sep 2019. 27, 45

[Nig76] M.P Nightingale. Scaling theory and finite systems. *Physica A: Statistical Mechanics and its Applications*, 83(3):561 – 572, 1976. 109

[NSLS86] P. Nordblad, P. Svedlindh, L. Lundgren, and L. Sandlund. Time decay of the remanent magnetization in a cumn spin glass. *Phys. Rev. B*, 33:645–648, Jan 1986. 9

[Nyq28] H Nyquist. Thermal agitation of electric charge in conductors. *Phys. Rev.*, 32:110, 1928. 27

[OAH85] M. Ocio, M. Alba, and J. Hammann. Time scaling of the ageing process in spin-glasses : a study in CsNiFeF 6. *Journal de Physique Lettres*, 46(23):1101–1107, 1985. 9

[OBKK56] J. Owen, M. Browne, W. D. Knight, and C. Kittel. Electron and nuclear spin resonance and magnetic susceptibility experiments on dilute alloys of mn in cu. *Phys. Rev.*, 102:1501–1507, Jun 1956. 3

[OHV90] M. Ocio, J. Hammann, and E. Vincent. Towards a phenomenological cluster picture for the spin-glass phase. *Journal of Magnetism and Magnetic Materials*, 90-91:329–330, 1990. 4

[Ons31a] Lars Onsager. Reciprocal relations in irreversible processes. i. *Phys. Rev.*, 27:405, 1931. 27

[Ons31b] Lars Onsager. Reciprocal relations in irreversible processes. ii. *Phys. Rev.*, 38:2265, 1931. 27

[Ons44] Lars Onsager. Crystal statistics. i. a two-dimensional model with an order-disorder transition. *Phys. Rev.*, 65:117–149, Feb 1944. 46, 48, 49

[Pag21] I. Paga. *From glassy bulk systems to spin-glass films:simulations meet experiments*. PhD thesis, 2021. 5

[Pap94] C. Papadimitriou. *Computational Complexity*. Addison-Wesley, Readings, 1994. 11, 21

[Par79a] G. Parisi. Infinite number of order parameters for spin-glasses. *Phys. Rev. Lett.*, 43:1754–1756, Dec 1979. 4, 15, 16, 96

[Par79b] G. Parisi. Toward a mean field theory for spin glasses. *Phys. Lett.*, 73A:203, 1979. 16

[Par80] G. Parisi. The order parameter for spin glasses: a function on the interval 0-1. *J. Phys. A: Math. Gen.*, 13:1101, 1980. 16

[Par88] G. Parisi. *Statistical Field Theory*. Addison-Wesley, 1988. 35, 38, 45, 48, 49, 55, 62, 63, 73, 100, 104, 135

[Par94] G. Parisi. *Field Theory, Disorder and Simulations*. World Scientific, 1994. 97

[Par23] Giorgio Parisi. Nobel lecture: Multiple equilibria. *Rev. Mod. Phys.*, 95:030501, Aug 2023. 3

[PC99] M. Palassini and S. Caracciolo. Universal finite-size scaling functions in the 3D Ising spin glass. *Phys. Rev. Lett.*, 82:5128–5131, 1999. 23, 103

[PR13] Giorgio Parisi and Tommaso Rizzo. Critical dynamics in glassy systems. *Phys. Rev. E*, 87:012101, Jan 2013. 59, 60, 61, 63, 64, 70, 171

[PRTR14] G Parisi, F Ricci-Tersenghi, and T Rizzo. Diluted mean-field spin-glass models at criticality. *Journal of Statistical Mechanics: Theory and Experiment*, 2014(4):P04013, apr 2014. 65, 66

[PRTRL98] G. Parisi, F. Ricci-Tersenghi, and J. J. Ruiz-Lorenzo. Dynamics of the four-dimensional spin glass in a magnetic field. *Phys. Rev. B*, 57:13617, 1998. 59

[PS79] G. Parisi and N. Sourlas. Random magnetic fields, supersymmetry, and negative dimensions. *Phys. Rev. Lett.*, 43:744–745, Sep 1979. 96

[PT02] G. Parisi and Francesca Tria. Spin glasses on bethe lattices for large coordination number. *Eur. Phys. J. B*, 30:533–541, 2002. 65

[PZBJ$^+$21] I. Paga, Q. Zhai, M. Baity-Jesi, E. Calore, A. Cruz, L. A. Fernandez, J. M. Gil-Narvion, I. Gonzalez-Adalid Pemartin, A. Gordillo-Guerrero, D. Iñiguez, A. Maiorano, E. Marinari, V. Martin-Mayor, J. Moreno-Gordo, A. Muñoz-Sudupe, D. Navarro, R. L. Orbach, G. Parisi, S. Perez-Gaviro, F. Ricci-Tersenghi, J. J. Ruiz-Lorenzo, S. F. Schifano, D. L. Schlagel, B. Seoane, A. Tarancon, R. Tripiccione, and D. Yllanes. Spin-glass dynamics in the presence of a magnetic field: exploration of microscopic properties. *Journal of Statistical Mechanics: Theory and Experiment*, 2021(3):033301, mar 2021. 5, 17, 45, 73, 76

[PZBJ$^+$23] I. Paga, Q. Zhai, M. Baity-Jesi, E. Calore, A. Cruz, C. Cummings, L. A. Fernandez, J. M. Gil-Narvion, I. Gonzalez-Adalid Pemartin, A. Gordillo-Guerrero, D. Iñiguez, G. G. Kenning, A. Maiorano, E. Marinari, V. Martin-Mayor, J. Moreno-Gordo, A. Muñoz Sudupe, D. Navarro, R. L. Orbach, G. Parisi, S. Perez-Gaviro, F. Ricci-Tersenghi, J. J. Ruiz-Lorenzo, S. F. Schifano, D. L. Schlagel, B. Seoane, A. Tarancon, and D. Yllanes. Superposition principle and nonlinear response in spin glasses. *Phys. Rev. B*, 107:214436, Jun 2023. 5, 17, 45

[RAS86] D. S. Rokhsar, P. W. Anderson, and D. L. Stein. Self-organization in prebiological systems: Simulations of a model for the origin of genetic information. *Journal of Molecular Evolution*, 23(2):119–126, Jun 1986. 11

[Riz13] Tommaso Rizzo. Replica-symmetry-breaking transitions and off-equilibrium dynamics. *Phys. Rev. E*, 88:032135, Sep 2013. 61

[RK54] M. A. Ruderman and C. Kittel. Indirect exchange coupling of nuclear magnetic moments by conduction electrons. *Phys. Rev.*, 96:99–102, Oct 1954. 3

[RSS94] H. Rieger, B. Steckemetz, and M. Schreckenberg. Aging and domain growth in the two-dimensional ising spin glass model. *EPL (Europhysics Letters)*, 27(6):485, 1994. 17

[RY94] H. Rieger and A. P. Young. Zero-temperature quantum phase transition of a two-dimensional ising spin glass. *Phys. Rev. Lett.*, 72:4141–4144, Jun 1994. 96, 97, 102, 103, 109, 111, 113, 115

[RY96] H. Rieger and A. P. Young. Griffiths singularities in the disordered phase of a quantum ising spin glass. *Phys. Rev. B*, 54:3328–3335, Aug 1996. 96, 115

[SCM00] Jairo Sinova, Geoff Canright, and A. H. MacDonald. Nature of ergodicity breaking in ising spin glasses as revealed by correlation function spectral properties. *Phys. Rev. Lett.*, 85:2609–2612, Sep 2000. 102

[Sei12] Udo Seifert. Stochastic thermodynamics, fluctuation theorems and molecular machines. *Rep. Prog. Phys.*, 75:126001, 2012. 27

[SGSN90] S. Caracciolo, G. Parisi, S. Patarnello, and N. Sourlas. Low temperature behaviour of 3-d spin glasses in a magnetic field. *J. Phys. France*, 51(17):1877–1895, 1990. 59

[SGSN91] Sergio Caracciolo, Giorgio Parisi, Stefano Patarnello, and Nicolas Sourlas. On computer simulations for spin glasses to test mean field predictions. *J. Phys. I France*, 1(5):627–628, 1991. 59

[SK75] David Sherrington and Scott Kirkpatrick. Solvable model of a spin-glass. *Phys. Rev. Lett.*, 35:1792–1796, Dec 1975. 4, 15

[SL22] Fabian Jan Schwarzendahl and Hartmun Lowen. Anomalous cooling and overcooling of active colloids. *Phys. Rev. Lett.*, 129:138002, 2022. 27

[SM88] H. Eugene Stanley and Paul Meakin. Multifractal phenomena in physics and chemistry. *Nature*, 335(6189):405–409, Sep 1988. 73

[SMDS11] John K. Salmon, Mark A. Moraes, Ron O. Dror, and David E. Shaw. Parallel random numbers: As easy as 1, 2, 3. In *Proceedings of 2011 International Conference for High Performance Computing, Networking, Storage and Analysis*, SC '11, New York, NY, USA, 2011. Association for Computing Machinery. 161

[SMFD08] Dubravko Sabo, Markus Meuwly, David L. Freeman, and J. D. Doll. A constant entropy increase model for the selection of parallel tempering ensembles. *The Journal of Chemical Physics*, 128(17):174109, 2008. 20

[SO99] Yuji Sugita and Yuko Okamoto. Replica-exchange molecular dynamics method for protein folding. *Chemical Physics Letters*, 314(1–2):141 – 151, 1999. 20

[Sok97] A. D. Sokal. Monte Carlo methods in statistical mechanics: Foundations and new algorithms. In C. DeWitt-Morette, P. Cartier, and A. Folacci, editors, *Functional Integration: Basics and Applications (1996 Cargèse School)*. Plenum, N. Y., 1997. 17, 18, 28, 40, 46, 163, 169

[SS00] Jesús Salas and Alan D. Sokal. Universal amplitude ratios in the critical two-dimensional ising model on a torus. *Journal of Statistical Physics*, 98(3):551–588, 2000. 63

[SS14] L. Seuront and H. E. Stanley. Anomalous diffusion and multifractality enhance mating encounters in the ocean. *Proceedings of the National Academy of Sciences*, 111(6):2206–2211, 2014. 73

[Suz76] Masuo Suzuki. Relationship between d-Dimensional Quantal Spin Systems and (d+1)-Dimensional Ising Systems: Equivalence, Critical Exponents and Systematic Approximants of the Partition Function and Spin Correlations. *Progress of Theoretical Physics*, 56(5):1454–1469, 11 1976. 97, 99, 133, 144

[SY17] R. R. P. Singh and A. P. Young. Critical and griffiths-mccoy singularities in quantum ising spin glasses on d-dimensional hypercubic lattices: A series expansion study. *Phys. Rev. E*, 96:022139, Aug 2017. 97, 115

[TAP77] D. J. Thouless, P. W. Anderson, and R. G. Palmer. Solution of 'solvable model of a spin glass'. *Phil. Mag.*, 35(3):593–601, 1977. 4

[TDD02] T. Temesvári and C. De Dominicis. Replica field theory and renormalization group for the ising spin glass in an external magnetic field. *Phys. Rev. Lett.*, 89:097204, Aug 2002. 59, 61, 66, 67

[TH95] MJ Thill and DA Huse. Equilibrium behaviour of quantum ising spin glass. *Physica A: Statistical Mechanics and its Applications*, 214(3):321–355, 1995. 97, 115

[TLCnL$^+$19] Aurora Torrente, Miguel A. López-Castaño, Antonio Lasanta, Francisco Vega Reyes, Antonio Prados, and Andrés Santos. Large mpemba-like effect in a gas of inelastic rough hard spheres. *Phys. Rev. E*, 99:060901, Jun 2019. 27, 45

[Tou77] G. Toulouse. Theory of the frustration effect in spin glasses. *Communications on Physics*, 2:115, 1977. 98

[Tro59] H. F. Trotter. On the product of semi-groups of operators. *Proc. Amer. Math. Soc.*, 10:545–551, 1959. 97, 99, 133, 144

[TT74] Jean Tholence and Robert Tournier. Susceptibility and remanent magnetization of a spin glass. *http://dx.doi.org/10.1051/jphyscol:1974442*, 35, 05 1974. 4

[VB66] C. E. Violet and R. J. Borg. Magnetic ordering in dilute solid solutions of iron in gold. i. *Phys. Rev.*, 149:540–551, Sep 1966. 3, 4

[VB67] C. E. Violet and R. J. Borg. Magnetic ordering in dilute solid solutions of iron in gold. ii. electric hyperfine interactions. *Phys. Rev.*, 162:608–615, Oct 1967. 3, 4

[Vec21] M. Veca. Numerical estimation of the exponent parameter of a spin glass model defined on random regular graphs in field. Master's thesis, Università La Sapienza-Roma, 2021. 64, 66

[VHO$^+$97] E. Vincent, J. Hammann, M. Ocio, J.-P. Bouchaud, and L. F. Cugliandolo. Slow dynamics and aging in spin glasses. In M. Rubí and C. Pérez-

Vicente, editors, *Complex Behavior of Glassy Systems*, number 492 in Lecture Notes in Physics. Springer, 1997. 8, 9, 73

[Wan50] G. H. Wannier. Antiferromagnetism. the triangular ising net. *Phys. Rev.*, 79:357–364, Jul 1950. 6

[Wil79] Kenneth G. Wilson. Problems in Physics with many Scales of Length. *Scientific American*, 241(2):158–179, August 1979. 73

[WK74] K. G. Wilson and J. Kogut. The renormalization group and the ϵ-expansion. *Physics Reports*, 12(2):75 – 199, 1974. 60

[WV21] Matthew R Walker and Marija Vucelja. Anomalous thermal relaxation of langevin particles in a piecewise-constant potential. *J. Stat. Mech.*, 2021:113105, 2021. 27

[Yan62] C. N. Yang. Concept of off-diagonal long-range order and the quantum phases of liquid he and of superconductors. *Rev. Mod. Phys.*, 34:694–704, Oct 1962. 102

[YK04] A. P. Young and H. G. Katzgraber. Absence of an Almeida-Thouless line in three-dimensional spin glasses. *Phys. Rev. Lett.*, 93:207203, 2004. 59

[Yll11] D. Yllanes. *Rugged Free-Energy Landscapes in Disordered Spin Systems.* PhD thesis, Universidad Complutense de Madrid, 2011. 81, 83, 92, 111

[Yos57] K. Yosida. Magnetic properties of cu-mn alloys. *Phys. Rev.*, 106:893–898, Jun 1957. 3, 12

[You98] A. P. Young. *Spin Glasses and Random Fields.* World Scientific, Singapore, 1998. 3, 59

[You12] A. P. Young. Everything you wanted to know about data analysis and fitting but were afraid to ask. School on ”Efficient Algorithms in Computational Physics”, Bad Honnef, September 2012. 167, 168

[Zim60] J.E. Zimmerman. Low-temperature specific heat of dilute cu-mn alloys. *J. Phys. Chem. Solids*, 17:52–56, December 1960. An additional author, F.E. Hoare, appears in Edwards' citation of this article. 3, 5, 7, 8

[ZJ05] J. Zinn-Justin. *Quantum Field Theory and Critical Phenomena.* Clarendon Press, Oxford, fourth edition, 2005. 45, 48, 62, 63

[ZOS22] Qiang Zhai, Raymond L. Orbach, and Deborah L. Schlagel. Evidence for temperature chaos in spin glasses. *Phys. Rev. B*, 105:014434, Jan 2022. 5, 76

[ZPBJ+20] Q. Zhai, I. Paga, M. Baity-Jesi, E. Calore, A. Cruz, L. A. Fernandez, J. M. Gil-Narvion, I. Gonzalez-Adalid Pemartin, A. Gordillo-Guerrero, D. Iñiguez, A. Maiorano, E. Marinari, V. Martin-Mayor, J. Moreno-Gordo, A. Muñoz Sudupe, D. Navarro, R. L. Orbach, G. Parisi, S. Perez-Gaviro, F. Ricci-Tersenghi, J. J. Ruiz-Lorenzo, S. F. Schifano, D. L. Schlagel, B. Seoane, A. Tarancon, R. Tripiccione, and D. Yllanes.

Scaling law describes the spin-glass response in theory, experiments, and simulations. *Phys. Rev. Lett.*, 125:237202, Nov 2020. 5, 17, 45, 73, 76

[Zwa28] Robert Zwanzig. Time-correlation functions and transport coefficients in statistical mechanics. *Annu. Rev. Phys. Chem.*, 16:67, 1928. 27

Acronyms

APBC anti-periodic boundary conditions 99, 101, 105, 106, 108, 109

AuFe Gold-Iron alloy 3

CPU computer processor unit 145–147, 149

CuMn Copper-Manganese alloy v, 3, 7, 8

D dimension 13, 28, 30, 38, 46, 50, 59–61, 65, 66, 68, 95–97, 135, 155, 171

dAT de Almeida-Thouless 59, 61, 65, 67, 70

DIL Ising link-diluted model vi, 74–78, 164, 165

EA Edwards-Anderson model vi, 13, 16, 22, 60, 63, 65–68, 74–79, 81–83, 90, 91, 150, 163–165, 171

ESR spectra electron spin resonance spectroscopy 3

GPU graphic processor unit 20, 101, 115, 145–147, 149

GS ground state 16, 38, 39, 95–99, 102, 104, 106, 107, 109, 112, 116

HB Heat Bath vii, 18–20, 28, 30, 40, 46–49, 51–55, 143

JK jackknife method 167, 168

LGT Landau-Ginsburg theory 60, 61

MC Monte Carlo x, xii, 17, 20, 40–44, 96, 97, 101, 102, 106–108, 120, 149–151, 153–155, 157

MET Metropolis v, vii, 18–20, 46–55

MF mean-field 59–62, 65, 67, 70

MUSA multispin MUlti-SAmple 19, 20, 149, 151

MUSI multispin MUlti-SIte 19, 20, 46, 149, 151, 153, 159, 160

PBC periodic boundary conditions 46, 74, 99–101, 104, 106, 108, 109, 113, 135

pdf probability distribution function 13, 74, 79, 83, 85, 86, 89, 112–115

PM paramagnetic phase 96

PT Parallel Tempering 17, 20, 21, 170

RAM random access memory 145

RFIM Random-Field Ising model 6

RG Renormalization Group 60, 61, 63, 66, 96, 97, 113

RKKY Ruderman-Kittel-Kasuya-Yosida 3, 4, 12

RS replica symmetric 14, 15, 61

RSB replica symmetry breaking 4, 5, 15, 16, 61

SG spin glass v, vi, 3–8, 10, 11, 13, 16, 17, 19–21, 59, 61, 70, 73, 74, 76, 80, 95–98, 116, 119, 122, 135, 143, 144, 149, 151, 154, 155

SK Sherrington-Kirpatrick model 4, 15, 16

SQUID superconducting quantum interference device 4

TAP Thouless-Anderson-Palmer 4, 5

TRM thermo-remanent magnetization 8, 9

ZFC zero-field cooled 9

Glossary

algorithm set of mathematical instructions or rules that, especially if given to a computer, will help to calculate an answer to a problem 5, 46

ansatz initial estimate of the solution to a mathematical or technical problem that is used to guide work to a more precise answer 14, 15, 51, 83

ergodicity property of a system or process, relating to or involving the probability that any state will recur 4

fractal a complicated pattern in mathematics built from simple repeated shapes that are reduced in size every time they are repeated 73

magnetic domain region inside of a material where groups of magnetic moments naturally align in the same direction 4

multifractal referred to a mathematical object that presents more than one fractal behavior 73, 74, 79

multispin coding technique used to accelerate Monte Carlo simulations, mainly in Ising spin systems, by encoding them in one bit 5, 19, 86, 149, 151, 159

qubit in quantum computation, the minimum logic unit 96

quenched refers to some parameters (the couplings) of the system, which are random variables that do not evolve with time 12, 64, 74, 97

replica Copy of a sample that evolves independently vii, 14–16, 22, 41, 46, 47, 64, 65, 67, 74, 75, 79, 84, 86, 101, 149–151, 163, 164, 168, 171, 172

replica method (also known as replica trick) mathematical tool developed by P. Anderson to study systems with quenched disorder 4

sample small amount of a substance that a doctor or scientist collects to examine it 9, 12, 19, 22, 74, 75, 85, 86, 97, 101, 105–108, 112, 114, 115, 149–151, 168–170

simulated annealing probabilistic technique that mimics the annealing process to approximate the global optimum of a given function 5

spin intrinsic form of angular momentum carried by elementary particles, and thus by composite particles such as hadrons, atomic nuclei, and atoms 3, 4

superpolinomically from computation complexity theory, an algorithm which resources or time scales faster than any polynomial of the agents. 97

ultrametric tree special kind of additive tree in which the tips of the tree are all equidistant from the root. 4